

Mechanisms of fatigue crack nucleation near non-metallic inclusions in Ni-based superalloys

Alexander Hoggan Bergsmo

March 2021

A thesis submitted in part fulfilment of the requirements for the degree of

Doctor of Philosophy at Imperial College London

Department of Materials, Imperial College London

Abstract

Ni-based superalloys used for turbine discs are typically produced via powder metallurgy, a process which introduces undesirable non-metallic inclusions. Inclusions can be regarded as fatigue crack nucleation hot-spots due to their differing mechanical properties compared with the matrix they are embedded in. In this thesis, a series of models and experiments were used to investigate the mechanistic drivers of fatigue crack nucleation in the vicinity of non-metallic inclusions.

The drivers of decohesion and fracture of inclusions, often precursors to crack nucleation, were found to be the normal stress acting on the interface and the inclusion maximum principal stress, respectively. Exact values of either criterion were found using a cohesive zone model in a crystal plasticity finite element (CPFE) model faithfully representative of a real microstructure under low cycle fatigue. Decohesion and inclusion fracture were contrasted against slip-driven nucleation by a stored energy criterion. The key finding here was that decohesion and inclusion fracture marginally reduce fatigue life.

The comparative fatigue performance of an inclusion, a twin boundary and a triple-junction were studied in a synthetic CPFE microstructure. The inclusion recorded a significantly lower fatigue life compared with the intrinsic microstructural features. Various hardening models were used to investigate cyclic decohesion in a stress-controlled regime. Under no hardening model was cyclic decohesion predicted, strongly suggesting that decohesion is purely a function of applied stress within the first cycle.

A discontinuity tolerant digital image correlation algorithm was developed to study fatigue crack nucleation near a non-metallic agglomerate at 300°C. Decohesion and fracture of inclusions occurred already within the first cycle of loading. Microcracks nucleated throughout the inclusion agglomerate after 6000 cycles. In addition, a fatigue crack nucleated adjacent a twin boundary in a coarse grain neighbouring the agglomerate. A high (angular) resolution electron backscatter diffraction (HR-EBSD) analysis and a discrete dislocation plasticity (DDP) model suggested that strong build-up of GNDs and slip near twin boundary owes to the elastic anisotropy of twin and parent.

Statement of originality

I hereby declare that the content of this thesis has produced by myself and that the work of others is acknowledged and referenced accordingly.

Copyright Declaration

The copyright of this thesis rests with the author. Unless otherwise indicated, its contents are licensed under a Creative Commons Attribution-Non Commercial 4.0 International Licence (CC BY-NC). Under this licence, you may copy and redistribute the material in any medium or format. You may also create and distribute modified versions of the work. This is on the condition that: you credit the author and do not use it, or any derivative works, for a commercial purpose. When reusing or sharing this work, ensure you make the licence terms clear to others by naming the licence and linking to the licence text. Where a work has been adapted, you should indicate that the work has been changed and describe those changes. Please seek permission from the copyright holder for uses of this work that are not included in this licence or permitted under UK Copyright Law.

Acknowledgements

I would like to sincerely thank my supervisor, Prof Fionn Dunne, for guiding and entertaining my research development the past three and a half years.

The team of students and researchers in the micromechanics team have provided ample discourse in addition to refreshing Friday morning coffee. Dr Ben Britton, Dr Yilun Xu, Dr Liu Yang, Dr Yi Guo (and more) have endured a string of silly questions and back of the envelope calculations (some which became integral to this thesis) and I am forever grateful to them.

The adventures in labs LG55C and D would not have been possible without the helpful hands of Ben Wood. Microscopy would have been frightfully difficult without the keen eyes of Dr Mahmoud Ardakani and Dr Ecaterina Ware.

To the boys and girls of engineering alloys, who, with great intentions, have given endless distractions through crosswords, “*pintinis*”, and last but not least “*coff*”.

I also wish to extend my gratitude to the knowledgeable people of Rolls Royce plc, principally: Dr Mark Hardy, Dr Paul Mignanelli, Dr Duncan Maclachlan, and Dr Iain Parr who have helped tremendously with insightful discussions and encouragement.

My family have encouraged my pursuit of this degree and have, in no small part, inspired me to complete it.

To my lovely partner Rowena, who has endured living with me during the “write-up” stage.

And finally, I am grateful to the coronavirus which has eased the writing of thesis by removing all *distractions*.

Contents

1	Introduction	27
1.1	The contemporary gas turbine.....	27
1.2	On Ni-based superalloys	29
1.3	Objective statement.....	33
2	Literature review.....	34
2.1	Cyclic plastic deformation	34
2.2	Non-metallic inclusions in powder metallurgy alloys.....	41
2.3	Effect of non-metallic inclusions on fatigue performance	45
2.3.1	Inclusion size	46
2.3.2	Inclusion morphology	46
2.3.3	Agglomeration	47
2.3.4	Properties of inclusions.....	48
2.3.5	Surface and subsurface initiations	48
2.3.6	Temperature effect.....	49
2.3.7	Competition with other microstructural features	50
2.4	Cyclic deformation around inclusions.....	50
2.4.1	Inclusion fracture	51
2.4.2	Inclusion decohesion.....	52
2.4.3	Slip-driven nucleation.....	54
2.5	Concluding remarks	56

3	Competing mechanisms of inclusion fracture, decohesion and slip-driven fatigue crack nucleation in a PM Nickel superalloy	57
3.1	Introduction	57
3.2	Methods.....	60
3.2.1	Crystal plasticity finite element formulation	60
3.2.2	Ni-base Superalloy Agglomerate model.....	66
3.2.3	Traction-separation model	69
3.3	Fracture strength of oxide particles	71
3.4	Modelling of metal-oxide interfacial decohesion and particle fracture using cohesive interfaces	78
3.5	Towards fatigue crack nucleation mapping	83
3.6	Summary	89
4	Microstructural feature sensitivity in fatigue crack nucleation in a polycrystalline Nickel superalloy.....	91
4.1	Introduction	91
4.2	Methods.....	93
4.2.1	Crystal plasticity formulation	93
4.2.2	Fatigue crack nucleation criterion.....	93
4.2.3	Microstructural representative volume element.....	94
4.2.4	Modelling non-metallic inclusions	97
4.2.5	Generation of a crack-inducing twin.....	99
4.2.6	Creating comparative features	100

4.3	Competing microstructural features in crack nucleation.....	100
4.4	Slip and stored energy density at twin boundary	104
4.5	Cyclic effects on inclusion decohesion	110
4.5.1	Effect of strain hardening level on inclusion decohesion	111
4.5.2	Kinematic hardening implementation.....	116
4.5.3	Effect of kinematic hardening on inclusion decohesion	118
4.6	Summary	123
5	Development of high temperature three-point bending rig and discontinuity tolerant digital image correlation	124
5.1	Introduction	124
5.2	High temperature three-point bend apparatus	126
5.2.1	IR lamps.....	127
5.2.2	Verification of beam temperature	129
5.3	Discontinuity tolerant digital image correlation.....	133
5.3.1	Coarse-fine method.....	134
5.3.2	Correlation criteria	135
5.3.3	Polynomial surface correction	137
5.3.4	Discontinuity tolerance	140
5.3.5	Determination of strain	143
5.3.6	Discontinuity detection on an artificial image set.....	145
5.4	Summary	148

6	Twin boundary fatigue crack nucleation in a polycrystalline Nickel superalloy containing non-metallic inclusions	150
6.1	Introduction	150
6.2	Methods.....	153
6.2.1	Material	153
6.2.2	Mechanical testing	155
6.2.3	Discontinuity tolerant DIC.....	156
6.2.4	Speckle patterning.....	158
6.2.5	DIC image capture	158
6.2.6	HR-EBSD	159
6.2.7	Crystal plasticity finite element model	160
6.2.8	Discrete dislocation plasticity formulations.....	161
6.3	Strain localisation.....	164
6.4	Cyclic strain behaviour.....	168
6.5	Fatigue crack nucleation at non-metallic inclusions	169
6.6	Fatigue crack nucleation at a twin boundary.....	172
6.7	Intragranular rotation, GNDs, and residual elastic stress.....	175
6.8	DDP modelling of twin boundary	178
6.8.1	On the effect of elastic anisotropy	180
6.9	Discussion	181
6.9.1	Competition between inclusion and twin fatigue crack nucleation	181
6.10	Summary	182

7	Conclusion and outlook.....	184
7.1	Conclusions.....	184
7.2	Future work.....	186

List of figures

Figure 1-1 – A Rolls Royce Plc Trent 800 turbofan jet engine. The turbine section is highlighted in red where Ni-based superalloys are concerned (adapted from [1])	27
Figure 1-2 – (a) Typical superalloy microstructure in single crystal configuration, the cubes are γ' with the channels between being γ . Each γ' cube is about 500 nm wide (kindly provided by Alessandro Piglione). (b) Schematic of polycrystalline microstructure of Udimet U720Li which is representative of typical turbine disc alloy microstructures (courtesy of [7]).....	30
Figure 1-3 – The L12 lattice structure that the γ' exhibits with chemical ordering of Al atoms at corners and Ni atoms at faces	31
Figure 1-4 – A typical non-metallic inclusion in RR1000, a disc alloy produced by powder metallurgy. The inclusion (centre) is surrounded by a coarse grain structure. The etching process used on this sample was extremely coarse and resulted in dislodging of primary γ' seen by dimples at grain boundaries and triple junctions to the to the sides.	32
Figure 2-1 – The S-N curve with labels showing the distinction between HCF and LCF. An endurance limit stress $\sigma_{endurance}$ is also shown.....	35
Figure 2-2 – Cyclic hardening and softening under fixed amplitude stress controlled (a) and strain controlled (b) loading with $R=-1$ (adapted from [17]).....	37
Figure 2-3 – TEM micrograph of the dislocation structure within pure Cu after fatigue loading. The structure consists of the slip band ladder structure and matrix dislocation veins (from [21])	39
Figure 2-4 - Powder metallurgy processing steps (adapted from [1]) (i.) Vacuum induction melting of ingot, (ii.) remelt and atomise (iii.) Sieving the powder through a mesh screen (iv.) Inserting powder into a canister followed by (v.) degassing to remove oxygen and nitrogen then seal the cannister (vi.) The can is then either HIPed or extruded (vii.) A final forging step is used to obtain the near net shape of component	42

Figure 2-5 – (a) SEM of a reactive type inclusion in Rene 95 (adapted from [39]) and (b) discrete non-metallic inclusions which are agglomerated in RR1000	44
Figure 2-6 - An S-N curve showing location of fatigue crack nucleation for several samples. In samples where fatigue cracks originate from inclusions, the life is notably reduced. (adapted from [41]).....	45
Figure 2-7 - Fracture of a TiN inclusions in Udimet 720 and subsequent crack growth. Fracture of inclusions has occurred early between cycle N=0 and N=5000. (adapted from [89])	51
Figure 2-8, (a) a reconstructed microstructural model of a ceramic inclusion with metal-oxide interface highlighted in red where D and D' indicate the start and end point of a perimeter path. (b) The stored energy density around the path D-D' with excerpts showing experimental fatigue crack initiation sites (Adapted from [47]).....	55
Figure 3-1 - Micrographs of (a) particle fracture in Ni-base superalloy RR1000 , (b) particle decohesion in RR1000 [49] and (c) slip-driven nucleation from an inclusion in a Ni-base superalloy FGH96 [47]. A schematic diagram of the nucleation modes is shown in (d)	57
Figure 3-2 – The slip systems in FCC	62
Figure 3-3 – A simplified schematic showing the process of the UMAT at each deformation increment.....	65
Figure 3-4 - (a) Front-view mesh of the full crystal plastic submodel, (b) a detailed close-up of various microstructural features and their meshing within the submodel	68
Figure 3-5 - (a) Schematic example of the oxide-oxide (particle fracture) interface is displayed as the black, dashed line and metal-oxide (decohesion) interface which is shown in white for particle F1 (b) the traction-separation relation used, and (c) the properties used for particle fracture and decohesion	71
Figure 3-6 - (a) trace of particles and grain boundaries in the agglomerate system with fractured particles highlighted in red and decohered particles highlighted in yellow. Annotations are	

provided for fractured particles (labelled F) and decohered particles (labelled D). (b) Experimental observation of the agglomerate region after loading with fracture and decohesion represented by red and yellow lines respectively, taken from [20]	72
Figure 3-7 - normal stress distributions with respect to the particle perimeters for which (a) and (b) are particles which decohere in experiment and particles (c) and (d) experience fracture after fatigue loading. Red arrows indicate the location of peak normal stress.	74
Figure 3-8 - profiles of normal stress distributions during unloaded, peak and partial ($F = F_{max} 2/3$) loads of the first cycle around the perimeter of particles. Plots a), b), c) and d) correspond to respective plots in Figure 3-7. The previously reported cohesive strength range of 1270 - 1480 MPa [49] is plotted as red bands. (a) and (b) are for particles observed to decohere; (c) and (d) are for particles observed to fracture.	74
Figure 3-9 - (a)-(d) Normal stresses on perimeter of particles are shown together with their corresponding experimental observations of particle matrix decohesion (from [49]) after fatigue loading. Red arrows indicate point of maximum normal stress. (The smaller white particles partially visible are silica particles used as DIC speckles.).....	75
Figure 3-10 - variation of particle mean of interfacial normal stress for particles which fractured in experiment and particles which decohered in experiment.	75
Figure 3-11 - Field plot of maximum principal stress (a) at the peak of the first cycle, and (b) a corresponding close-up of the region with several fractured particles (F1, F2, F3), and (c) the corresponding SEM image shown after fatigue loading [85].	77
Figure 3-12 - Maximum principal stress is plotted as arrows which indicate magnitude (size and colour) and direction for the peak of the first cycle.	78
Figure 3-13 - (a) Schematic of the interfaces predicted to fail (highlighted in red for fracture and yellow for decohesion). Failure is here defined as the peak normal traction exceeding the predefined strength of either fracture or decohesion. (b) Experimentally observed particle	

fracture (red) and decohesion (yellow) are annotated on a SEM micrograph of the corresponding region.	81
Figure 3-14 - (a) the number of failure events (sum of fracture and decohesion) in the entire agglomerate region and their type predicted by the model and observed in experiment during the first and second cycles at a peak applied stress of 1366 MPa. (b) the model predicted number of failure events per cycle for differing applied loadings (1366, 1300 and 1260 MPa) demonstrating the dependence of failure on remote stress.	81
Figure 3-15 - The development of stored energy density in a model utilising cohesive zones for capturing particle fracture and decohesion. (a) shows the stored energy density at the end of the first cycle and (b) after the 10th cycle. (c) shows the same region in an SEM micrograph after 2000 cycles of loading [49]	85
Figure 3-16 - Predicted cycles to crack nucleation based on the stored energy density in a model incorporating particle decohesion and fracture. Experimental decohesion (D1-D8) and fracture (F1-F5) sites are labelled.	86
Figure 3-17 - S-N plot for cycles to crack nucleation estimated from cyclic stored energy accumulation for the case in which failure (via particle fracture and decohesion) is allowed and for when it is inhibited. Particle fracture and decohesion do not occur below the stress threshold of 1230 MPa.....	87
Figure 4-1 - the morphology of the representative microstructure with i) a triple junction, ii) a twin lamella and iii) a non-metallic inclusion.....	95
Figure 4-2 - (a) Grain size and sphericity distributions of the synthetic microstructure, (b) typical texture mapping expanded to comprise 1000 grains and (c) the design process for the RVE construction.....	96
Figure 4-3 – (a) typical inclusion agglomerate morphology (b) inclusion area distribution (c) inclusion sphericity distribution.....	98

Figure 4-4 – (a) Cohesive zone geometry around inclusion, (b) bilinear traction-separation curve.....	99
Figure 4-5 - (a) the effective plastic strain distribution of the microstructure after the 10 th cycle of loading for a given peak load of 1400 MPa and (b) the stored energy of the respective microstructure after the 10 th cycle.	101
Figure 4-6 - Field plots for stored energy density at each respective microstructural feature. The white arrows indicate locations with peak accumulated stored energy density after 10 cycles of loading for a peak load of 1400 MPa	101
Figure 4-7 - The life prediction of non-metallic inclusion, annealing twin, triple-junction with appropriate trendlines for inclusion (blue) and intrinsic crystallographic feature (red).	102
Figure 4-8 – (a) mean slip histogram comparison between parent and twin grains, (b) schematic of grain showing slip directions (s4 and s8 point diagonally out of plane), (c) Slip tetrahedron in the reference configuration, and (d) the unpacked slip tetrahedron showing the slip directions and the corresponding slip plane normal. Slip direction conventions are given in	105
Figure 4-9 – (a)-(d) Field plots of slip distributions corresponding to the slip indices given in Table 4-2. The top row (a), (b) shows slip systems parallel to the twin boundary and the bottom row (c), (d) slip systems incident to the twin boundary.....	108
Figure 4-10 - Field plot of stored energy distribution in parent-twin grains	109
Figure 4-11 – Monotonic hardening curves showing the difference in behaviour of a low ($\lambda = 150 \mu\text{m}^{-2}$) and a high ($\lambda = 2000 \mu\text{m}^{-2}$) strain hardening level.....	110
Figure 4-12 - The variation of peak normal stress on the inclusion interface as a function of cycles for a low and high strain hardening material. Red horizontal lines indicate the peak stress achieved after 10 cycles of cyclic loading.	112

Figure 4-13 – Field plots of (a) σ_{xx} , (b) σ_{yy} , and (c) σ_{xy} for a low and high strain hardening material. The stress components are obtained at the peak load of the 10 th cycle. The inclusion lies in the centre with grain boundaries overlaid.	113
Figure 4-14 – Field plots of $d\sigma_{xx}/dN$ after the tenth cycle of loading for a (a) low strain hardening case and a (b) high strain hardening case with (c, d) pick-outs of $d\sigma_{xx}/dN$ for probe locations indicated in (a) and (b) respectively	115
Figure 4-15 – (a) An RVE comprised of 130 grains representing conventional fine grained RR1000 and (b) the experimental and modelling response of RR1000 in strain-controlled fatigue loading after 10 cycles of loading.....	117
Figure 4-16 – The model mean strain for the various kinematic, low strain hardening and high strain hardening material models under stress-controlled loading with a peak load of 1200 MPa for 10 cycles.....	118
Figure 4-17 - The variation of peak normal stress on the inclusion interface as a function of cycles for a kinematic material. the red horizontal line indicates the peak stress achieved after 10 cycles of cyclic loading.....	119
Figure 4-18 – (a) Field plots of $d\sigma_{xx}/dN$ with the pick-outs of $d\sigma/dN$ (b) with location indicated in (a)	120
Figure 5-1 – (a) A schematic of testing specimen showing region of interest and boundary conditions, (b) The IR lamps inserted to Shimadzu test frame.....	127
Figure 5-2 – (a) The beam holder with tungsten carbide support and alignment pins, (b) the beam holder with IR lamps mounted in a close configuration with annotations showing the observation window, IR window and thermocouple inlet.	129
Figure 5-3 – The 3D FE model used to investigate thermal gradients across the beam. Half the beam is omitted here.	130

Figure 5-4 – (a) The temperature gradient across the half beam and (b) the evolution of temperature at edge and centre integration points over 600 seconds.....	131
Figure 5-5 – Three thermocouples spot welded to a 12 x 3 x 3 mm beam.....	133
Figure 5-6 – The general methodology of the Coarse-fine method.....	134
Figure 5-7 – Correlograms of (a) the conventional cross correlation and (b) the normalised square difference criterion for a subset size of 32 px. The red arrows indicate location of the best match.	137
Figure 5-8 – A demonstration of the correction routine. The coarse pass displacements (a,b) with corresponding peak cross correlation heights (c). The changes subjected to the deformed image (d) are shown in (e) where the remapping routine attempts to remap the deformed image to the reference image (f). An outline of the remapping shape (g) with the corresponding shifts in x (h) and shifts in y (i). The image sets are kindly provided by Dr Benjamin Poole.	139
Figure 5-9 – A subset partitioned along a line with polar coordinates r, θ assumed from subset centre.....	141
Figure 5-10 – The search space for discontinuity parameters (a) r and (b) θ for a subset containing a discontinuity, the search spaces have been expanded to include a large array of values to show the behaviour of the (c) sum of correlation coefficients. The red circle shows the location of discontinuity for the value of r and θ	142
Figure 5-11 – (a) The neighbourhood of displacement cells considered for determination of the deformation gradient of the central cell (i,j). (b) A schematic representation of finding the displacement gradient based on fitting a polynomial to the neighbourhood of displacement values	143
Figure 5-12 – A kinematic shift applied artificially to an image set such that the top half shifts to the right and the bottom half shifts to the left.....	146

Figure 5-13 – The horizontal displacements and corresponding correlation coefficients for the conventional (a,b) and H-DIC (c,d) respectively for the artificial kinematic shifts shown in Figure 5-12.....	146
Figure 5-14 – The maps of outputs of the H-DIC method. Discontinuity location parameters r (a) and θ (b) with a discontinuity jump magnitude (c)	147
Figure 6-1 – IPF-Z map of the agglomerate region prior to testing. The EBSD map has been processed to remove extremely small grains and inclusions are omitted.	154
Figure 6-2 – (a) The three point bend specimen showing loading constraints and applied heat, (b) the applied loading history, (c) field plot of σ_{xx} at applied load of 1800 N, (c) An image of the experimental set-up with infrared heaters active.	155
Figure 6-3 – (a) A schematic showing implementation of the logical masking routine for subsets, (b) the process flow for the discontinuity tolerant DIC method.....	156
Figure 6-4 – (a) Subset size, (b) a 6x7 stitch of BSE micrographs of inclusion agglomerate and coarse grain region.....	159
Figure 6-5 – The CPFE model geometry showing uniaxial force controlled boundary conditions	161
Figure 6-6 - (a) the slip systems and orientation relationship between a pair of parent and twin grain in RR1000. (b) the slip system configuration along the $\langle 111 \rangle$ plane of a RR1000 grain.	162
Figure 6-7 - (a) the region of interest (ROI) modelled using DDP and the applied boundary conditions. (b) the stress strain response curve of the ROI when a monotonic strain-controlled loading applies.	164
Figure 6-8 – Map of ϵ_{xx} after one cycle of loading. Large coarse grains are indicated by white GBs. Smaller grain boundaries are omitted. The inclusion agglomerate located in the centre sees high strains arising from inclusion fracture and decohesion.....	165

Figure 6-9 – BSE micrograph of agglomerate region after one cycle of loading. The backscatter quadrupole has switched polarity to allow for topographic detail. Pull-outs of inclusion initiation phenomena are shown. Gold speckle particles can be seen throughout the sample surface. They appear as white dots in the image.	166
Figure 6-10 – (a) the strain accumulation across the entire DIC region measuring the strain relative to the reference image and (b) a sequential exx map showing the strain between cycle 2 to 20	168
Figure 6-11 – Nucleation of two types of fatigue crack from inclusions after 3000 cycles of loading. (a) A fatigue crack emanating from a cracked inclusion developing a crystallographic crack. (b) Coalescence of decohesion leading to a microcrack. Small white particles are Au speckles.....	170
Figure 6-12 – Growth of microcracks to form cracks over the whole agglomerate region (a) A backscatter micrograph of the agglomerate region showing fatigue cracks. (b) exx strain map of agglomerate region between cycles 5000 to 6000 showing fatigue cracks in the form of high strain slivers.	171
Figure 6-13 – Sequential exx strain maps of the inclusion agglomerate region with discontinuity magnitude maps for the first and the last image intervals. Red arrows show initiation and fatigue crack nucleation events. Grain boundaries are omitted here due to their size and complex morphology. Scale bars are 10 μm	172
Figure 6-14 – (a) An SEM image of the twin boundary crack with annotations indicating slip banding and the twin boundary, (b) A exy strain map of the region containing the twin boundary crack and (b) a pull out showing the location within the coarse grained region	173
Figure 6-15 – Strain and discontinuity maps after the first cycle and for the last 1000 cycles in which a twin boundary crack nucleates. The red arrow indicates peak discontinuity within map and fatigue crack nucleation. Scale bars are 10 μm	174

Figure 6-16 – Slip traces and cube orientations for the Parent and twin grain after the first cycle of loading	175
Figure 6-17 – The HR-EBSD GND density field map of the twin region prior to loading...	176
Figure 6-18 – Residual stresses near the twin boundary crack region pre-loading. Scale bar shown in black is 10 μm	177
Figure 6-19 – Kernel average misorientation and Hough-based GND estimations for the twin region pre-loading (prior to test) and post-loading (after 6000 cycles)	178
Figure 6-20 - The distribution of the (a) stress, (b-d) effective strain and (e) geometrically necessary dislocation (GND) in the DDP sub-model. The results are obtained at the instant of peak applied loading.	180
Figure 6-21 - the comparison of effective strain distribution predicted by (a) the isotropic DD modelling and (b) the anisotropic DD modelling.	181

List of tables

Table 3-1, isotropic elasticity properties for Hafnia inclusions	67
Table 3-2, the properties used for the slip rule.	68
Table 3-3 - the test matrix of the parametric study performed to find the interfacial strength SC, and the oxide strength SC.....	79
Table 4-1 - The properties of the traction separation curve.....	99
Table 4-2 - Slip system numbering convention	106
Table 4-3 – Properties for back-stress evolution	117
Table 5-1 – thermal properties used for the FE model	130
Table 6-1 – DDP material properties for RR1000	163

List of Acronyms

CPFE – Crystal plasticity finite element

HR-EBSD – High (angular) resolution electron backscatter diffraction

HR-DIC – High (spatial) resolution digital image correlation

H-DIC – Heaviside digital image correlation

HIP – Hot isostatic pressing

PPB – Prior particle boundary

GND – Geometrically necessary dislocation

SEM – Secondary electron microscopy

EDS – Energy dispersive X-ray spectroscopy

TB – Twin boundary

RVE – Representative volume element

CZM – Cohesive zone model

PID – Proportional integral derivative

List of Publications

A. Bergsmo, F.P.E. Dunne, Competing mechanisms of particle fracture, decohesion and slip-driven fatigue crack nucleation in a PM nickel superalloy, *Int. J. Fatigue*. 135 (2020) 105573. <https://doi.org/10.1016/j.ijfatigue.2020.105573>.

A. Bergsmo, Y. Xu, F.P.E. Dunne, Twin boundary fatigue crack nucleation in a polycrystalline Nickel superalloy containing non-metallic inclusions, *Acta Materialia*, (2021) (in preparation)

A. Bergsmo, F.P.E. Dunne, Comparative fatigue performance of microstructural features, 2021 (in preparation)

1 Introduction

1.1 The contemporary gas turbine

A holistic understanding of a turbojet can be summarised in the mnemonic “suck, squeeze, bang, blow”. Atmospheric air is drawn to a low-pressure area at the inlet of the jet engine. Air entering the inlet is compressed by a series of compressor blades attached to discs which are connected to a shaft. The compressed air then flows into a combustion chamber. Fuel is atomised and dispersed in the flowing air. Continuous ignition of the fuel adds heat to the compressed air which leads to rapid expansion of the gas. Downstream, the air meets a series of turbine blades which are connected to a turbine disc. The turbine disc drives the same shaft as the compressor. The extracted energy from the hot air is fed back to the compressor. This feed-back process, or thermodynamic process, is known as the “Brayton” cycle. Only a fraction of the kinetic energy is extracted from the hot air in the turbine, the remainder is ejected (at high speed) through the exit where it acts as thrust.

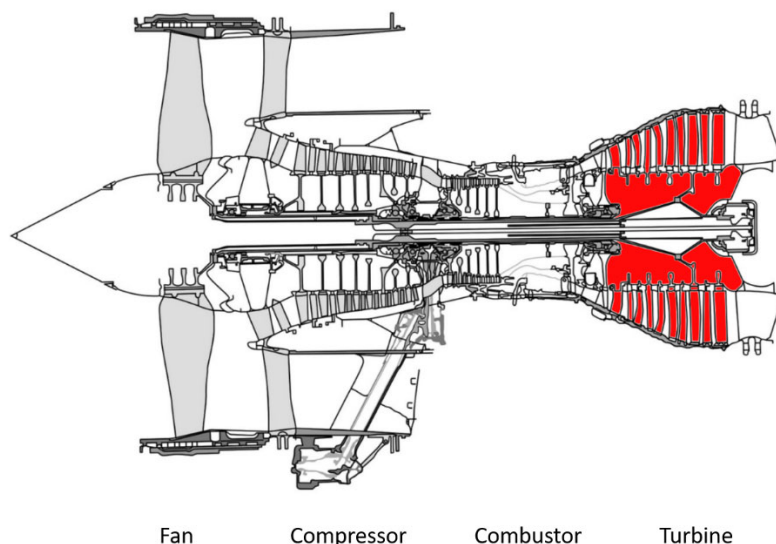


Figure 1-1 – A Rolls Royce Plc Trent 800 turbofan jet engine. The turbine section is highlighted in red where Ni-based superalloys are concerned (adapted from [1])

Modern jet engines are far more complicated than the description given above and rely on several key modifications to increase thrust, improve fuel efficiency, reduce noise pollution, and reduce component mass. Here, some typical modifications are outlined. The conventional gas turbine typically comprises several compressor and turbine stages with multiple shafts to optimise pressure ratios between atmospheric air and that within the combustion chamber. Most commercial aerospace applications require high thrust and therefore often employ turbofans (see Figure 1-1) instead of pure turbojets [2]. The turbofan sees a large fan attached to the shaft in the front of the engine. The majority of thrust produced by the fan is diverted to a bypass duct and is not compressed by the core engine thereby increasing the propulsive efficiency.

The gas turbine is a highly engineered technology due to the extremities of conditions it performs under. Components are subject to high cyclic loads, high temperatures and potentially corrosive environments. The material selection is vital for component lifetime and safety. The compressor typically uses Ti alloys to combat high cyclic stresses, relatively low temperatures and corrosion in addition to being lightweight [3]. While the high temperature performance of Ti alloys are admirable, the oxidation resistance degrades over increasing temperature [3]. The turbine, of which this work pertains to, uses Ni-based superalloys to mitigate creep from high temperatures, increase fatigue lifetimes, and reduce corrosion [1,4]. This comes at a cost to the mass, as Ni-based superalloys are far denser than Ti alloys (7.7 gcm^{-3} [4] vs. 4.4 gcm^{-3} [3], respectively)

The turbine section comprises a series of discs with blades. The blades are complex components made of single-crystal Ni-based superalloy and are used to extract energy from the fast and hot air stream. The blades are typically connected to the disc by fir tree joints [5]. Discs will rotate around the shaft at high rotational velocities and due to their high mass, are safety critical [6]. The cyclic loading conditions of the disc are two-fold, they experience the highest

loads at take-off and then experience lower loads at cruising speed giving rise to both low cycle fatigue (during take-off and landing) and high cycle fatigue (during cruise) regimes, respectively.

1.2 On Ni-based superalloys

Ni-based superalloys are alloys comprising several elements. Principally, Ni is alloyed with Al to form precipitates of γ' in a matrix of γ . These two phases control the key properties of the alloy. Elements other than Ni and Al are used for a number of reasons; to promote segregation to either of the phases, as solid solution strengtheners, oxygen scavengers or prevention of detrimental phases. Figure 1-2 (a) shows a typical arrangement of the γ and γ' phases. The exact morphology is dependent on the alloying elements and thermal processes taken in manufacturing and can superalloys therefore exhibit a plethora of microstructural configurations. Blades are typically manufactured to consist of a single grain and are therefore termed single crystal. The single crystal configuration is used to promote the highest possible creep resistance. Discs, however, place a greater emphasis on strength due to their load bearing nature and lower applied temperatures. Therefore, a polycrystalline microstructure is desirable to obtain a Hall-Petch strengthening effect. In a Ni-based superalloy polycrystal, the γ and γ' are still present but display a different configuration, the polycrystalline microstructure is shown schematically in Figure 1-2 (b). The γ' phase segregates to several features; large primary γ' at grain boundaries, intragranular intermediate secondary γ' and intragranular small tertiary γ' particles. The prevalence of these three features is dependent on the thermal processes taken during manufacturing.

(a)



(b)

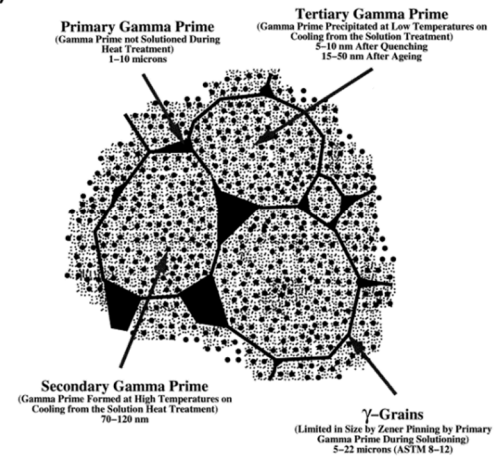


Figure 1-2 – (a) Typical superalloy microstructure in single crystal configuration, the cubes are γ' with the channels between being γ . Each γ' cube is about 500 nm wide (kindly provided by Alessandro Piglione). (b) Schematic of polycrystalline microstructure of Udimet U720Li which is representative of typical turbine disc alloy microstructures (courtesy of [7])

The γ phase is a chemically unordered FCC phase which exhibits high strength and excellent ductility. The γ phase is often regarded as “channels” between the γ' precipitates. The γ' precipitates are chemically ordered with a cubic phase $L1_2$. The chemical ordering assumes the Nickel atoms to position at the faces of the periodic lattice while aluminium atoms inhabit the corners. The $L1_2$ structure is shown in Figure 1-3. The lattice is similar to the FCC crystal structure (and has in most cases a similar lattice parameter similar to the γ phase) and exhibits similar slip behaviour with 12 octahedral slip systems [8]. However, at high temperatures, the slip behaviour may transition from octahedral to cuboidal slip causing an effect widely known as the Kear-Wildsorf lock [9]. The chemical ordering of the $L1_2$ structure inhibits the motion of a dislocation and forces the formation of an anti-phase boundary (APB) where a trailing dislocation is required to complement the forward dislocation in dislocation motion [1]. The APB of a dislocation which has cross-slipped to a cuboidal slip plane makes the dislocation pair sessile. In nominal terms, the microstructure may experience no decrease in yield strength at high temperatures due to the thermal dependence of the Kear-Wildsorf lock, which increases in frequency for higher temperatures.

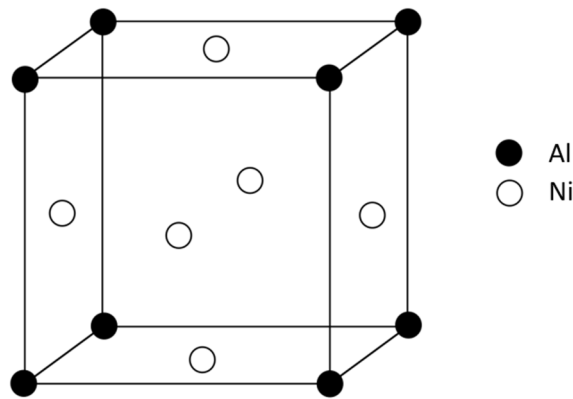


Figure 1-3 – The L1₂ lattice structure that the γ' exhibits with chemical ordering of Al atoms at corners and Ni atoms at faces

Gas turbine manufacturers are constantly developing and improving gas turbine performance. Two critical parameters for performance of a jet engine are the pressure ratio and thrust efficiency [2]. The thrust efficiency compares the energy input to the useful thrust produced by the engine. The thrust efficiency is proportional to the temperature difference between the exit and combustion chamber. A higher temperature difference provides a higher efficiency. By increasing efficiency, gas turbine manufacturers can provide a product which is more fuel efficient. Fuel efficiency is critical to aeroengine operators as it reduces operational costs. The rising global average temperatures due to global warming also motivates operators to reduce their fuel consumption. Environmental policy change will only increase this motivation in the near future. It is therefore desirable to increase the operating temperature of the gas turbine which poses increasingly higher demands on the disc component as it will be subject to more severe thermal environments.

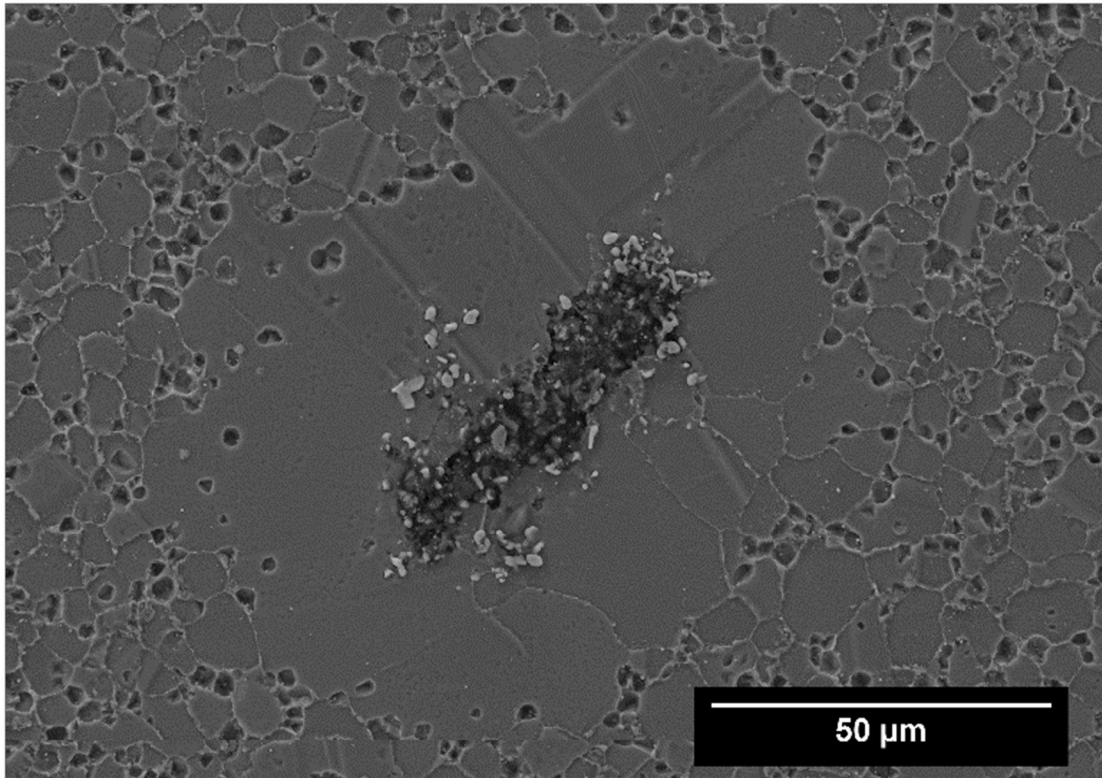


Figure 1-4 – A typical non-metallic inclusion in RR1000, a disc alloy produced by powder metallurgy. The inclusion (centre) is surrounded by a coarse grain structure. The etching process used on this sample was extremely coarse and resulted in dislodging of primary γ' seen by dimples at grain boundaries and triple junctions to the to the sides. This micrograph was obtained in a Zeiss Sigma microscope of an etched RR1000 specimen containing coarse inclusions.

Disc components are often produced by powder metallurgy to give fine grain sizes, homogenous grain size distribution, reduced macro-segregation and near net-shape components [10]. Non-metallic inclusions are a biproduct of the powder metallurgy process and can be considered as a “weakest-link” for fatigue crack nucleation. Figure 1-4 shows a typical inclusion in an alloy produced by powder metallurgy. While non-metallic inclusions are detrimental to fatigue life, the benefits of the powder metallurgy process often outweigh the potential fatigue crack nucleation risks. Owing much to their size, the mechanics of fatigue crack nucleation near non-metallic inclusions is elusive and requires further research to

understand fully. Under a mechanistic framework, fatigue life prediction frameworks can be improved and thus life of disc components can improve.

1.3 Objective statement

This thesis addresses the mechanics of fatigue crack nucleation around non-metallic inclusions using a host of state-of-the-art modelling and experimental techniques. The overarching scientific objective is to determine under what conditions non-metallic inclusions drive fatigue crack nucleation under normal gas turbine operation and what mechanisms drive this fatigue.

Here, a summary is given of the contents of the thesis. In chapter 2, a literature review is given concerning the current state of research on fatigue around non-metallic inclusions. In chapter 3, an investigation of the competing nature of inclusion decohesion, fracture and slip-driven fatigue crack nucleation is given. In chapter 4, several types of microstructural features are compared in terms of fatigue performance within a representative model framework. In chapter 5, the development of experimental methodologies is outlined of which the experimental results are shown in chapter 6. Chapter 6 regards the investigation of fatigue crack nucleation near a non-metallic inclusion under high temperature low cycle fatigue. Finally, in chapter 7, conclusions are given with suggestions for future work.

2 Literature review

In this chapter an overview of the field of fatigue and inclusions is provided. First, a brief overview of classical fatigue and more recent developments in the field of fatigue crack nucleation is given. Following this, the literature concerning the properties and fatigue behaviour of non-metallic inclusions is reviewed. The literature review aims to elucidate the origins of non-metallic inclusions, their response to cyclic deformation and the nucleation of fatigue cracks resulting from cyclic loading in the vicinity of inclusions.

2.1 Cyclic plastic deformation

Fatigue (often confused with *tiredness* by the layperson) concerns the gradual degradation of components which are cyclically loaded under the perceived nominal strength of the material. Early rationalisations of fatigue concluded that while loaded below the material strength, cyclic loading causes growth of microstructural defects (i.e., cracks) which results in the progressive weakening of the material. Some notable examples of fatigue failures are the De Havilland Comet jet passenger aircraft [11], where aggressive riveting on the fuselage introduced defects which grew to failure during operation; Alexander L Kielland oil platform [12], in which cyclic stresses from waves caused the fatigue failure of a structural brace and resulted in the collapse of the platform; cold dwell fatigue of a titanium alloy fan blade in an Engine Alliance GP7270 engine [13]. Fatigue dominates engineering failure incidents around the world and therefore attracts intense research by engineers and material scientists attempting to predict and prevent future failures. In the following paragraphs, a top-down approach is used to explain various concepts and important developments in fatigue, from macroscale concepts such as stress controlled loading down to fatigue crack nucleation at the dislocation scale. For the sake of brevity, the following review concerns fatigue crack nucleation and cyclic deformation without reviewing fatigue crack growth.

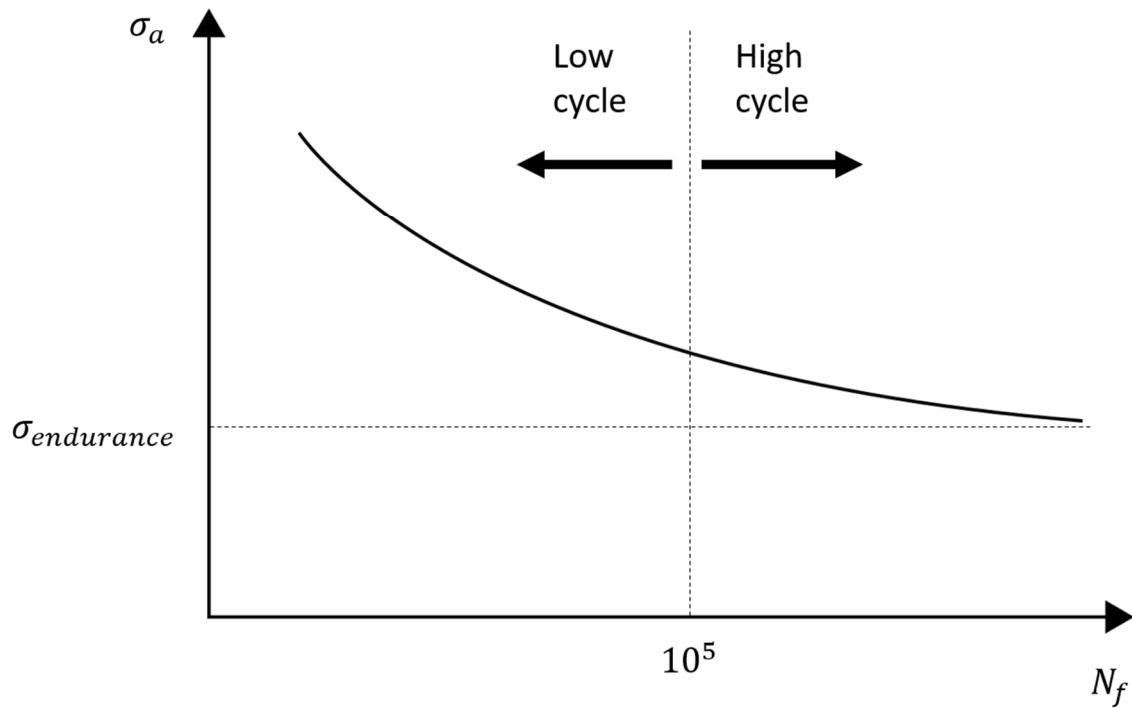


Figure 2-1 – A schematic of the typical S-N curve with labels showing the distinction between HCF and LCF. An endurance limit stress $\sigma_{endurance}$ is also shown. [14]

In stress-controlled loading, the S-N curve (shown schematically in Figure 2-1) describes several important concepts in fatigue. It is also known as the Wöhler curve after its inventor [15]. The S-N curve describes the number of cycles to failure N_f of a sample for a given applied stress σ_a . Here, the fatigue life assumes the entirety of the multi-level fatigue process, that is to say it considers the sum of number of cycles to fatigue crack nucleation and the sum of number of cycles for that crack to grow to failure. This is of course assuming the specimen begins from a pristine, crack-free condition. The endurance limit of fatigue describes the minimum stress at which fatigue failure may present itself. An important distinction in literature is the separation between high-cycle and low cycle fatigue regimes. High-cycle typically concerns N_f greater than 10^5 where nominal applied stresses cause bulk elastic strains and low-cycle fatigue concerns N_f less than 10^5 cycles where the applied stresses cause bulk plasticity. Despite bulk elastic strains in HCF, plasticity is still expected to occur at the

microstructural level – making the distinction somewhat arbitrary and largely dependent on material properties rather than number of cycles to failure (i.e., 10^5). The mean stress of cyclic loading ($\sigma_m = (\sigma_{max} + \sigma_{min})/2$) also plays a large role in fatigue failure where a large σ_m will reduce the fatigue life of the specimen (shifting the curve in Figure 2-1 downwards).

The fatigue life can also be viewed from the perspective of strain-controlled loading. Coffin [16] and Manson [17] independently developed a relationship between the logarithm of applied plastic strain and the logarithm of cycles to failure. The relationship is linear and inversely proportional such that a higher plastic strain amplitude reduces the number of cycles to failure. It is however noted here that turbine discs are typically considered under stress-controlled approaches due to the nature of loading under operation. This literature review (and thesis by extension) therefore primarily concerns itself with topics integral to stress-controlled approaches.

Strain hardening may take the form of kinematic, isotropic or a combination of both. Isotropic hardening describes the isotropic expansion of the yield surface under plastic motion. The Bauschinger effect describes the key phenomenon of kinematic hardening, where a material loaded in reverse experiences a different yield point compared with the forward loading introduced previously. These hardening models result in hysteresis effects in fatigue loading. In effect, cyclic loading may result in hardening effects unique to fatigue. This is briefly described in the next paragraph.

In low cycle fatigue, the first few cycles of loading introduce residual stresses due to the plastic deformation. Continued fatiguing cycles can result in a steady-state where the residual stresses introduced in the first few cycles inhibit further plastic deformation – this is known as *elastic shakedown* [14] wherein cyclic deformation has become entirely elastic and is closed-cycle. *Shakedown* may also be plastic, where a closed cycle of plastic deformation occurs with no net

accumulation in plasticity. In the case where plastic deformation in forward loading is not equally opposed in reverse loading, net accumulation of plastic strains occur per cycle. Net accumulation of plasticity under fatigue is known as *ratchetting*. In strain-controlled loading, *mean stress relaxation* is the analogous equivalent of *ratchetting* where a cyclic strain range will result in cyclically softening of the mean stress. Cyclic responses for stress-controlled and strain-controlled loading are shown in Figure 2-2. Under fixed amplitude stress-controlled loading, the strain response may either reduce in *cyclic hardening*, or increase in *cyclic softening*.

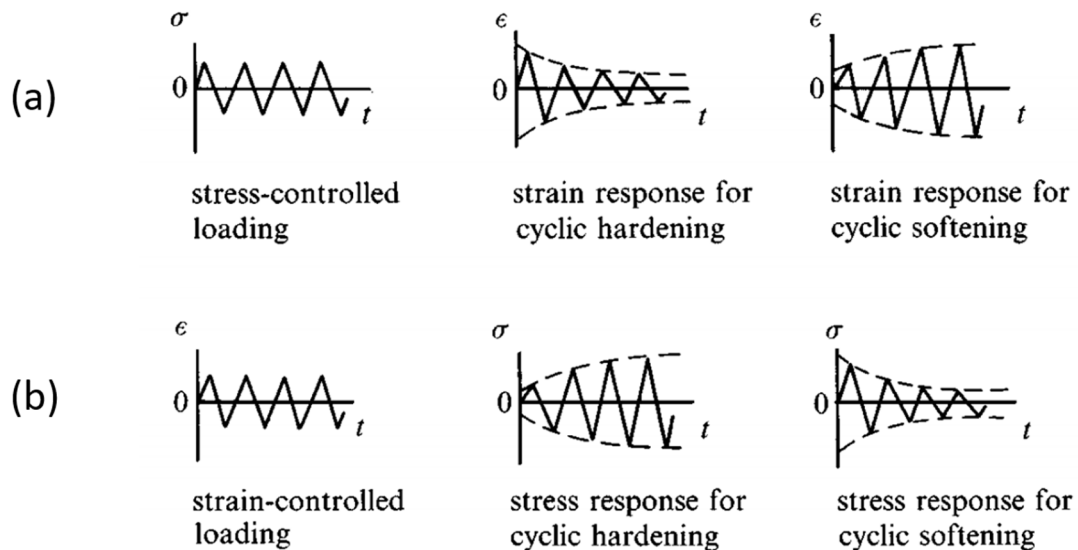


Figure 2-2 – Cyclic hardening and softening under fixed amplitude stress controlled (a) and strain controlled (b) loading with $R=-1$ (adapted from [14])

Residual stresses are introduced into a material due to incompatible deformation of the material after application of a load (a load here may be from a stress or thermal source). The distribution of residual stresses depend strongly on the local grain morphology and can result in local residual stress heterogeneities which promote fatigue crack nucleation and growth phenomena [18]. In particular, residual stresses on the free surface can either suppress fatigue phenomena

if the surface is in compression or reduce fatigue lifetimes if in tension. Complete surface compression is therefore a desirable effect and is introduced via shot-peening a surface [19]. Surface tension, on the other hand, typically deals with random residual stresses introduced unintentionally in processing steps or by operating conditions. In given microstructures, residual stresses are rate-dependent giving rise to important fatigue phenomena such as cold dwell fatigue [20].

In a single crystal, cyclic loading introduces plasticity heterogeneously. Forward and reverse loading produces dislocations (positively and negatively signed) on activated slip systems which accumulate irreversibly [14]. Assuming the loaded slip system is equally activated in forward and reverse loading then the equal generation of positive and negative dislocations results in a small net Burgers vector. Continued cycling results in formation of dislocation dipoles from mutually trapped edge dislocations. Networks of dislocation dipoles form “veins” in the bulk material. Veins impede further dislocation motion, providing a slip system hardening effect over the bulk of the material. Further plastic loading causes formation of a localised structure known as a slip band. Slip bands span a large number of slip planes and form a lamellar structure. Within the lamella, a ladder-like arrangement of grouped dislocations exist. Each ladder step consists of mainly edge dislocations normal to the Burgers vector of the slip band. Deformation between the ladders mainly consists of screw dislocations. Figure 2-3 shows a TEM micrograph of the dislocation structure after fatigue loading in a Cu sample performed by Mughrabi et al.[21].

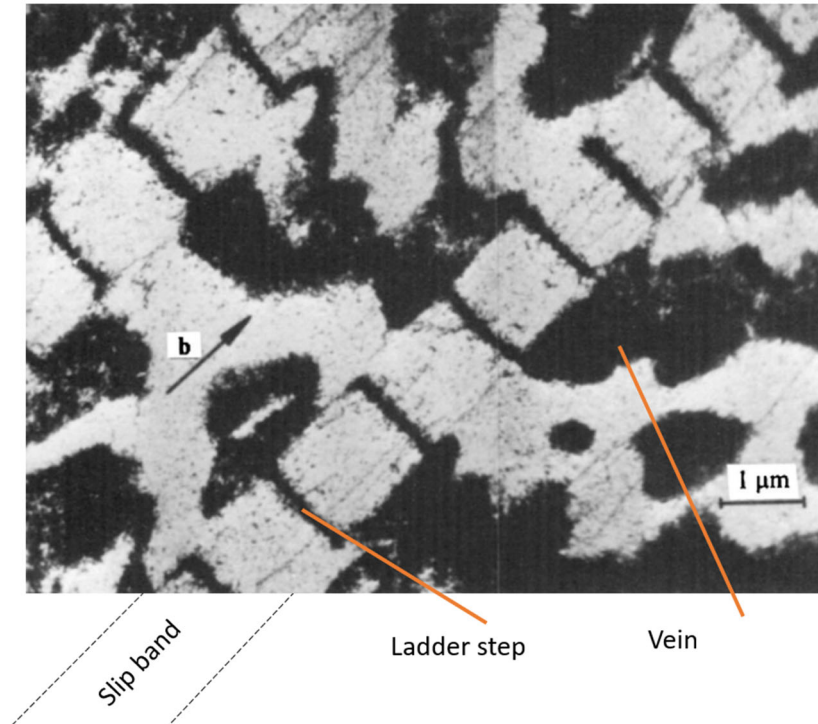


Figure 2-3 – TEM micrograph of the dislocation structure within pure Cu after fatigue loading. The structure consists of the slip band ladder structure and matrix dislocation veins (from [21])

Persistent slip bands (PSBs) are persistent in the sense the cyclic loads activate slip on the same slip bands in forward and reverse loading. The exact nature of origin of slip banding is still unknown. Recent work by Wang et al. develops the formation of slip banding via cross-slip [22]:

1. Loading of slip systems causes dislocations to glide,
2. Stress between parallel and active slip systems is increased,
3. Slip systems between two parallel slip systems become active and lead to cross-slip.

Net slip accumulation on slip systems drives formation of slip banding, and irreversible accumulation of local strain. The mutual trapping of oppositely signed dislocations results in localised hardening within slip bands. Multitudes of slip bands on the surface of material introduces roughness in the form of steps (e.g. intrusions and extrusions). Wood [23] hypothesised that the intrusions and extrusions of the roughness on the free surface act as stress

concentrators further promoting slip until a fatigue crack may nucleate. It is noted here however, that crack nucleation may also occur from other features such as grain boundaries, twins, pores, and inclusions which do not necessarily observe surface roughening from PSBs [24]. It also does not explain internal nucleation sites in which the troughs and asperities of PSBs act against grain boundaries and therefore do not cause surface roughening but rather grain boundary roughening.

The character of the grain boundary and the interactions a slip band has upon meeting a grain boundary also important for understanding fatigue crack nucleation. A slip band may be blocked or transfer through a grain boundary to form a slip band in the adjacent grain [25]. Distinct types of grain boundary have also been reported to improve the fatigue life of a material by acting as barriers to slip [26].

The development of slip banding and subsequent fatigue crack nucleation is therefore crucially dependent on the development of local plastic strain accumulation. Stroh [27] considered that the nucleation near a slip band was a process which dependent strongly on the density of dislocations and the fracture toughness of the material. Crystal plasticity models have shown that fatigue cracks do not crack at locations with the predicted highest amount of accumulated plastic strain [28]. Fatemi and Socie [29] developed a parameter which considers the accumulated plastic strain as well as the normal stress acting on the maximum shear range plane which has become a widespread fatigue indication parameter. Sangid et al.[30] considered an energy approach of fatigue crack nucleation from PSBs wherein the stability of the PSB energy with respect to its dislocation motion is used as a criterion to predict fatigue crack nucleation. Recent work, by Wan et al.[31] which considers local dislocation densities as well as the necessary stress and plastic strain required for nucleation have shown excellent agreement with experiments.

At the present, fatigue life prediction models in component design ignore early stages of fatigue life owing much to its complexity but also due to the unknown nature of exact mechanistic drivers at the micron scale and below. However, advances in experimental techniques and computational models (in addition to computational processing power) have driven continued research into the field. Current fatigue research is therefore motivated by discovering micromechanical drivers, improving prediction methodology and developing fatigue resistant materials.

2.2 Non-metallic inclusions in powder metallurgy alloys

Turbine discs are commonly produced by powder metallurgy (PM) to produce fine, homogenised grain sizes and eliminate macro segregation. Non-metallic inclusions are an undesired biproduct of PM processing. The PM process can be broken into two essential steps: (i) powder atomisation (ii) hot isostatic pressing [1]. A schematic of the full process is shown below in Figure 2-4. An ingot is initially produced by vacuum induction melting (VIM) with great care taken to reduce contamination from oxygen and nitrogen. The ingot is then melted in a vacuum induction furnace. The molten metal is funnelled through a nozzle. The tip of the nozzle is impinged by jets of unreactive gas (typically argon). The impinging jets cause the flowing melt to spray and form droplets. The droplets rapidly cool and form powder particles. Finally, powder particles fall to a chamber after passing through meshing filters which reduce the size distribution of the final powder product.

The powder is then ready to be hot isostatically pressed (HIP). A final forging step is performed to obtain the near-net shape of the component. Machining is typically omitted from the processing steps, but manufacturers will often apply late machining for cooling systems such as ducts in which air can circulate during operation.

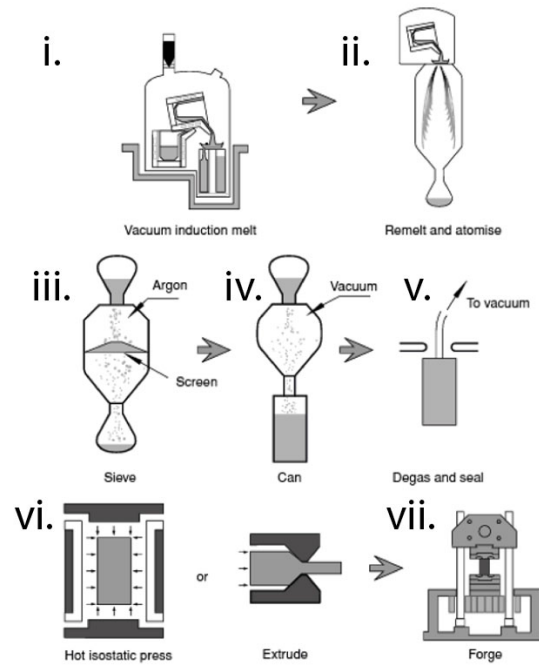


Figure 2-4 - Powder metallurgy processing steps (adapted from [1]) (i.) Vacuum induction melting of ingot, (ii.) remelt and atomise (iii.) Sieving the powder through a mesh screen (iv.) Inserting powder into a canister followed by (v.) degassing to remove oxygen and nitrogen then seal the cannister (vi.) The can is then either HIPed or extruded (vii.) A final forging step is used to obtain the near net shape of component

Non-metallic inclusions may arise from several steps in powder atomisation process but in modern processes the principal contaminant arises from erosion of the melt crucible when the molten metal is in contact with the crucible lining [32]. The products of the erosion arrive in the melt and downstream in the powder particles. Once HIPed, components contain a distribution of non-metallic inclusions of varying sizes and types. To remove the propensity of inclusions arriving in the components, manufacturers often apply the mesh sieve with the intention of catching the large inclusions. Despite this, inclusions evade the mesh and can even agglomerate within the metal during the HIPing process [10]. The exact nature of this process is unknown and requires further investigation. Researchers are continuously improving the cleanliness in Ni-based superalloy melts to reduce inclusion occurrence. Recent studies have investigated removal by electron beam smelting [33] and electromagnetic levitation melting

[34]. While powder metallurgy is in this context used to create turbine discs, metal powder is also used for additive manufacturing where inclusions also persist [35–37].

Early studies of inclusions found that granular-type inclusions may be formed by reaction with the metal matrix [38,39]. These inclusions bond and diffuse into the metal matrix thus forming pseudo grains which are detrimental to fatigue life. In many ways these reactive inclusions form their own grains, effectively becoming a separate phase within the microstructure. This is in contrast with discrete inclusions, which may still experience bonding at the interface but do not diffuse into the matrix. Inclusions were therefore categorised into “reactive” and “non-reactive” types. Figure 2-5 shows reactive (also known as prior particle boundary (PPB)) and non-reactive types of inclusions. Note that the non-reactive defect is much larger in size compared with that of the discrete inclusion. PPB inclusions diffuse into the matrix material yet may often contain a core of the original refractory material. Chang et al. [39] note that the formation of PPBs requires a source of oxygen or carbon and may originate from refractory binder or organic contaminants. It is hypothesised that trapped gas within the particle reacts with the surrounding matrix during HIPing by dissolving into the surrounding matrix [40]. Reactive types were considered the “worst-case” inclusions for fatigue lifetimes [41] owing much to their size, however, improvements in the processing of powders lead to a significant reduction of reactive type inclusions [39] and their relative importance in literature has faded as a consequence.

Non-reactive, discrete inclusions have therefore become the dominant defect type which poses a problem in PM alloys. The non-reactive inclusions are ceramic in nature and form discretely such that there is clear separation from the matrix. Inclusions found in RR1000 have been found to be discrete yet have bonded with the matrix to some extent [42]. It is therefore noted that the separation between the two types of inclusions is a distinction between the degree of diffusion the inclusion undergoes as it is incorporated in the matrix. The nature of the matrix bonding is

particularly important for considering the mechanical interaction of the inclusion with the matrix. An inclusion without bonding will impose a lower constraint on the matrix during loading. Debonding of the inclusion-matrix interface during loading is discussed thoroughly in a later section. The nature of bonding at the interface is, however, poorly understood, and further research is required to determine the exact nature of inclusion bonding within superalloys.

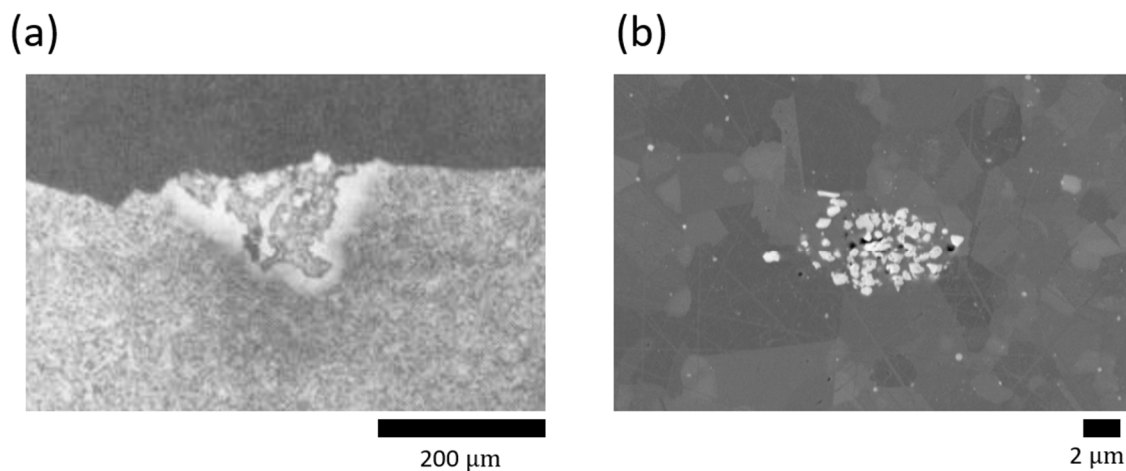


Figure 2-5 – (a) SEM of a reactive type inclusion in Rene 95 (adapted from [39]) and (b) discrete non-metallic inclusions which are agglomerated in RR1000 captured in an SEM

Caton et al.[43] studied the effect on inclusions on the fatigue life of a superalloy, Rene 88 DT (where the designation DT indicates damage tolerance), and found that in samples where nucleation occurred from inclusions, lifetimes were reduced. An SN curve of various fatigue specimens in their study is shown in Figure 2-6 and importantly depicts the reduction of fatigue life in samples where fatigue crack initiated at inclusions. Barrie et al.[19] found that surface inclusions reduced fatigue life by three orders of magnitude compared to samples with no inclusions. Hu et al.[44] found similar conclusions in FGH96 where the discrete inclusions are comparable to the grain size.

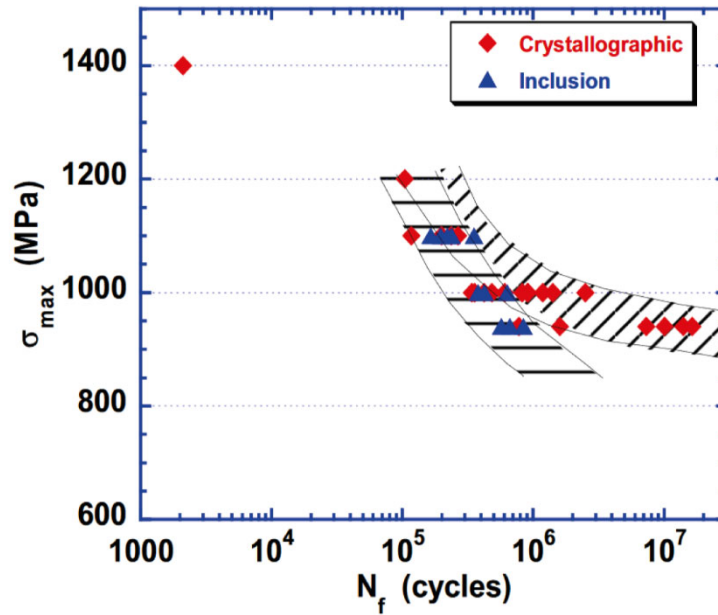


Figure 2-6 - An S-N curve showing location of fatigue crack nucleation for several samples. In samples where fatigue cracks originate from inclusions, the life is notably reduced. (adapted from [43])

2.3 Effect of non-metallic inclusions on fatigue performance

The nucleation of fatigue cracks is complex and has spawned a vast field of literature which is still being developed. This section is therefore kept brief to portray information relevant to the non-metallic inclusions and Ni-based superalloys. Several researchers have given recent reviews on the topic of fatigue crack nucleation [24,45–47].

It is outlined above that non-metallic inclusions that occur within polycrystalline Ni-based superalloys negatively affect the fatigue performance of Ni-based superalloys. The factors that affect the crack nucleation process are numerous; inclusion size [48], morphology [49,50], agglomeration [51], inclusion material properties [52,53], applied temperature [54] and inclusion debonding strength [51,55]. Each of these factors affect the loading performance of the material where the inclusion presents itself as a stress concentrator – thus driving fatigue crack nucleation. Inclusions may also play a role in pitting corrosion which later drives fatigue initiation [56], but this is strongly dependent on local chemistries and has not been seen in recent superalloy compositions. It is noted that the while the summary above considers

inclusion fatigue nucleation under operation, initiation may also occur during processing of components which later develop into fatigue cracks (e.g., [57,58]).

2.3.1 Inclusion size

Several reports indicate the importance of inclusion size on the behaviour of fatigue crack nucleation location within an alloy [38,39,59]. Manufacturers often consider a critical-size below which they are considered dangerous for fatigue life [57]. Shabrov and Needleman investigated void nucleation near inclusions and found the size dependency to dominate the nucleation response [60]. Their results indicate that inclusions size is the key factor in crack nucleation – yet they acknowledge the mechanical properties of the inclusions also play a role. A quantitative study into the effect of inclusions size on fatigue life in a tool steel by Yao et al.[61] similarly shows the inverse relationship between inclusion size and fatigue life. A critical size for harmfulness can be determined for inclusions below which the likelihood of fatigue crack nucleation is suppressed [57]. Salajegheh et al.[62] developed a probabilistic framework for predicting fatigue crack initiation near non-metallic inclusions considering the size of inclusions. Pineau and Antolovich [63] created a Coffin-Manson like framework for fatigue which also considers the size and distribution of inclusions. On the other hand, Kantzos et al.[10] found that even with a small size distribution, a large number of inclusions may still be detrimental to fatigue life.

2.3.2 Inclusion morphology

The shape of the inclusion may affect the performance in fatigue simply through being rough and promoting stress concentration at corners [64] or, sections of the particle may be recipient of large stresses driving inclusion fracture [65]. On the subject of aspect ratio, Yeratapally et al.[66] observed that the aspect ratio of a given inclusion will affect the particle fracture behaviour. Particles with high aspect ratios would prefer fracture along their longest axis

whereas particles with low aspect ratio would fracture normal to the direction of maximum principal stress. High aspect ratio particles with their major axis perpendicular to the direction of maximum principal stress may therefore have arrested crack growth as their cracks are not effectively aligned. Bozek et al.[67] studied the relationship between inclusion aspect ratio and the maximum principal stress generated for an applied strain. Their research developed inclusion fracture criteria using the size, aspect ratio and particle properties. Schäfer et al. [68] found similar results on aspect ratio in an experimental and modelling study. Shabrov and Needleman [60] developed elastic-viscoplastic models to study the effect of inclusion morphology on void nucleation at the inclusion interface. Murakami and Endo studied the shape of inclusions and found that the difference in fatigue life between angular and spherical particles was negligible and attributed size as a larger contributor to limiting fatigue life [69].

2.3.3 Agglomeration

In some circumstances, inclusions form agglomerates consisting of several discrete particles embedded in the metal matrix near each other. Huron and Roth [70] found that agglomeration of inclusions resulted in a higher incidence of inclusion initiated fatigue. They artificially seeded an alloy with two types of inclusions; a large discrete ceramic type and an elongated agglomerate type. Out of a number n of dog-bone specimens tested, for specimens with agglomerates, 75% of initiations began at the seeds whereas specimens with blocky inclusions recorded 40% of failures initiating from seeds. The remainder of failures arose from grain boundaries. Fan et al.[71] studied cyclic plasticity at pores and carbides and found the spacing of carbides to correlate with the local plastic shear strain range, suggesting a tighter cluster promotes plasticity. Shenoy et al.[72] found that a shorter inclusion spacing reduced lifetimes but the effect became negligible at higher applied strains.

2.3.4 Properties of inclusions

The propensity for fatigue cracks to initiate at inclusions will also depend crucially on the mechanical properties of the inclusion material. Hard, brittle inclusions are usually the most deleterious in steels [57]. Classical studies have naturally considered the effect of differing elastic moduli on local stress behaviour [73]. However, much owing to their size, the properties of inclusions are often elusive. In addition, the origin of the inclusions is often unknown making characterisation difficult. Modelling methodologies such as CPFE are often reduced to describing inclusions as elastically isotropic particles [74,75] yet contemporary important inclusions such as HfO_2 may present monoclinic crystal structures lending to highly anisotropic stiffness [76,77]. This anisotropy also presents itself in the thermal coefficient of expansion [76], however, no research has investigated the effects of this. As the thermal expansion of the inclusion will be dissimilar to that of the matrix, Bandyopadhyay [52] investigated the effects of differing thermal expansion on inclusion driven fatigue crack nucleation and found that a high coefficient of thermal expansion will increase the nucleation probability at elevated temperatures. Zhang et al.[75], in a similar vein, found plasticity to prematurely develop near an inclusion under thermal loading due to the differing coefficient of thermal expansion. In another study, they found the effect of differing thermal expansion to be negligible compared with the plastic strains introduced in loading [51]. The strength of the inclusion and the strength of the interface between inclusion and metal matrix also affects the behaviour of inclusion fracture and decohesion respectively, these are discussed in detail later.

2.3.5 Surface and subsurface initiations

Observations of fatigue crack initiation at subsurface inclusions has prompted several studies investigating the discrepancy between surface and subsurface initiations [62,78,79]. Zhang et al.[78] developed a criterion for fatigue crack nucleation which postulates a critical depth which factors in surface stresses arising from shot-peening, gradients of applied bending and

carburisation of the surface (a surface treatment strictly for steels). They also find that the inclusion shape has a minimal effect on the fatigue life relative to the effect provided by the residual stress of the surface. Shot peening in a superalloy has been found to have a positive effect on surface initiations but initiations from the subsurface may still occur and high temperature negates the effect [70]. Conversely, Hyzak and Bernstein [80] found no dominant cracks to initiate at the subsurface in an unpeened alloy.

2.3.6 Temperature effect

Turbine discs operate at elevated temperatures. This has motivated several studies into the effects of temperature on nucleation near inclusions. The effects of the coefficient of thermal expansion has been mentioned above in 2.3.4 however, thermal expansion will only affect the local strain upon heating. Under high temperature, creep and transitions from octahedral to cuboidal slip will occur, changing the deformation behaviour in the neighbouring metal matrix. In addition, at high temperatures superalloys retain their strength during temperature increase [81] which may alter the local stress state. Huron and Roth [70] found fatigue life of inclusions to strongly correlate with the applied temperature during low cycle fatigue tests where a higher temperature increased the probability of failure at inclusions. Qiu and Wu [82] found a similar conclusion where they argue that the interface between matrix and inclusion agglomerates degrade at higher temperatures. Despite this, few studies have attempted to characterise the mechanisms which drive this change at high temperature. Hyzak and Bernstein [80] argued that the ease of heterogeneous slip-banding at lower temperatures produced pronounced features which increased probability of fatigue cracking in the matrix, at higher temperatures, environmental effects play a role in initiating failure at inclusions.

2.3.7 Competition with other microstructural features

Inclusions may be considered to compete with intrinsic crystallographic features such as twin boundaries in the case where they are below a critical size and that their properties are not extremely dissimilar from the matrix. Stinville et al. [83] note that nucleation from inclusions is more severe at lower applied stresses where at high stresses, samples preferred to fail from crystallographic facets (e.g. twin and grain boundaries). Pineau and Forest [84] also found inclusions to be the primary site at high cycle regimes. They conclude, however, that this is primarily due to early initiation at these sites. Another study by Stinville et al. [85] saw reduced initiation events at very high cycle regime where fatigue cracks would instead initiate at twin boundaries. In the next section the mechanisms which take place around inclusions in fatigue and promote early localisation are discussed.

2.4 Cyclic deformation around inclusions

During loading, particles embedded in the metal matrix impart a local enhancement to the stress field. A particle stiffer than the matrix will elevate local stress thus causing early onset of slip and development of slip banding. In early cycles of low cycle fatigue (meaning relatively high peak stresses) several studies observe particles decohering from the metal-oxide interface or fracture developing within the particle [38,86–88]. The properties of the inclusion are argued to be the cause of the competition between particle fracture and decohesion where fracture strength controls fracture and interface strength controls decohesion. In observations where neither fracture nor decohesion occur but the stresses are still high, crystallographic cracks nucleate on persistent slip bands impinging upon the particle. Thus, three scenarios may occur local to inclusions if subjected to cyclic stresses: (i) inclusion fracture, (ii) interfacial decohesion or, (iii) slip-driven nucleation. Here, literature that exists with case examples of each is explored. It is worth noting that while all three mechanisms are vitally important to understand fatigue crack initiation, particle fracture and particle decohesion are not the

nucleation of a fatigue crack, rather a nucleation of a void which may later develop fatigue cracks. The third mechanism, slip-driven nucleation, involves direct nucleation of a crystallographic crack which may immediately grow in what is termed the short-crack growth regime.

2.4.1 Inclusion fracture

Texier et al. [86] reported that fracture of particles in Inconel 718 may occur below 60% of the macroscopic yield stress. However, initiation from fractured particles did not necessarily reduce fatigue life of the dog-bone specimens in their study. An incubation period was observed post particle fracture, where a significant number of cycles passed before a crystallographic fatigue crack nucleated. In a follow-up study, they investigated the effect of “pre-fractured” particles by applying a pre-strain to the fatigue test [89]. The study identified that particle fracture may lead to (i) incubation (ii) metal-oxide decohesion from fracture void (iii) nucleation of transgranular crack nucleation from fracture void. These mechanisms were observed to be dependent on the neighbouring metallic grain crystallographic orientations. Pre-fracture was hypothesised to arrest crack growth as the macroscopic yield strength would increase after straining but a follow up study found that fatigue life decreased as most cracks would nucleate at pre-fractured inclusions [90].

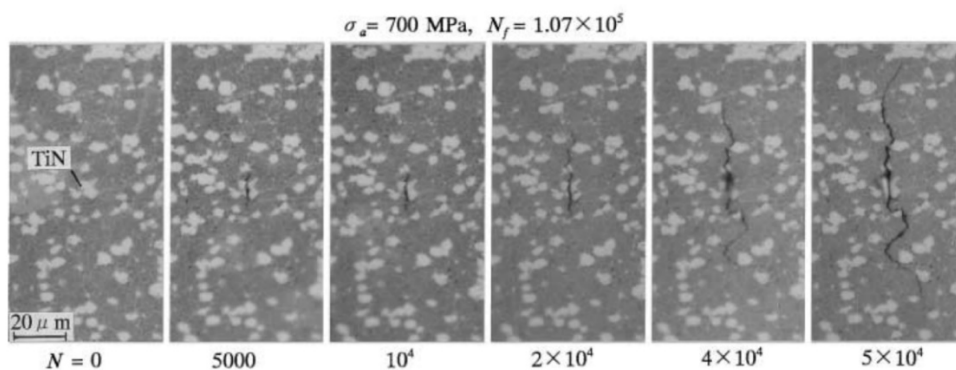


Figure 2-7 - Fracture of a TiN inclusions in Udimet 720 and subsequent crack growth. Fracture of inclusions has occurred early between cycle $N=0$ and $N=5000$. (adapted from [91])

Goto and Knowles [91] performed a low cycle fatigue experiment on Udimet 720 Li via 4pt-bending. Their results show that inclusions fracture by exceeding this critical principal stress and 80% of particles fracture within the first few cycles of loading. In addition, fractures within particles are near perpendicular to the loading direction – further suggesting that the maximum principal stress drives the fracture. An example TiN inclusion fracture is shown in Figure 2-7. They conclude that the inclusions are the major limiting factor of fatigue for this material. Texier et al.[92] found that inclusion fracture was dependent on the applied strain level, where higher strains resulted in more cracked inclusions. They also observed that fractured particles occurred early without slip activity in neighbouring grains.

2.4.2 Inclusion decohesion

An inclusion may be perfectly bonded, partially debonded or completely debonded [93]. For this discussion, studies which contain bonded inclusions are shown. In a low alloy steel, Lankford [94] found that decohesion of the metal-oxide interface occurred within the first tensile loading at stresses well below macroscopic yield. After debonding, a fatigue crack would develop from the decohesion void after a considerable number of cycles indicating that decohesion does not birth a crystallographic crack but may develop into a fatigue crack after continued loading. This is a similar observation to the previously discussed particle fracture.

Zhang et al.[87] studied the development of strain around an agglomerated inclusion. They argue that thermal residual stresses from processing resulted in early onset of plasticity in the proximity of inclusions, indicating that high stresses near particles may not be solely caused by the stiffer nature of particles. Using HR-DIC and HR-EBSD they found establishment of significant densities of geometrically necessary dislocations (GNDs) which indicate high residual stresses from fatigue loading. The follow up study [51], decohesion was argued to be brittle in nature where the stress component is that normal to the interface. If σ_n exceeds a critical value $\sigma_{decohesion}$ then decohesion will occur:

$$\sigma_n > \sigma_{decohesion}.$$

2.1

In a similar vein, Landron [95] found the strength of decohesion using a modified version of the Argon decohesion criterion [96] which accounts for local stress triaxiality.

Considerable work has been performed on the nature of interface deformation using the cohesive zone model [60,97,98]. Xu and Needleman [99] investigated a similar model of a plane inclusion suspended in a crystal matrix to investigate whether localisation in the crystal matrix or decohesion occur first. They concluded that localisation may occur in the matrix if the interfacial strength remains high enough – indicating that if the neighbouring matrix experiences ratchetting and stress elevation, any interfacial strength may be overcome. They also found that the development of decohesion was relatively insensitive to the parameters describing the shear response compared with the description of normal response which strengthens the argument that normal stress is a key driver in decohesion.

By seeding a large inclusion in a matrix, Naragani et al.[74] studied subsurface debonding and crack nucleation in-situ in RR1000 using absorption contrast computed micro-tomography (μ -CT) and far-field high energy diffraction microscopy (FF-HEDM). They observe that the crack did not initiate at sharp inclusion features or at the broadest cross-section. Instead, the crack nucleated from the debonded section. Comparing FF-HEDM results to elasto-viscoplastic modelling results show that debonding of the inclusion creates large stress gradients which drive crack nucleation. In particular, debonding and associated residual stress create large gradients in neighbouring grains which drive plasticity and create the necessary conditions for crack nucleation.

In some studies, particle fracture may occur alongside particle decohesion, exhibiting a mixed-mode initiation. Zhang et al.[87] studied the development of slip using HR-DIC near an agglomerated non-metallic inclusion and observed fracture and decohesion events occurring in

early cycles. A micro crack nucleates from these initiations in later cycles. A follow-up study using a representative crystal plasticity finite element (CPFE) model investigated the ratchetting phenomenon in the surrounding grains but did not find a conclusive stress for fracture of particles [51]. Experimental studies by Chen et al.[100] conclude that fracture takes place is softer and weaker inclusions whereas harder inclusions would prefer decohere from the matrix.

2.4.3 Slip-driven nucleation

Fatigue cracks have been observed to nucleate directly in the metal matrix adjacent to ceramic inclusions [101], rather than from voids introduced by decohesion and inclusion fracture. While studying deformation around an inclusion in low cycle fatigue, Jiang et al.[102] observed several cracks nucleating along grain and twin boundaries or persistent slip bands in FGH96. They further noted that GND density and plastic were high in vicinity of cracks and concluded that these were prerequisite for fatigue crack nucleation but not exclusively required as other locations neighbouring the inclusion with high GND density and plasticity did not crack. A follow-up study by Chen et al.[49] considered a faithfully representative CPFE model of the inclusion with grain structure incorporated. Their results show that a stored energy criterion was successful in the capture of fatigue crack nucleation sites. The stored energy criterion is a measure of (elastic) stored energy at a material point considering the stress and plasticity but providing a length scale normaliser in the form of dislocation density [103]. It may be expressed as:

$$\Delta G = \int \frac{\xi |\boldsymbol{\sigma} : d\boldsymbol{\epsilon}^p|}{\sqrt{\rho_{ssd} + \rho_{gnd}}}. \quad 2.2$$

ΔG is the change in stored energy per plasticity increment and is the integral of the double inner product of the stress tensor $\boldsymbol{\sigma}$, the plastic strain tensor $\boldsymbol{\epsilon}^p$, normalised by the dislocation densities. Bold variables indicate tensors. ξ is a fraction of the total dissipated energy stored in dislocation structures, normally considered to be $\xi = 0.05$ [104,105]. Figure 2-8 shows the correlation between stored energy and sites of crack nucleation.

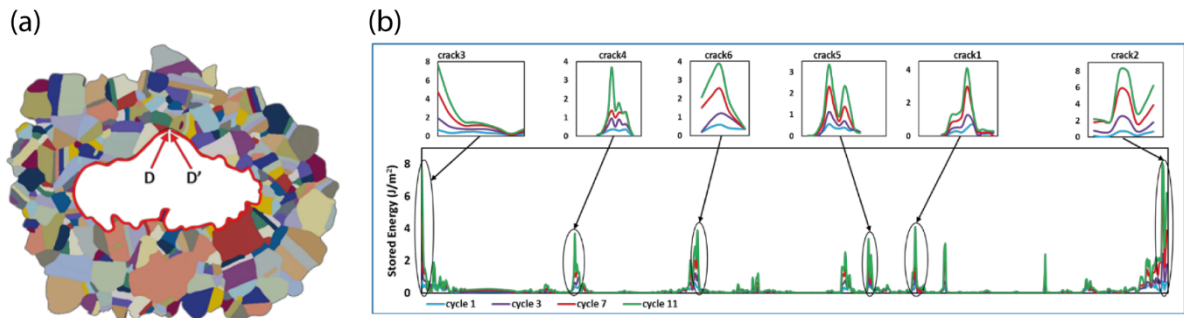


Figure 2-8, (a) a reconstructed microstructural model of a ceramic inclusion with metal-oxide interface highlighted in red where D and D' indicate the start and end point of a perimeter path. (b) The stored energy density around the path D-D' with excerpts showing experimental fatigue crack initiation sites (Adapted from [49])

Tanaka and Mura [106] modelled the nucleation of a slip-band crack emanating from an inclusion by approximating the dislocation pile-up on the inclusion boundary under a remote stress. They estimate, in the case of slip-driven cracks, that nucleation occurs once an energy condition is satisfied [107]. The self-stored energy U stored after n cycles is expressed as:

$$\sum_{i=1}^{2n} U_i = U_1 + 2n\Delta U. \quad 2.3$$

The first righthand term concerns dislocations introduced in the first loading, which Tanaka and Mura consider to be insignificant in long-term fatigue. The energy stored per half cycle ΔU is then written as:

$$\Delta U = \frac{(\Delta\tau - 2k)^2 \pi l^2}{2\mu} \quad 2.4$$

where $\Delta\tau$ is the cyclic shear stress acting on a slip band, k is the frictional stress of dislocation motion, μ is the shear modulus and l is the length of the slip band. They then estimate the nucleation life n_c from:

$$2n_c \Delta U = 4lW_s \quad 2.5$$

where W_s is the specific fracture energy on the slip band. They also consider the specific fracture energy of grain boundaries W_g . They conclude that their results are in qualitative agreement with experimental results.

2.5 Concluding remarks

In this chapter, literature concerning the origin of non-metallic inclusions both for powder metallurgy and processing methods which use metal powder (i.e. additive manufacturing), the effect of inclusions on fatigue life, and finally the mechanisms which occur during cyclic deformation around inclusions has been reviewed.

It has been made clear that non-metallic inclusions pose a debit to the fatigue life of any alloy they inhabit but the present literature has not yet answered key questions about the microstructural and micro-mechanical drivers for fatigue crack nucleation around these defects. A complete probabilistic framework for predicting fatigue crack nucleation in an alloy containing non-metallic inclusions will need a thorough understanding of the contribution these mechanisms give to crack nucleation. This will improve the accuracy and thus increase the confidence in component lifetimes.

3 Competing mechanisms of inclusion fracture, decohesion and slip-driven fatigue crack nucleation in a PM nickel superalloy

3.1 Introduction

Fatigue crack nucleation at non-metallic inclusions may begin as voids introduced by inclusion-matrix decohesion, inclusion fracture or slip-driven nucleation. These phenomena of early-stage fatigue crack nucleation have all been observed around inclusions in Ni-based superalloys and understanding their mechanistic drivers is vital for developing comprehensive predictive frameworks for lifing of turbine disc components. SEM micrographs of inclusion fracture (a), inclusion decohesion (b) and slip-driven nucleation (c) are all shown alongside a schematic representation (d) in Figure 3-1.

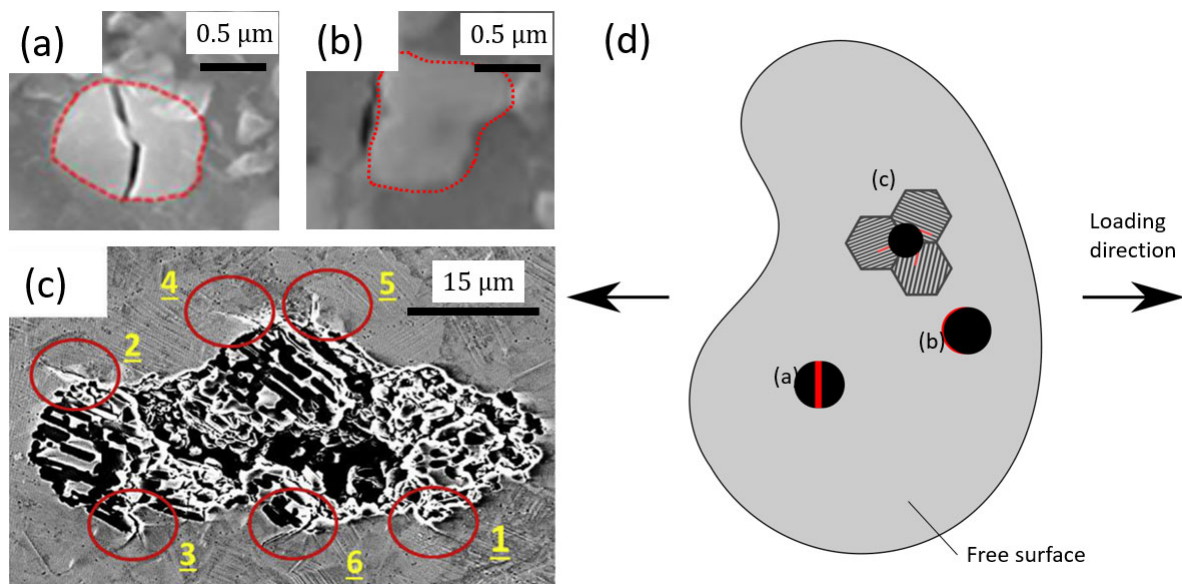


Figure 3-1 - Micrographs of (a) particle fracture in Ni-base superalloy RR1000 , (b) particle decohesion in RR1000 [51] and (c) slip-driven nucleation from an inclusion in a Ni-base superalloy FGH96 [49]. A schematic diagram of the nucleation modes is shown in (d)

The cohesive zone model was conceived by Dugdale [108] and Barenblatt [109] to describe non-linear crack tip problems. In a contemporary cohesive zone model, surfaces (or elements) are assigned a traction-separation relation which describes the behaviour of fracture (or decohesion) as a load is applied. The approach is widely used to study delamination in composites (e.g.[110,111]) but is applicable to any surfaces held together by cohesive forces. In the context of decohesion of second-phase particles, the method has been used to model elastic particles in an elastic-viscoplastic matrix [97], crystal plastic [99] matrix, silicon carbide fibre decohesion in metal matrix composites [111], decohesion of thermal barrier coatings [112], particulate decohesion in composites [110], and to investigate the influence of a surface oxide in microcantilever experiments [113]. Elzas et al. [114] implemented a cohesive zone model in a discrete dislocation plasticity framework and investigated crack growth at iron-precipitate interfaces.

The traction-separation behaviour is often characterised by maximum traction, displacement at failure and fracture energy (area under the traction-separation curve). The differing fracture behaviours from mode I to mode II are well known [115]. The cohesive zone model is therefore often described using mixed-mode relations [116]. The form of the traction-separation relationship is argued to be of utmost importance by several researchers (e.g. [111,114,117]). The physical significance of the relationship is in many cases based on atomistic predictions, including the exponential based curve of Needleman [97], related to fundamental work on binding energies of atomistically sharp planes by Rose et al. [118]. The exponential based curve is potential-based as it derives directly from the separation of atomic entities whereas non-potential shapes may be derived from phenomenological observations of fracture surfaces. The potential versus non-potential view is argued by Park et al. [119] who have recently introduced a generalised potential based cohesive zone model which is path dependent.

Three distinctive fatigue crack nucleation modes - particle decohesion, particle fracture and slip-driven nucleation – have been observed in relation to powder metallurgy nickel alloys containing agglomerates. Previous work has assessed the particle-matrix decohesion by quantitative study of interfacial normal stresses. However, the mechanistic basis of particle fracture (as opposed to decohesion) has not yet been quantitatively assessed. In addition, neither the particle-matrix decohesion nor particle fracture have been explicitly incorporated in to model microstructural representations in order to account for the stress redistribution which occurs from both mechanisms. Further, decohesion and particle fracture have not been investigated in terms of how they influence subsequent slip-driven fatigue crack nucleation and effect on fatigue life. Hence these are the objectives of this study which introduces cohesive zone modelling in to faithful polycrystal plasticity representations of an experimentally characterised microstructure. Both particle-matrix decohesion and particle fracture are therefore allowed explicitly to occur such that the resulting stress redistributions and corresponding changes to stored energy density may be captured. The stress redistribution resulting from a particle fracture event, for example, then leads to significant changes to local interfacial normal stresses at an adjacent particle thereby radically changing the local driver for decohesion. Further, the stress redistributions resulting from both fracture and decohesion change the distributions and magnitudes of the stored energy density accumulations and hence the cycles required to give slip-driven fatigue crack nucleation. Hence the three failure mechanisms are shown to be strongly coupled. In addition, the mechanistic basis of experimentally observed particle fracture is addressed, revised interfacial particle-matrix cohesive strengths are obtained, and their influence on slip-driven crack nucleation investigated. This leads to the formulation of a preliminary mechanisms-based S-N curve for PM nickel alloys with agglomerated inclusions.

3.2 Methods

3.2.1 Crystal plasticity finite element formulation

In this section a detailed description of the crystal plasticity finite element formulation which is used throughout the thesis in chapters 5 and 7. Specific modifications, such as kinematic hardening and incorporation of stored energy density measurements, are given in their respective chapters.

The key motivation for crystal plasticity is the desire to model heterogeneous deformation at the grain level scale. Analytical and finite element methods which are assessed at the engineering length scale often consider a material as homogenous in mechanical properties. As a result, microscopic phenomena such as cracks, were often considered without considering the effect of microstructural features (chiefly grains and their related properties). Thus, these models were often over-idealised and resulting predictions were erroneous. Following key developments by Pierce et al.[120], crystal plasticity became the eminent method for modelling deformation at the grain scale.

In this thesis, implementation of crystal plasticity into a finite element framework is done through a user-subroutine in the commercial FEA software Abaqus [121]. The formulation follows that of Dunne et al.[122] in which a user-element (UEL) subroutine was written. In this work, the implementation has been rewritten for a user-material (UMAT) subroutine. User subroutines are element sub-models which solve the stress, tangent stiffness, and other user-defined variables per deformation increment in a finite element model. The details of the finite element model are not discussed in this thesis, instead the material formulation is discussed. A discrete finite element will have assigned properties to determine the material response. Locally, the material points need to define the orientation of the crystal lattice which determines the anisotropic elasticity and the slip systems which will activate under a given deformation.

Material properties, which will be discussed later, are naturally material dependent and determine the stiffness, the criterion for plastic slip, the rate of plastic slip, the evolution of dislocation densities and, the hardening resulting from dislocation densities.

The classical deformation gradient \mathbf{F} may be decomposed to elastic \mathbf{F}^e and plastic \mathbf{F}^p parts [123]:

$$\mathbf{F} = \mathbf{F}^e \mathbf{F}^p \quad 3.1$$

Deformation at a material point therefore needs to be described in both elastic and plastic terms. In an FCC crystal system of which this thesis is concerned with, the elastic behaviour is anisotropic according to geometry of the crystal lattice. FCC anisotropic elasticity is incorporated via the compliance matrix, \mathbf{D} :

$$\mathbf{D} = \begin{bmatrix} \frac{1}{E_1} & -\frac{\nu_{12}}{E_1} & -\frac{\nu_{13}}{E_1} & 0 & 0 & 0 \\ -\frac{\nu_{12}}{E_1} & \frac{1}{E_1} & -\frac{\nu_{13}}{E_1} & 0 & 0 & 0 \\ -\frac{\nu_{13}}{E_1} & -\frac{\nu_{13}}{E_1} & \frac{1}{E_1} & 0 & 0 & 0 \\ 0 & 0 & 0 & \frac{1}{G_{12}} & 0 & 0 \\ 0 & 0 & 0 & 0 & \frac{1}{G_{13}} & 0 \\ 0 & 0 & 0 & 0 & 0 & \frac{1}{G_{23}} \end{bmatrix} \quad 3.2$$

where E_i is the Young's modulus, ν_{ij} is the Poisson's ratio and G_{ij} is the shear modulus. The subscripts i, j indicate orthogonal axes. The compliance matrix describes anisotropic Hookean elasticity at a global scale may be rotated to the axes of a local crystal through rotation matrices \mathbf{T}_σ and \mathbf{T}_ϵ :

$$\mathbf{C} = \mathbf{T}_\sigma \mathbf{D} \mathbf{T}_\epsilon^{-1} \quad 3.3$$

For plastic motion, a shear stress τ acting on a slip system a will have to exceed a critically resolved shear stress τ_{crss} . The shear stress acting on an individual slip system can be found through:

$$\tau^a = (\boldsymbol{\sigma} \mathbf{n}^a) \cdot \mathbf{s}^a \quad 3.4$$

where $\boldsymbol{\sigma}$ is the Cauchy stress tensor, \mathbf{n} is the slip system normal vector and \mathbf{s} is the slip system direction vector. Ni-based superalloys have an FCC structure which exhibits 12 slip systems. The slip systems in FCC are shown schematically in Figure 3-2. As deformation occurs, the slip plane vectors are recalculated to account for any rotations the crystal undergoes.

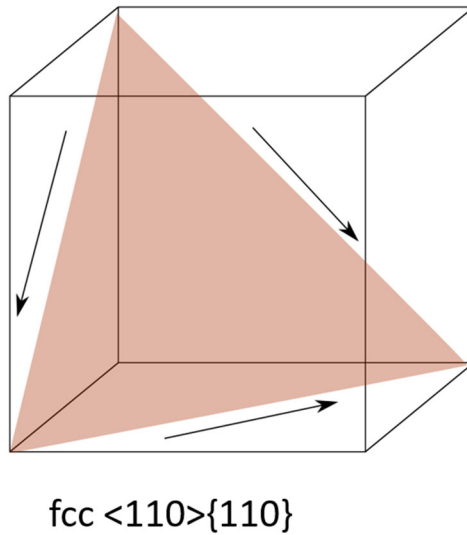


Figure 3-2 – The slip systems in FCC

The plastic velocity gradient \mathbf{L}^p may be expressed as [124]:

$$\mathbf{L}^p = \dot{\mathbf{F}}^p \mathbf{F}^{p-1} = \sum_a \dot{\gamma}^a \mathbf{s}^a \otimes \mathbf{n}^a \quad 3.5$$

The rate change of the plastic deformation gradient is therefore found by the sum of slip rate $\dot{\gamma}$ on all slip systems α . The slip rate [122] is governed by a physically based interpretation:

$$\dot{\gamma}^a = \rho_m \nu b^2 \exp\left(-\frac{\Delta F}{kT}\right) \sinh\left(\frac{(\tau^a - \tau_{crss})\Delta V}{kT}\right) \quad 3.6$$

where here, the parameters are based on material properties. ρ_m is the density of mobile dislocations, ν is the frequency of attempts to overcome the dislocation energy barrier, b is the Burger's vector, ΔF is the activation energy of the system, ΔV is the activation volume, k is the Boltzmann constant, and T is the temperature. The slip rate equation models the motion of dislocations encountering pinning barriers and the thermal activation of escape from these barriers.

Under plasticity, dislocations glide and encounter obstacles in the form of other dislocations [125]. In addition, plasticity generates dislocations through, for example, Frank-Read sources [126]. With increasing plasticity, the material hardens as plastic motion becomes impeded with increasing dislocation densities. Here, hardening is incorporated through the classical Taylor equation:

$$\tau_{crss} = \tau_{crss_0} + Gb\sqrt{\rho_{ssd} + \rho_{gnd}} \quad 3.7$$

in which τ_{crss_0} is the initial slip strength, ρ_{ssd} is the density of statistically stored dislocations and ρ_{gnd} is the density of geometrically necessary dislocations. The material point may therefore harden at every deformation increment if the density of dislocations grows. In a volume element of crystallographic material, the dislocations which are stored can be dissociated into GNDs and SSDs [127]. SSDs arise from chance encounters with other dislocations in the material which results in mutual trapping and thus causes work hardening. GNDs are geometrically necessary in that they are required for accommodating the plastic deformation of the crystal. They are responsible for length scale effects [128] which result in gradient plasticity effects within the model.

The evolution of statistically stored dislocations is governed by a linear relationship between the evolution of effective plastic strain p and the hardening constant λ :

$$\dot{\rho}_{ssd} = \lambda \dot{p} \quad 3.8$$

Where the effective plastic strain can be found through:

$$\dot{p} = \sqrt{\frac{2}{3} \boldsymbol{\epsilon}^p : \boldsymbol{\epsilon}^p} \quad 3.9$$

While the obtainment of SSDs is relatively trivial, GND densities are somewhat more difficult to determine. The determination of GND density follows the formulation of Arsenelis and Parks [129], a brief description is given here. The density of geometrically necessary dislocations can be obtained from Nye's dislocation tensor $\mathbf{\Lambda}$ [130] which can be related to the curl of the plastic deformation gradient:

$$\mathbf{\Lambda} = \text{curl}(\mathbf{F}^p) = \sum_{i=1}^{12} \rho_{Gs}^i \mathbf{b}^i \otimes \mathbf{s}^i + \rho_{Get}^i \mathbf{b}^i \otimes \mathbf{t}^i + \rho_{Gen}^i \mathbf{b}^i \otimes \mathbf{n}^i \quad 3.10$$

The GNDs within a crystal may be discretised into 36 components of screw and edge types depending on their line properties. ρ_{Gs} is the density of screw dislocations on a given slip plane with directional vector \mathbf{m} , ρ_{Get} is the density of edge dislocations in the direction of $\mathbf{t} = \mathbf{s} \times \mathbf{n}$, and ρ_{Gen} is the density of edge dislocations in the direction \mathbf{n} .

By application of a linear combinator, \mathbf{A} , the vector density of geometrically necessary dislocations $\boldsymbol{\rho}_{gnd}$ can be related to Nye's dislocation tensor through [129]:

$$\mathbf{A} \boldsymbol{\rho}_{gnd} = \mathbf{\Lambda} \quad 3.11$$

in which $\boldsymbol{\rho}_{gnd}$ is a concatenation of geometric dislocation "types" ρ_{Gs} , ρ_{Get} , ρ_{Gen} into a 36-component vector. Nye's dislocation tensor is in equation 3.10 and 3.11 a nine-dimensional

column vector which contains the dyadic product of Burgers vectors and direction vectors for each discrete dislocation type. \mathbf{A} is therefore a 9x36 matrix and requires Moore-Penrose pseudo-inverse \mathbf{A}^+ to get:

$$\rho_{gnd} = \mathbf{A}^+ \mathbf{\Lambda} \quad 3.12$$

A scalar sum of the density of GNDs may then be found through a Euclidian norm:

$$\rho_{gnd} = \sqrt{\rho_{Gs}^2 + \rho_{Ge}^2 + \rho_{Gea}^2} \quad 3.13$$

At each increment in the model, an implicit scheme is used to integrate the constitutive equations described above. A full description of the integration scheme and related Newton-loop is given in [122]. A schematic of the incremental scheme is shown in Figure 3-3.

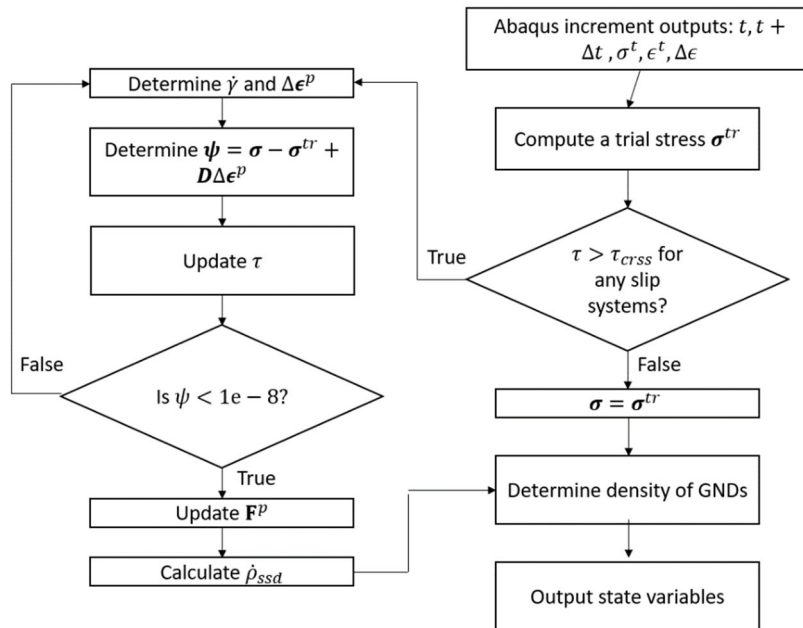


Figure 3-3 – A simplified schematic showing the process of the UMAT at each deformation increment.

CPFE considers the deformation of a crystal at the continuum scale. Typical element sizes can be from the 100s of nm to several μm . Discrete deformation features such as slip bands are therefore not captured explicitly. Instead, crystal plasticity captures the homogenised deformation over the element related to the influence of the crystal structure and development of dislocation densities.

The stored energy density, which is that part of the plastic work which is stored by virtue of the establishment of dislocation structural interactions [131] over a length scale determined by the dislocation density, can be expressed as:

$$U = \int \frac{\xi \boldsymbol{\sigma} : d\boldsymbol{\epsilon}^p}{\sqrt{\rho_{SSD}}} \quad 3.14$$

where U is the stored energy density and ξ is the fraction of plastic energy in a cycle used to establish dislocation structures. This quantity has been used successfully to predict the location of cracks in polycrystal models and is discussed further in the next section.

3.2.2 Ni-base Superalloy Agglomerate model

In a previous study [87], a three-point bend specimen was subjected to low-cycle, load controlled fatigue. The specimen (12.7x3.5x1.94mm) was deliberately machined to contain an oxide agglomerate inclusion on the tensile fibre of the front, free face. In the experiment, developments of strains were recorded at interrupted intervals by using HR-DIC. In this study, a new explicit model representation of the agglomerate microstructure has been developed. This is related to that presented in [51] but very different in that it contains cohesive zone surface interactions to facilitate the study of agglomerate decohesion and fracture which have not been addressed before. The geometry was created from EBSD and SEM micrographs showing oxide particles, fine inter-oxide grains and coarse grains. As subsurface characterisation was not possible, edges were extruded to form columnar grains. This type of

idealised model has been used in several prior studies with successful predictions of deformation [132,133]. Appropriate crystallographic orientations were applied to the coarser grains.

The small grains located between particles are numerous and obtaining accurate crystallographic orientations is difficult owing to their size. They are therefore assigned a reference orientation (i.e. the $[1\ 0\ 0]$ pointing in x-direction and the $[0\ 1\ 0]$ pointing in the y-direction). The oxide particles were identified as hafnia via secondary electron microscopy (SEM) energy dispersive X-ray spectroscopy (EDS). They were assigned elastic properties obtained from reported values in the literature [76]. Isotropic elasticity was assumed due to their size and difficulty in obtaining a surface finish sufficient enough to yield diffraction patterns. The properties are shown in Table 3-1. The ensemble was contained within an elastically isotropic medium representing the fine-grained, homogenous RR1000 microstructure. The physical properties used for the slip rule were obtained from calibration against tensile tests performed at Rolls-Royce plc. The resulting slip rule properties are shown in Table 3-2. Loading conditions local to the agglomerate region were inferred from a full beam model utilising von Mises plasticity, as described in [51] together with the independent experimental loading conditions and strain measurements. Therefore, a cyclic load controlled boundary condition was applied such that the peak tensile stress experienced was 1366 MPa (145% of yield stress).

Table 3-1, isotropic elasticity properties for Hafnia inclusions

E	G	ν
280 GPa	90 GPa	0.295

Table 3-2, the properties used for the slip rule.

ρ_{ssd}^m	b	ν	ΔH	T	τ_{crss}	λ	ΔV
$0.05 \mu\text{m}^2$	$3.51 * 10^{-4} \mu\text{m}$	$1 * 10^{11} \text{s}^{-1}$	$3.456 * 10^{-20} \text{J}$	293 K	450 MPa	$150 \mu\text{m}^{-2}$	1.28b^3

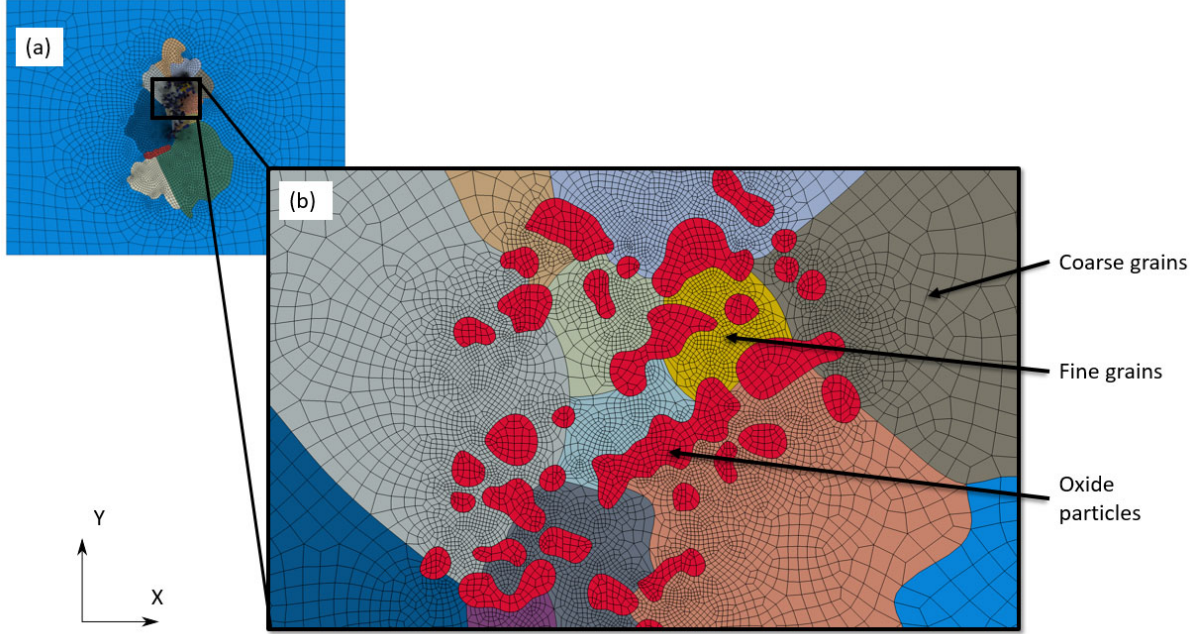


Figure 3-4 - (a) Front-view mesh of the full crystal plastic submodel, (b) a detailed close-up of various microstructural features and their meshing within the submodel

The new microstructural model contains around 60,000 swept C3D20R finite elements representing the agglomerate oxide particles, and the coarse and fine Ni grains, and is shown in Figure 3-4, together with a close-up image to demonstrate the microstructural features captured. The mesh is refined local to the agglomerates since these are primary areas of interest in the present work. The crystal plasticity constitutive behaviour is incorporated through a user-material (UMAT) subroutine. Loading is applied on the right-hand surface to reproduce the load created in the 3pt-bend experiment as discussed in [51].

On surfaces separating oxide particles from Ni matrix, an interaction is defined using an elemental surface master-slave formulation with cohesive zone properties. This facilitates

explicitly particle-matrix decohesion to be modelled. In addition, surfaces are also created within oxide particles which have normals parallel to the direction of loading. These oxide-oxide interfaces are also assigned cohesive zone properties, and this enables particle fracture to be modelled independently. The cohesive zone model, and associated properties, used in this study are outlined in the next section. In total, 135 interactions are defined with an initial clearance between slave and master surfaces equal to zero. Example model predictions of local strain distributions along defined paths are shown in the appendix along with the independent experimental measurements taken from [51], showing reasonable agreement.

3.2.3 Traction-separation model

Both particle fracture and decohesion are observed in the Ni-base superalloy agglomerate containing system. Here, the definition of the traction-separation behaviour between selected oxide-oxide surfaces and metal-oxide surfaces to describe both particle fracture and decohesion respectively. *Decohesion* has been argued to occur only when the normal stress acting on the surface is sufficiently high [51]. It is therefore reasonable to assume that the tangential (mode II) and transverse (mode III) shear behaviours of the interface play little role in the decohesion and appropriately simplify the traction-separation behaviour by assigning relatively high tangential and transverse shear strengths, t_s^{max} and t_t^{max} respectively, while keeping the normal strength, σ_n^{max} physically representative of the true decohesion strength. The strength has been found to lie in the range of 1270 – 1480 MPa in terms of normal stress acting on the surface [51]; a parametric analysis is performed later in this study to investigate the validity of this range. Experimentally, it is observed that decohesion occurs in a brittle-manner where the stress carried normal to the interface eventually leads to the sudden decohesion of the metal-oxide interface. It may therefore be postulated that the separation of surfaces is stress controlled. The shape of the traction-separation curve is therefore argued to be of secondary importance as, ideally, cohesion should cease after peak stress is reached. A bilinear traction-

separation, originally developed by Geubelle et al. [134] and Alfano et al. [135] is therefore used. A definition of the initial traction-separation gradient, k_n , which is physically representative of the interfacial stiffness, was made. Complete separation of surfaces is typically said to occur when traction reduces to zero subsequent to attaining its peak value. Here, the assumption is that decohesion occurs when the peak has been attained. While there is little physical basis to assert that there is material continuity once this stress limit has been exceeded, rapid unloading of traction post-nucleation poses potential convergence problems for the three-dimensional finite element analysis. Convergence also becomes an issue when large slope changes are present. The elastic snap-back effect is mitigated here by adding a viscous regularisation term of $\mu=0.01$ [136]. In addition, in the current geometric representation of the microstructure, while decohesion may have occurred at the oxide-matrix interface on the sample free surface, the sub-surface material continues to provide constraint such that the average through-thickness normal stress remains finite and non-zero. These factors justify the need for a progressive linear interfacial unloading as shown in Figure 3-5 (b). A separation distance, δ^f , is chosen such that the progressive linear unloading produces results reflective of experimental results.

Fracture of brittle particles is considered in a similar manner where a bilinear traction-separation is used with the assumption being that fracture is driven by a maximum principal stress. Surfaces are therefore orientated to be normal to the direction of loading (shown schematically in Figure 3-5 (a)) with a σ_n^{max} term controlling the nucleation of fracture in a particle. The value of k_n is chosen to represent the elastic modulus of the oxide particle at the length scale of a micron. Properties for both *decohesion* and *fracture* are given in Figure 3-5 (c).

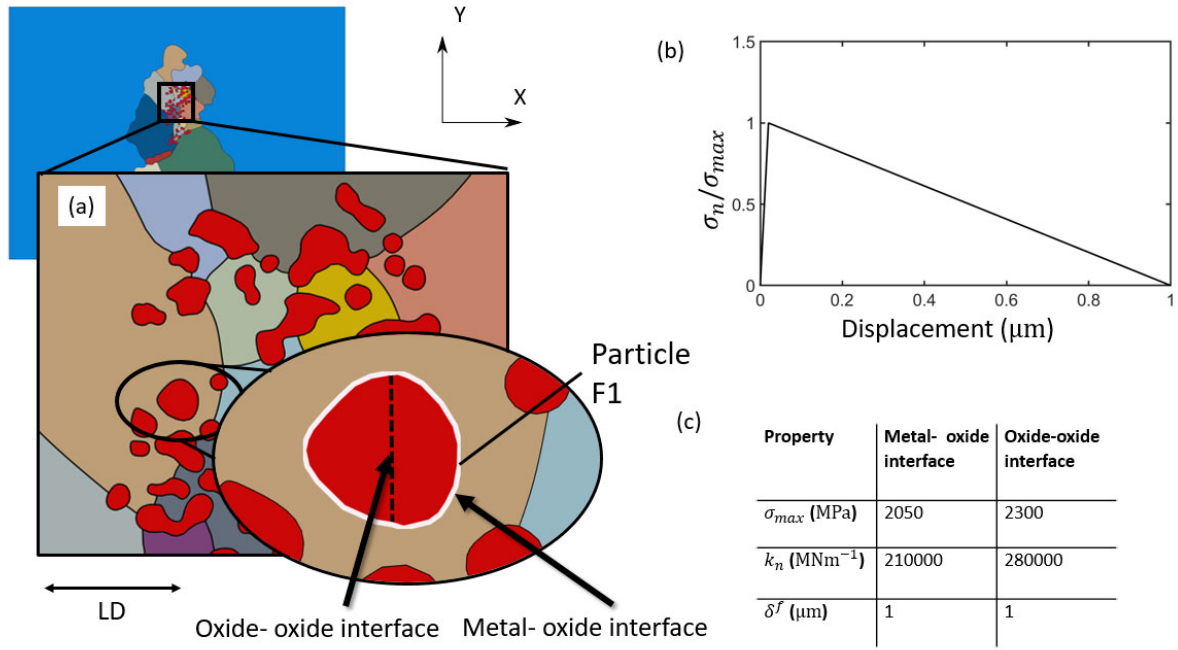


Figure 3-5 - (a) Schematic example of the oxide-oxide (particle fracture) interface is displayed as the black, dashed line and metal-oxide (decohesion) interface which is shown in white for particle F1 (b) the traction-separation relation used, and (c) the properties used for particle fracture and decohesion

The traction-separation behaviour is implemented through the Abaqus surface interaction framework. The constitutive tensile behaviour of the cohesive zone is defined through contact separation and contact stress. In compression, no damage is accumulated and hard contact is defined.

3.3 Fracture strength of oxide particles

The experimental observations reported in [51] showed that both particle fracture and particle decohesion occurred early during cyclic loading (within 1st -20th cycle). Figure 3-6 shows those particles where fracture occurred and those for which decohesion occurred. In this section, the microstructurally representative crystal plasticity model established above is firstly used to investigate key quantities local to experimentally observed particle fractures in order to extract the mechanistic drivers for the particle fracture phenomenon rather than particle decohesion.

This is carried out by studying the local behaviour prior to the occurrence of any particle-matrix decohesion or particle fracture. Explicit incorporation of the failure processes using cohesive zone modelling is addressed in a later section.

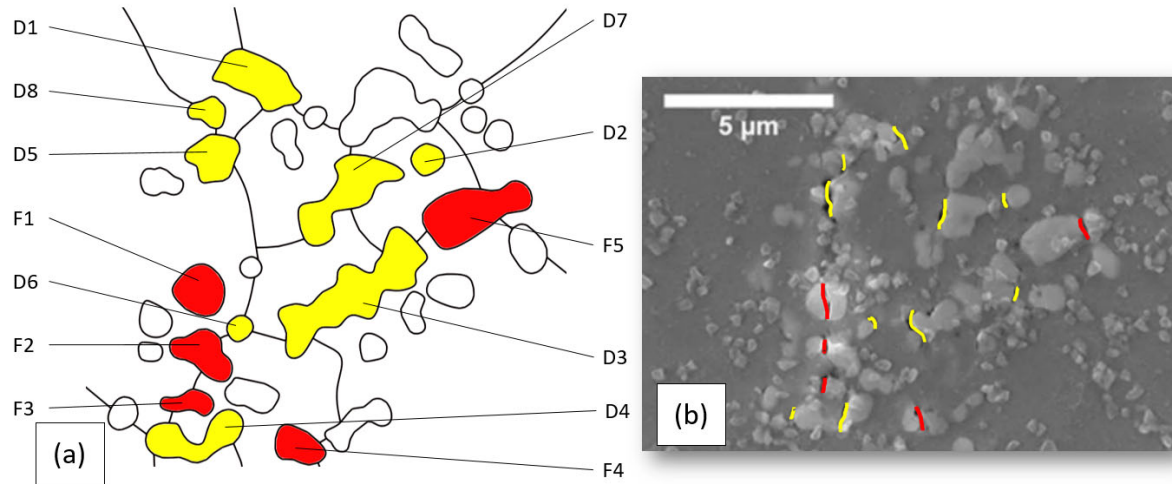


Figure 3-6 - (a) trace of particles and grain boundaries in the agglomerate system with fractured particles highlighted in red and decohered particles highlighted in yellow. Annotations are provided for fractured particles (labelled F) and decohered particles (labelled D). (b) Experimental observation of the agglomerate region after loading with fracture and decohesion represented by red and yellow lines respectively, taken from [20]

Stresses normal to the particle-matrix interfaces around a range of particles have been extracted. Figure 3-7 shows the predicted normal stress $\sigma_n = (\boldsymbol{\sigma}\mathbf{j}) \cdot \mathbf{j}$ (where \mathbf{j} is a vector normal to the surface of a particle) distribution around particles which (a) and (b) decohered, and (c) and (d) fractured in the experimental observations shown in Figure 3-6. The stress is obtained here from the Ni integration points on the oxide boundary. The size of the arrow indicates magnitude of stress with red arrows indicating locations of maximum normal stress. Plots of stress magnitudes are given against the perimeter paths in Figure 3-8 for (a), (b), (c) and (d) respectively. Cohesive interface strengths of 1270 – 1480 MPa previously reported in [51] are plotted on the graph. This range of decohesion strength was obtained by considering the mean normal stress of decohered particles at peak loading conditions and comparing this value against peak normal stress of unaffected (non-decohered) particles. Stresses at peak loads

are found to exceed the cohesive strengths indicating that decohesion should have occurred for all four particles (D1, D2, F1 and F2). For particles D1 and D2 (and others reported in [51]) the observed locations of decohesion are found to directly coincide with the location of peak normal stress in a significant number of decohered particles. The peak normal stresses were observed on interfaces which were normal to the direction of loading. Direct comparisons of predicted decohesion sites and experimental observations are shown in Figure 3-9 with good agreement. However, particles which were observed to crack in the experiment (eg F1 and F2 discussed above and in Figure 3-6) also develop high magnitudes of predicted interfacial peak normal stress, suggesting that they also should decohere unless, in fact, they had already fractured. This therefore suggests a quite separate mechanism is associated with particle fracture and that the local drivers were high enough to cause fracture before the interfacial stresses were high enough to drive decohesion. The variation of mean peak normal stresses during the peak load at the interface is investigated for particles which decohered in the experiment and particle which fractured in experiment. This is shown Figure 3-10.

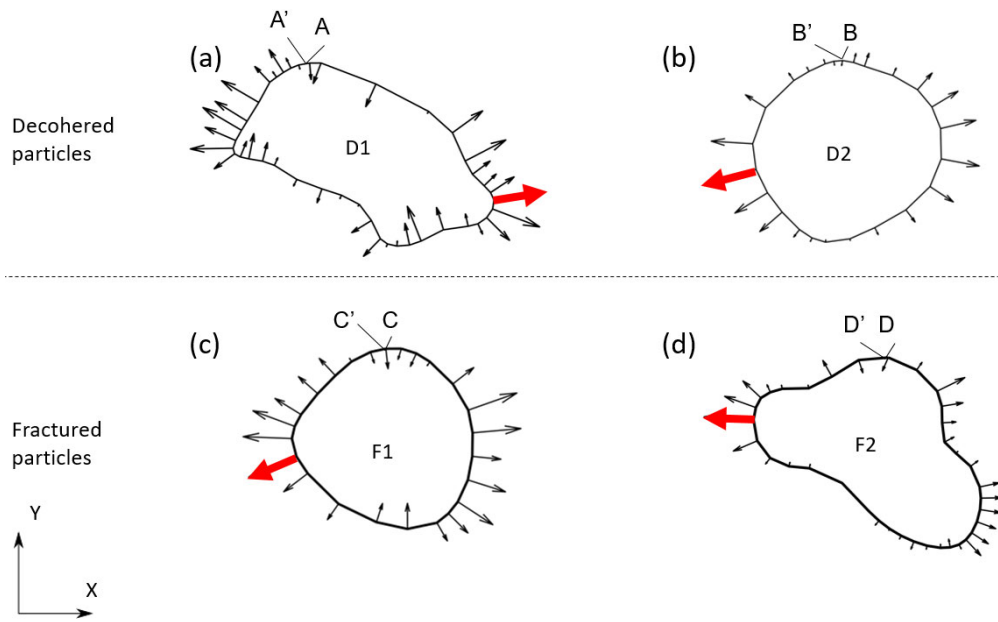


Figure 3-7 - normal stress distributions with respect to the particle perimeters for which (a) and (b) are particles which decohere in experiment and particles (c) and (d) experience fracture after fatigue loading. Red arrows indicate the location of peak normal stress.

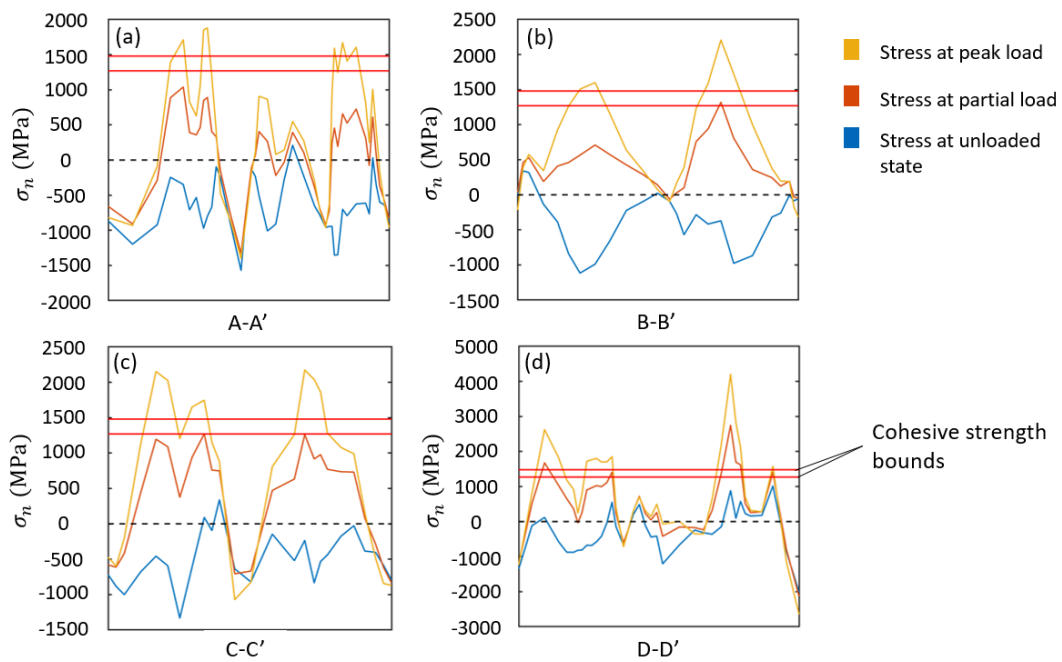


Figure 3-8 - profiles of normal stress distributions during unloaded, peak and partial ($F = F_{\max} 2/3$) loads of the first cycle around the perimeter of particles. Plots a), b), c) and d) correspond to respective plots in Figure

3-7. The previously reported cohesive strength range of 1270 -1480 MPa [51] is plotted as red bands. (a) and (b) are for particles observed to decohere; (c) and (d) are for particles observed to fracture.

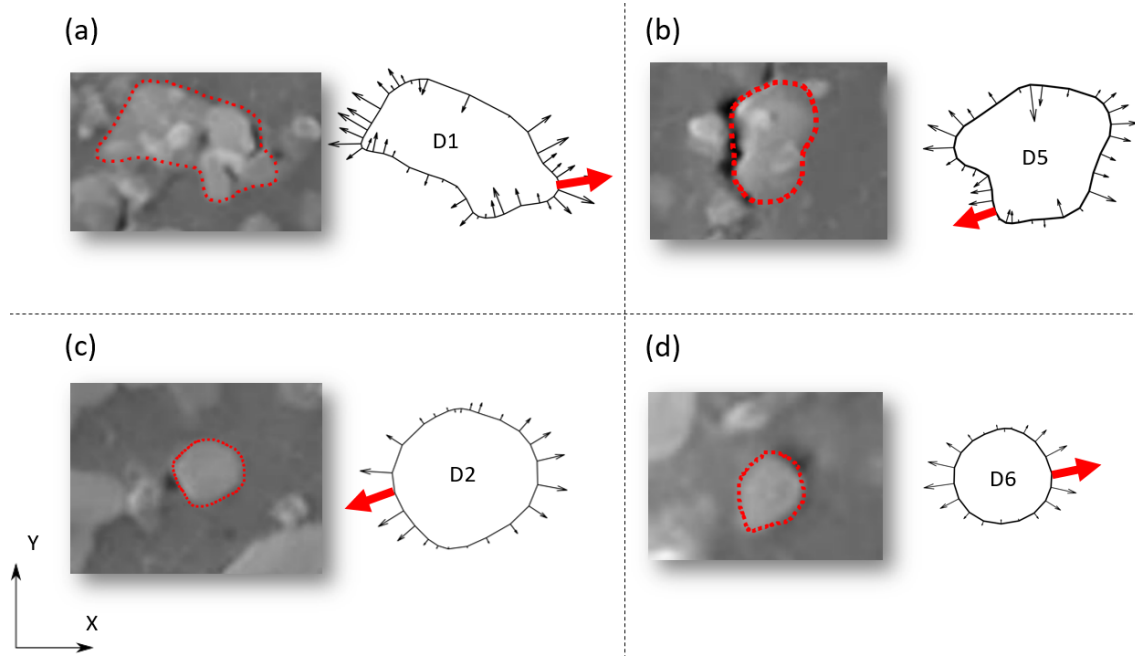


Figure 3-9 - (a)-(d) Normal stresses on perimeter of particles are shown together with their corresponding experimental observations of particle matrix decohesion (from [51]) after fatigue loading. Red arrows indicate point of maximum normal stress. (The smaller white particles partially visible are silica particles used as DIC speckles.)

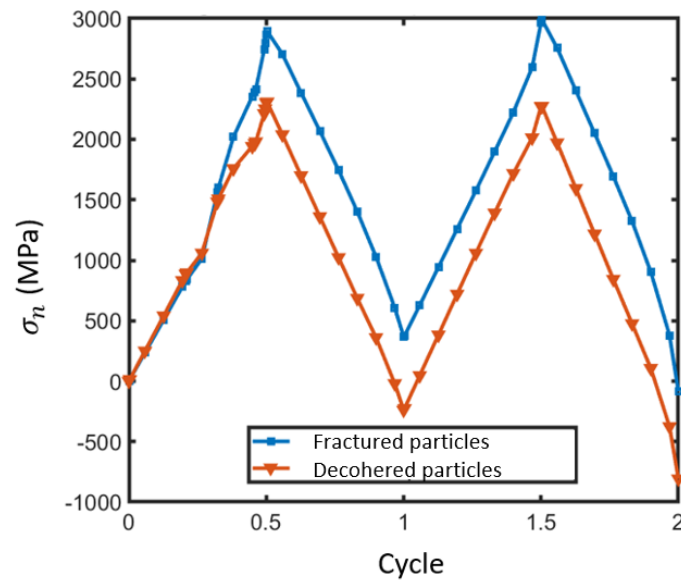


Figure 3-10 - variation of particle mean of interfacial normal stress for particles which fractured in experiment and particles which decohered in experiment.

The perimeter normal stresses are predicted to be higher for fractured particles so an alternative driver for particle fracture is required. Maximum principal stress was investigated as the potential primary driver of fracture in the brittle oxide particles. A maximum principal stress criterion of a Rankine type supposes that fracture occurs once a principal stress exceeds a critical value. Field plots of maximum principal stress are shown for the agglomerate region at the peak of the 1st cycle in Figure 3-11. Peak stresses are notably higher in the oxide particles due to their higher elastic modulus, and do seem to indicate the locations of particle fracture observed in experiments, as shown in Figure 3-11 (b) and (c). Figure 3-12 shows arrow plots of the direction of maximum principal stress for the peak the first cycle. These are primarily orientated in the direction of loading during peak load. Some particles observed to fracture in experiments are predicted to be subject to large maximum principal stresses. Particles F1, F2, and F3 in particular are observed to have high maximum principal stresses in the direction normal to the fracture plane indicating strong agreement with experimental observations for these particles.

However, while the model predictions show some good agreement with experimental observations, it is not always the case as certain oxides which remain unfractured in the experiment are predicted to carry extremely high maximum principal stress. The model predictions indicate that some particles with high interfacial normal stress should fracture (as opposed to decohere) and some with high maximum principal stress should decohere (as opposed to fracture). However, it is well recognised that the process of particle-matrix decohesion and oxide fracture lead to stress redistribution and local relaxation which may significantly alter the local stress distribution in the region. For example, decohesion taking place at an interface orientated approximately normal to the primary loading direction would have the effect of substantially reducing any axial (X-direction) stresses in the vicinity of the

interface, thus reducing the propensity for both decohesion and particle fracture at adjacent particles lying along the same line of loading. Hence a more detailed and complete analysis is required to investigate and differentiate the mechanistic observations associated with particle decohesion and particle fracture, which explicitly accounts for the process and effect of the fracture and decohesion which occur. This is addressed in the next section.

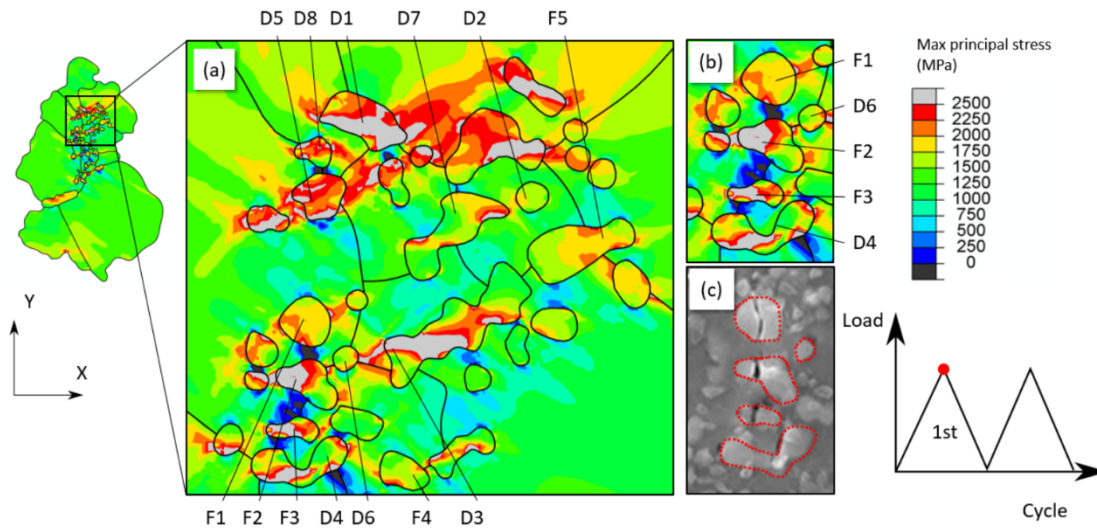


Figure 3-11 - Field plot of maximum principal stress (a) at the peak of the first cycle, and (b) a corresponding close-up of the region with several fractured particles (F1, F2, F3), and (c) the corresponding SEM image shown after fatigue loading [87].

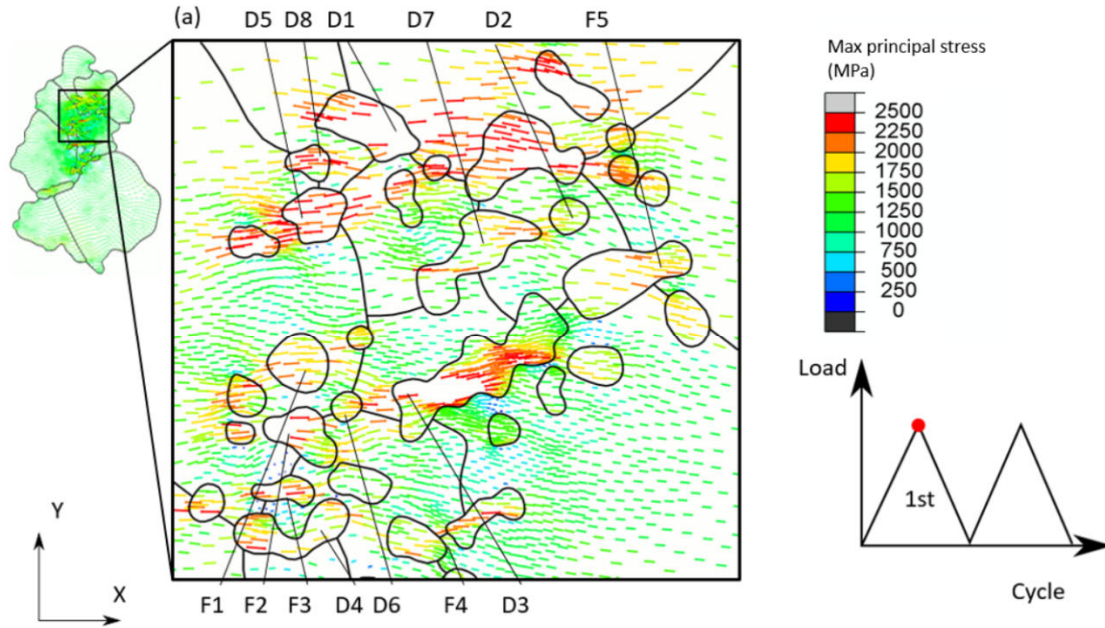


Figure 3-12 - Maximum principal stress is plotted as arrows which indicate magnitude (size and colour) and direction for the peak of the first cycle.

3.4 Modelling of metal-oxide interfacial decohesion and particle fracture using cohesive interfaces

Cohesive zones are introduced at all metal-oxide interfaces and within oxide particles to investigate decohesion and particle fracture respectively in the agglomerate system. The microstructural agglomerate model utilised above and shown in Figure 3-4 enhanced in this way was employed to carry out the study with the same loading conditions presented above. From the results obtained in the previous section (for which explicit decohesion and particle fracture was not included), the oxide-matrix interfacial cohesive strength \hat{S}_C was estimated to be 1270 MPa and the oxide particle fracture strength \hat{S}_F to be 1580 MPa. However, the analysis incorporating explicit decohesion and particle fracture led to early failure of all interfaces (be they decohesion or fracture failures), demonstrating that the local interfacial normal stresses

and intra-oxide maximum principal stresses exceeded the strengths given above. This indicates that both decohesion and fracture strengths are higher than previously estimated by the model which did not explicitly incorporate the failure processes. A sensitivity study (shown in Table 3-3) was therefore carried out using the microstructural model with a range of strengths for both \hat{S}_C and \hat{S}_F . Careful comparison of model results with the experimental observations of particle decohesion and intra-oxide fracture facilitated the extraction of more appropriate values for the strengths \hat{S}_C and \hat{S}_F . The metal-oxide interfacial strength and oxide particle fracture strength were therefore determined in this way to be $\hat{S}_C = 2050$ MPa and $\hat{S}_F = 2300$ MPa respectively.

Table 3-3 - the test matrix of the parametric study performed to find the interfacial strength \hat{S}_C , and the oxide strength \hat{S}_F

\hat{S}_C (MPa)	\hat{S}_F (MPa)	Qualitative results
1270	1580	All interfaces damaged
1480	1800	All interfaces damaged
1800	1950	All interfaces damaged
2050	2300	<i>Partial interfaces damaged in keeping with experimental observations</i>
2050	2500	Damage pertaining only to metal-oxide interfaces

These strengths gave computed results in which the number of initiations of interfacial decohesion and particle fracture best reflected the experimental observations. Figure 3-13 (a) shows interfaces which are predicted to fail in the model. Note that the stresses acting on the interfaces peak within the first two cycles. The traction on metal-oxide and fracture interfaces then declines since some stress relaxation is observed in the vicinity of particles after the first

few cycles. Nucleation events are therefore exclusively observed within two cycles of the applied load considered. SEM micrographs of the corresponding topography after fatigue loading of 1000 cycles (Figure 3-13 (b)) show fractured particles [20], and in particular, as predicted by the model in Figure 3-13 (a) in the particles labelled F1-F3. In this region, several particles fracture and are arranged in parallel with the direction of loading. The density and proximity of particles in this region are likely to drive locally high stresses which lead to the onset of particle fracture. Of the experimental particle fractures (F1 to F5) considered in the region of interest in Figure 3-13, four (F1, F2, F3, F5) were correctly predicted to fracture. Of the experimental oxide-matrix decohesions (D1 to D8), three (D1, D3, D5) were predicted to decohere in this region. However, after the first cycle of loading at peak stress 1366MPa, the total number of experimentally observed particle failures events was 14, compared to a predicted total of 16. Of these, six were observed to be fractures and eight decohesions. The model predicted nine particle fractures and seven decohesions. Hence some of the experimental observations have been captured and it is clear that the hypothesised mechanisms (interfacial normal stress and particle maximum principal stress for decohesion and fracture failures respectively) do differentiate the observed failure types, even if not completely successfully in all cases. Regrettably, some of the experimental observations [51] are obscured by DIC speckles. A summary of the results is given in Figure 3-14.

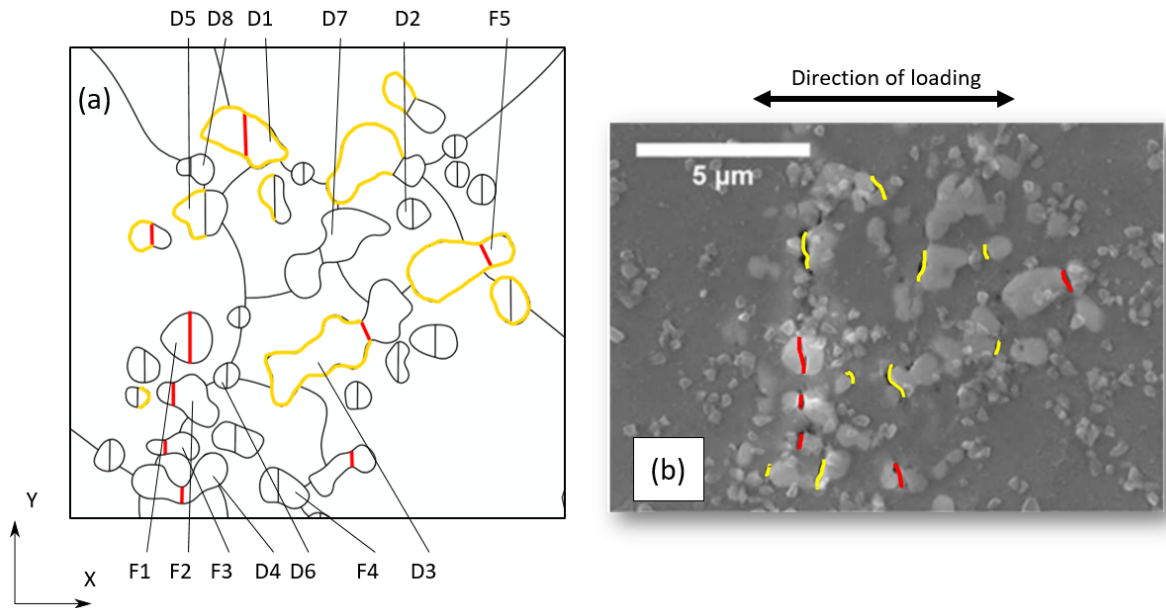


Figure 3-13 - (a) Schematic of the interfaces predicted to fail (highlighted in red for fracture and yellow for decohesion). Failure is here defined as the peak normal traction exceeding the predefined strength of either fracture or decohesion. (b) Experimentally observed particle fracture (red) and decohesion (yellow) are annotated on a SEM micrograph of the corresponding region.

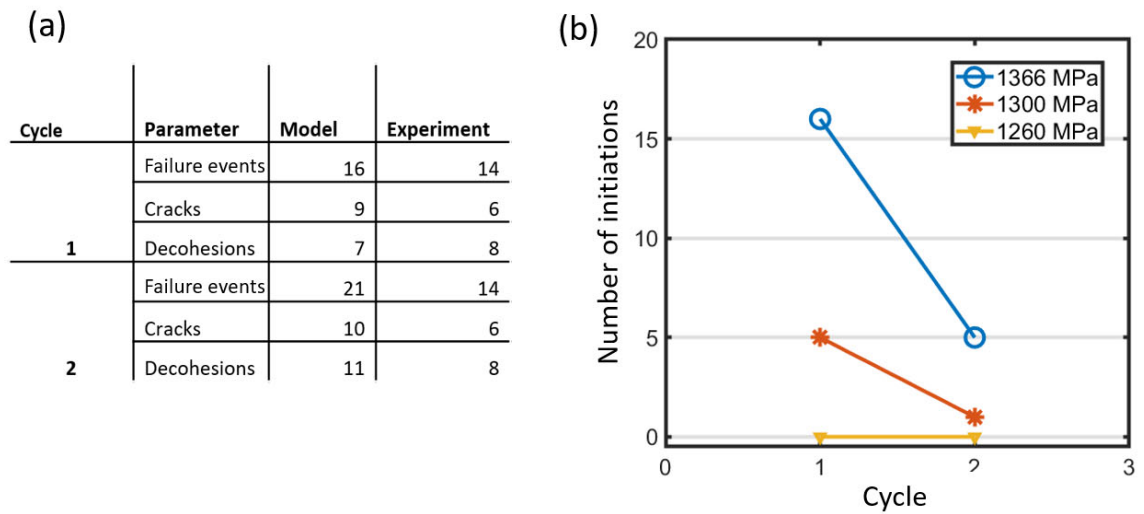


Figure 3-14 - (a) the number of failure events (sum of fracture and decohesion) in the entire agglomerate region and their type predicted by the model and observed in experiment during the first and second cycles at a peak applied stress of 1366 MPa. (b) the model predicted number of failure events per cycle for differing applied loadings (1366, 1300 and 1260 MPa) demonstrating the dependence of failure on remote stress.

The model facilitates an investigation of the effect of applied stress magnitude on the nature (decohesion versus particle fractures) and number of failure initiations. In Figure 3-14, the

model predicted number of failure events is shown for different applied peak loading for the first two cycles for applied peak stresses of 1366, 1300 and 1230 MPa respectively. The first cycle drives the largest number of failure events. A higher stress naturally causes a higher number of failure initiations to occur. Failure initiations were found to cease to occur (in both experiment and model prediction) after the second cycle. The frequency of initiation events is however extremely sensitive to the remote loading. In the studied system, a 5% drop in remote loading from 1366 MPa to 1300 MPa gives rise to an 80% drop in initiation events from 21 to 4 events. At 1230 MPa or 90% of original load, no initiation events are observed. Further experimental and modelling studies are required to validate these results.

An abrupt change in decohesion and fracture events due to a decrease in applied stress suggests the failure mechanisms (fracture and decohesion) are sensitive to the strain-hardening properties of the material. A low strain-hardening would result in peak stresses occurring in early cycles. The material considered in this study shows relatively low strain-hardening and the failure mechanisms occur early. Early initiation is therefore likely stress-threshold based and a reduction of applied maximum stress would result in a change of failure mechanism. It is therefore possible to approximate a peak stress for which particle decohesion and fracture initiations do not occur at all and thus provide a solution to inhibit initiations of this type. In a high-strain hardening material, the expected response would be the development of significant plastic straining near the oxide/matrix interface. In such a material, if early stresses are lower than the initiation threshold, then fracture and decohesion may occur subsequently in later cycles due to cyclic hardening.

Particle fracture and decohesion are processes which nucleate voids in the material and precede fatigue crack growth yet the onset of these phenomena is not sufficient to predict crack nucleation. Slip-driven crack nucleation occurs along persistent slip-bands impinging on the oxide/matrix interface. These cracks are different from particle fracture and decohesion in that

they are crystallographic in nature and may therefore begin to grow immediately. In the experiment, it is observed that while fracture and decohesion occur early, a crystallographic fatigue crack does not nucleate until after 1000 cycles. Fracture and decohesion may therefore influence fatigue life, potentially redistributing stress and influencing the nucleation of slip-driven crack nucleation. The next section addresses the competition of nucleation between the particle fracture, decohesion and slip-driven initiations.

3.5 Towards fatigue crack nucleation mapping

Nucleation of fatigue cracks from non-metallic inclusions potentially originates from voids created by particle decohesion, particle fracture but certainly by slip-driven crystallographic fatigue crack nucleation. In this section, the three nucleation modes are contrasted mechanistically. It is therefore sensible to utilise the criterion for crystallographic slip-driven nucleation introduced above in equation 3.14.

The stored energy density, U , has been shown to give quantitative predictions of fatigue crack nucleation sites and good prediction of fatigue life in steels [103], Ni-base superalloys [31] and recently at non-metallic inclusions [49]. A critical stored energy density value, U_c , was introduced at which a fatigue crack is argued to nucleate. In [137], the critical stored energy density was determined for fine grained Ni alloy RR1000 to be 404 Jm^{-2} . The number of cycles to nucleation is found from

$$U_c = N_f \int \dot{U} dN \quad 3.15$$

determined once the cyclic rate of stored energy accumulation has stabilised. In the present study, the stored energy density has been employed as the criterion for slip-driven fatigue crack nucleation. The agglomerate model above is utilised to investigate the role of the oxide particles, together with their decohesion and fracture, on stored energy density evolution for

the case of an applied load of 1366 MPa. After 10 cycles of loading in the model, the rate increase of stored energy density per cycle stabilises and it is therefore reasonable to extrapolate the stored energy rate at the end of this cycle and use equation 3.15 to find the fatigue life.

Figure 3-15 shows the predicted development of stored energy density in a model in which both decohesion and particle fracture are enabled (using the cohesive and particle fracture strengths from earlier). After the second cycle of loading, all decohesion and particle fracture events have taken place. Subsequent cycling then leads to the progressive evolution of stored energy density in the presence of the voids. Comparison is shown with the experimental microstructure where a crystallographic microcrack was found to nucleate between 1100 – 2000 cycles. The microcrack nucleation is localised in a region with predicted high stored energy density. Using $U_c = 404 \text{ Jm}^{-2}$ as the criterion for microcrack nucleation, it was found that the predicted cycles to fatigue crack nucleation are close to those obtained in the experiments [51]. A region that lies above particle D5 has a predicted nucleation lifetime of ~500 cycles and lies directly in the experimentally observed crack path. In the region above fractured particle F1, the model predicts a nucleation life of 1100 cycles.

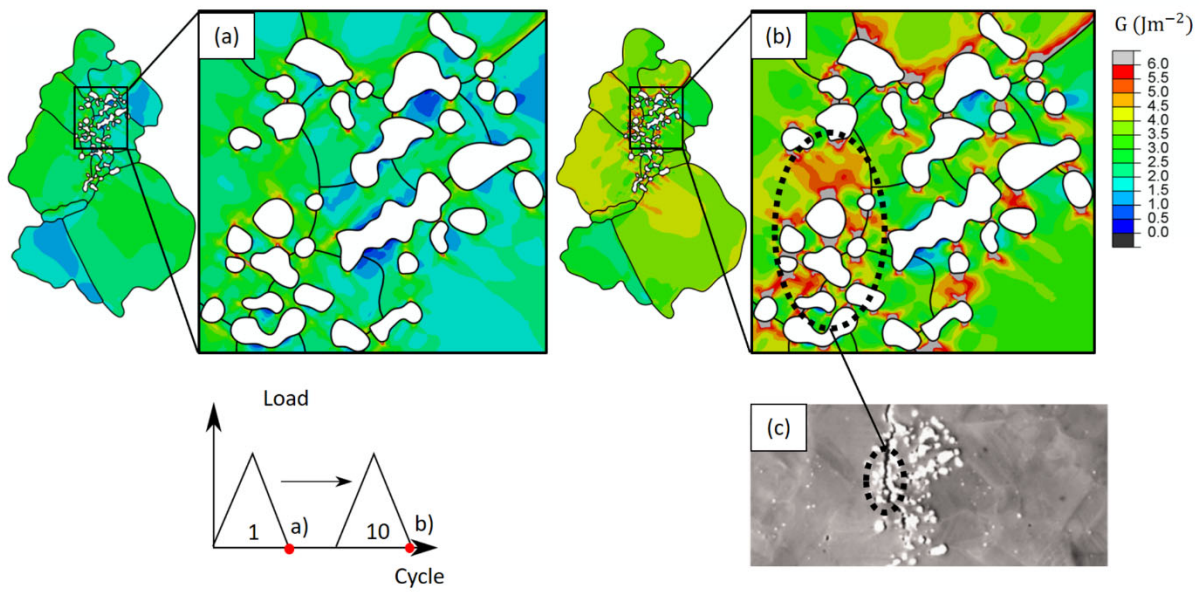


Figure 3-15 - The development of stored energy density in a model utilising cohesive zones for capturing particle fracture and decohesion. (a) shows the stored energy density at the end of the first cycle and (b) after the 10th cycle. (c) shows the same region in an SEM micrograph after 2000 cycles of loading [51]

This shows some agreement with the experimental observations in which crack nucleation occurs between 1100-1900 cycles. Factors affecting crack nucleation behaviour which are not accounted for include gamma prime depletion near agglomerates, as well as sub-surface grain morphology and crystallography. The tertiary gamma prime particles in the vicinity of particles are of the order of 40-50 nm. They likely influence the crack nucleation process but at a length scale smaller than that which has been investigated. Primarily, the gamma prime particles influence the slip resistance on a slip system and thus control the activation of slip and by extension slip banding. In a material system without large defect features such as inclusions, persistent slip bands and intrusions/extrusions will dominate the fatigue crack nucleation sites. In the present system, however, the influence of inclusions (which are sized on the order of 1-3 μm) on fatigue crack nucleation is much greater.

A field plot of predicted cycles to crack nucleation within the entire microstructure modelled based upon stored energy density is provided in Figure 3-16. Nucleation is predicted to occur

exclusively near oxide particles. Locations above and below oxide particles, with the horizontal loading considered, are found to be most prone to crack nucleation. Particles F1, F2, F3, D1, and D5 lie on the nucleated microcrack site (see Figure 3-15 (c)) in the experiment which strongly suggests that their fracture (F) and decohesion (D) respectively drive the nucleation process.

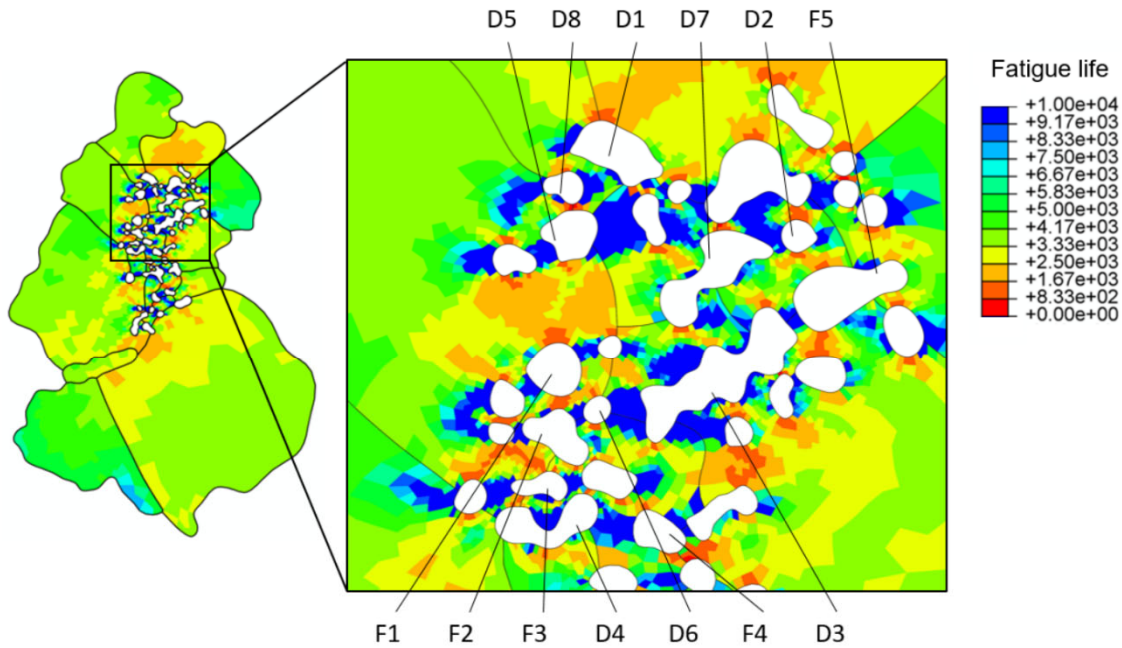


Figure 3-16 - Predicted cycles to crack nucleation based on the stored energy density in a model incorporating particle decohesion and fracture. Experimental decohesion (D1-D8) and fracture (F1-F5) sites are labelled.

Slip-driven fatigue crack nucleation has been observed to occur in a different but related Ni alloy system containing inclusions [49]. Cracks develop at the metal-oxide interface and align with crystallographic planes with high slip accumulation. Local stress, slip accumulation and geometrically necessary dislocation density have all been shown to be important factors in this nucleation type but a high magnitude of local stored energy density has been found to unambiguously identify sites of crack nucleation. The agglomerate system considered in this

chapter exhibits decohesion and particle fracture early in the loading history, which have then linked by crystallographic slip-driven crack growth. The stored energy density has been shown to evolve significantly in the vicinity of the particles and is influenced by the decohesion and particle fracture. There is clearly an interplay between the three mechanisms. In order to investigate this further, decohesion and particle fracture were inhibited in the crystal plasticity model by assigning very high interfacial and fracture strengths such that the sole failure mechanism is slip driven fatigue crack nucleation and compare with the previous study.

A range of analyses with the same polycrystal agglomerate model were carried out with differing applied stress level (from 1500 down to 820 MPa) to obtain predicted cycles to slip-driven crack nucleation (taking $U_c = 404 \text{ Jm}^{-2}$ as before) when both allowing particle fracture and decohesion and when inhibiting it. The results are summarised in Figure 3-17.

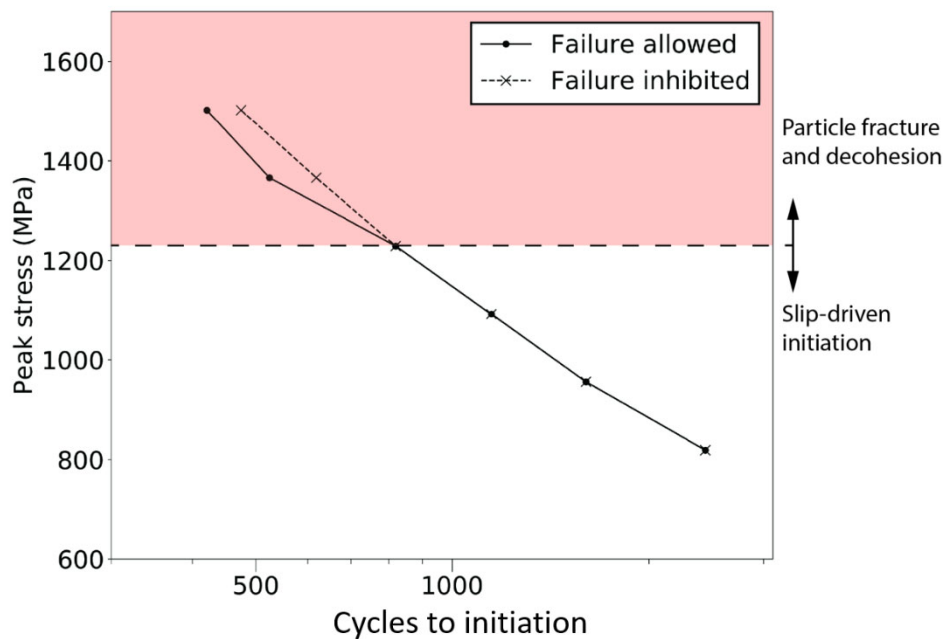


Figure 3-17 - S-N plot for cycles to crack nucleation estimated from cyclic stored energy accumulation for the case in which failure (via particle fracture and decohesion) is allowed and for when it is inhibited. Particle fracture and decohesion do not occur below the stress threshold of 1230 MPa.

Particle fracture and decohesion have been shown to be stress dependent such that in a fatigue scenario with high stress, debonding and decohesion occur early, leading to a change in local stress and strain states and the corresponding stored energy density evolution with subsequent cycles. When neither debonding nor particle fracture occur, the rate of evolution of stored energy density at particles (but within the Ni matrix) is different, thereby changing the numbers of cycles to fatigue crack nucleation. In the case where decohesion and particle fracture occur, stored energy density is predicted to increase subsequently at a faster rate therefore leading to shorter fatigue lives. This is demonstrated in Figure 3-17 where predicted cycles to crack nucleation are plotted against applied cyclic peak stress for the cases in which debonding and fracture are allowed to occur and when they are inhibited.

While crack nucleation from inclusions dominate in this study, it is important to consider that crack nucleation may occur at other microstructural features within the same alloy. Several studies have shown that in alloys containing inclusions, nucleation may occur at grain boundaries rather than from particle decohesion and fracture, particularly at lower applied stresses [70]. At low applied stresses, Heinz et al. [138] have observed that fatigue crack nucleation originates from favourably oriented twin-boundaries with $\{1\ 1\ 1\}$ slip systems activated parallel with the twin boundary. The origin of this phenomenon was argued to be due to the elastic incompatibility stresses and the ability for dislocations to travel relatively long distances along the twin boundary as opposed to neighbouring oblique grain boundaries. This observation has also been recorded by Stinville et al. [85] and Miao et al. [139] who have recorded twin boundary cracking in high-cycle fatigue. At lower stresses, it is therefore likely that the nucleation location shifts from non-metallic inclusions – for which decohesion and fracture are stress threshold dependent - to twin boundaries. A study is currently underway to investigate the competition between such microstructural features and their dependence on local hardening behaviour.

3.6 Summary

A microstructurally explicit oxide agglomerate-matrix model incorporating cohesive zone modelling of both particle/matrix interfacial decohesion and particle fracture has been developed for load-controlled fatigue in order to investigate the micromechanical drivers for crack nucleation observed in experiment on nickel alloy RR1000 containing oxide agglomerates.

High stresses normal to particle boundaries were found to be coincident with observed sites of oxide/metal decohesion reinforcing that interfacial normal stress is the controlling factor in decohesion. Analysis of stresses at peak loading conditions also revealed that particles observed to fracture in experiment are subject to the highest maximum principal stresses normal to the observed fracture planes. Both particle decohesion and fracture, modelled using cohesive zone formulations, were found to lead to the redistribution of stress within the microstructure, strongly influencing the stress states local to other oxide particles, in turn influencing the subsequent decohesion and fracture events. Explicit representation of the stress redistribution was found to be essential in order to capture the experimental observations. The oxide/metal interfacial strength and the oxide particle fracture strength were respectively found to be 2050 MPa and 2300 MPa. An upper bound applied stress therefore exists below which neither particle decohesion nor fracture occur.

Slip-driven fatigue crack nucleation was investigated using stored energy density. The latter was found to be influenced locally by particle/matrix decohesion and particle fracture which caused higher rates of stored energy accumulation and hence shorter fatigue life. Modelling studies showed that inhibiting particle/matrix decohesion and particle fracture increased fatigue life modestly. The critical energy density 404 Jm^{-2} determined in [45] was found to give

predicted fatigue life times close to the present experimental observations, and to capture correctly the observed site of microcrack nucleation and growth.

4 Microstructural feature sensitivity in fatigue crack nucleation in a polycrystalline Nickel superalloy

4.1 Introduction

Disc alloys are comprised of several microstructural features which promote strain localisation and fatigue crack nucleation. Due to the lengthscale of the problem, fatigue crack nucleation predictions from intrinsic (crystallographic) and extrinsic (inclusions) are statistical in nature and ignore the mechanistic drivers present. Investigating the interactions between microstructure and mechanisms bridge the way to better predictive models and thus may increase component lifetime.

Fatigue crack nucleation within polycrystalline Ni-base superalloys has been observed to occur at twin boundaries [90,140,141] and non-metallic inclusions [86–88]. A study by Miao et al.[139] found that nucleation occurs parallel to twin boundaries at a site close to, but not on the boundary. Recent studies by Stinville et al.[141] have investigated nucleation sites next to twin boundaries and assessed the competition between resolved shear stress, elastic anisotropy, and twin boundary length. Heinz and Neumann [138] are often credited for suggesting the elastic anisotropy and the plasticity adjacent to the twin boundary are vital in the twin nucleation phenomena. In terms of twin morphology, several papers have indicated that the length of the twin boundary is another key factor in nucleation [142] where a twin boundary (TB) with length larger than average grain diameter typically presents a larger risk. Gustafson et al.identified high intragranular misorientation as another driver for fatigue crack nucleation [143]. Non-metallic inclusions are often a hotspot for fatigue crack nucleation owing to their mismatching mechanical properties with the metallic matrix [38]. Inclusion size [106], properties [42], local grain orientation [88], and morphology [72] all play a role in nucleation.

Drivers for nucleation at these microstructural features have been identified but there remains a poor understanding of the competition of fatigue crack nucleation between the features. Texier et al.[90] investigated the crack nucleation sensitivity at twin boundaries and non-metallic inclusions and found that the transition between the two features depended on the density of twins in their microstructure. A higher density of twins shifted nucleation sites from inclusions to twin boundaries. This suggests that there is inherent competition between the microstructural features but the degree of competition remains elusive. Stinville et al. [85] found that, at lower stresses, crystallographic facets (twin boundaries) dominated over inclusion fatigue crack nucleation.

Inclusion decohesion may be a precursor to fatigue crack nucleation. Decohesion typically presents itself in early cycles of fatigue loading and introduces voids in the material which acts as a stress concentrators, eventually leading to microstructural fatigue crack nucleation. Bergsmo et al.[144] found that early cycle particle fracture and decohesion is a monotonic (rather than a cyclic) phenomenon. A mean stress relaxation was observed on the normal metal/oxide boundary where decohesion is expected to occur suggesting that decohesion occurs early in the cyclic regime. This may also mean that cyclic decohesion is strain-hardening dependent; a high strain hardening material may induce cyclic ratchetting creating a situation where cyclic decohesion is possible (given that first cycle stresses are lower than the decohesion threshold).

This behaviour may also be dependent on the material hardening behaviour. Kinematic-isotropic hardening models have been incorporated in several crystal plasticity models. Hennessey et al.[145] used a phenomenological kinematic-hardening rule to evaluate local ratchetting and mean stress relaxation responses with back-stresses acting on individual slip systems. Bayley et al.[146] investigated the feasibility of a dislocation induced back stress formulation.

Using energy-based criteria for fatigue crack nucleation has proven to be a popular approach to predict fatigue crack nucleation. Yeratapally et al.[147] approximated the critical energy of a persistent slip band to nucleate a crack in the presence of a twin boundary. Energies of slip bands were obtained from atomistic (γ' shearing and extrusion formation at GBs) and continuum scale (hardening, pile-up, and applied work) contributions. Chen et al.[49] used a stored energy criterion to predict the location of slip-driven initiation on the perimeter of an experimental non-metallic inclusion. The study showed a strong, unambiguous correlation between sites of peak stored energy and sites of fatigue crack initiation.

In this study, a representative volume element microstructure was constructed with key microstructural features incorporated. Here, microstructural designs and rigorous parametric studies aimed at investigating the competing nature of fatigue crack nucleation near twin boundaries and non-metallic inclusions is studied. The key scientific questions investigated are the suitability of the stored energy criterion in determining nucleation near twin boundaries and the degree of severity each microstructural feature imposes on fatigue life. In addition, competition between monotonic decohesion and cyclic decohesion for isotropic and combined isotropic-kinematic hardening models is investigated.

4.2 Methods

4.2.1 Crystal plasticity formulation

The crystal plasticity finite element formulation used in the chapter is described in detail within 3.2.1.

4.2.2 Fatigue crack nucleation criterion

To predict fatigue crack nucleation, a stored energy criterion is employed. This criterion has been successfully used to predict fatigue crack nucleation in a ferritic alloy [31]. A fatigue crack is said to nucleate if the energy exceeds a critical material-dependent value. For RR1000,

this value has been determined to be 404 Jm^{-2} in a study by Chen et al.[148]. Stored (elastic) energy, is determined non-locally by computing the mean integration point value in elements. It is expressed in terms of stress σ , plastic strain $d\epsilon^p$ and density of dislocations (both SSD and GND) ρ_{tot} :

$$G = \int \frac{\xi \sigma : d\epsilon^p}{\sqrt{\rho_{tot}}}. \quad 4.1$$

Cyclic accumulation of stored energy may be extrapolated to approximate crack nucleation given that cyclic rate of increase ΔG often becomes steady-state.

4.2.3 Microstructural representative volume element

A synthetic representative microstructure was generated using the Voronoi-tessellation software Neper [149] and in-house editing scripts. The morphology, shown in Figure 4-1, consists of an extruded planar microstructure utilising pseudo three-dimensional geometry. The pseudo three-dimensional microstructure has been shown to approximate real microstructures with good agreement in separate crystal plasticity studies [49,75]. Three repeating grain structures are placed in parallel with the loading direction. These internal structures are periodic along the planar axes and are built in order to allow similar local stresses to be applied on three microstructural features: i) a triple-junction, ii) an annealing twin, and iii) a non-metallic inclusion. The triple-junction is used as a control feature to allow comparison between an idealised microstructure.

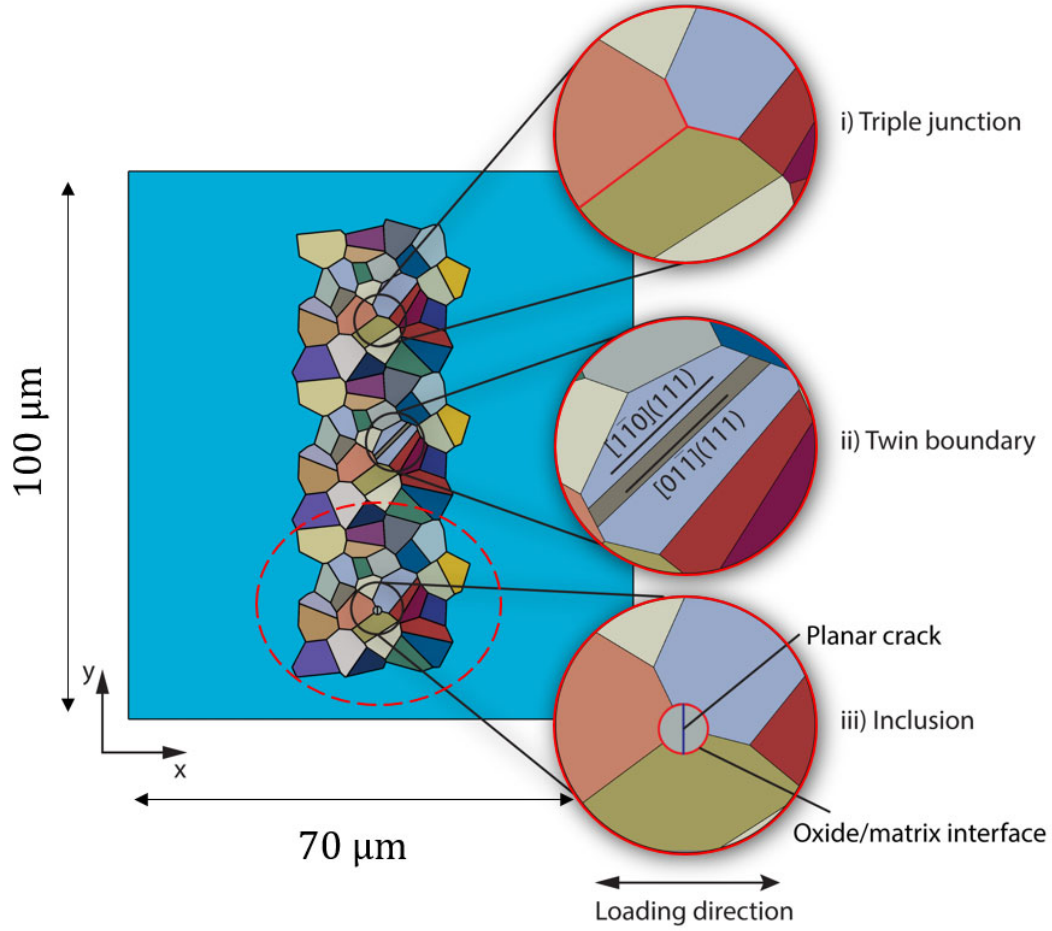


Figure 4-1 - the morphology of the representative microstructure with i) a triple junction, ii) a twin lamella and iii) a non-metallic inclusion

The overall texture and local crystallographies chosen are modelled on a polycrystalline Ni-base superalloy, RR1000. The preferred route of processing for this alloy is *via* powder metallurgy which provides a random texture. The latter is obtained by assigning random Euler angles in a ZYZ order with Gaussian and uniform distributions such that the sampling space does not cluster orientations at the poles. Each Euler angle is independent and the angle distributions were obtained as follows:

$$\phi = u \in [0, 2\pi], \quad \theta = \pi - \arccos(v \in [-1, 1]), \quad \psi = w \in [0, 2\pi]. \quad 4.2$$

Using these angles, a rotation matrix is constructed representing the crystallographic orientation by the rotation from a reference state. This process is described in detail in [150]. Grain size distributions are generated using log-normal distributions obtained from EBSD characterisation of RR1000 sample surfaces. EBSD was performed on a finely grinded and polished RR1000 specimen within a Zeiss Sigma SEM. Electron backscatter patterns were collected using an Oxford Instruments nanodetector. The EBSD step size was $0.4\ \mu\text{m}$ over a region of $500\ \mu\text{m} \times 300\ \mu\text{m}$. The grain morphology was reconstructed using an open-source processing software, MTEX [151], within Matlab. The grain size distributions are shown in Figure 4-2 (a). To demonstrate the uniform texture and remove data bias, a thousand random orientations are plotted on a texture map in Figure 4-2 (b). The general representative volume element (RVE) design process is given in Figure 4-2 (c).

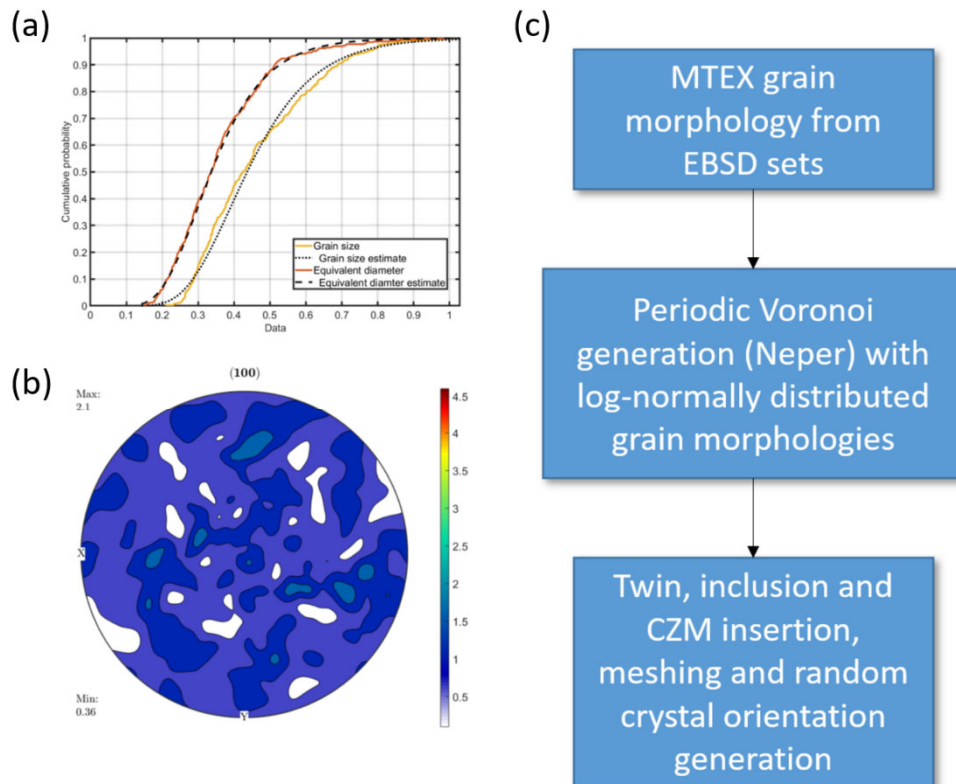


Figure 4-2 - (a) Grain size and sphericity distributions of the synthetic microstructure, (b) typical texture mapping expanded to comprise 1000 grains and (c) the design process for the RVE construction

The RVE is subjected to cyclic load-controlled uniaxial loading with an R-ratio of $R = -0.9$ for 10 cycles. The a range of peak loads are applied from 1500 MPa (equivalent to 150% yield stress in RR1000) to 600 MPa (equivalent to 63% yield stress in RR1000). At the 10th cycle, the cyclic plasticity has reached steady-state with steady evolution of stored energy density evolution such that approximation of lifing is possible by extrapolation of the cyclic rate.

4.2.4 Modelling non-metallic inclusions

A singular circular inclusion was inserted at a grain boundary intersection. Figure 4-3 (a) shows a typical agglomerated non-metallic inclusion in RR1000. The shape and size of the particle was chosen to approximate that of real inclusions in fine grained RR1000 [42] where near spherical morphologies are not uncommon. Distributions of inclusion area and sphericity are given in Figure 4-3 (b) and (c). These were obtained from analysis of backscatter micrographs of inclusion agglomerates within RR1000. The mechanical properties of the inclusion are chosen in line with its chemistry, HfO₂ [76]. The inclusions are assumed to be elastically isotropic. While the oxide material is anisotropic [76], a first-order approximation is appropriate to model the stresses around inclusions and has been shown to fit well [144].

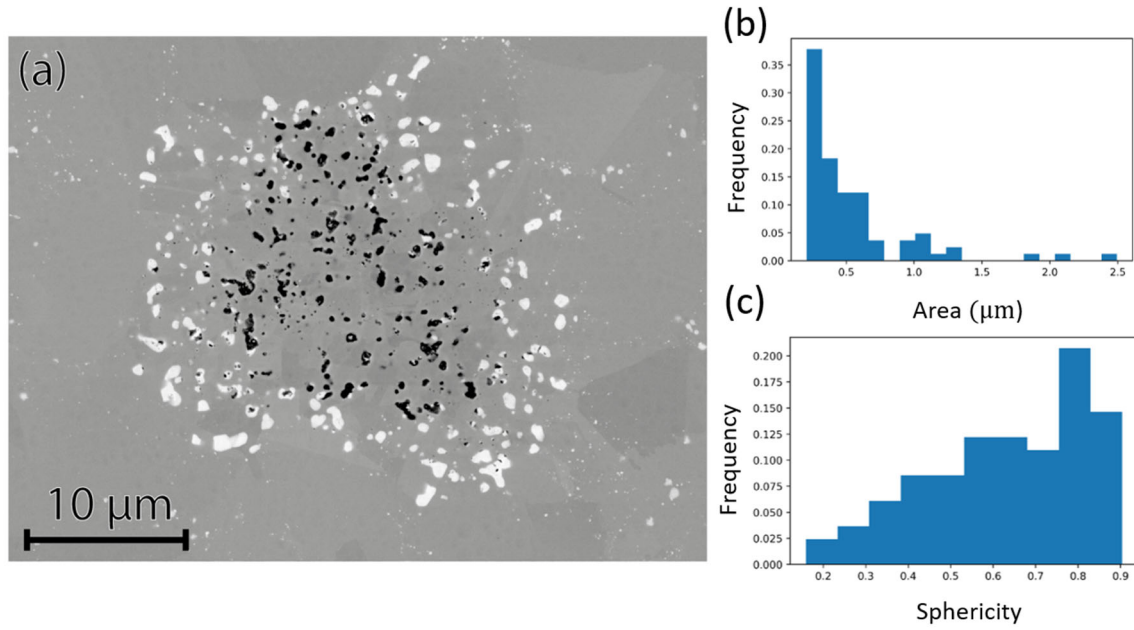


Figure 4-3 – (a) typical inclusion agglomerate morphology (b) inclusion area distribution (c) inclusion sphericity distribution

A cohesive zone model was employed to simulate the phenomena of particle fracture and decohesion which have been reported to occur in real microstructures [51,144]. The traction-separation relation is stress-threshold based where the opening of the cohesive-zone begins once a maximum stress has been exceeded. This method is discussed in detail in an earlier study [144]. Figure 4-4 (a) and (b) shows the cohesive zone locations and the traction separation curve, respectively. The properties of the traction-separation curve were obtained from a study considering observations of experimental particle fracture and decohesion [144], and are given in Table 4-1. After particle fracture or decohesion has occurred, stresses redistribute to form highly localised areas often above or below the void introduced by the fracture or decohesion event. This high stress drives plasticity and thus stored energy increases accordingly promoting fatigue crack nucleation. As inclusion fracture and decohesion are stress-threshold based, fatigue crack nucleation from voids become more significant at higher stress levels. However, if no decohesion and fracture occurs, slip-driven fatigue crack nucleation may still occur due to persistent slip banding in the metal matrix near inclusions (e.g. [49]).

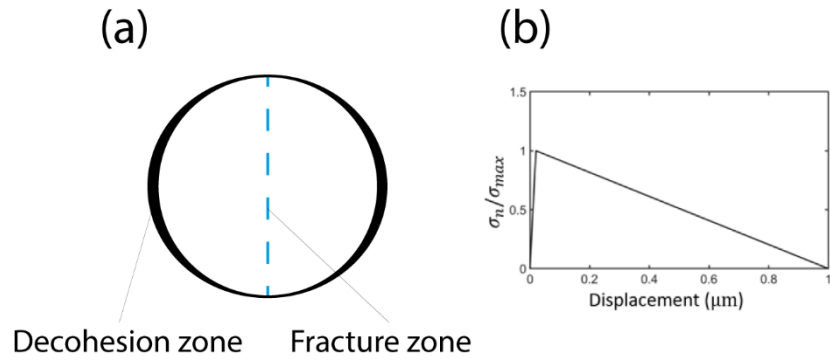


Figure 4-4 – (a) Cohesive zone geometry around inclusion, (b) bilinear traction-separation curve

Table 4-1 - The properties of the traction separation curve

	σ_{max} (MPa)	k_n (MNm ⁻¹)	δ^f (μm)
Fracture	2050	230 000	1
Decohesion	2300	210 000	1

4.2.5 Generation of a crack-inducing twin

Several recent studies have provided detailed insight to properties of “worst-case” annealing twins [30,141]. The important qualities of a crack-inducing twin are: (i) A parallel slip system with high resolved shear stress, (ii) a large elastic-anisotropy mismatch between twin and parent, (iii) twin length larger than average grain diameter. As (i) and (ii) are controlled by the crystallographic orientation and the parent-twin relationship inherits a constrained crystallographic relationship they can be manipulated solely by the twin morphology. Therefore, the objective of this morphology is to maximise the plasticity induced by deformation. A twin morphology is therefore chosen so that a $[1\ 1\ 1]$ plane parallel to the twin boundary has the maximum resolved shear stress. The twin is inserted into a large grain to simulate the size effect of (iii).

To predict cracking at annealing twin grains, the stored energy density accumulation at the continuum scale is assessed. The location of maximum value stored energy density lying on the twin boundary is considered to be the site of future fatigue crack nucleation.

4.2.6 Creating comparative features

The microstructural features generated for the model are designed to be comparative in the sense that they exist on the same length scale. In conventional samples of RR1000 – inclusions do not necessarily agglomerate (see Figure 4-3) and may exist in isolation, yet fatigue experiments show that fatigue crack nucleation typically occurs preferentially near these inclusions as opposed to crystallographic features such as twin boundaries. While agglomeration and clustering of inclusions is likely to increase the local accumulation of stored energy density, the relative size of the agglomerate compared with the conventional twin boundary is large and does not create a framework for comparing the fatigue performances. Results and discussion of comparative performance are given in Section 4.3.

4.3 Competing microstructural features in crack nucleation

The accumulation of effective plastic strain in the microstructure after 10 cycles of loading with $\sigma_{peak} = 1400$ MPa is shown in Figure 4-5 (a). Strong localisation of plasticity occurs near the non-metallic inclusion and the twin boundary. Selected grains near the triple-junction also display elevated plasticity after loading. The stored energy is displayed in Figure 4-5 (b) and shows elevated storage near the twin boundary and inclusion but high storage is also displayed near the triple junction. High levels of stored energy density are also present in grains separated from the microstructural features of interest.

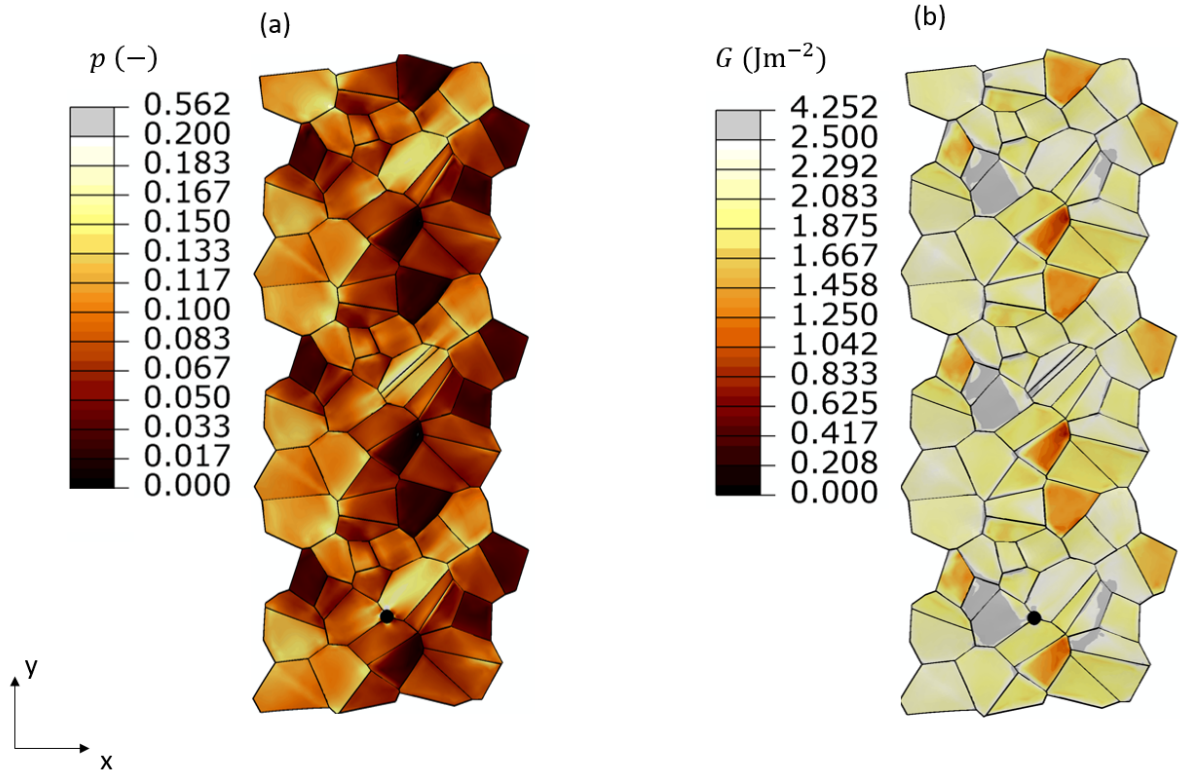


Figure 4-5 - (a) the effective plastic strain distribution of the microstructure after the 10th cycle of loading for a given peak load of 1400 MPa and (b) the stored energy of the respective microstructure after the 10th cycle.

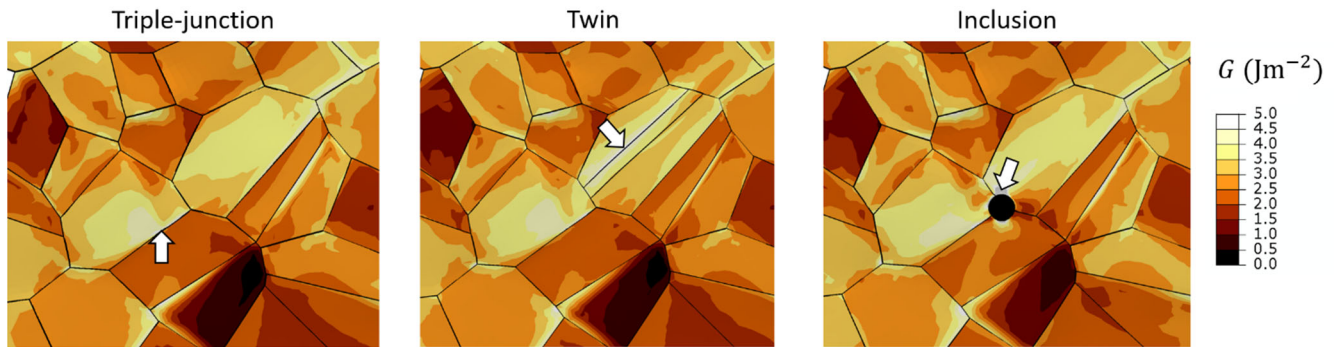


Figure 4-6 - Field plots for stored energy density at each respective microstructural feature. The white arrows indicate locations with peak accumulated stored energy density after 10 cycles of loading for a peak load of 1400 MPa

The stored energy density accumulation at each microstructural feature is shown in Figure 4-6.

While the twin and inclusion regions record peak values of stored energy density at their

respective features, the triple junction records peak values at the grain boundary of a grain which experiences high stored energy density.

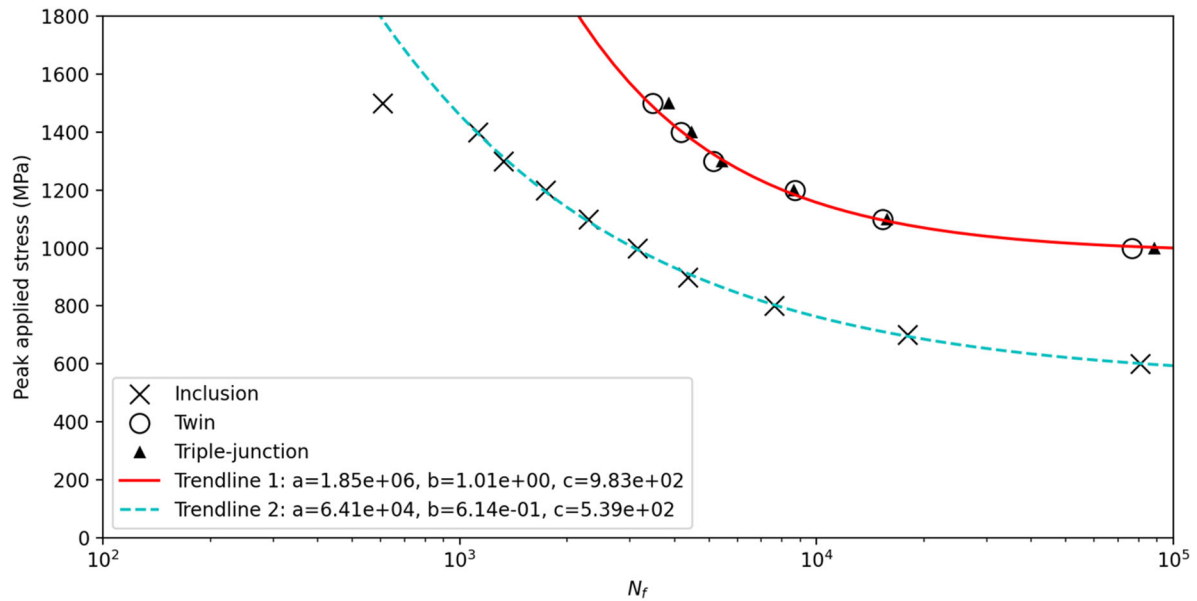


Figure 4-7 - The life prediction of non-metallic inclusion, annealing twin, triple-junction with appropriate trendlines for inclusion (blue) and intrinsic crystallographic feature (red).

At each microstructural feature, the peak site of accumulated stored energy was extracted to create an S-N curve, shown in Figure 4-7, of life predictions for fatigue crack nucleation made on the basis of achieving the critical stored energy density defined above. With the given size and material properties, the non-metallic inclusion unambiguously dominates the accumulation of stored energy. A discontinuity presents itself in the S-N curve for the inclusion where, above a particular stress level (1400 MPa), decohesion has occurred. The loss of cohesion between the particle and matrix increases the cyclic accumulation of stored energy consistent with findings in [144]. Decohesion occurs between macroscopic tensile stresses of 1400-1500 MPa. Stored energy densities at the twin boundary and the triple-junction appear to be very similar with little distinction between the two however the twin appears to exhibit a marginally worse fatigue life. An exponential equation ($y = a \exp(-bx) + c$) was fit to the data points using least-square regression. Two trendlines were fit. Due to the similarity in data between the

crystallographic features (twin and triple-junction), a single trendline is plotted in Figure 4-7 to model their behaviour. A fatigue limit presents itself in the crystallographic features at 1000 MPa. Below 1000 MPa, no plasticity and hence no stored energy accumulation could be predicted on the crystallographic features. The trendline fitted to the inclusion data treated the point of decohesion as an outlier. The inclusion trendline, in contrast to the crystallographic features, predicts a lower fatigue limit at 600 MPa. Below 600 MPa, no plasticity was predicted in proximity of the inclusion and therefore no fatigue crack nucleation could be predicted.

For inclusions, the development of stored energy density is heightened which drives earlier fatigue crack nucleation and due to the mismatching elastic constants of inclusion and matrix the plasticity is significant even in lower applied remote stresses. The stiff elastic inclusion (relative to matrix) is expected to cause higher stresses in the adjacent vicinity. The high stresses drive plasticity and local dislocation accumulation thus creating a high stored energy. Caton et al.[43] showed that, when present in sufficient size, inclusions can dominate fatigue crack nucleation in a Ni-base superalloy. Similar findings are present in several studies [19,90].

The fatigue limits of the inclusion and crystallographic features suggest that while the fatigue life of twin and triple junction is improved, they require an elevated stress level to activate slip. Experimental studies have suggested that twin driven crack nucleation may be directly competing with inclusion driven crack nucleation [90]. Stinville et al.[83] show that there exists a transition between nucleation from internal microstructural features and non-metallic inclusions dependent on the applied stresses. For lower stresses, they observe nucleation from crystallographic facets and at elevated stresses, nucleation occurs at inclusions. This behaviour is attributed to damage accumulation (particle fracture and decohesion) within the early cycles. In the current model, fracture and decohesion occur at a threshold stress. However, below the threshold stress the inclusion region still accumulates higher stored energy than the intrinsic microstructural features indicating that, given enough cycles, the (intact) inclusion will still

generate a crystallographic fatigue crack earlier than the twin and triple-junction. This fatigue crack will not emanate from a decohesion void or particle fracture but from a persistent slip band originating from the inclusion. Slip-driven fatigue cracks at inclusion boundaries have been observed by Jiang et al.[51].

4.4 Slip and stored energy density at twin boundary

In this section, an investigation of the accumulation of stored energy at the twin boundary in the model (see Figure 4-1) is investigated. The crystallography of the twin region was chosen such that slip systems parallel to the twin boundary accumulate high levels of slip. Figure 4-8 shows the grain-averaged slip on various slip systems following the notation given in Table 4-2. Parallel slip systems (S1 and S2) are seen to contain the highest mean slip magnitudes, but incident slip systems (S4 and S8) also experienced slip activation, but at smaller magnitude, but demonstrating multiple slip. Non-zero slip is only observed in these slip systems.

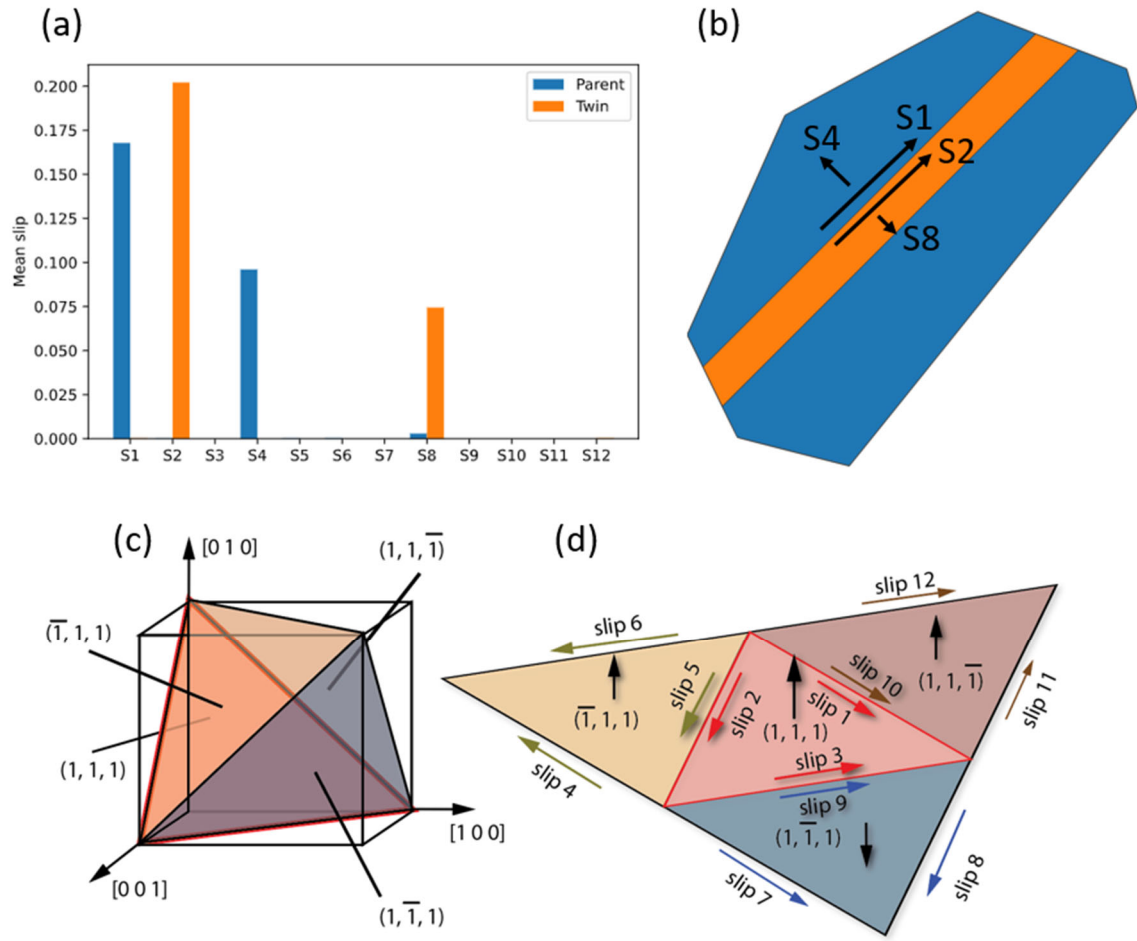


Figure 4-8 – (a) mean slip histogram comparison between parent and twin grains, (b) schematic of grain showing slip directions (s_4 and s_8 point diagonally out of plane), (c) Slip tetrahedron in the reference configuration, and (d) the unpacked slip tetrahedron showing the slip directions and the corresponding slip plane normal. Slip direction conventions are given in

Table 4-2 - Slip system numbering convention

Slip system	Slip plane normal	Slip direction
1	(1, 1, 1)	[1, $\bar{1}$, 0]
2	(1, 1, 1)	[0, 1, $\bar{1}$]
3	(1, 1, 1)	[1, 0, $\bar{1}$]
4	($\bar{1}$, 1, 1)	[$\bar{1}$, 1, 0]
5	($\bar{1}$, 1, 1)	[0, 1, $\bar{1}$]
6	($\bar{1}$, 1, 1)	[1, 0, 1]
7	(1, $\bar{1}$, 1)	[1, 1, 0]
8	(1, $\bar{1}$, 1)	[0, 1, 1]
9	(1, $\bar{1}$, 1)	[1, 0, $\bar{1}$]
10	(1, 1, $\bar{1}$)	[1, $\bar{1}$, 0]
11	(1, 1, $\bar{1}$)	[0, 1, 1]
12	(1, 1, $\bar{1}$)	[1, 0, 1]

Stinville et al.[140] have recently emphasised the importance of slip band intensity parallel to the twin boundary for fatigue crack nucleation. The crystal plasticity finite element analysis does not explicitly capture highly localised (e.g. a single trace of) slip as this is a phenomenon taking place at a length scale finer than that of the element size (in this case $\approx 0.4 \mu\text{m}$). Instead, CPFE considers the homogenised crystal plastic behaviour within an element – which can indicate which slip systems are active and the slip magnitudes developed. Figure 4-9 shows field plots of slip magnitude for the slip systems outlined in Figure 4-8 c-d. Of particular importance is the localisation of parent grain parallel slip (S1) near the twin boundary (Figure 4-9 a-b). This exhibits high magnitudes on the top (left) boundary. This behaviour results from the elastic anisotropy and constraint effect provided by the dissimilar crystal orientation of parent and twin lamina. The level of elastic anisotropy in this case can be quantified by the difference in elastic modulus between the parent and twin grains with respect to the loading direction. The elastic modulus difference is 30 GPa with the twin being the stiffer grain. It is recognised that the complex stress state that arises within a grain (even during uniaxial loading)

is not limited to a single (uniaxial) stress component. However, the component in the loading direction is typically the largest here, and the elastic constant in this direction is therefore a first-order approximation of the respective elastic stress state.

In addition to parallel slip, the twin and parent grains also non-zero slip activation on incident slip systems S4 and S8 (Figure 4-9 c-d) albeit at lower levels than parallel slip (see Figure 4-8 a). Incident slip is oblique to the twin boundary and, depending on the morphology of twin with respect to the loading direction, may drive slip transmission across the twin boundary. Twin boundaries that experience slip transmission have been reported to have lower strain concentration at the twin boundary [140]. In the current crystal plasticity framework, slip transmission is not explicitly modelled yet the lower levels of slip incident activation indicate that parallel slip band formation may take precedence over slip transmission. Furthermore, the importance of incident slip in fatigue crack nucleation parallel to the twin boundary has been diminished in recent years due to the observation that fatigue cracks nucleate parallel to twin boundaries [139].

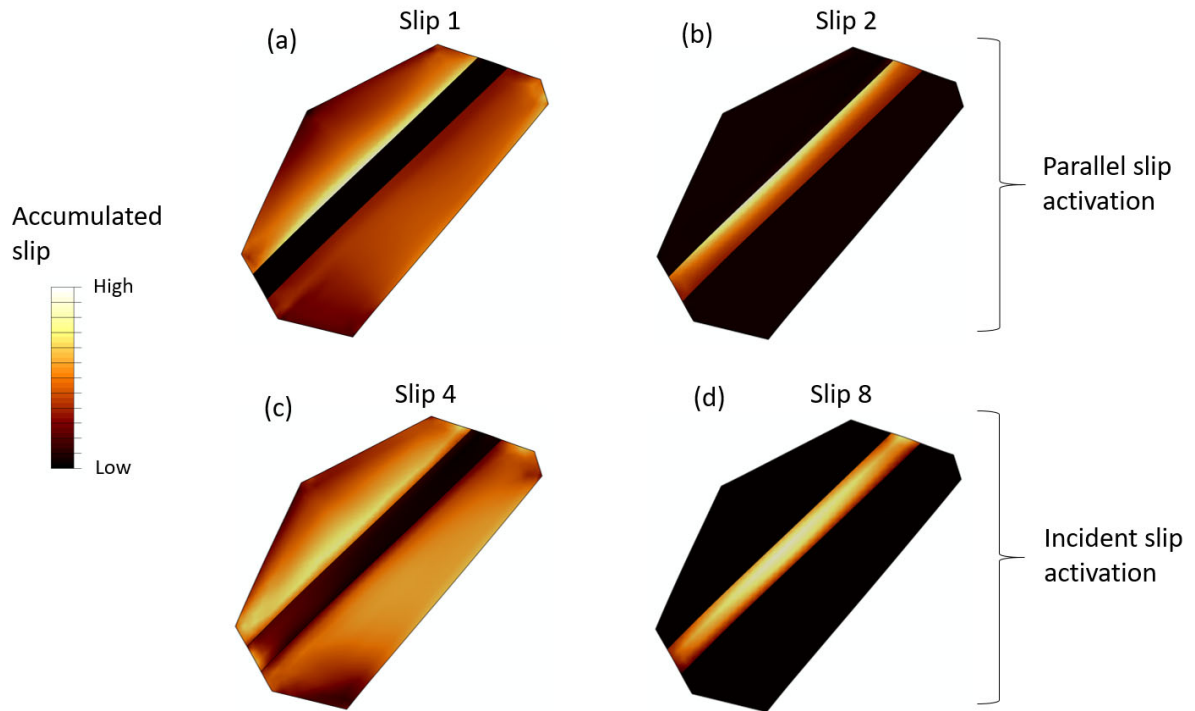


Figure 4-9 – (a)-(d) Field plots of slip distributions corresponding to the slip indices given in Table 4-2. The top row (a), (b) shows slip systems parallel to the twin boundary and the bottom row (c), (d) slip systems incident to the twin boundary

The stored energy density given in Figure 4-10 shows corresponding localisation on the upper twin boundary. Localisation on the twin boundary indicates that crystallographic fatigue crack nucleation preferentially occurs at this location given sufficient cycles to achieve the critical stored energy density of 404 Jm^{-2} . While the localisation on the twin boundary is correctly captured by the model, the magnitude of stored energy calculated is comparable to those at several grain boundaries within the polycrystal model. This suggests that despite selecting idealised morphologies and crystallographic orientations anticipated to give high stored energies, the crystal plasticity model does not necessarily demarcate a preference for early or first fatigue crack nucleation at the twin boundary compared with other regular features of the microstructure. The inability to differentiate between a regular grain boundary and twin boundary in terms of stored energy density may rely on several factors. For one, the role of discrete slip banding adjacent and parallel to the twin boundary may form an important

localised feature from which a fatigue crack may nucleate, which may not be captured by the crystal plasticity approach; as mentioned above, highly localised slip events below the element size ($0.4\ \mu\text{m}$) are neglected. Twin boundary crack nucleation may crucially depend on these small length scale phenomena. A transition mode scanning electron microscopy study by Stinville et al.[152] found precipitate shearing, dislocation decorrelation and antiphase boundary-couple shearing to occur near the twin boundary. Secondly, a larger parent grain size may be required to produce the required stored energy magnitudes. Several researchers note that twin boundary fatigue cracks nucleate in grains which are 2-3 times the average grain size [139,142]. Clayton et al.[153] found that while a high resolved shear stress is associated with crack nucleation, the length of the adjacent slip band is a stronger indicator of cracking. A follow-up study is underway exploring the effects of twin-boundary length and slip banding adjacent to the twin boundary on stored energy magnitude.

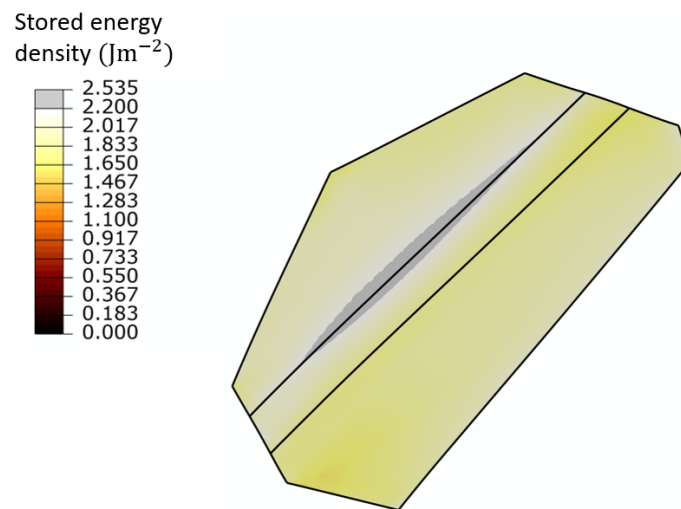


Figure 4-10 - Field plot of stored energy distribution in parent-twin grains

This concludes the assessment of the comparative fatigue performance of the microstructural features and the stored energy accumulation on the twin boundary. The following section concerns the investigation into cyclic inclusion decohesion.

4.5 Cyclic effects on inclusion decohesion

To investigate the effects of cyclic hardening on inclusion decohesion, the model outlined above was run (see Figure 4-1) under stress-controlled loading for three material models: (i) a low isotropic strain hardening material, (ii) a high isotropic strain hardening material, and (iii) a purely kinematic hardening material. While the model inclusion has the ability to fracture, this investigation primarily concerns the decohesion phenomenon and discusses the incidence of fracture in detail later.

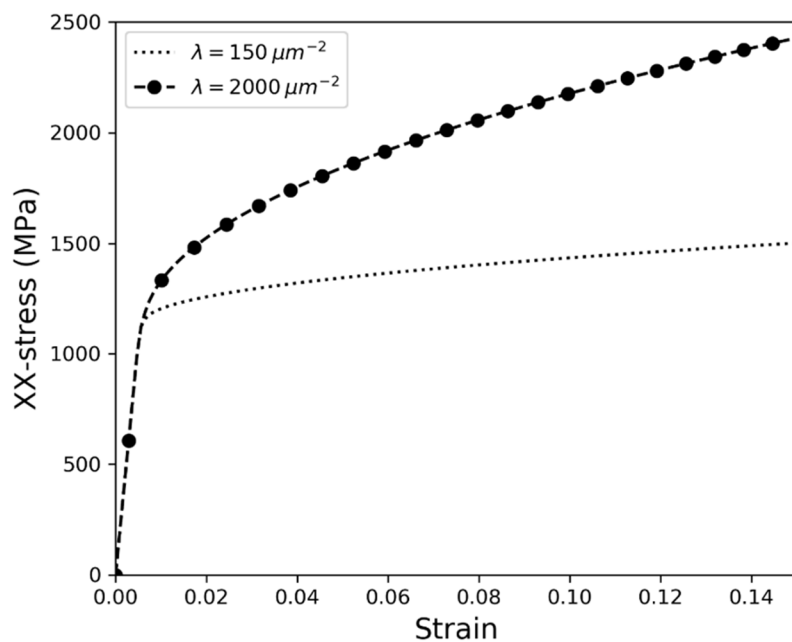


Figure 4-11 – Monotonic hardening curves showing the difference in behaviour of a low ($\lambda = 150 \mu m^{-2}$) and a high ($\lambda = 2000 \mu m^{-2}$) strain hardening level

For assessing the effect of strain hardening level, two different materials were modelled, a low strain hardening material ($\lambda = 150 \mu m^{-2}$) and a high strain hardening material ($\lambda =$

2000 μm^{-2}). The low strain hardening material follows the model calibration to RR1000 while the high strain hardening is given a higher strain hardening behaviour. The two materials were subject to a uniaxial stress-controlled loading of 10 cycles with a peak load of 1200 MPa. At this applied stress, decohesion does not occur within the first cycle of loading, instead, cyclic decohesion might be anticipated. The applied loading had a fatigue ratio of $R = -0.95$. The monotonic hardening curves for both hardening materials are shown in Figure 4-11. The strain hardening level of 150 μm^{-2} may be considered as low and 2000 μm^{-2} as high due to their respective response on the strain hardening behaviour. A low strain hardening material can expect a hardening curve closer to perfect plasticity and a high strain hardening material sees a larger increase in stress for an increment in plasticity.

4.5.1 Effect of strain hardening level on inclusion decohesion

To investigate the effect of strain hardening level on the inclusion, the model described above was run under a peak applied stress of 1200 MPa. The normal stress σ_n acting on the inclusion-matrix interface has been shown to be the main determinant of decohesion both above in the previous chapter and in work by Zhang et al.[51]. The peak normal stress on the interface is shown for both high and low hardening scenarios in Figure 4-12. The peak is taken at an integration point experiencing the maximum normal stress and is assessed at mid-cycle where the applied remote stress is maximised. The low strain hardening material experiences the lowest peak σ_n within the first few cycles after which it increases until it reaches an asymptote and does not progressively increase in value. The high strain hardening material experiences peak stresses within the first cycle after which it declines until it similarly reaches an asymptote. The key difference between the two material models is the difference in stress magnitude. As the model is subject to stress-controlled loading, the low strain hardening material is able to experience a higher degree of plastic deformation compared with that of the high strain

hardening and as a result the stresses increase. This is effect is compounded in the vicinity of the inclusion, which further increases the stress in the matrix close to the particle.

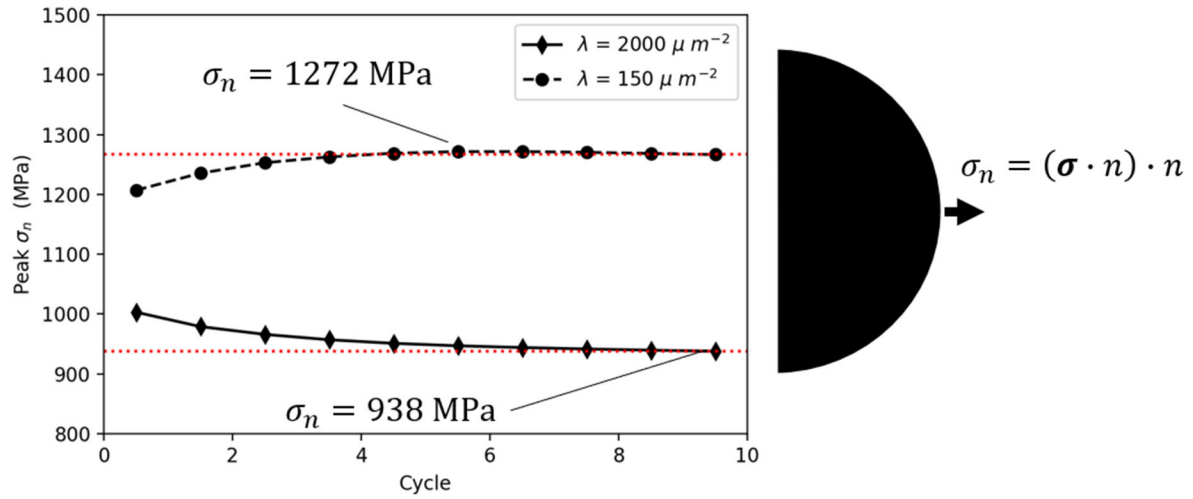


Figure 4-12 - The variation of peak normal stress on the inclusion interface as a function of cycles for a low and high strain hardening material. Red horizontal lines indicate the peak stress achieved after 10 cycles of cyclic loading.

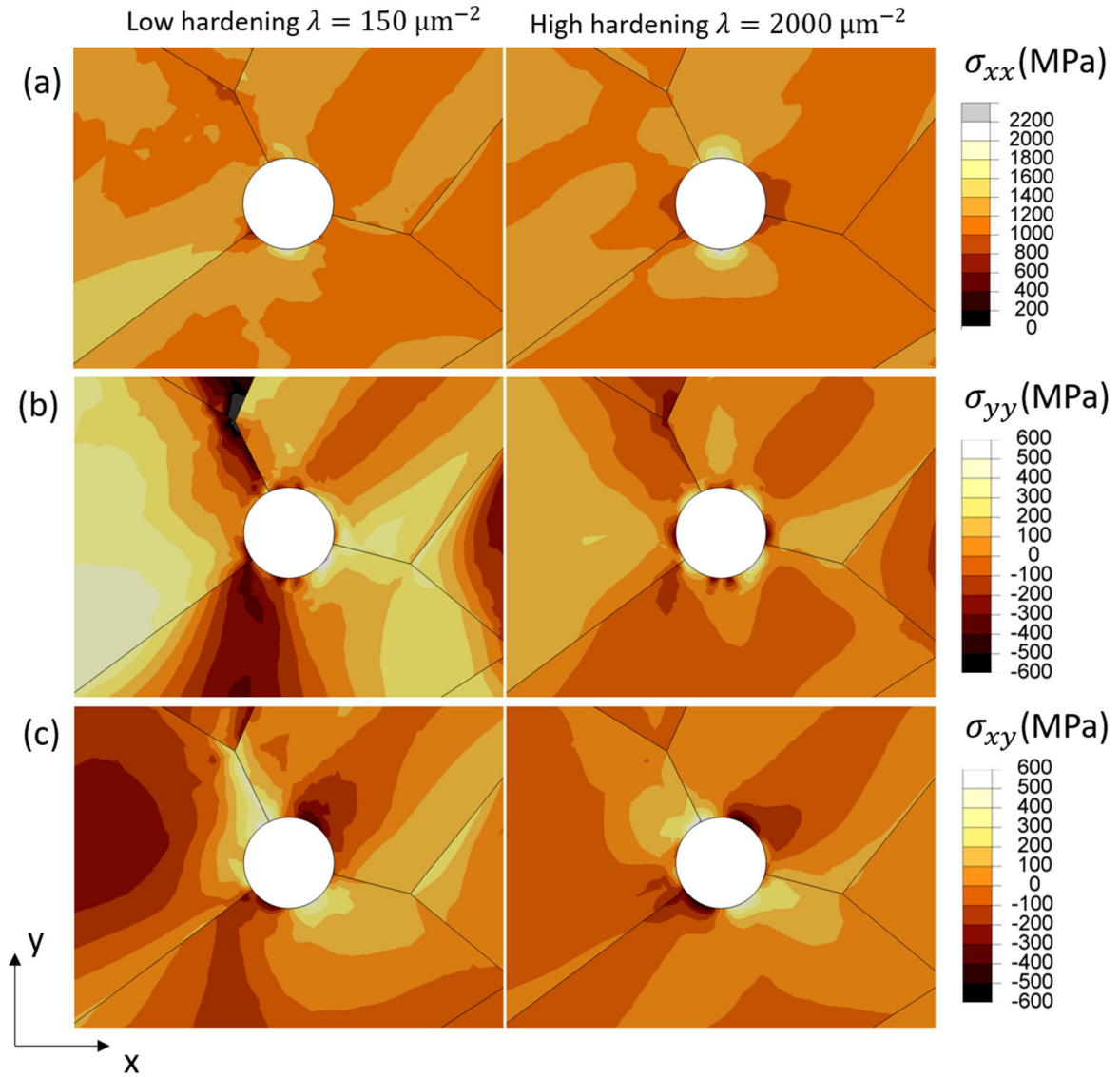


Figure 4-13 – Field plots of (a) σ_{xx} , (b) σ_{yy} , and (c) σ_{xy} for a low and high strain hardening material. The stress components are obtained at the peak load of the 10th cycle. The inclusion lies in the centre with grain boundaries overlaid.

Interestingly, the high strain hardening material records a lower interfacial stress compared with the low strain hardening material. This non-intuitive behaviour is expanded upon in Figure 4-13 in which field plots of σ_{xx} , σ_{yy} and σ_{xy} are shown for the peak of the 10th cycle. The σ_{xx} (a) component shows a difference in behaviour between the low and high strain hardening materials where the low strain hardening material exhibits high stresses on the interface normal to the direction of loading (x), conversely, the high hardening material exhibits low stresses in this normal interfacial area but comparatively higher stresses in the pole regions of the particle

aligned in the y-direction. This suggests that inclusion decohesion is more likely in a low strain hardening material. The other components σ_{yy} and σ_{xy} show similar behaviours between the two material configurations however the low hardening material shows a higher degree of polarisation. These two components are of course non-primary and exhibit lower magnitudes than the loading direction stress σ_{xx} .

The peak σ_n in either material model fails to reach the decohesion criterion ($S_D = 2050$ MPa) within 10 cycles. In addition, the cyclic change, $d\sigma_n/dN$, appears to approach zero with continued cycling. Cyclic decohesion may present itself at later cycles if the normal stress is allowed to rise to the decohesion threshold. To assess cyclic decohesion within the limit of 10 cycles, the values of positive $d\sigma_n/dN$ are extrapolated assuming that they have reached a stable value after 10 cycles. Therefore, spatial distributions of $d\sigma_{xx}/dN$ and cyclic evolution of $d\sigma_n/dN$ at the selected points are shown in Figure 4-14.

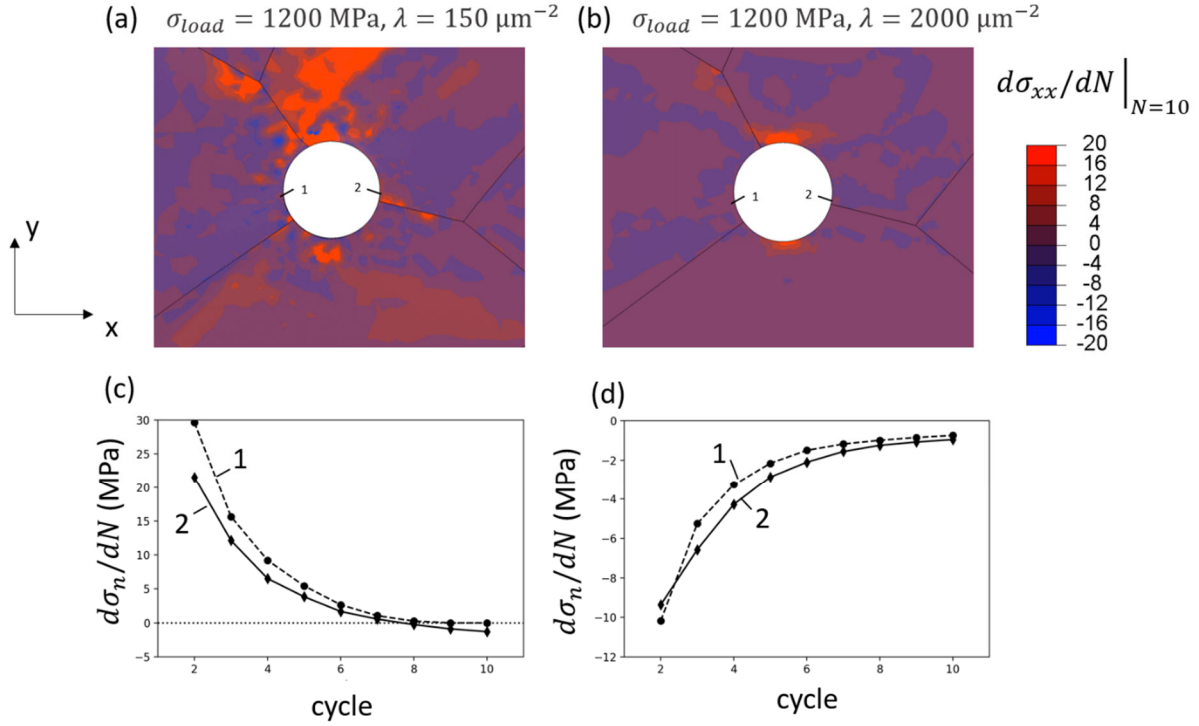


Figure 4-14 – Field plots of $d\sigma_{xx}/dN$ after the tenth cycle of loading for a (a) low strain hardening case and a (b) high strain hardening case with (c, d) pick-outs of $d\sigma_n/dN$ for probe locations indicated in (a) and (b) respectively

The probe assessments (at 1 and 2) in Figure 4-14 (c) and (d) are chosen from interface integration points and are close to locations of peak σ_n on either side of the inclusion. The trend shows that for a high hardening material the cyclic change in peak normal stress either decreases after 10 cycles or tends towards zero. In a low hardening material, there exists a slight positive indication of cyclic stress increase, but the trend shows an approach towards zero. If this trend decreases to zero, then the stresses on the interface will not reach the threshold stress required for decohesion after continued cycles. For other locations around the inclusion, lower σ_n values are recorded and their respective $d\sigma_n/dN$ values showed similar results to the pick-outs in (c) and (d). This suggests that decohesion is unlikely to develop even when considering for a stable $d\sigma_n/dN$ over many subsequent extrapolated cycles. It is noted that under a strain-controlled loading regime, the cyclic hardening induced would introduce an entirely different effect than that shown above. However, as turbine discs are subject to stress-

controlled loading the investigation is confined to stress-controlled scenarios. Additional forging steps introduced after HIPing of PM components may indeed act to decohere non-metallic inclusions given enough deformation which may affect future fatigue life performance, but this requires separate investigation.

The assessment of strain hardening level on cyclic decohesion is concluded here and a more detailed discussion is provided later. In the next section, implementation of a kinematic hardening model and its effect on the phenomenon of cyclic decohesion are presented.

4.5.2 Kinematic hardening implementation

In addition to high and low (isotropic) strain hardening materials, a phenomenological kinematic hardening law based on Armstrong-Frederick [154] evolution was adopted within the existing CPFE framework. Kinematic hardening was used within the same polycrystal model (see Figure 4-1) under 10 cycles of stress-controlled loading at a peak load of 1200 MPa. The isotropic hardening was assumed to be zero, which was imposed by prescribing a zero Taylor hardening coefficient (see equation 3.7 in the previous chapter). Kinematic hardening is incorporated via a back-stress term τ_b^i which is subtracted from the resolved shear stress:

$$\dot{\gamma} = \rho_m b^2 v \exp\left(-\frac{\Delta F}{kT}\right) \sinh\left(\frac{(\tau^i - \tau_b^i) - \tau_c}{kT} \Delta V\right). \quad 4.3$$

The direct and dynamic hardening terms (h_{dir} and h_{dyn} respectively) are material constants used to control the back-stress evolution. They are written such that:

$$d\tau_b^i = h_{dir} d\gamma^i - h_{dyn} \tau_b^i |d\gamma^i|. \quad 4.4$$

In this formulation, the back-stress τ_b^i is considered on the i^{th} slip system and thus considers kinematic hardening over all available slip systems individually rather than across the stress tensor directly [145]. To obtain values for h_{dir} and h_{dyn} careful parametric studies were

performed on a representative volume element comprising 130 grains. The synthetic microstructure is generated in Dream3D using mean and standard deviations of grain size and sphericity obtained from EBSD measurements of a typical fine grained RR1000 sample. A uniaxial displacement boundary condition was used to represent a cyclic strain-controlled uniaxial experiment. The experiment shows both isotropic and kinematic hardening effects albeit the isotropic hardening is minimal. The RVE geometry and calibrated response after 10 cycles of cyclic loading is shown in Figure 4-15. The parameters for the back-stress evolution are given in Table 4-3.

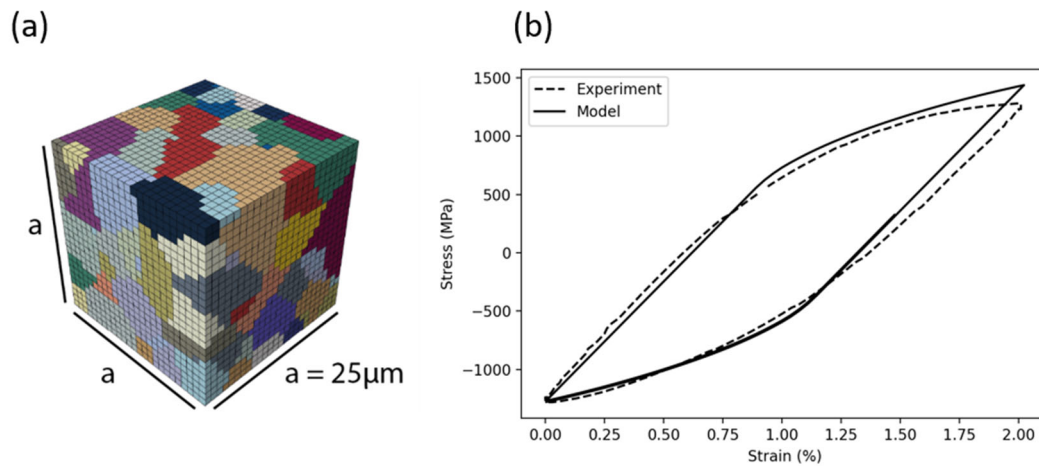


Figure 4-15 – (a) An RVE comprised of 130 grains representing conventional fine grained RR1000 and (b) the experimental and modelling response of RR1000 in strain-controlled fatigue loading after 10 cycles of loading.

Table 4-3 – Properties for back-stress evolution

h_{dir}	h_{dyn}
$3 * 10^4$ MPa	$4.5 * 10^2$ MPa

A comparison of mean cyclic strain accumulation over the entire model region (see Figure 4-1) is given in Figure 4-16 for all the material models described above under uniaxial stress-controlled loading at a peak load of 1200 MPa.

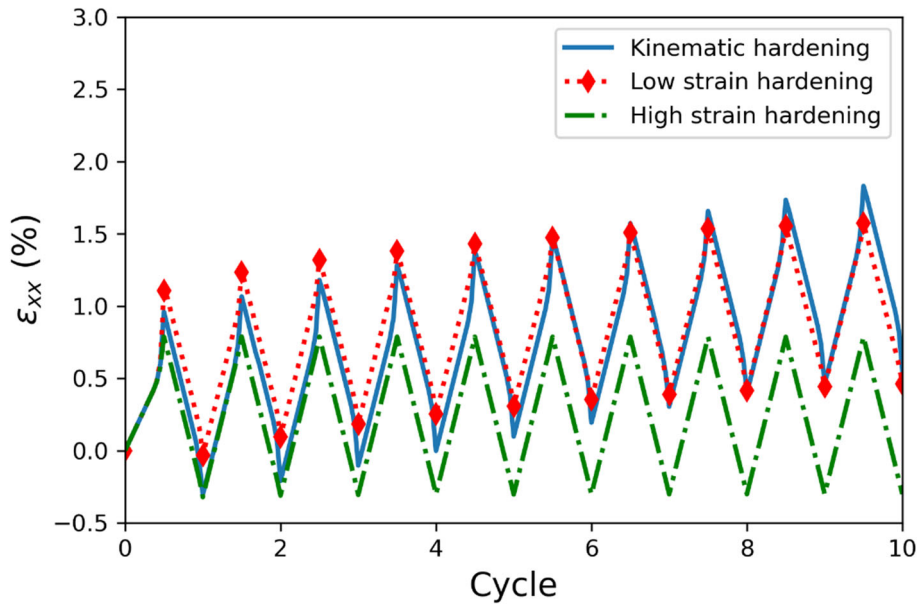


Figure 4-16 – The model mean strain for the various kinematic, low strain hardening and high strain hardening material models under stress-controlled loading with a peak load of 1200 MPa for 10 cycles

4.5.3 Effect of kinematic hardening on inclusion decohesion

In the same manner of the assessment of the effect of strain hardening level in 4.5.1, the trend of peak σ_n is shown for the inclusion under a kinematic hardening model in Figure 4-17. The peak σ_n is obtained from an integration point experiencing the highest normal stress at the peak of the cycle. The model is also subject to a peak stress of 1200 MPa. The σ_n appears to approach a final value of 1441 MPa as indicated by the red dashed line. The magnitude of stress is higher compared with that of either isotropic strain hardening model shown before (see Figure 4-12).

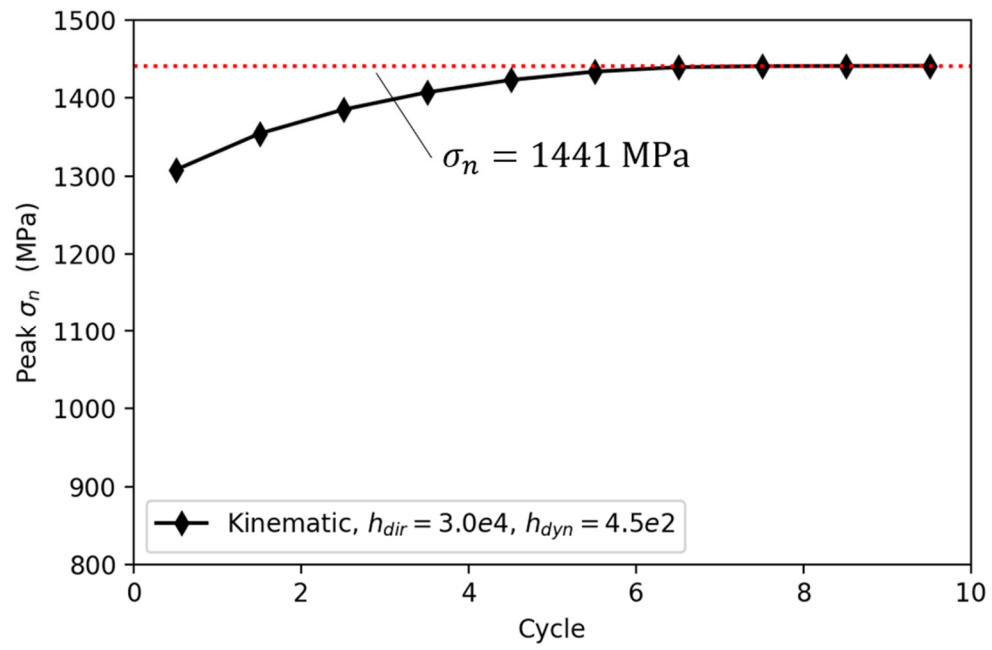


Figure 4-17 - The variation of peak normal stress on the inclusion interface as a function of cycles for a kinematic material. the red horizontal line indicates the peak stress achieved after 10 cycles of cyclic loading.

$$\sigma_{load} = 2000 \text{ MPa}, h_{dir} = 3.0 \times 10^4 \text{ MPa}, h_{dyn} = 4.5 \times 10^2$$

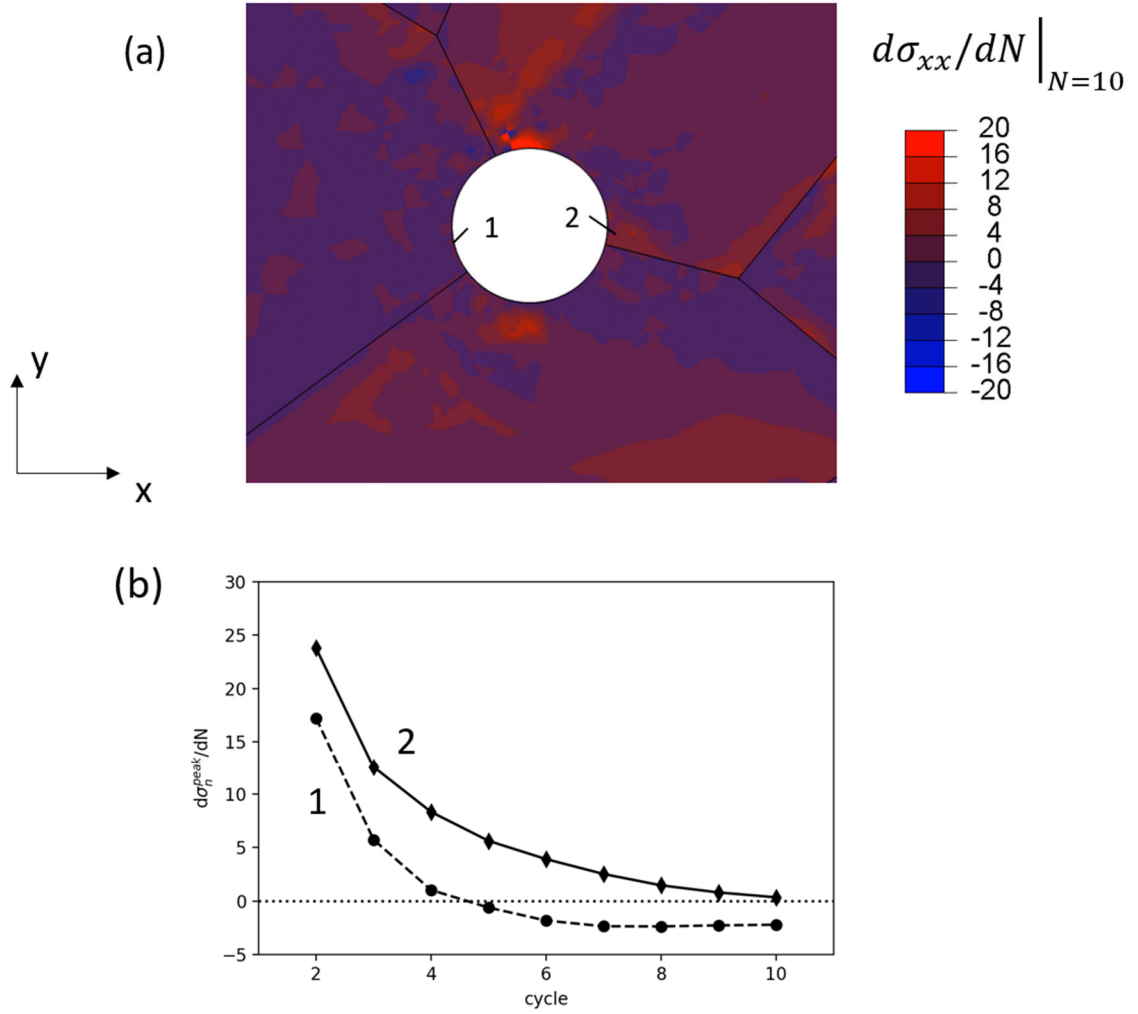


Figure 4-18 – (a) Field plots of $d\sigma_{xx}/dN$ with the pick-outs of $d\sigma/dN$ (b) with location indicated in (a)

The field plot of $d\sigma_{xx}/dN$ after 10 cycles, along with the cyclic evolution of $d\sigma_n/dN$ at locations 1 and 2 are shown in Figure 4-18. As before, the cyclic evolutions of $d\sigma_n/dN$ are obtained from locations experiencing high σ_n and other locations around the particle show similar trends of $d\sigma_n/dN$ as shown in (b). The trend shows in general that while high initial increases in stress on the interface can be expected (see Figure 4-18), the cyclic change in stress quickly approaches zero or lower. The model therefore does not predict cyclic decohesion on the basis of extrapolation of $d\sigma_n/dN$.

Recent investigations by Bandyopadhyay et al.[155] and Kapoor et al.[156] have suggested that kinematic hardening models based on GND development are able to capture cyclic plasticity effects better than the conventional Armstrong-Frederik [154] hardening model. Ultimately, a physically based hardening model which incorporates the development of dislocation densities into the back-stress will be able to capture a better representation of the cyclic plasticity and therefore stress levels near the inclusion agglomerate. This requires further separate research.

Ni-based superalloy discs in operation are subjected to stress-controlled fatigue loading. It is therefore important to understand the stress-controlled behaviour as opposed to the strain-controlled behaviour. In the high- and low- isotropic strain hardening models and the kinematic hardening model, the peak normal stress acting on the inclusion interface approaches a stable value and does not increase. The normal stress acting on the inclusion interface has been shown to relate unambiguously to decohesion by Zhang et al.[51] and decohesion was found to be stress-threshold based by Bergsmo et al.[144]. If the normal stresses acting on the inclusion boundary do not increase over continued stress-controlled loading, then decohesion is unlikely to occur. Inclusion decohesion may only be relevant if the first cycle stresses exceed the decohesion stress threshold. Furthermore, if applied stresses are low enough to prevent decohesion, this may mean an improvement in fatigue crack nucleation life. Experimental studies similarly show inclusion decohesion occurs within the first few cycles of loading [94]. In the context of a turbine disc, it is important to consider the effect of temperature which may serve to degrade the interfacial strength thus presenting a scenario in decohesion is also a function of temperature. Cavities have been reported at non-metallic inclusions at high temperature in other alloy systems [157]. Further research is required to understand this effect in RR1000.

Inclusion fracture is also exhibited in experimental studies of inclusions of RR1000 [87]. In the modelling framework described in this chapter, the inclusion has the ability to decohere as well as fracture, however, in the model used, decohesion is observed exclusively. In the current alloy system, inclusion fracture may be a function of the agglomeration. Inclusions which are stiffer than the matrix may form a local particulate strengthening morphology which restricts plastic motion in the metal matrix. Under this assumption, stresses within the particles will climb and may exceed the critical maximum principal stress required for inclusion fracture (found to be 2300 MPa in this case [144]). Solitary inclusions are therefore unlikely to exhibit fracture and instead decohere assuming that the strength of decohesion lies at 2050 MPa. Ultimately, the competition between decohesion and fracture relies on the physical strength of the inclusion in terms of decohesion and fracture.

Cyclic decohesion is not predicted to occur by the CPFE model under stress controlled cyclic loading for any hardening case. The stiff inclusion promotes elevated stresses in neighbouring metallic matrix, but the cyclic behaviour of this stress stabilises quickly (within 10 cycles) in the sense that $d\sigma_n/dN$ approaches zero or goes negative. In the absence of inclusion decohesion and fracture, slip-driven fatigue crack nucleation may occur (e.g. [49]). Slip-driven fatigue cracks rely on development of persistent slip banding impinging upon the inclusion. Over cyclic loading, the stored energy reaches a critical threshold after which a fatigue crack may nucleate [49]. However, experimental studies have failed to produce slip-driven fatigue cracks near agglomerate fields in RR1000 in the low cycle fatigue regime. Fatigue experiments at lower applied stresses are required to understand this behaviour conclusively.

4.6 Summary

A rigorous study was performed studying the fatigue crack nucleation propensity in a representative microstructure of RR1000 and the effect of strain hardening on inclusion decohesion under stress-controlled fatigue. The conclusions can be summarised as follows:

1. Inclusion dominates stored energy accumulation and therefore poses as the worst-case site for fatigue crack nucleation
2. Twin boundary observes localised stored energy density suggesting that in the locality of Parent-Twin grain combination, a fatigue crack would nucleate on or adjacent to the twin boundary.
3. The stored energy density accumulation on twin boundary compared with other grain boundaries is negligible. In some cases, conventional grain boundaries accumulate more stored energy than the twin boundary. The crystal plasticity method is not able to capture the micromechanisms driving fatigue crack nucleation. It may be hypothesised that this is due to the inability to predict discrete events such as slip banding. This requires further research to understand.
4. Neither the level of isotropic strain-hardening or kinematic hardening affects the early inclusion decohesion. Both high and low strain-hardening behaviours exhibited a stable value of peak normal stresses after 10 cycles of cyclic loading which indicates that under stress controlled loading with fixed peak stress, cyclic decohesion is not predicted to occur as it is dependent on exceeding a stress threshold.

5 Development of high temperature three-point bending rig and discontinuity tolerant digital image correlation

5.1 Introduction

Non-metallic inclusions and their neighbourhoods exist at the micron-scale in RR1000 and therefore require experimental methodologies which can capture the evolution of strain fields at a relevant length scale. In addition, the turbine section of the gas turbine operates at elevated temperature. The turbine disc experiences lower temperatures than the turbine blades yet still significant enough to require the use of superalloys. In this chapter, an outline of the development of experimental methodologies for capture of strain fields at high resolution and application of temperature to a three-point bend experiment.

The three-point bend is a classical experiment which has recently been successfully used to study small length scale problems such as fatigue crack nucleation [102], slip accumulation [158], and fatigue crack growth [159,160]. The principal advantage of studying these small length scale problems using three-point bending is a-priori knowledge of deformation concentration. Given a stress concentrator such as a notch [159] or a non-metallic inclusion [87] in the tensile fibre of the beam, it is with high probability that strain localisation occurs in the region of interest. Jiang et al.[161] used three point bending to study strain localisation in an advanced disc alloy. Zhang et al.[87], similarly, used the method to study fatigue crack nucleation near inclusions in RR1000. While these experiments provide key local deformation quantities, they are often performed at room temperature, which does not reflect the conditions that Ni superalloys are routinely subject to in service.

To characterise the deformation on the surface of three point-bend experiments, DIC has proven to become the prevailing method (e.g. [88,102,158,159]). The DIC method has been assessed recently in several reviews [162,163]. Conventional DIC relies on pattern matching

methods such as image cross-correlation to obtain zeroth-order shape functions (i.e., rigid body displacement terms u, v) [164]. Higher order shape functions are often employed to characterise complex displacement behaviour but require optimisation on displacement gradients [165]. Contemporary DIC techniques assume continuous displacement occurs on a plane, however, in real deformation at the micron scale, phenomena such as cracking and slip banding kinematically displace local speckle patterns such that displacement fields become discontinuous. Recently, methods such as Heaviside digital image correlation (H-DIC) have been used to quantify kinematic shifts in displacement fields [166]. H-DIC is an extension of the classical DIC based on optimisation of the first order shape function where a subset is partitioned to track multiple displacements [167]. Bourdin et al.[168] have used this method in high-spatial resolution to quantify slip band magnitudes. Stinville et al.[169] used H-DIC to track slip irreversibility in fatigue of a Ni-based superalloy specimen under fatigue loading and have recently used the method to quantify dwell fatigue behaviours within Ti [170]. Hassan et al.[171] have, in a similar fashion, incorporated subset splitting to determine strain fields with discontinuities using subset splitting with a Burger's vector parameter. Discontinuity tolerance has also been incorporated into extended DIC using the finite element method [172].

In this chapter an outline and discussion is provided on the development of two methods for experimentation on RR1000 samples with inclusions, namely three-point bending with an integrated infrared (IR) heating system to allow for isothermal heating conditions and discontinuity tolerant digital image correlation (H-DIC) which is used to quantify discontinuous displacement events such as cracking, slip banding and decohesion. Validation of the H-DIC technique is supplied after discussion of the methodology. The results of these methods for an RR1000 sample with inclusions are shown and discussed in detail within the following chapter.

5.2 High temperature three-point bend apparatus

A three-point bend experiment applies bending motion to a beam specimen which can be used to estimate flexural stiffness. In experiments which consider micromechanical deformation, the bottom of the front free surface (shown in Figure 5-1 (a)), can be assumed to be in uniaxial tension during peak load if the region height is small enough for shear strains to be negligible. The experiments included within this thesis are focused on the bottom of the front free surface to create uniaxial experimental conditions on a deliberately chosen region such that stress features such as fatigue cracking can be created without a-priori knowledge of their location. All three-point bending experiments were performed on a 10kN Shimadzu AGS-X [173] tensile tester and the following modifications are all done on the Shimadzu frame.

The conventional three-point bend experiment is limited in its capacity to subject turbine-like conditions to the material specimen. These conditions include high temperatures and atmosphere. To replicate high temperature conditions, two infrared lamps were set up (shown in Figure 5-1 (b)), providing a heat source to the specimen. While the temperature of turbine components can reach in excess of 600 °C, the aim here is to conduct experiments at an intermediate temperature of 300 °C and leave higher temperature experiments for the future investigations. At 300 °C and higher, Ni-based superalloys experience a transition from tetrahedral to cube slip which may show in experimental results [174]. This transition is material-dependent and the experiment conducted at 300 °C is required to confirm the transition temperature in RR1000.

5.2.1 IR lamps

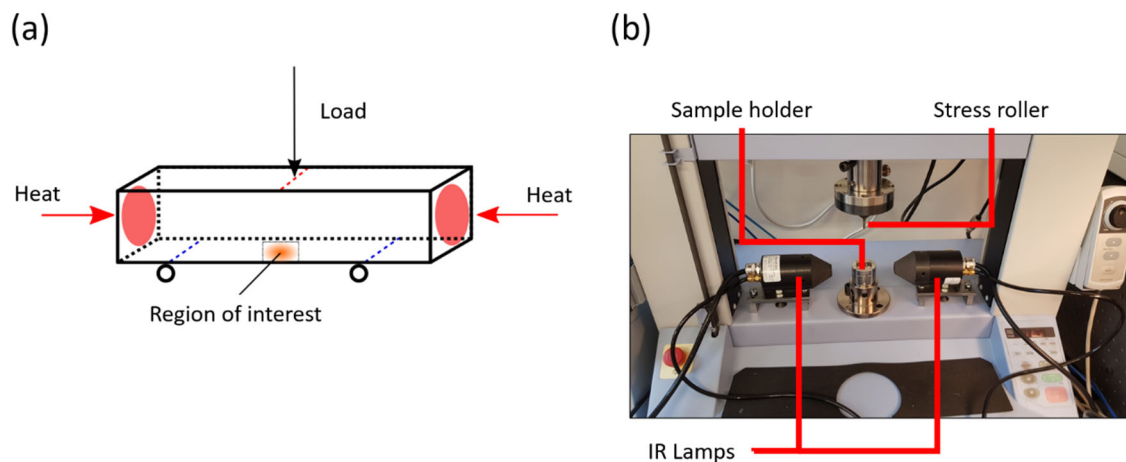


Figure 5-1 – (a) A schematic of testing specimen showing region of interest and boundary conditions, (b) The IR lamps inserted to Shimadzu test frame

Two *Research Inc.* SpotIR 4150 lamps were added to the system (See Figure 5-1 (b)). The IR lamps heat a 5mm circular section (at the focal point) with high density heat provided by infrared radiation. The lamps can provide a maximum heat flux of $1.7 \times 10^6 \text{ W/m}^2$. Cooling of the lamp system is provided by a constant flow of air and is necessary to increase the lamp lifetime due to the high temperature generated.

As the sample is small ($< 12 \times 3 \times 3 \text{ mm}$), it requires only moderate heating to achieve high temperatures rapidly and uniformly. Another advantage is the ability to prepare the beam for SEM with minimal delay. By polishing a sample prior to an experiment, EBSD can be performed on the sample post-mortem in “as is” condition, needing only an application of a conductor such as silver paint to prevent charge build up on the surface. In specimens with inclusion agglomerates, the inclusions and surrounding coarse grain region encompass a region no wider than $100 \mu\text{m}$ and are therefore only 3% of the beam width.

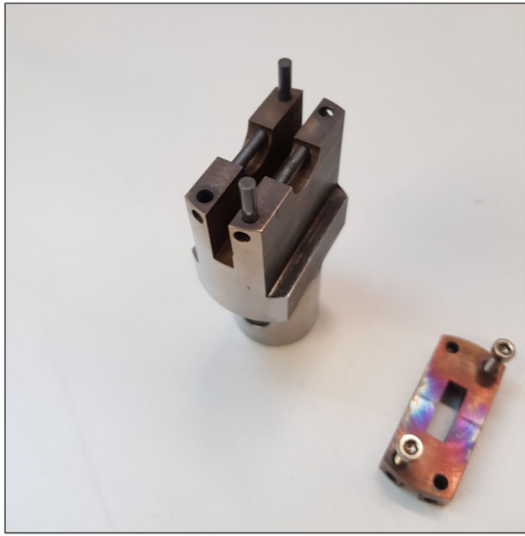
Temperature control is provided by a Eurotherm 2416 [175] proportional integral derivative (PID) controller which receives a thermocouple connection and outputs the relay logic for the

infrared lamps. The output power of the infrared lamps is therefore controlled by the signal output of the thermocouple. The control system is programmable and capable of isothermal and cyclic thermal loading of the specimen. In the research of this thesis, the experiments are limited to isothermal loading at 300°C. A thorough discussion of the development of the control system is given in [176].

K-type thermocouples were spot welded to the surface of the samples. The main thermocouple providing temperature readings to the control system is spot weld on the back of the beam specimen, on the opposite side of the region of interest to prevent any interference with the deformation response on observation surface. The thermocouple therefore provides the temperature reading at the axial centre of the thermocouple beam. For temperature recording, a TC-08 Pico data logger [177] was used.

An H13 tool steel holder (Figure 5-2 (a)) was machined to contain the support rollers, with heating and observation windows (Figure 5-2 (b)) to allow for thermocouple entry and in-situ sample observation *via* an optical microscope. The holder contains tungsten carbide support and alignment pins. The design of the holders was completed by Benjamin Poole [176].

(a)



(b)

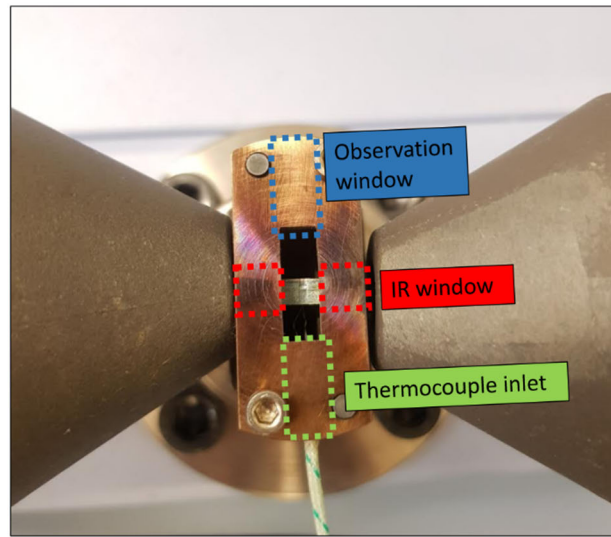


Figure 5-2 – (a) The beam holder with tungsten carbide support and alignment pins, (b) the beam holder with IR lamps mounted in a close configuration with annotations showing the observation window, IR window and thermocouple inlet.

5.2.2 Verification of beam temperature

Experimental and modelling studies were performed to determine the accuracy of temperature estimation near the centre of the beam specimens for fine grained RR1000. The uniformity of temperature across the beam was also investigated to determine thermal gradients.

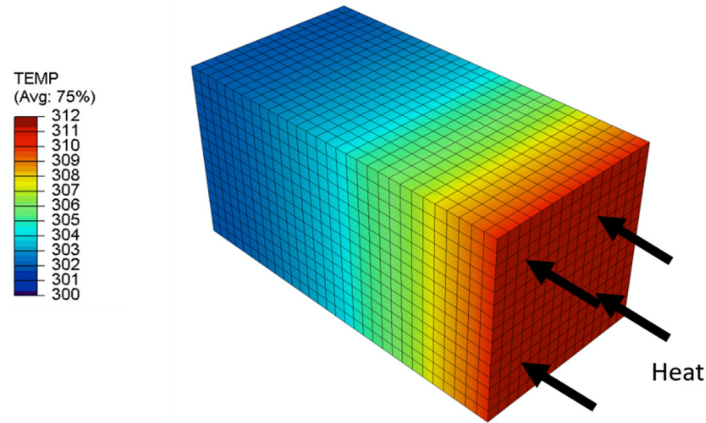


Figure 5-3 – The 3D FE model used to investigate thermal gradients across the beam. Half the beam is omitted here.

A 3D FE model of the beam (shown in Figure 5-3) was created to estimate the thermal gradients of the beam subject to constant heat flux of 5% total heat output of a heater on the free end surfaces. The thermal material properties used were estimated based on common properties of Nickel superalloys and are shown in Table 5-1. While the thermal properties are temperature dependent, the maximum desired temperature is 300 °C which shows negligible changes over the temperature range. It is assumed here that the beam is subject to an ambient environment with convective heat transfer with a film coefficient between the sample and air of $30 \text{ W m}^{-2}\text{K}^{-1}$ [176].

Table 5-1 – thermal properties used for the FE model

Property	Value	Source
Density	8.2 g m^{-3}	[4]
Specific heat	$11 \text{ J kg}^{-1}\text{K}^{-1}$	[178]
Thermal conductivity	$11 \text{ Wm}^{-1}\text{K}^{-1}$	[4]

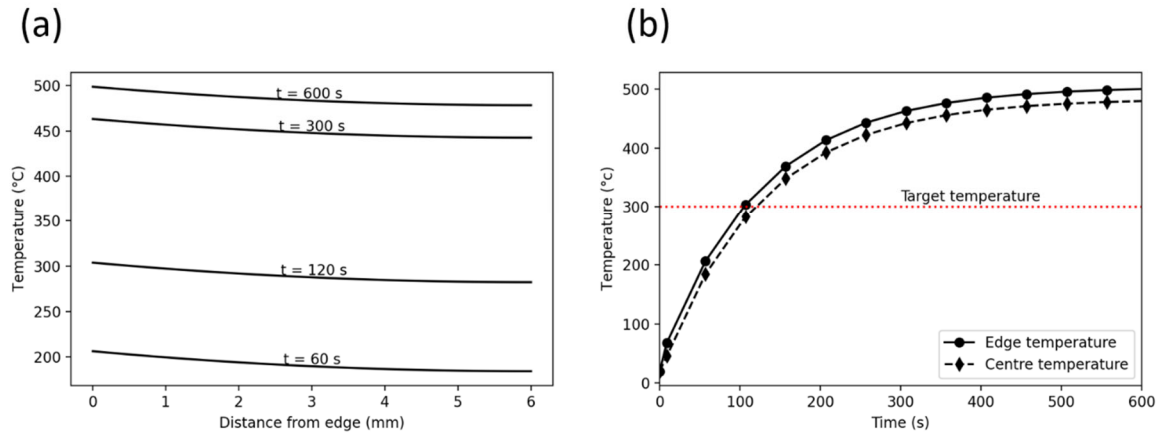


Figure 5-4 – (a) The temperature gradient across the half beam and (b) the evolution of temperature at edge and centre integration points over 600 seconds.

The temperature gradient across the axial profile of the half beam is shown in Figure 5-4 (a). The difference of temperature between edge and centre of the beam is 20 K showing a temperature gradient of roughly 3 K mm^{-1} . However, closer to the centre, the gradient eases showing a relatively flat section. This suggests a uniform gradient to exist near centre. The temperature variation over time for the edge and centre are shown in Figure 5-4 (b). The curves show minimal difference after continued time suggesting thermal gradients do not change with time.

The above analysis neglects the role of rollers as heat sinks acting through heat conduction. The support and stress rollers are in effect, heat sinks and must be dealt with in the experiment. However, the support rollers are made of tungsten carbide, a poor conductor of heat. As a result, all experiments conducted within this thesis are accompanied by a heat soak period of 10 minutes to allow surrounding experimental apparatus to approach the desired experimental temperature. It is therefore important to bring the stress roller into contact with the beam prior to heating. Heating then thermally expands the stress roller and requires adjustment of cross head position to negate the increased load on the beam.

Attempts were made at measuring the temperature gradients across the beam experimentally. Figure 5-5 shows three thermocouples spot welded to an RR1000 beam specimen. Accurate measurements of temperature gradients proved difficult to obtain due to the small size of the beam specimen (12 x 3 x 3 mm). Each spot weld was made manually by a two-step process; a thermo couple bead is made by spot welding, then, the thermocouple is spot welded to the surface of the beam. To obtain a useful thermal gradient at least 3 thermocouples are desired across the half-length of the beam to obtain a better curve. However, 3 thermocouples proved to be too large on the beam specimen. K-type thermocouples typically have an error of 2 K [177] but the accuracy is further dependent on the quality of the spot weld which is more difficult to assure with a tight configuration of thermocouples. Furthermore, another error is introduced through the control system of the lamps. The lamp output was controlled by phase-angle control [179] which resulted in temperature variations of 1-2 K about the set point. These errors resulted in a variable distribution across the length of the beam not comparable with the FE model above.

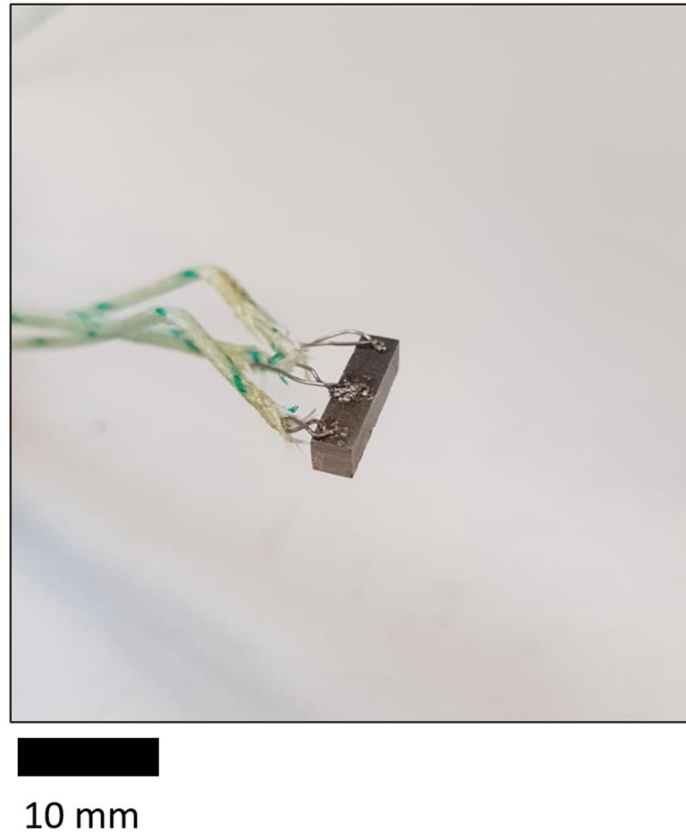


Figure 5-5 – Three thermocouples spot welded to a 12 x 3 x 3 mm beam

The development of the three-point bend with heating is concluded here. This method is used within the next chapter to study fatigue crack nucleation at elevated temperature near non-metallic inclusions in RR1000. The next section in this chapter deals with the development of discontinuity tolerant DIC for observations of strain fields produced by the three-point bend experiment.

5.3 Discontinuity tolerant digital image correlation

The DIC method described below is based upon an implementation following Jiang et al.[180] but has been significantly altered. In the interest of improving strain map resolution at the micron scale, several improvements have been incorporated. These improvements are primarily rigid body correction by polynomial surface fitting and discontinuity tolerance via the Heaviside method, but significant improvements have also been made in code optimisation

and structure. Contrary to conventional methods in the literature, this is performed using the coarse-fine method as opposed to optimisation on the first order shape function. The code is written in Python 3.7 and makes use of several open-source image process libraries such as OpenCV [181], parallel pipelining interfaces such as Joblib [182], and general-purpose array operation and linear algebra package NumPy [183].

5.3.1 Coarse-fine method

To obtain full field displacement fields a coarse-fine methodology is employed. The coarse-fine process for generating displacement maps is shown in Figure 5-6. The process is composed of two image correlation passes. The coarse pass uses larger subset sizes and coarse subset overlaps to infer rigid body displacement fields across the sample surface. The rigid body displacements are used to map the deformed image over the undeformed image by subtraction of rigid body displacements. This is defined here as a correction step, which is described in detail later. Using corrected images, a fine pass is performed with a fine subset size and overlap. Within the fine pass, a discontinuity detection treatment may be added to find discontinuity parameters dx_c, dy_c, dx_h, dy_h and j . These are described in detail later.

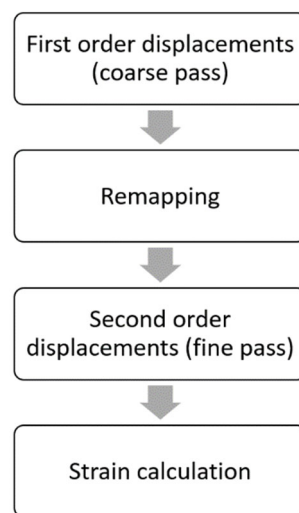


Figure 5-6 – The general methodology of the Coarse-fine method

5.3.2 Correlation criteria

To obtain the highest accuracy of correlation shift, an interpolation scheme is often needed to up-sample the image [184]. Subpixel shift registration is performed by a transform to Fourier space to assuming grayscale values of reference image and deformed image are time dependent. Subpixel accuracy is obtained by up sampling the region near the peak shift in integer accuracy correlograms. This method is described in detail elsewhere [185] but a short description is given here. In the following, the reference subset grayscale array is referred to as f and the deformed subset grayscale array as g . For two subsets of size $(M \times N)$ Cross correlation is defined as [186]:

$$r_{cc}(i, j) = \sum_{x=0}^{M-1} \sum_{y=0}^{N-1} f(x, y) g(x + i, y + j) \quad 5.1$$

where r_{cc} is the correlogram. The deformed image g is zero-padded to allow for a compatible product in the correlation coefficient. The correlogram may be obtained in a more computationally efficient manner via the fast Fourier transform [187]. Transformation of subsets to Fourier domain is written as:

$$\mathbf{f} = \mathcal{F}\{f\}, \quad \mathbf{g} = \mathcal{F}\{g\} \quad 5.2$$

Here, the bold format indicates a transformed variable. The Fourier transform of the correlogram, \mathbf{R} is therefore:

$$\mathbf{R} = \mathbf{f} \circ \mathbf{g}^* \quad 5.3$$

where \mathbf{g}^* is the complex conjugate of \mathbf{g} . The correlogram can then be obtained through the inverse Fourier transform:

$$r_{cc} = \mathcal{F}^{-1}\{\mathbf{R}\} \quad 5.4$$

This correlogram is only accurate to the integer pixel value. To determine subpixel shifts, algorithms often up sample the entire image domain using bicubic spline interpolation. Here, a refinement of the peak of the integer shift correlogram is performed to estimate the subpixel shift. This method is computationally efficient and is described thoroughly in [185].

Subpixel accuracy is useful for finding decimal shifts in displacement for final approximation of displacement fields but is computationally expensive for up-scaling. To minimize correlation coefficients for discontinuity detection, a fast, integer-accuracy correlation criterion was used. The minimization procedure is described later but introduces up to 100 additional cross correlation calculations per subset. This follows a normalised sum of square difference criterion (NSSD) [188]:

$$r_{NSSD}(i, j) = \frac{\sum_{x=0}^{N-1} \sum_{y=0}^{M-1} (f(x, y) - g(x + i, y + j))^2}{\left[\sum_{x=0}^{N-1} f(x, y)^2 \sum_{y=0}^{M-1} g(x + i, y + j)^2 \right]^{\frac{1}{2}}} \quad 5.5$$

The NSSD criterion allows for robust measurement of peak heights without errors introduced through changes in greyscale intensity in deformed image [189]. NSSD does however reduce the peak width in the correlogram potentially removing desired peak matches which are available in the correlation criterion in equation 5.1. This equation may therefore be to find the peak height for subpixel accuracy but equation 5.5 may be used for a fast approximation of the correlation coefficient. A comparison of the two correlation criteria is shown in Figure 5-7 (a,b) where the resulting correlograms of two 32 px subset are shown. It is important to note that the NSSD criterion is a difference measurement which means a lower correlation value corresponds to a better match. The red arrows indicate location of the peak where the array indices are the displacement values. While code transparency is desirable, highly optimised packages such as OpenCV [181] offer fast methods which are instead used.

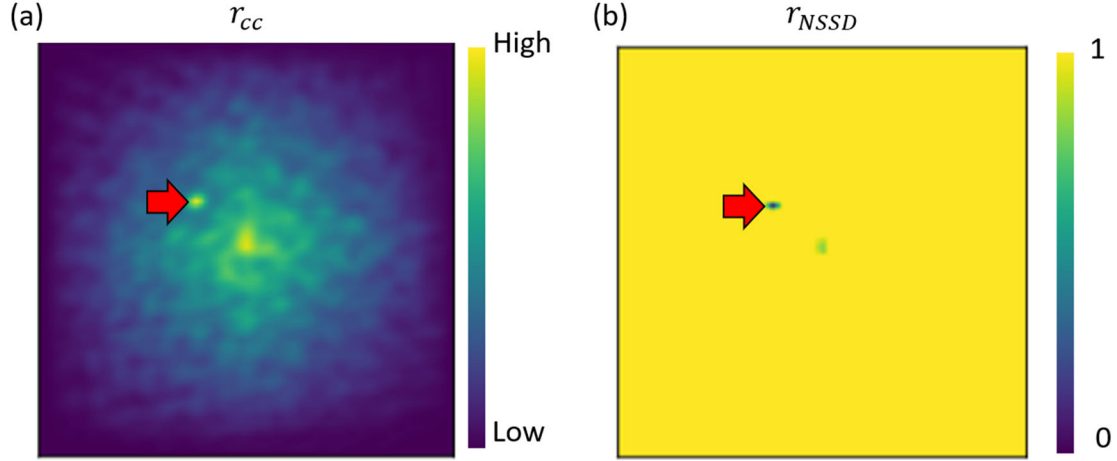


Figure 5-7 – Correlograms of (a) the conventional cross correlation and (b) the normalised square difference criterion for a subset size of 32 px. The red arrows indicate location of the best match.

Both correlation criteria described above obtain zeroth-order displacement functions after minimisation of the correlation coefficient:

$$u = x + dx, \quad v = y + dy \quad 5.6$$

Higher order displacements are not obtained on each subset in this code as is common in other codes [163], rather a field-wide optimisation is performed on rigid body translations which corrects for coarse rigid body deformation yet preserves fine displacements. This method is described in detail within the next section.

5.3.3 Polynomial surface correction

Deformation across a sample surface introduces rigid body displacement, rotation and shear which cause loss of correlation for shift registration. In the case of large deformation, smaller subsets used to obtain small scale displacements may not correlate at all and therefore fail to produce accurate shifts. Larger subset sizes are able to find correlation matches but the displacements obtained are based upon large amounts of speckles. Large subsets may therefore detect homogenised displacement across large regions which can be inferred as rigid body

deformation. Under this assumption, large subsets may be used to map the reference image unto the deformed image, correcting for rigid body translation, rotation and shear while preserving finer displacements for strain calculation in the final step. However, if the deformation within a large subset is sufficiently complex, the correlation will fail.

Displacement maps (dx and dy) of a coarse first “pass” of the correlation function are used to model a quadratic plane of best fit using least squares regression. The fit plane is used to map the coordinates of the deformed image unto the reference image. While the plane used in this thesis is quadratic, it can be generalised to any n^{th} degree polynomial surface. First, subset centre coordinates are inferred from the zeroth order shape functions such that the measured coordinate, x of the deformed set is a linear translation resulting from dx . The measured coordinates are used to find the coefficients of the bivariate quadratic polynomial:

$$f(x, y) = q_1x^2 + q_2x + q_3y^2 + q_4y + q_5xy + q_6, \quad 5.7$$

where q_i is column vectors of bivariate quadratic coefficients, x and y are the subset coordinate centres of the reference image. This sets up a set of linear equations to be minimised:

$$\min \left[||\mathbf{b} - \mathbf{A}\mathbf{q}||^2 \right] \quad 5.8$$

Where \mathbf{A} is a matrix containing the values of x and y under equation 5.7, and \mathbf{b} is a matrix containing the measured coordinates of x, y . The minimum value of equation 5.8 will equate to the fit parameters of \mathbf{q} . The coordinates of the deformed image are then translated according to the best fit model of the linear translations with linear transformations \hat{x} and \hat{y} . As the arising coordinates are not coincident with the pixel values of the reference image, a bicubic interpolation is used to map the coordinates accurately. As a result, the deformed image has now been corrected to map unto the reference image. Border values which are no longer within the image dimensions are filled with zeros.

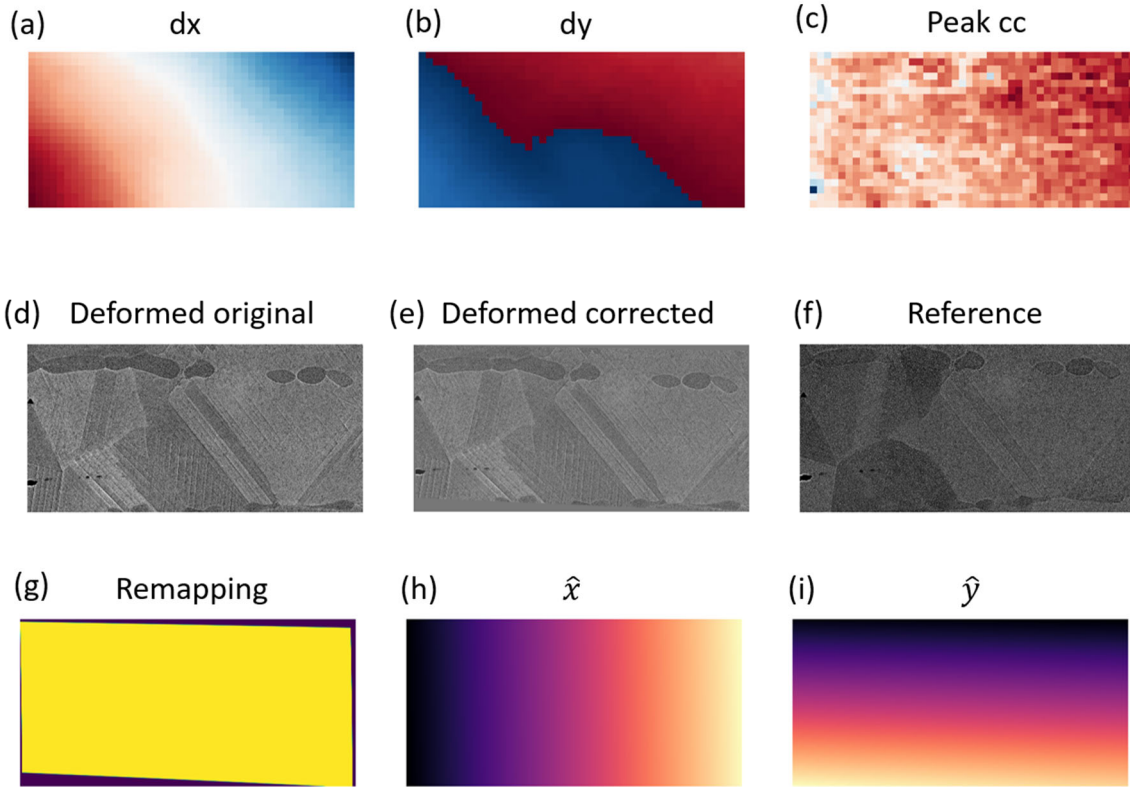


Figure 5-8 – A demonstration of the correction routine. The coarse pass displacements (a,b) with corresponding peak cross correlation heights (c). The changes subjected to the deformed image (d) are shown in (e) where the remapping routine attempts to remap the deformed image to the reference image (f). An outline of the remapping shape (g) with the corresponding shifts in x (h) and shifts in y (i). The image sets are kindly provided by Dr Benjamin Poole.

Figure 5-8 shows the remapping technique in detail. The coarse pass provides rigid body displacements dx and dy (a, b) which the routine fits a model and obtains correction transformations \hat{x} and \hat{y} (h,i). Here, the bold text format indicates matrices as opposed to Fourier transformed variables. The outline of the remapping procedure can be seen in (g) and the resulting correction on the deformed image in (e). In this case, the deformation results from a three-point bend test and will be investigated in detail later for the Heaviside method.

Given that the coarse displacement pass successfully captures rigid body displacement, the remapping will conserve local displacements while correcting for rigid body deformation. The corrective step allows for a fine pass to achieve high correlation coefficients. A key assumption

used in the correction algorithm is that strain on the sample surface is small. In the case of large rigid body rotations and shear, decorrelation will occur within the coarse pass and the correction will fail to approximate the deformation.

5.3.4 Discontinuity tolerance

Discontinuity detection is incorporated via minimization of the square difference correlation criterion for a masked subset. This method, inspired by the works of Valle et al.[166] and Bourdin et al.[168], attempts to find discontinuous deformation by partitioning a subset. Instead of performing a Newton-Raphson optimisation on the correlation coefficient, the correlogram for every subset is obtained using equation 5.5. A novel method of finding the discontinuity in the form of a reduced search function is described later.

A binary mask is applied to the undeformed subset such that the peak correlation coefficient, $r(i, j)$, is dependent on parameters r and θ . r is a vector from the centre of subset to the tangent of the discontinuity line and θ is the angle of the discontinuity with respect to a horizontal axis. Figure 5-9 shows the subset mask and the discontinuity line parameters.

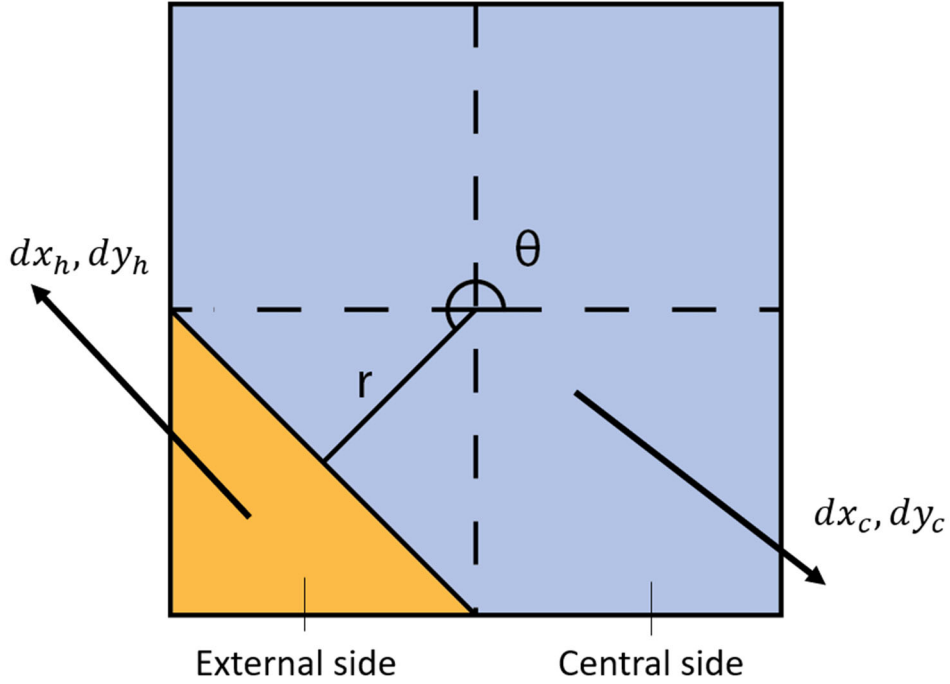


Figure 5-9 – A subset partitioned along a line with polar coordinates r, θ assumed from subset centre

As the correlation function dependent on r and θ is ill behaved, noisy and non-convex, optimisation regimes are ineffective in determining the global minimum in an efficient manner. A search space is defined for r and θ , and a minimum from the sum of correlation of the central side and external side ($r_{NSSD}^c + r_{NSSD}^e$) is obtained. The goal of the correlation is to find a best “match” of pixels, it is therefore prudent to obtain the best fit from the sum of correlation coefficients. This allows us to find the exact location of the discontinuity. Figure 5-10 shows the search space of r and θ with the corresponding sum of correlation coefficients. By considering the symmetric nature of the sum of correlation coefficients, a reduced brute force minimisation can be performed. A brute force search of the angles close to the centre of the subset can reveal the angle θ , at which the discontinuity occurs. A search cone may then be

defined for angles $\theta - 5 < \theta < \theta + 5$ and all r values. The algorithm therefore only searches a reduced space as opposed to all combinations of r, θ .

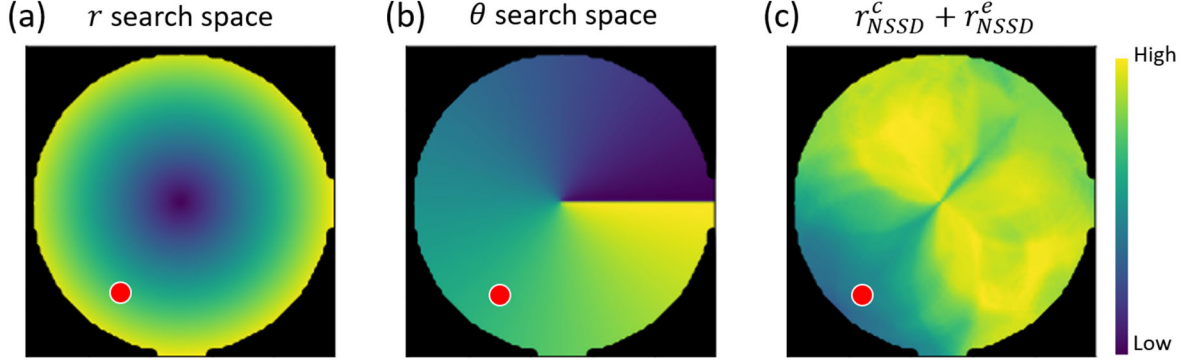


Figure 5-10 – The search space for discontinuity parameters (a) r and (b) θ for a subset containing a discontinuity, the search spaces have been expanded to include a large array of values to show the behaviour of the (c) sum of correlation coefficients. The red circle shows the location of discontinuity for the value of r and θ

It is worth noting that the minimization routine is not performed with subpixel accuracy. Once a best match has been found, a subpixel accuracy correlation is performed to obtain the displacements of the respective sides. The displacements are compared through a jump vector magnitude:

$$j = \sqrt{(dx_c - dx_h)^2 + (dy_c - dy_h)^2}. \quad 5.9$$

As j approaches zero, no discontinuity is found, and the algorithm may continue to the next subset. In the case of a non-zero j , the central side displacements are assumed to be the subset displacements and the jump vector is recorded as well as r and θ . The value of correlation is dependent on the number of pixels which are able to successfully match. The correlation is therefore dependent on the magnitude of r , where a large r will cause information loss on the external side. The r search space is limited to $1/4$ of the subset window width to obtain optimal values of correlation for the external side. This also limits the minimum size of the subset, for small scale displacement maps, a minimum subset size has been found to be around 32px.

The original versions of H-DIC modify the displacement field such that the jump term (see equation 5.8) is incorporated into their displacement function [168]. This results in a strain field which is modified by the jump step. Instead, the discontinuity detection is used as a method of characterising slip events rather than modifying the strain field.

5.3.5 Determination of strain

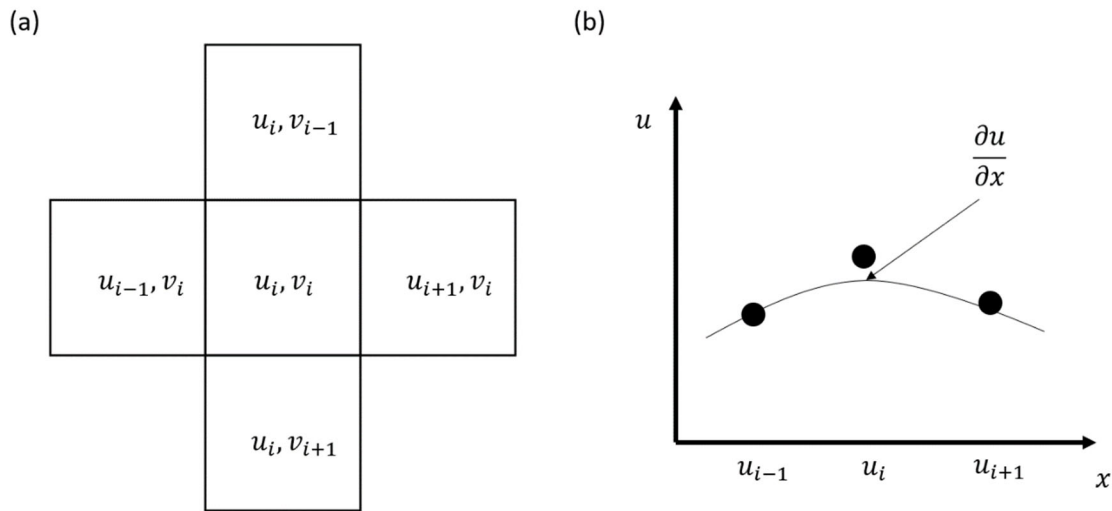


Figure 5-11 – (a) The neighbourhood of displacement cells considered for determination of the deformation gradient of the central cell (i,j). (b) A schematic representation of finding the displacement gradient based on fitting a polynomial to the neighbourhood of displacement values

Strain is calculated based displacement sets obtained from the fine pass, these are arrays of dx and dy . By considering a neighbourhood of displacements (see Figure 5-11 (a)) the deformation gradient of the central displacement element can be approximated. The classical displacement gradient, F , is written as [123]:

$$\mathbf{F} = \begin{bmatrix} \frac{\partial u}{\partial x} & \frac{\partial u}{\partial y} & \frac{\partial u}{\partial z} \\ \frac{\partial v}{\partial x} & \frac{\partial v}{\partial y} & \frac{\partial v}{\partial z} \\ \frac{\partial w}{\partial x} & \frac{\partial w}{\partial y} & \frac{\partial w}{\partial z} \end{bmatrix} \quad 5.10$$

Assuming motion in DIC images occur in plane, the out of plane gradients with components in z reduce to zero, e.g;

$$\frac{\partial u}{\partial z} = \frac{\partial v}{\partial z} = \frac{\partial w}{\partial x} = \frac{\partial w}{\partial y} = 0 \quad 5.11$$

The displacement gradient is therefore:

$$\mathbf{F} = \begin{bmatrix} \frac{\partial u}{\partial x} & \frac{\partial u}{\partial y} & 0 \\ \frac{\partial v}{\partial x} & \frac{\partial v}{\partial y} & 0 \\ 0 & 0 & 0 \end{bmatrix}. \quad 5.12$$

This leaves 4 components of displacement gradients to be obtained from the displacement maps. Each component is obtained from fitting quadratic equations based on the neighbourhood of displacements. Figure 5-11 (b) shows the obtainment of displacement gradient. In HR-DIC, the radius of strain calculation is best taken from a small neighbourhood to allow for capture of local strain phenomena such as slip bands. However, large neighbourhoods may be used in component-scale DIC to obtain a larger degree of strain homogenisation.

The Green strain tensor is determined from the symmetric and anti-symmetric parts of the displacement gradient:

$$\mathbf{E} = \frac{1}{2}(\mathbf{F}^T \cdot \mathbf{F} - \mathbf{I}) \quad 5.13$$

The effective strain can be calculated directly from:

$$\epsilon_{eff} = \sqrt{\left(\frac{2}{3}\mathbf{E}:\mathbf{E}\right)} = \left[\frac{2}{3}(E_{11}^2 + E_{22}^2 + E_{12}^2)\right]^{\frac{1}{2}} \quad 5.14$$

Strain determination is therefore determined over a neighbourhood of displacements and shear components of the strain tensor are determined from the relative displacement of neighbourhoods of displacement. It is therefore important to consider the impact of discontinuity tolerance on this calculation of strain. In this implementation of DIC, no modification is made to the strain calculation to account for discontinuities in displacement (e.g. a slip band is still considered as a strain in strain maps). The H-DIC implementation is therefore primarily used for characterisation of slip band behaviours.

In this chapter the discontinuity detection methodology has been outlined and the next section discusses the application of the method to an artificial data set. The application of the H-DIC method to a real data set is detailed in the next chapter

5.3.6 Discontinuity detection on an artificial image set

An image set of speckles is artificially deformed such that the deformed image manifests a discontinuous displacement representing a physical slip band. Figure 5-12 shows the deformed image with the respective displacements performed. No displacement gradients are subject to the image such that a DIC routine will only detect rigid body translation. The purpose of this artificial image set is to demonstrate the effectiveness of the H-DIC routine and the ability to capture discontinuous motion within a planar field. The parameters used for this analysis is a subset width of 32 pixels and a 90% overlap. A single “pass” is made on the image set without the correction routine as the images are not subject to complex motion.

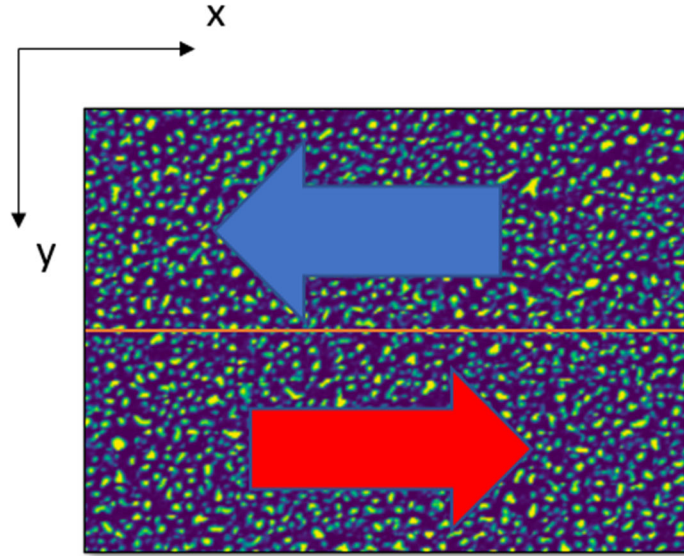


Figure 5-12 – A kinematic shift applied artificially to an image set such that the top half shifts to the right and the bottom half shifts to the left.

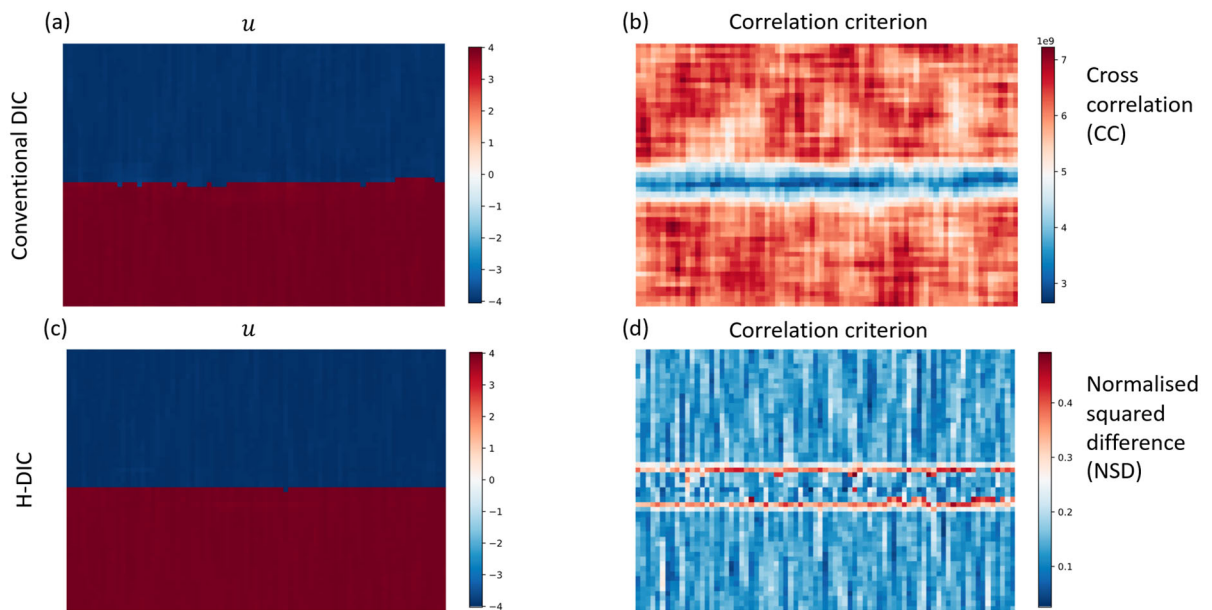


Figure 5-13 – The horizontal displacements and corresponding correlation coefficients for the conventional (a,b) and H-DIC (c,d) respectively for the artificial kinematic shifts shown in Figure 5-12

The displacement and correlation maps are shown for the conventional DIC and H-DIC in Figure 5-13 for the same subset size and overlap. Horizontal displacement, u , can be seen (a,c)

for the conventional DIC and H-DIC methods. The primary difference of conventional and H-DIC displacement maps can be seen in the reduction of complexions at the line of discontinuity. This can be explained by the improvement in correlation provided by the Heaviside treatment (b,d) where the H-DIC method is able to improve the correlation near the discontinuity due to the accurate detection of discontinuity and corrects the displacement of the central side.

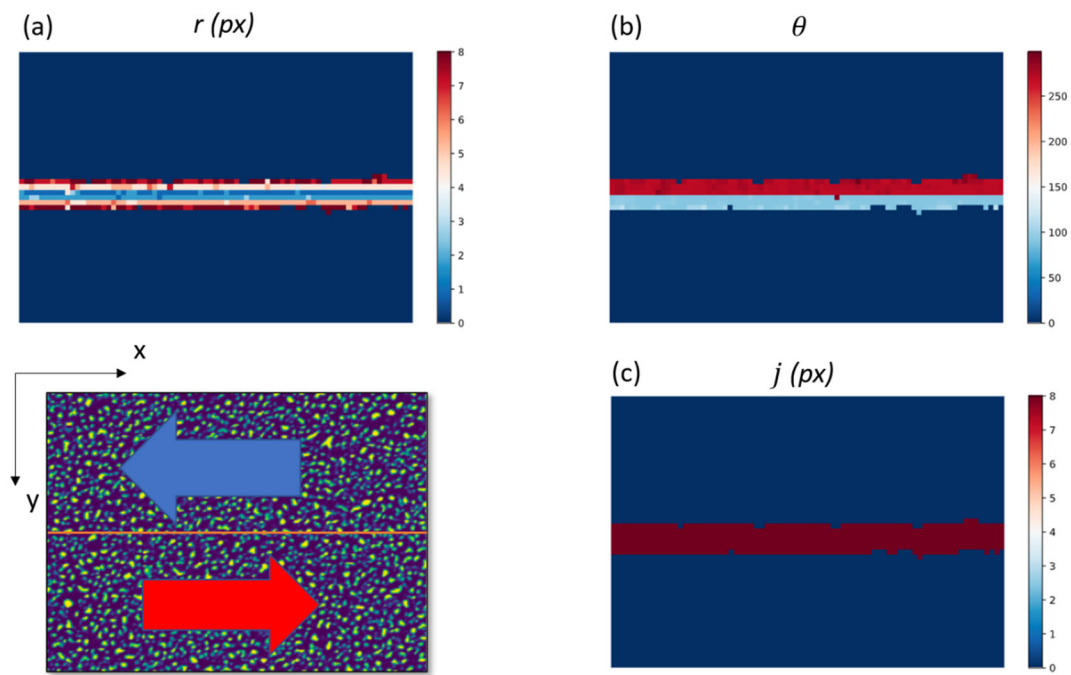


Figure 5-14 – The maps of outputs of the H-DIC method. Discontinuity location parameters r (a) and θ (b) with a discontinuity jump magnitude (c)

The H-DIC method outputs the r, θ values per subset as the kinematic jump j . Figure 5-14 shows the output value for the artificial image set described above (see Figure 5-12). The exact location of the discontinuity can be detected (a,b) and the corresponding jump value in pixels (c) can be seen to be uniform across the discontinuity.

The quality of the analysis provided by the H-DIC method is dependent on the size of the subset used. In conventional DIC a small subset size limits the signal size available for cross correlation, in H-DIC this dependency is compounded due to the splitting of the subset. In a

24-pixel subset, a discontinuity split will limit the pixels containing speckles which may then interfere and prevent useful correlation to occur. The subset splitting method does, however, allow for larger subsets to be used without significantly affecting the resolution of strain maps as each subset is treated. This has been referred to in literature as an improvement to the signal-to-noise ratio [168].

An advantage of the H-DIC method described above is its ease of implementation and computational efficiency. Each subset is treated independently, and therefore can be parallelised across CPU “workers”. However, this advantage comes at a cost to the robustness of the displacement mapping. As each reference subset is limited to only correlate with its corresponding deformed subset, large local displacements are not captured. This is particularly a problem for discontinuities as the external side (see Figure 5-9) will lose correlation if the speckles displace beyond the subset boundaries. In addition, as the first order deformation gradients are inferred from neighbourhoods of displacements rather than directly from the subset, the correlation quality may be poor. To improve the quality of correlation, the deformation gradients should be found directly within the image subsets as is done in other works [168] and the field of search for the correlation should be expanded such that the match to the deformed subset may be found over a larger field in the reference image. These improvements will significantly improve the correlation and would allow for the tracking of discontinuities over a large distance (e.g. large crack openings).

5.4 Summary

In this chapter, the methodology and validation of the three-point bend experiment with integrated heating and the Heaviside digital image correlation have been discussed. Development of the three-point bend experiment with heating have shown the capability of providing isothermal heating conditions to the experimental specimen. The method of tracking

discontinuous displacements within the digital image correlation has been expanded upon and the advantages and limitations have been outlined. In addition, suggestions for future work have been highlighted in the discussion of the validation wherein an emphasis is placed upon the addition of more displacement gradient terms obtained directly from subset rather than from a neighbourhood of displacements to improve the correlation quality.

These methods are used in the next chapter which investigates the fatigue crack initiation near a non-metallic inclusion agglomerate in an RR1000 specimen under elevated temperature and low cycle fatigue loading conditions.

6 Twin boundary fatigue crack nucleation in a polycrystalline Nickel superalloy containing non-metallic inclusions

6.1 Introduction

Polycrystalline Ni-based superalloys are used in turbine discs in the turbine section of conventional gas turbines. While widely considered as high-performance materials with excellent strength, fatigue crack growth resistance and excellent creep properties, there are a number of microstructural features which can promote fatigue crack nucleation during operation [1].

Annealing twin boundaries nucleate during high temperature forming processes and often present themselves as thin lamellae in a parent grain. The twinning of a grain adds a low energy $\Sigma 3$ boundary which can act as a barrier to dislocation motion and therefore strengthen the plastic response [190]. However, twin boundaries have been reported to concentrate local plastic strain [140,161] which has been linked to fatigue crack nucleation [85].

While known as fatigue crack nucleation sites, the mechanistic drivers for twin boundary crack nucleation are not fully understood. Heinz and Neumann observed twin boundary cracking for a host of orientations in austenitic steel samples and argued that the elastic anisotropy of the FCC lattice configuration and the local crystallography are the root causes of twin boundary fatigue crack nucleation [138]. In an FCC crystal lattice, the twin boundary lies on a $[1\ 1\ 1]$ plane and therefore permits slip to run parallel to the twin plane. Stinville *et al.* [140] distinguished between parallel slip and transmitted slip adjacent to and across twin boundaries and found parallel slip to exhibit the largest strain concentration in their samples. In another study, they created bounded criteria for fatigue crack nucleation near boundaries based on Schmid factor, elastic mismatch (between twin and parent) and the twin boundary length [141].

A favourably orientated large twin-containing grain will allow unimpeded dislocation motion parallel to the twin boundary. Large accumulation of dislocations in the form of slip bands and large stresses resulting from the twin boundary modulus mismatch create the necessary driving forces for fatigue crack nucleation. On the other hand, Zhang *et al.* [191] reported that twin boundaries containing γ'' precipitates were responsible for early plasticity and resulted in fatigue crack nucleation after cyclic loading. Their study sees complexions on the twin boundary which increases premature plasticity near the twin due to the differing elastic properties of the γ'' precipitates. This study was performed on Inconel 945X, an alloy designed to resist stress-corrosion cracking. Their observations may therefore be distinct and not representative of the general superalloy population.

Fatigue crack nucleation in Ni based superalloys also manifests at non-metallic inclusions. Non-metallic inclusions are an unavoidable defect of powder metallurgy. To achieve a homogenous grain structure in near-net shape components, manufacturers use powder metallurgy. Erosion products in the melt persist through screening processes and arrive in the final microstructure [10].

Inclusions are generally known to be deleterious to fatigue life where larger inclusions are inversely proportional to fatigue life [66,70]. Recent studies have suggested that there may be competition between fatigue crack nucleation at inclusions and twin boundaries [90,92]. Texier *et al.*[90] reported on the competition between non-metallic inclusions and twin boundaries in several variants of Inconel 718. They found a transition going from cracking at inclusions to twin boundaries existed and correlated with the density of $\Sigma 3$ twins in the microstructure. Stinville *et al.*[85] found that the competition is strongly dependent on the applied stress where fatigue cracking at inclusions is a low-cycle phenomenon while cracking at twin boundaries is dominant at high cycle fatigue. However, in some alloys, non-metallic inclusions seem to be the limiting microstructural feature for fatigue life. Zhang *et al.*[87]found that inclusion

fracture and decohesion within the first cycle of loading led to fatigue crack nucleation at high applied stresses. It is likely that the competition between these features is strongly influenced by the size, mechanical properties and distribution of inclusions in addition to the length and orientation of twins. In a crystal plasticity framework, Yeratapally *et al.*[147] predicted cracking at twin boundary to experience high amounts of normal stress (relative to the loading direction).

High spatial resolution DIC (HR-DIC) has recently become a popular tool for analysing heterogeneous strain fields and their role in fatigue crack nucleation [162,174,192]. The scanning electron microscope (SEM) is commonly used to capture small scale speckle patterns in ex-situ and in some cases, in-situ. New problems arise when considering displacement fields at this length scale. The largest issue is the introduction of new artefacts from the electron imaging [162,193]. At smaller length scales, slip banding also becomes prevalent. The DIC method typically assumes a continuous displacement field; however, slip bands are discrete kinematic discontinuities. Bourdin *et al.*[168] observed local kinematic discontinuities in the form of slip bands by modifying the second order displacement calculation with a method they term Heaviside-DIC. The method, developed by Valle *et al.*[166], splits a subset to obtain two sets of displacements for both sides of a discontinuity. This enables identification of slip banding without *a priori* knowledge of the discontinuity. Stinville *et al.*[169] used this method to identify regions of irreversible slip. In this study, similar method is introduced to identify regions of discontinuous displacement such as slip bands, fatigue crack nucleation and inclusion decohesion and fracture.

Discrete dislocation plasticity (DDP) is a numerical framework that explicitly models the activities of individual dislocations along defined slip planes. A conventional, isotropic DDP method has been widely applied to understand deformation at the dislocation level under various loading conditions, including tension [194], micro-pillar compression [195], bending

[196], indentation [197] and sliding [198]. The discrete nature of the DDP modelling method uncovers the highly localized, individual slip bands [199] opposed to an averaged behaviour of activated slip systems that are commonly predicted by using crystal plasticity (e.g. [200]). Although conventional isotropic DDP simulations were used to simulate the interactions between γ and γ' phases in Nickel superalloys [201] and [202], it still remains challenging to incorporate the strong elastic anisotropy of Nickel superalloys into the DDP framework when the detailed deformation near the twin boundary is required at the slip band scale. In this work, an elastically anisotropic DDP model is introduced that considers the elementary microstructure of a twin-parent grain combination as a multi-phase sample, and the elastic anisotropy is introduced by applying the O'day superimposition methodology [203].

The primary purpose of this chapter is to present a combined experimental and modelling investigation of fatigue crack nucleation at non-metallic inclusions and twin boundaries at elevated temperature, resembling operational gas turbine conditions. While the experiment was designed to nucleate fatigue cracks at inclusions, cyclic loading also produced fatigue cracks at a favourably orientated twin boundary. This has enabled us to address the competition between inclusions and twin boundary fatigue crack nucleation and discuss mechanistic drivers for fatigue crack nucleation at the twin boundary.

6.2 Methods

6.2.1 Material

The material investigated in this study is a polycrystalline nickel superalloy produced via the powder metallurgy processing route. The material was supplied by Rolls-Royce plc and has the name designation RR1000. Agglomerated non-metallic inclusions were detected on the sample surface. The inclusions cause an anomalous grain structure to persist in the immediate vicinity of the agglomerate. This unique grain structure, shown in Figure 6-1, consists of large,

coarse grains with a high density of $\Sigma 3$ twin boundaries. The acquisition of EBSD maps is detailed in a later section. The large grains are surrounded by the conventional equiaxed fine grain structure with an average grain size of 5 μm . The Ni matrix between inclusions within the agglomerate comprises extremely fine grains. The nature of the origin of coarser grains is hitherto unknown and is not addressed in this study.

The material was cut and machined to a three-point bend beam with dimensions 2 x 3 x 12 mm. The inclusion is deliberately located in the tensile fibre of the front surface shown in Figure 6-2 (a). Prior to mechanical testing, the sample was subjected to a fine grinding procedure with a 0.25 μm diamond suspension and then subject to polishing with a 0.1 μm alumina suspension. Due to the fine nature of the agglomerate, no coarse grinding was performed. An ion etch was performed in a PECS Gatan II to achieve high quality electron backscatter patterns (EBSPs) for EBSD.

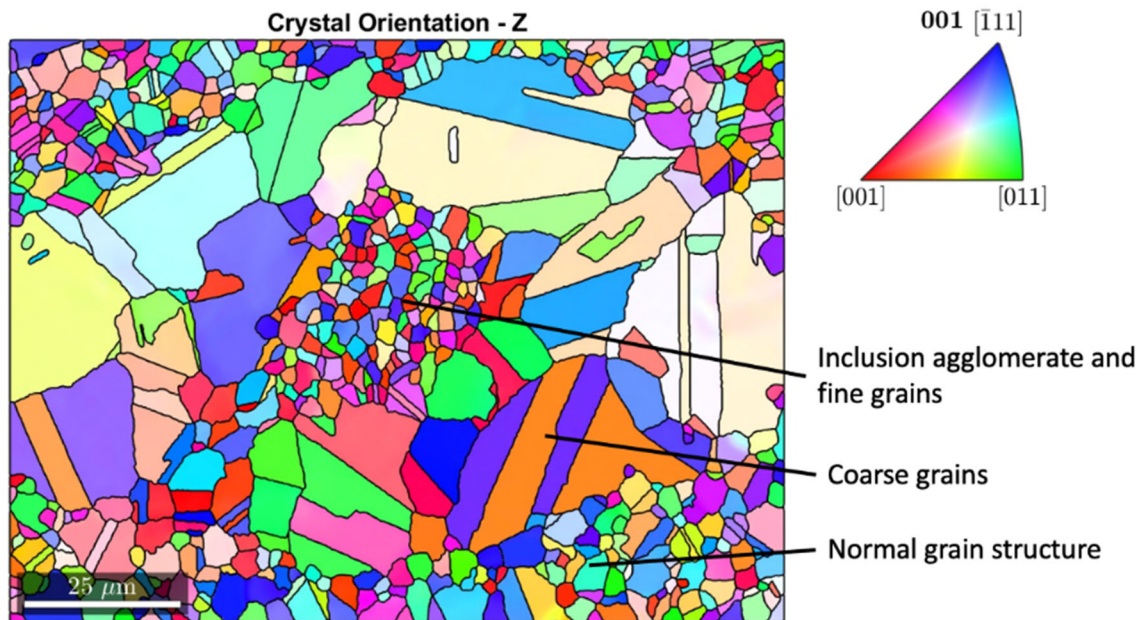


Figure 6-1 – IPF-Z map of the agglomerate region prior to testing. The EBSD map has been processed to remove extremely small grains and inclusions are omitted.

6.2.2 Mechanical testing

The specimen was subject to low cycle fatigue loading in isothermal conditions at 300°C. Images were captured ex-situ in a scanning electron microscope (SEM) Zeiss Auriga at intervals of 1, 2, 20, 100, 1000, 2000, 3000, 4000, 5000 and finally 6000 cycles. The mechanical test was performed in a Shimadzu 10kN tensile tester rigged to handle push-push three-point bending. A load-controlled regime was applied where the peak load during cycles 1 to 4000 was kept at 1800 N, 1900 N for 4000 to 5000 and 2100 N for 5000 to 6000. The stress increase was given to provide sufficient local stresses for fatigue crack nucleation at the region of interest. A schematic of the loading regime is shown in Figure 6-2 (b). A Von Mises plasticity model (Figure 6-2 (c)) of the beam predicted the peak tensile stress in the agglomerate region to be 1200 MPa during an applied load of 1800 N. The peak tensile stress at the region of interest is equivalent to 125% of the yield stress of pristine fine-grained RR1000.

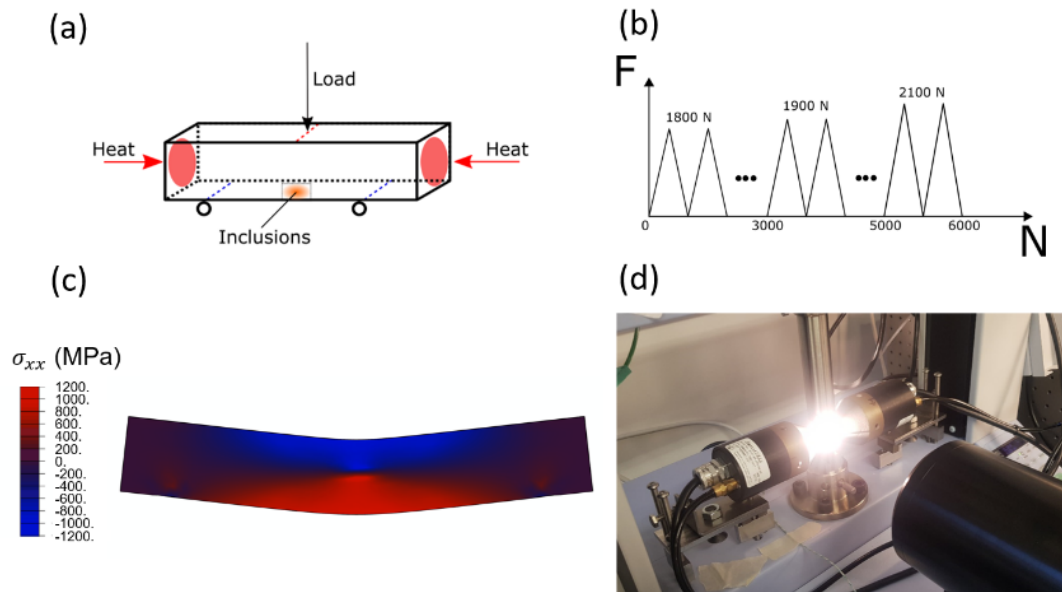


Figure 6-2 – (a) The three point bend specimen showing loading constraints and applied heat, (b) the applied loading history, (c) field plot of σ_{xx} at applied load of 1800 N, (d) An image of the experimental set-up with infrared heaters active.

6.2.3 Discontinuity tolerant DIC

To obtain high spatial resolution in DIC, a discontinuity tolerance capability and a rigid body correction algorithm were implemented in an existing DIC algorithm. The code follows that of Jiang *et al.*[180]. This DIC algorithm utilises the conventional fast subset cross-correlation methodology but has additional functionality in the form of discrete discontinuity detection. Such algorithms have been recently demonstrated to provide valuable insight into slip band formation [168].

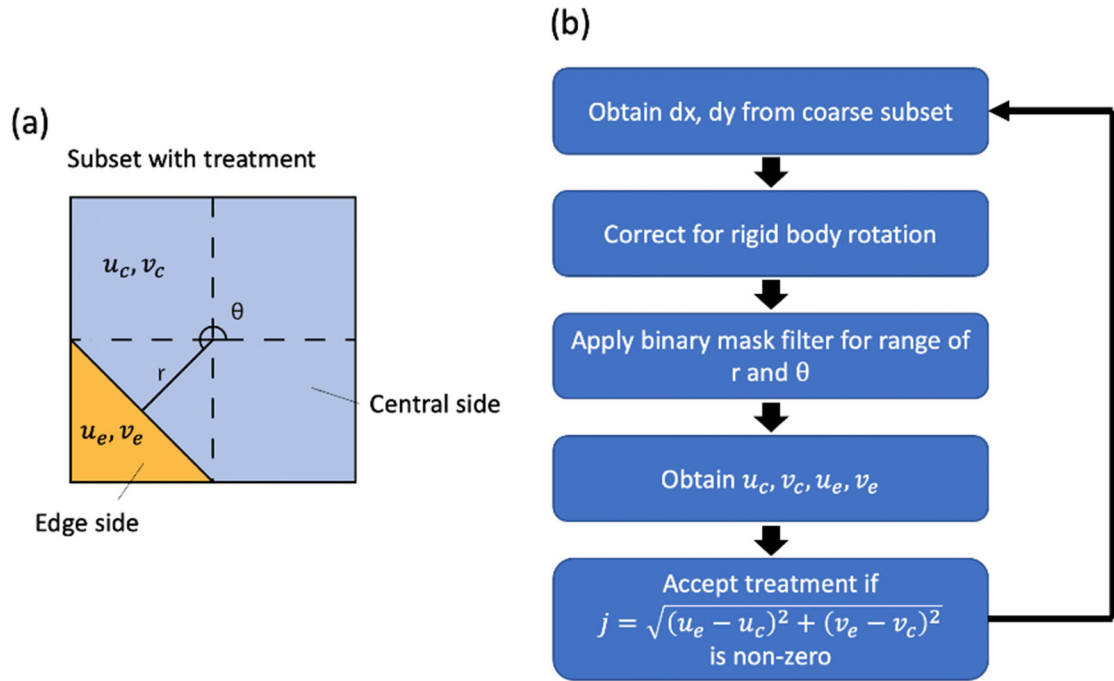


Figure 6-3 – (a) A schematic showing implementation of the logical masking routine for subsets, (b) the process flow for the discontinuity tolerant DIC method

To correct for rigid body translation and rotation, a coarse-fine subset correlation method is used. A coarse pass is applied to obtain first order displacement over the region of interest. A least-squares minimisation is performed on a polynomial surface over dx and dy . The surface is then used to remap coordinates in the deformed map using bicubic interpolation.

A slip band, or a crack, is a local kinematic discontinuity. A subset containing a discontinuity will face poor correlation coefficients as pixel information is lost through local rigid body translation and rotation. In extreme cases, it becomes necessary to correlate small amounts of information. In addition, normalisation of the correlation product is required to achieve comparative correlation coefficients. A two-dimensional discrete normalised square-difference is employed to tackle these issues.

The algorithm implemented in this study applies a logical mask to subset arrays to handle local discontinuities (see Figure 6-3 (a)). During the first pass, an arbitrary line is placed across the subsets, dividing it into two sides (central and edge). The sides are cross correlated with the respective sides on the undeformed subset. A suitable match is found when the sum of cross correlation for both sides is minimised. The correlation product function dependent on r and θ is ill-behaved, non-convex and noisy, rendering conventional minimisation routines ineffective. Instead, a brute force method is employed to determine the global minimum. Every subset is treated, increasing computational cost significantly but allowing for detection of discontinuities throughout the displacement field without prior knowledge of their location. In the case of multiple discontinuities within a subset, the algorithm identifies the discontinuity closest to the subset centre. Once displacements have been obtained for both sides, the central side displacement is assumed to be the subset displacement and the edge side displacement is used to calculate the discontinuity displacement magnitude. The magnitude, j , is the norm of the respective displacements ($j = \sqrt{u^2 + v^2}$, $u = dx_c - dx_e$, $v = dy_c - dy_e$).

This implementation is written in Python and makes use of several common packages such as OpenCV, joblib, numpy etc. It is parallelised over CPU cores and can be scaled-up to run on high-performance clusters. A process flow chart can be seen in Figure 6-3 (b).

6.2.4 Speckle patterning

In this work, a fine speckle pattern of gold particles with an average size of 60 nm is used. The speckle pattern was produced by water-vapour assisted gold remodelling which has been reported by several researchers [204,205]. The gold pattern is stable at elevated temperature and provides excellent background contrast in the backscatter detector. Removal of gold speckles to allow for EBSD measurements was accomplished by gentle oxide suspension polishing.

6.2.5 DIC image capture

Backscatter micrographs are captured in a grid containing 6x7 images with an overlap of 20% at 10 keV accelerating voltage. They are later stitched together in a commercial software package. To align and correct for perspective changes, a python script using OpenCV packages is used. A subset size of 32 px is used for determination of the strain field maps. The subset size and inclusion agglomerate stitched image are shown in Figure 6-4.

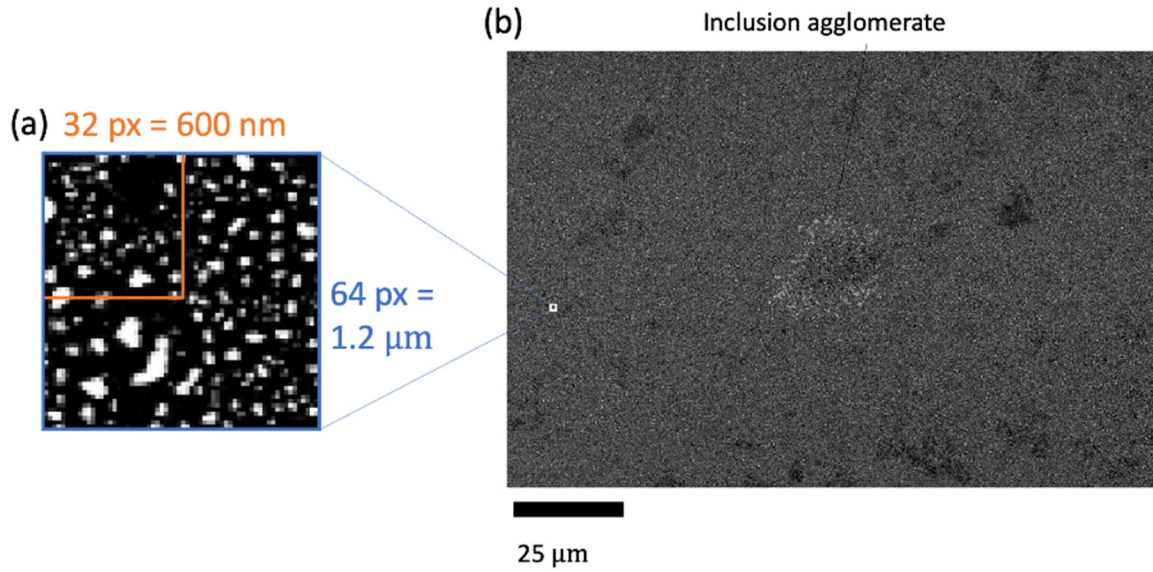


Figure 6-4 – (a) Subset size, (b) a 6x7 stitch of BSE micrographs of inclusion agglomerate and coarse grain region

6.2.6 HR-EBSD

To investigate the sample crystallography, a high-angular resolution electron backscatter diffraction mapping was performed using a Zeiss Sigma SEM equipped with an Oxford instruments EBSD Nanodetector. A region of interest was designated around the inclusion agglomerate, encompassing the coarse-grains as well as some of the conventional finer grains. An accelerating voltage of 20 keV with an aperture of 240 μm was used at a working distance of 20 mm. The sample was pre-tilted at 20 degrees with respect to the electron beam. The SEM parameters were chosen to provide clear and high-quality patterns necessary for HR-EBSD analysis.

Two maps were obtained in this study, pre- and post-deformation. The pre-deformation scan used a map size of 123 x 92 μm with a step size of 180 nm over the entire agglomerate and coarse-grained region. A relatively fine step size is required to obtain high quality information on lattice curvature. Patterns were obtained with a resolution of 600 x 600 with a 2 x 2 binning.

A post-mortem scan was performed on an area of interest within the coarse-grained region. This map used a map size of 82 x 61 μm with the same parameters outlined above.

HR-EBSD analysis in this study used two methods, Correlation based and Hough-based. The correlation based method follows that of Wilkinson *et al.* [206,207] and is described in detail elsewhere. In short, the correlation-based methodology calculates shifts in local EBSD measurements using two-dimensional cross correlation products. These shifts are interpreted as measured local lattice rotations. Residual elastic strain gradients are then obtained from the measured lattice rotation. The rotation gradients allow for determination of six lattice curvature components. The curvature components can then be used to estimate GND densities. The Hough-based method is used to provide qualitative indications of geometrically necessary dislocation densities neglecting elastic stresses [208]. This has been chosen to substitute correlation-based methods where pattern qualities were insufficient to provide detailed analysis.

6.2.7 Crystal plasticity finite element model

To provide accurate boundary conditions for a discrete dislocation plasticity model, two finite element models were constructed: an engineering-scale model of the beam, and a grain-scale model of the coarse-grains containing twin boundaries. As the experiment was load-controlled, so were the models.

The beam model was subject to loads imposed during the experiment to obtain stresses in the tensile fibre where the agglomerate region is located. Five loading cycles were modelled with Von Mises plasticity. While Von Mises is not able to capture cyclic effects such as kinematic back-stresses, it can be used to accurately estimate the peak stresses experienced. It is also noted that the reverse stress is not known and needs to be obtained manually, by carefully

comparing model strains to experimental strains from DIC. This method has been used successfully in the past and is described in detail elsewhere [51].

A faithfully representative finite element sub-model was also constructed with knowledge of grain boundaries and crystallographies obtained from EBSD. This sub-model considers a twin boundary in the coarse grain region which is used later for DDP. The grain structure is processed in MTEX in order to remove small grains and smooth coarse grain boundaries. The sub-model is subject to load-controlled fatigue with boundary conditions obtained from the beam model. The geometry and boundary conditions are summarised in Figure 6-5. This model is subject to the crystal plasticity detailed in 3.2.1.

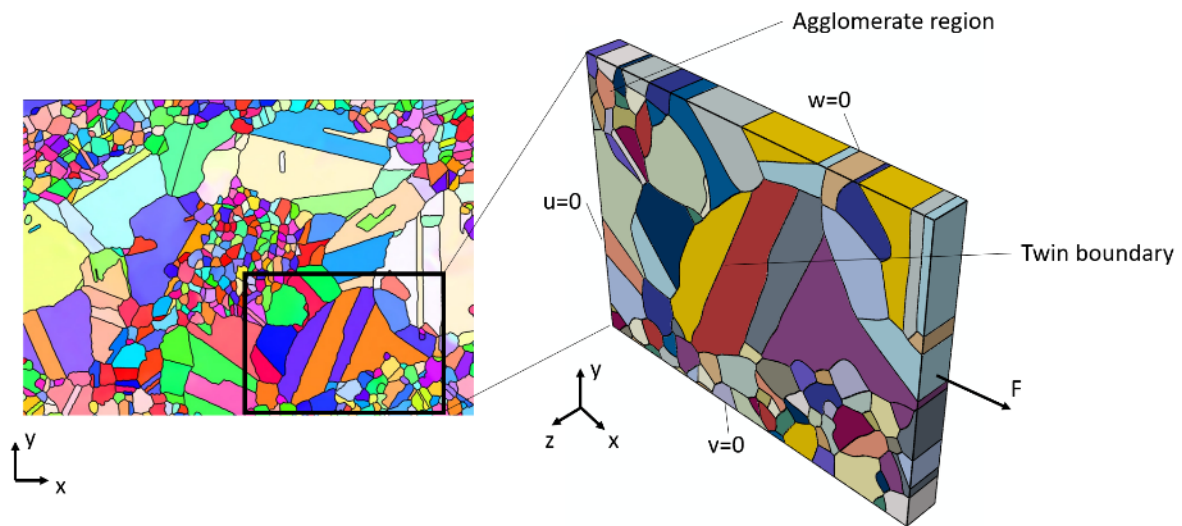


Figure 6-5 – The CPFE model geometry showing uniaxial force controlled boundary conditions

6.2.8 Discrete dislocation plasticity formulations

A two-dimensional discrete dislocation plasticity model was created using an existing framework [209] to investigate the micromechanical behaviour in vicinity of the a region of interest. The region of interest is comprised of the twin lamella and parent grains shown centrally in Figure 6-5 and is a faithful representation of their respective geometries. Elastic

anisotropy was incorporated into the DDP framework through the O'Day superimposition [203]. Although the model is restricted to two dimensions, it nevertheless facilitates insights into the mechanistic detail of localised deformation at the scale of slip banding which CPFE cannot capture explicitly near the twin boundary. The DDP modelling was performed kindly by Dr Yilun Xu.

The plane strain constraint is achieved by confining the FCC slip activation to three $\langle 111 \rangle$ slip systems (originally introduced by Rice [210]), which are inclined 60° with respect to each other. The orientation relationship between a parent and twin grain are shown in Figure 6-6 (a). The 2D configuration of three slip systems wherein dislocation sources, obstacles and dislocations are populated, is shown in Figure 6-6 (b). The spacing between each set of parallel slip planes is taken to be $100b$.

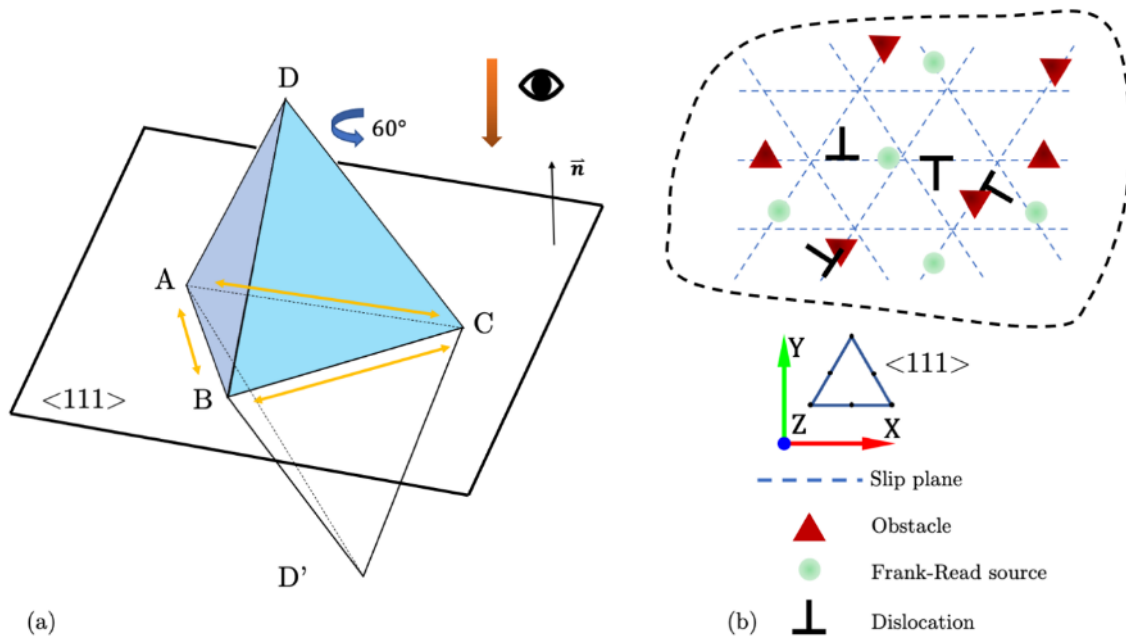


Figure 6-6 - (a) the slip systems and orientation relationship between a pair of parent and twin grain in RR1000. (b) the slip system configuration along the $\langle 111 \rangle$ plane of a RR1000 grain.

The plastic flow in the model results from collective dislocation glide. The collective glide is determined by a set of constitutive equations which have been described thoroughly in literature (e.g. [196,211,212]). The material properties for RR1000 within the DDP framework have been calibrated against tensile test data [213], these are seen within Table 6-1.

Table 6-1 – DDP material properties for RR1000

$E_T(\text{GPa})$	$E_P(\text{GPa})$	ν	$B(\text{Pa} \cdot \text{s})$	$\lambda(\mu\text{m}^{-2})$
210	190	0.31	5×10^{-4}	0.05
$b(\text{nm})$	$\rho_{nuc}(\mu\text{m}^{-2})$	$\tau_{nuc}(\text{MPa})$	$\rho_{obs}(\mu\text{m}^{-2})$	$\tau_{nuc}(\text{MPa})$
0.351	60	600	360	1800

Due to the high computational demand of the DDP framework, a region of interest within the polycrystalline sample is chosen in order to minimize the computational demand while retaining a large enough area to reflect the twin boundary features. The region can be seen in Figure 6-7 (a) and contains a three-grain DDP sub-model which represents the parent and twin grains configuration. The dimensions of the region are 20 x 5 μm . The morphology and crystallographic orientation of the grains is obtained from EBSD and DIC observations of the sample surface (see Figure 6-1 and Figure 6-8). The boundary conditions imposed on the DDP sub-model are obtained from the CPFE model described in the previous section such that a multi-scale modelling strategy is performed at the slip plane and crystal scale [214]. The macroscopic stress response of the DDP sub-model is shown in Figure 6-7 (b) under a monotonic displacement-controlled loading. The potentially activated slip systems (indicated by the blue dashed lines for the parent grain and yellow dashed lines for the twin grain) are illustrated in the sub-figure for reference.

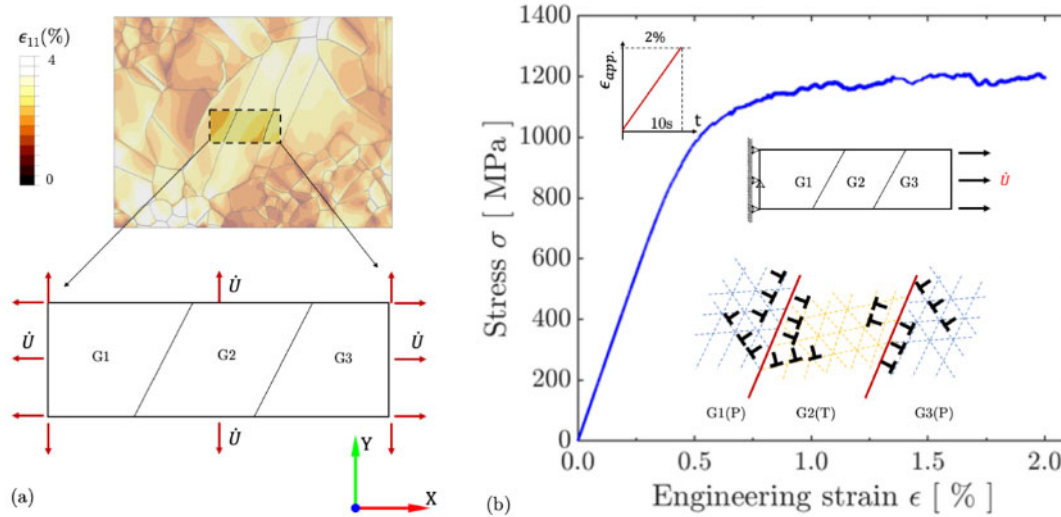


Figure 6-7 - (a) the region of interest (ROI) modelled using DDP and the applied boundary conditions. (b) the stress strain response curve of the ROI when a monotonic strain-controlled loading applies.

6.3 Strain localisation

Three-point bend testing under load-controlled fatigue was performed on the beam sample with ex-situ capture of speckle fields in an SEM with a quadrupole backscatter detector set for chemical contrast. The BSE micrographs were used as images for DIC and processed to create strain fields. Highly localised strain occurred heterogeneously throughout the microstructure within the first cycle of loading. Figure 6-8 shows ϵ_{xx} strain distributions after one cycle of loading. Highly localised strain develops in the form of slip bands originating within the coarse grains surrounding the agglomerate region. Strain is also visible in the form of gradient fields which is due to microslip not directly observable by the current DIC configuration. The two forms of strain are termed as slip banding and microslip in the following paragraphs.

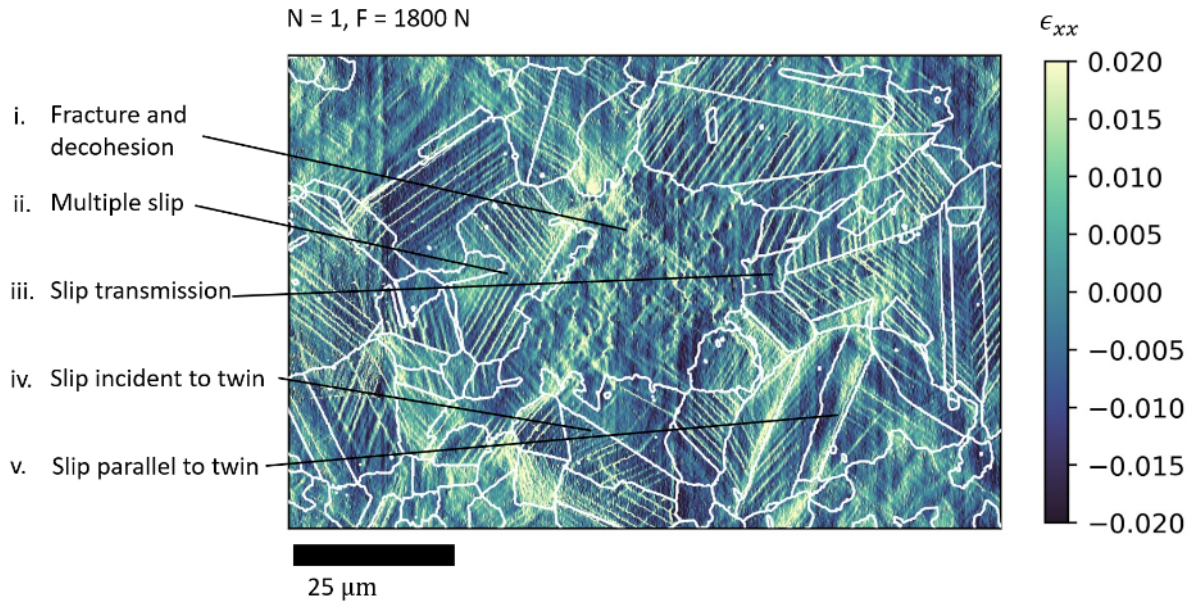


Figure 6-8 – Map of ϵ_{xx} after one cycle of loading. Large coarse grains are indicated by white GBs. Smaller grain boundaries are omitted. The inclusion agglomerate located in the centre sees high strains arising from inclusion fracture and decohesion.

A variety of slip banding phenomena can be seen in the coarse grains in the strain map of Figure 6-8. Multiple slip banding can be observed in a large grain (labelled ii.). Multiple slip activation appears to occur in the grain due to its unique morphology and adjacency to the agglomerate field which likely creates a complex stress state acting on the grain. This behaviour is exhibited in several large grains. Slip transmission can also be seen taking place over several grains (labelled iii.). Slip transmission occurs across active slip systems well orientated for transmission across grain boundaries.

The microstructure of the sample includes several twin boundaries. The twin boundaries see several slip band behaviours. Slip behaviour near the twin boundary can be categorised into slip transmission and parallel slip (labelled iv. and v.). Parallel slip is discussed thoroughly in the next section.

The fine grains dispersed between the inclusion agglomerate see little to no slip banding using the DIC method. Instead, strain is localised in small regions resembling packets of highly

localised strain and microslip. The packets of highly localised strain are associated with initiation events manifested as inclusion decohesion and fracture. A BSE micrograph with quadrupole polarity set to topographical view is shown in Figure 6-9 with pull-outs showing both inclusion fracture and decohesion. Importantly, fracture and decohesion occur uniformly across the agglomerate regardless of inclusion chemistry. Furthermore, several inclusions observe mixed-mode initiation exhibiting both fracture and decohesion. Fracture and decohesion effectively nucleate voids which kinematically shift the speckle pattern locally within the agglomerate. In effect, the high measured ‘strains’ are not straining but rigid body translation. This kinematic shift may also shift neighbouring subsets and local disturbances can be seen in the strain maps.

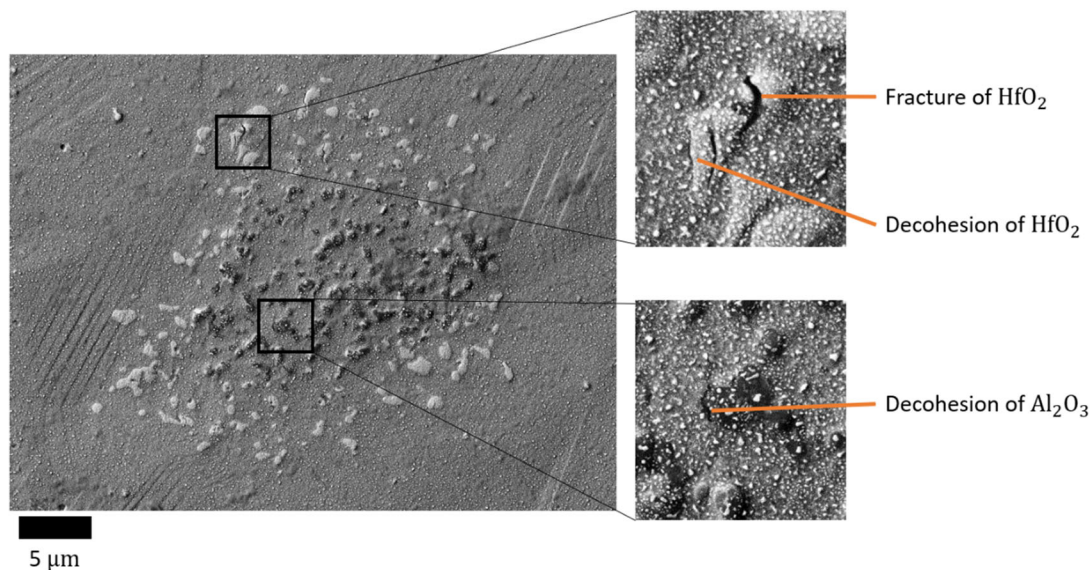


Figure 6-9 – BSE micrograph of agglomerate region after one cycle of loading. The backscatter quadrupole has switched polarity to allow for topographic detail. Pull-outs of inclusion initiation phenomena are shown. Gold speckle particles can be seen throughout the sample surface. They appear as white dots in the image.

Fatigue damage phenomena (i.e., fracture and decohesion) were observed even after the first cycle of loading. Early damage has been observed in several other studies [82,144]. Inclusion

decohesion and particle fracture occurred on (or within) the majority of non-metallic inclusions. Decohesion of the metal/oxide interface has been found to be stress-threshold dependent [51] where a normal stress component (acting normal to the metal/oxide interface) is the primary mechanism at the continuum scale. Particle fracture has been analysed in a separate study and was found to be unambiguously related to the internal maximum principal stress acting within the inclusion [144]. As both phenomena are typically observed within the first few cycles of loading and crystal plasticity models suggest local ratcheting is negligible [144], it is argued that these mechanisms are stress threshold dependent. High stresses in the initial cycle are likely to cause inclusion decohesion and fracture, evidently also in this study.

Zhang *et al.*[51] performed a three point bend experiment on the same material system with an inclusion agglomerate and found that decohesion of the HfO_2 inclusions is likely to occur when the normal stress lies between 1270 – 1480 MPa, however, observations of high residual stresses proceeding shot peening suggested that the strength was higher. A follow up study utilised cohesive zone models to find the true interfacial strength to be around 2000 MPa [144]. The experiment performed by Zhang *et al.* took place at room temperature and at a lower stress level than the experiment performed in this study. This suggests that the interfacial strength of the inclusions is temperature dependent, but this requires confirmation.

The experiment presents two sets of inclusions with different mechanical properties which may modify the stress field given that the central Al_2O_3 inclusions are stiffer than the matrix and particularly if they are stiffer than HfO_2 . Owing much to their size, exact characterisation of the Al_2O_3 phase is challenging and requires further investigation. In addition, the agglomerate field is larger in the current experiment compared with that of Zhang *et al.* A larger inclusion field may drive up stress gradients due to the stiffer elastic modulus of the particles compared with matrix. As the decohesion and fracture phenomena are stress threshold dependent, an elevated stress field will cause more fracture and decohesion events. The morphology of the

agglomerate field (from a planar perspective) must also be considered. In the current study, the agglomerate is spread in a circular pattern whereas in the work of Zhang *et al*, the agglomerate is lenticular with the short axis orientated parallel to the loading direction. The geometrical reality of the agglomerate field may change the stress distribution within – particularly for the uniaxial loading case. Inclusions orientated in “parallel” versus “series” configuration may play a large role in the distribution of stress and cascade failure events.

6.4 Cyclic strain behaviour

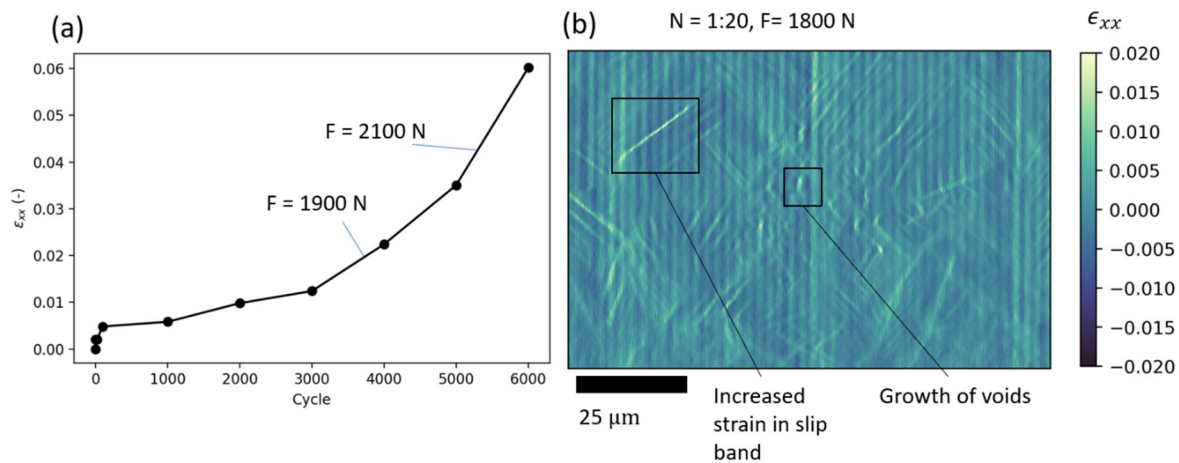


Figure 6-10 – (a) the strain accumulation across the entire DIC region measuring the strain relative to the reference image and (b) a sequential ϵ_{xx} map showing the strain between cycle 2 to 20

The beam sample recorded a moderate level of plasticity after the first cycle of loading but subsequent cyclic loading provided ϵ_{xx} strains largely below the noise threshold of the DIC algorithm. Figure 6-10 (a) and (b) show the ϵ_{xx} plastic strain accumulation over cyclic loading and the sequential ϵ_{xx} map between the 2nd and 20th cycle respectively. The strain accumulation is calculated from with respect to the reference image, showing the approximate strain level at every cycle interval relative to the undeformed configuration. Vertical bands can be seen in the strain map which are artefacts introduced by the SEM. Sutton et al.[215] has suggested

sinusoidal artefacts are introduced through the SEM instrument. Strain is found to be localised to two features here: discrete slip bands and growth of voids introduced by decohesion and particle fracture after continued cyclic loading.

The load applied to the sample was increased incrementally after 4000 cycles to produce crystallographic cracks within the agglomerate. Between cycles 4000 to 5000, the effective plastic strain accumulation can be seen to increase. Between cycles 5000 to 6000 the effective plastic strain rises dramatically. This rise can be attributed to the increase of load to 2100N but the nucleation of several fatigue cracks is likely to provide a bias to the mean strain data. This bias is arguably negligible due to the relatively small area the cracks govern compared with the total size of the DIC map.

6.5 Fatigue crack nucleation at non-metallic inclusions

After 3000 cycles of loading, two distinct fatigue cracks nucleated in the inclusion agglomerate region. These fatigue cracks are unique as they originate from different sources: decohered particles leading to void coalescence and fractured particles leading to crystallographic fatigue crack nucleation. Examples are shown in Figure 6-11 where (a) shows a crystallographic fatigue crack emanating from a fractured particle and (b) shows a fatigue crack formed from several decohered inclusions. These early microcracks develop after 3000 cycles of loading.

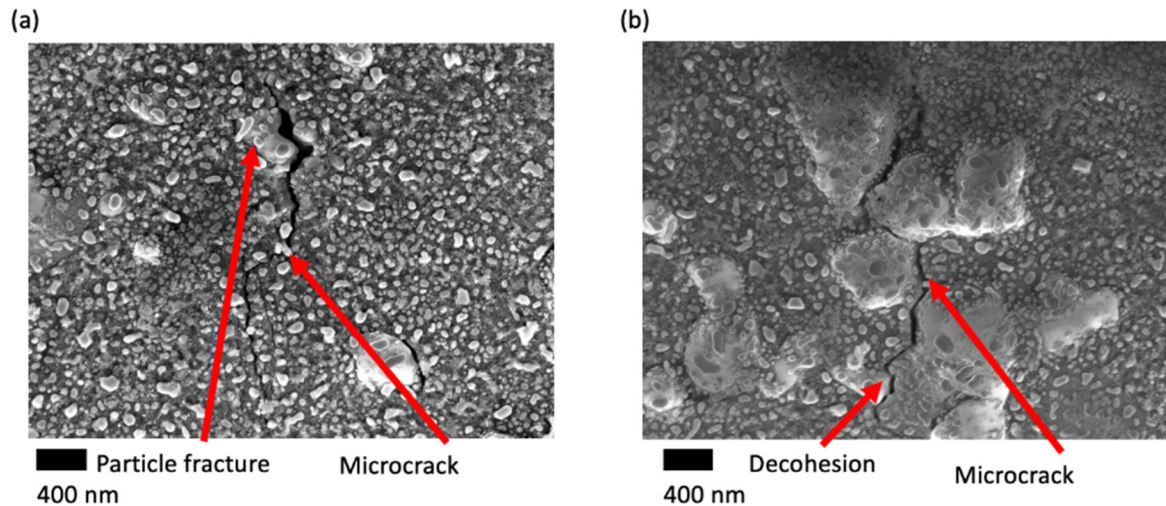


Figure 6-11 – Nucleation of two types of fatigue crack from inclusions after 3000 cycles of loading. (a) A fatigue crack emanating from a cracked inclusion developing a crystallographic crack. (b) Coalescence of decohesion leading to a microcrack. Small white particles are Au speckles.

These two types of fatigue crack nucleation from non-metallic inclusions are characteristically different because of the way they interact with the metal matrix. A fatigue crack emanating from the fractured particle grows directly in the matrix along crystallographic slip lines and is dominated by the local crystallography, grain boundaries and non-metallic inclusions. A fatigue crack nucleating near several decohered particles consists of the coalescence of decohered voids. In this particular example (showed in 9 (b)) several inclusions are clustered in a tight configuration. This tight configuration and the prevalence of decohesion likely promotes elevated plasticity and stored energy density within the matrix which drives the coalescence.

After 6000 cycles, the microcracks grow to form fatigue cracks which span across the width of the agglomerate region. A micrograph and ϵ_{xx} strain map of the agglomerate region after 6000 cycles is shown in Figure 6-12. The micrograph shows several smaller cracks dispersed throughout the agglomerate. The corresponding ϵ_{xx} DIC map of the agglomerate region shows bands of high strain spread through the height of the agglomerate region. These bands are the cracks stretching through the agglomerate region. In the unloaded condition, local sections of

the fatigue cracks close and thus are not immediately obvious in Figure 6-12 (a). There are therefore several fatigue cracks present in the agglomerate, these are annotated in Figure 6-12 (b).

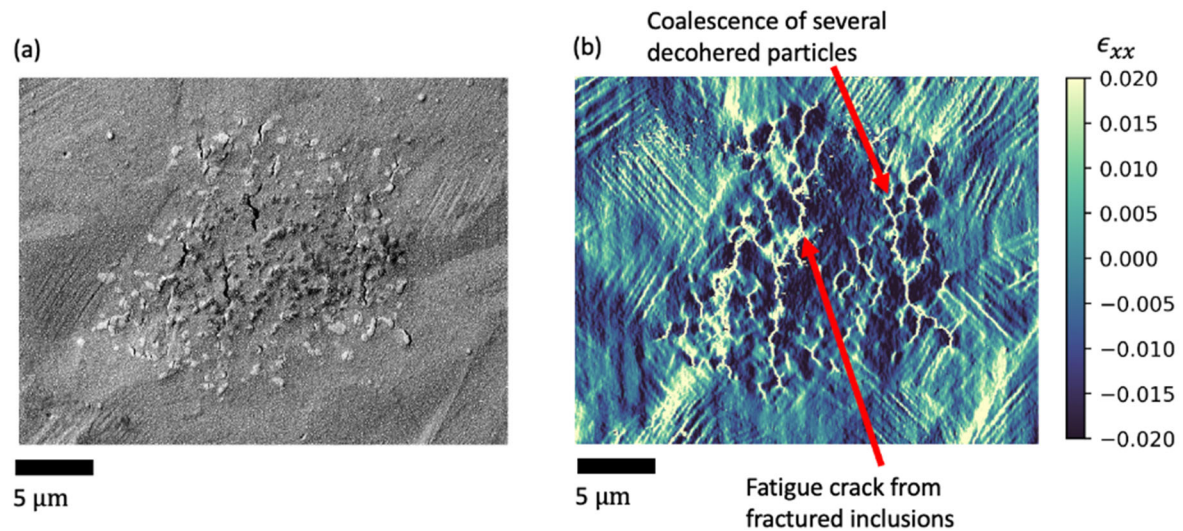


Figure 6-12 – Growth of microcracks to form cracks over the whole agglomerate region (a) A backscatter micrograph of the agglomerate region showing fatigue cracks. (b) ϵ_{xx} strain map of agglomerate region between cycles 5000 to 6000 showing fatigue cracks in the form of high strain slivers.

The discontinuity tolerance algorithm shows regions of connected coalescence from decohered particles in Figure 6-13. The algorithm is also able to determine locations of decohesion and particle fracture shown by red arrows. While the algorithm can detect slip bands and inclusion decohesion and fracture it also detects noise in the DIC imaging. Significant regions of excessive displacement can be seen. These are regions where excessive rigid body displacement has shifted subsets beyond subset unicity.

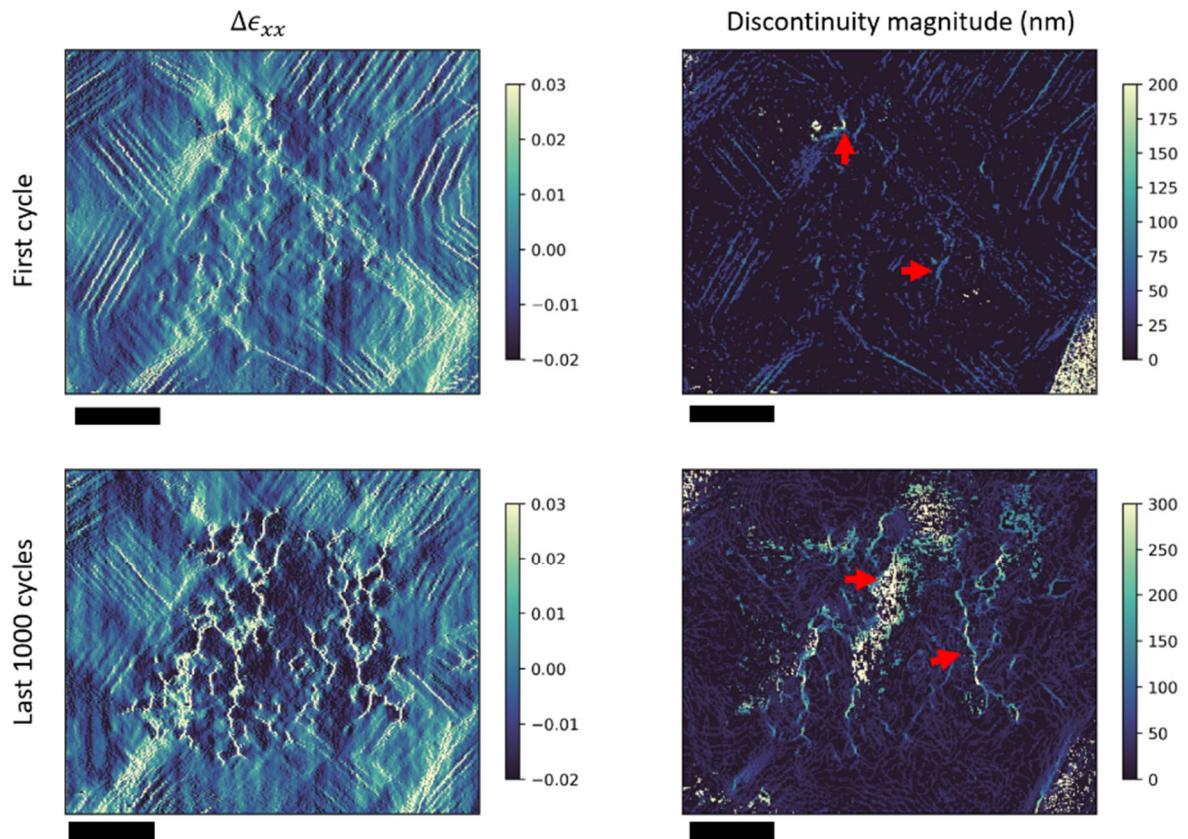


Figure 6-13 – Sequential ϵ_{xx} strain maps of the inclusion agglomerate region with discontinuity magnitude maps for the first and the last image intervals. Red arrows show initiation and fatigue crack nucleation events. Grain boundaries are omitted here due to their size and complex morphology. Scale bars are 10 μm .

6.6 Fatigue crack nucleation at a twin boundary

After 6000 cycles of loading, a fatigue crack was found to nucleate at a twin boundary situated in a large coarse grain below and removed from the agglomerate region. The fatigue crack and ϵ_{xy} strain map local to the twin are shown in Figure 6-14. Significant multiple slip is present within the parent grain in which the fatigue crack nucleated. Slip bands developed parallel and immediately adjacent to the twin boundary while incident slip bands exist removed from the twin boundary but colliding with the parallel slip bands.

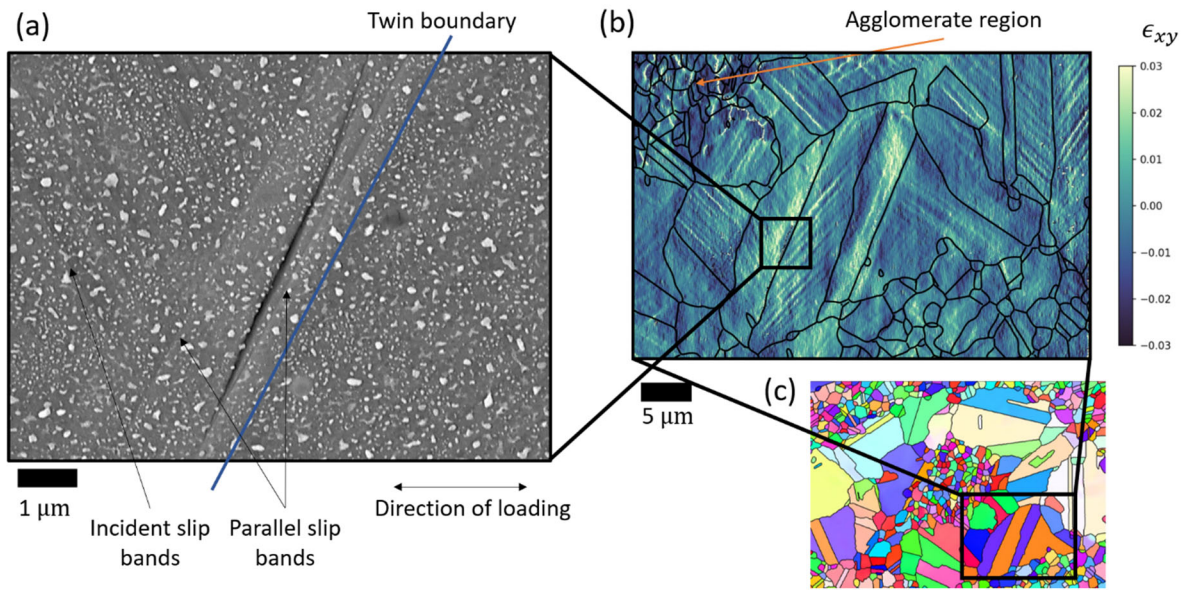


Figure 6-14 – (a) An SEM image of the twin boundary crack with annotations indicating slip banding and the twin boundary, (b) A ϵ_{xy} strain map of the region containing the twin boundary crack and (c) a pull out showing the location within the coarse grained region

The slip characteristics develop within the first cycle of loading and further cyclic loading does not introduce further clearly observable slip bands (Figure 6-14). Microslip of course continues to develop in heterogeneous fields. Figure 6-15 shows the ϵ_{xx} strain and the discontinuity jump magnitude j for cumulative slip bands of the first cycle and 5000th to 6000th cycle. Within the first cycle, high strain bands and microplasticity can be observed in both the parent and twin grain, extreme discontinuity presence can be observed parallel to two twin boundaries (of which the left parallel slip band develops a crack). During the last 1000 cycles, tensile slip band development can be observed, and significant tensile strain can be observed in the parent grain. Importantly, the slip detected on the twin boundary of interest in the first cycle contains the largest slip band magnitude over the entire DIC map. During the final strain interval, a fatigue crack has nucleated which has introduced rigid body translation and rotation to the speckle field. The fatigue crack can be seen in the discontinuity field map where a local region has registered a high discontinuity magnitude.

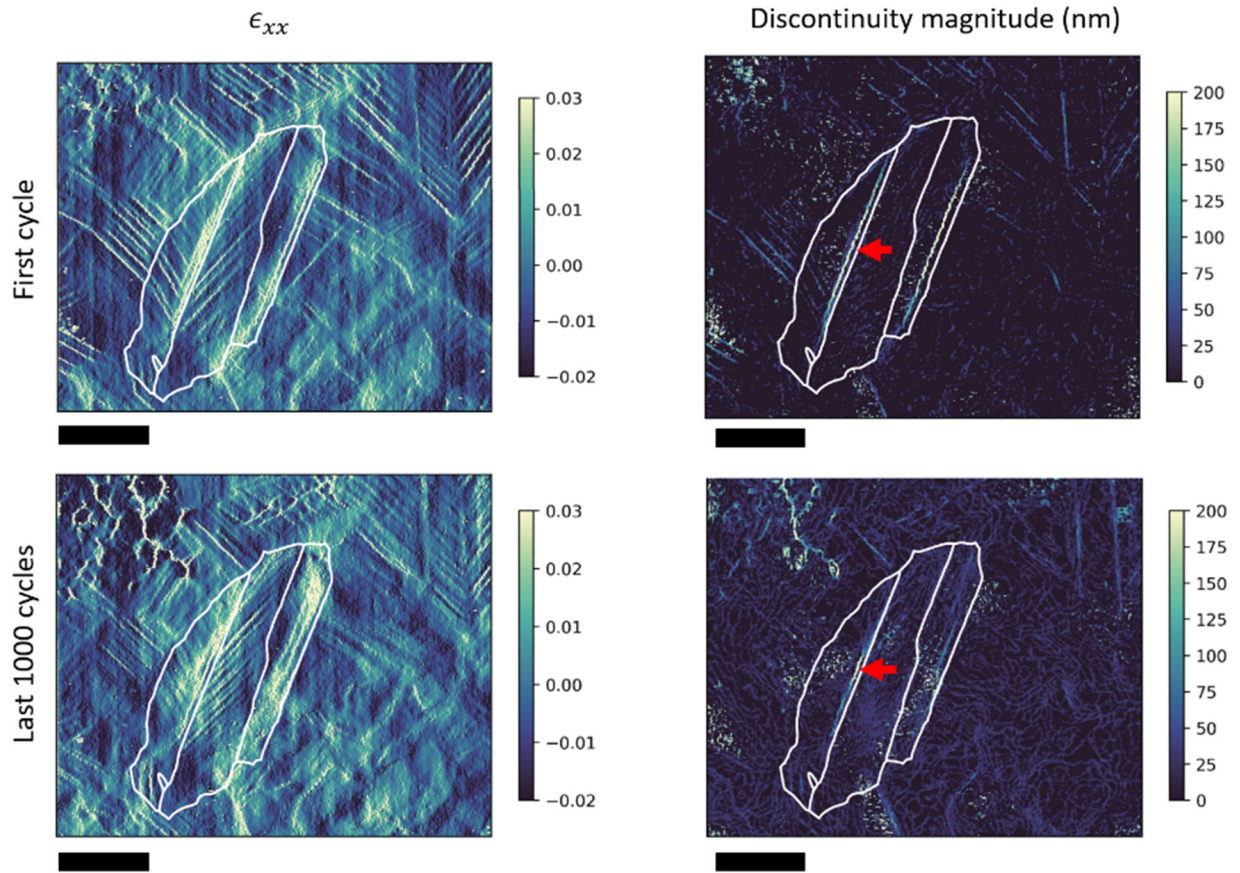


Figure 6-15 – Strain and discontinuity maps after the first cycle and for the last 1000 cycles in which a twin boundary crack nucleates. The red arrow indicates peak discontinuity within map and fatigue crack nucleation. Scale bars are 10 μm

The twin and parent grains accrue significant slip during the experiment. Studies in other Ni-based superalloys have also shown that strain localisation occurs preferentially adjacent to and parallel to twin boundaries leading to fatigue crack nucleation [140,161]. Figure 6-16 shows the slip traces of active slip bands in the parent and twin grains. Schmid factor calculations with respect to the loading axis show erroneous predictions. This is likely due to the complex stress state experienced by the two grains which lie close to the agglomerate.

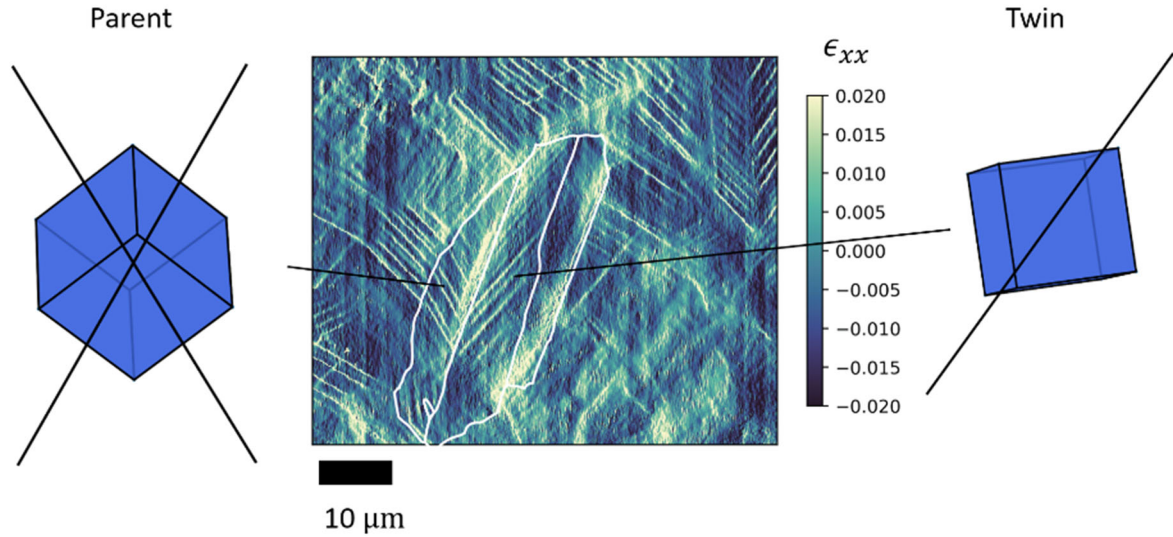


Figure 6-16 – Slip traces and cube orientations for the Parent and twin grain after the first cycle of loading

6.7 Intragranular rotation, GNDs, and residual elastic stress

Prior to loading, an EBSD scan was performed to evaluate the initial local GND densities, residual elastic strains and stresses. Elevated geometrically necessary dislocations in the parent and twin grains may indicate that early localisation was promoted during the first cycle of loading. Figure 6-17 shows the logarithmic density of GNDs in the region of interest prior to mechanical loading. GND densities are distributed grainwise. The twin and parent grains both record similarly low GND densities (around 10^{13}m^{-2}). The surrounding small grains show relatively large densities. A large grain next to the inclusion agglomerate shows elevated GND densities of $\sim 10^{14}\text{m}^{-2}$.

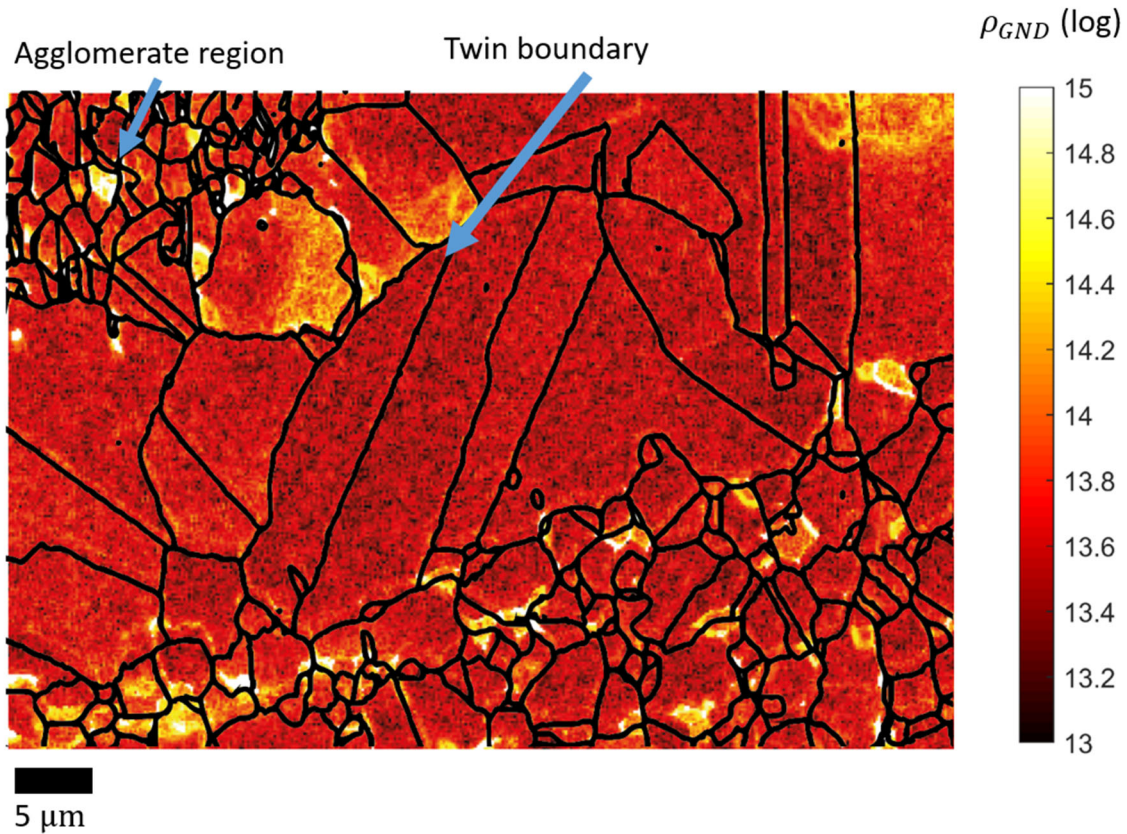


Figure 6-17 – The HR-EBSD GND density field map of the twin region prior to loading

Figure 6-18 shows the measured residual stresses in the twin region prior to loading obtained from correlation based HR-EBSD. Uniform stress fields are recorded within the parent and twin grains although large tensile stresses can be seen in surrounding smaller grains above and below the twin boundary. This may indicate that the twin and parent grains are surrounded by harder (by virtue of residual stresses) grains which may promote some slip activity within the parent and twin after loading.

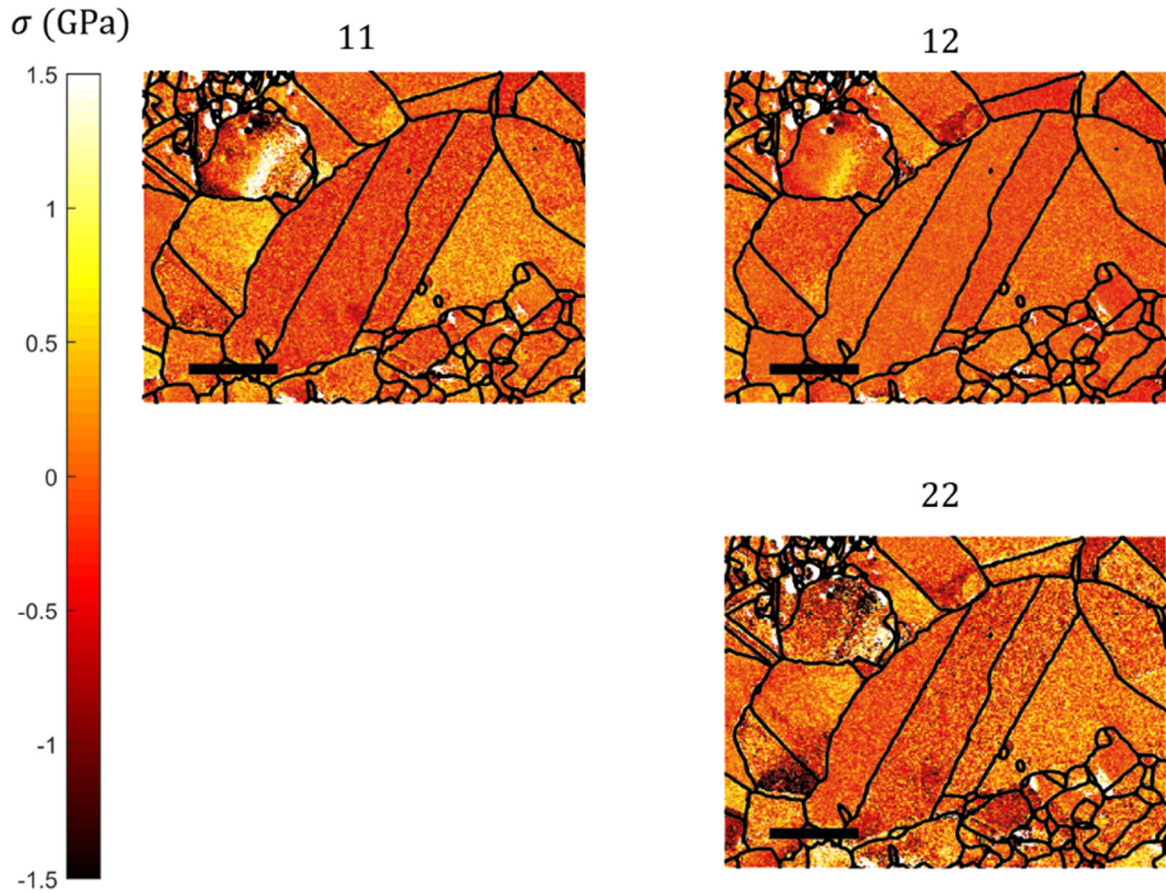


Figure 6-18 – Residual stresses near the twin boundary crack region pre-loading. Scale bar shown in black is 10 μm

While slip in both parent and twin see mirrored slip patterns about the twin boundary (see Figure 6-16), the parent sees a parallel slip band formation where a fatigue crack nucleates between two parallel slip bands. The fatigue crack (see Figure 6-14 (a)) at first appears to diverge from one of the parallel slip bands and then rotates. This non-linear crack path may be a function of the intragranular rotation which occurs due to the complex loading experienced in the grain. Figure 6-19 shows a comparison of kernel average orientation and GND densities obtained by Hough based methods for the pre-test and post-mortem states. While a post-mortem correlation-based HR-EBSD analysis of the region is of interest, excessive rotation of the free surface in the out-of-plane direction and poor pattern quality prevented accurate determination of crystal rotation. Instead, Hough methods are utilised to estimate crystal

rotations and GND densities. It is therefore important to note that GND maps are indicative of rotation distributions in the post-mortem specimen and not quantitative for thorough analysis.

Strong intragranular rotation can be seen in the twin and parent grains with gradients peaking at the twin boundary. For the post-mortem maps, the fatigue crack may contribute significantly to local apparent rotations.

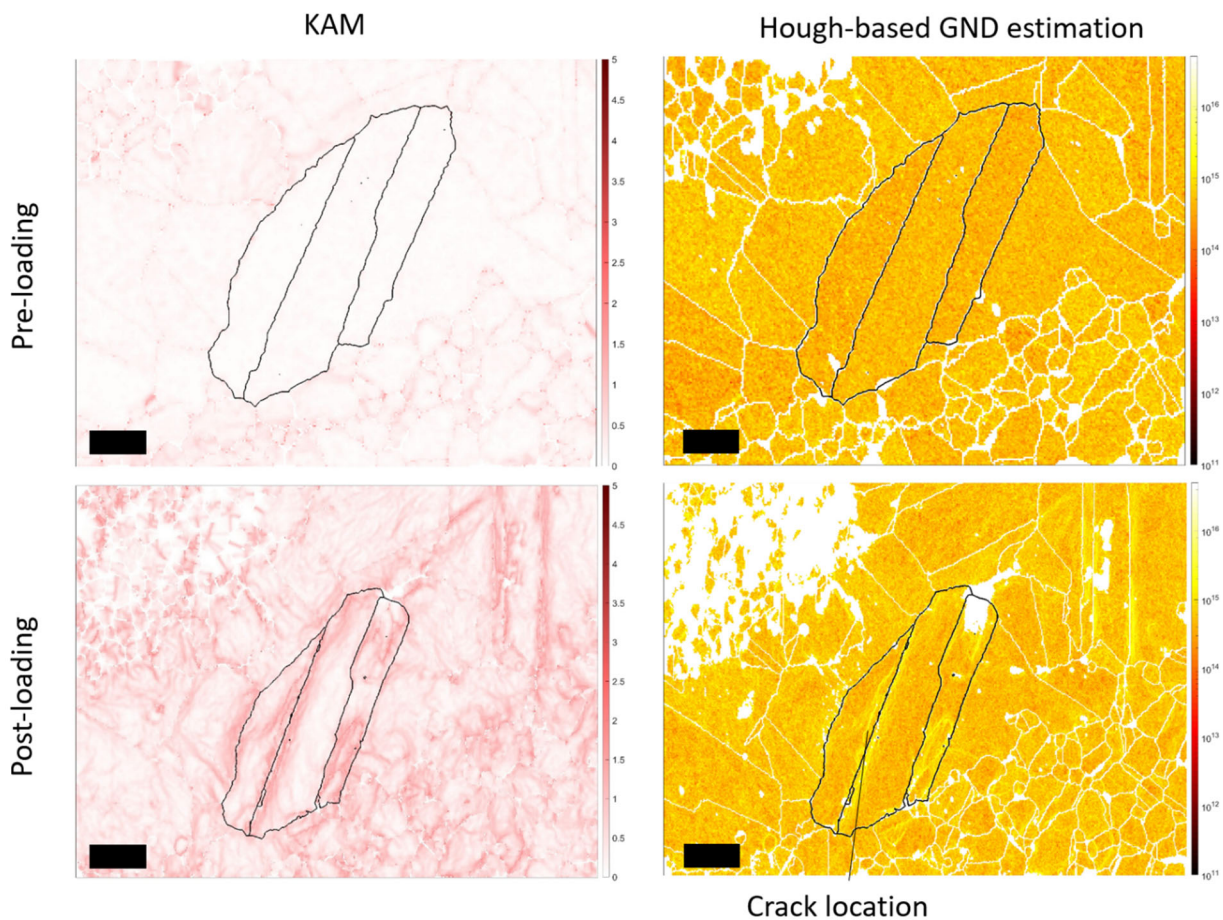


Figure 6-19 – Kernel average misorientation and Hough-based GND estimations for the twin region pre-loading (prior to test) and post-loading (after 6000 cycles)

6.8 DDP modelling of twin boundary

DDP modelling results shown below were collected by Dr Yilun Xu as a part of the investigation into the nature of stored energy accumulation at the twin boundary.

Results obtained from the DDP sub-model of the parent and twin grains (shown in Figure 6-7) are considered next. The predicted major-axial stress σ_{xx} and effective strain ϵ_{eff} field plots are shown in Figure 6-20 (a) and (b), respectively. The results were obtained from the peak load of the 1st cycle. Strong localisation and high heterogeneity of both variables are predicted by the DDP sub-model, and the deformation tends to develop more significantly near the twin boundaries. Symmetric slip patterns are observed around the twin boundary from the inclined slip (with respect to twin boundary) and conforms to observations in DIC observations (see Figure 6-16). Strong accumulation of strain can be seen near the twin boundary which is also consistent with other independent experimental observations [140]. A close-up inspection of strain and dislocation structure near both twin boundaries (shown in Figure 6-20 (c) and (d) respectively) reveals that dislocations along parallel and inclined slip systems both nucleate and pile-up near the twin boundary which results in parallel and inclined slip lines. The GND density distribution determined from the net Burgers vector [212] is shown in Figure 6-20 (e). The GND distribution shows accumulation near the twin boundary indicated by the white arrows), which reflects the strong strain gradient and lattice rotation [129] observed in the EBSD results (see Figure 6-19). The combination of slip localisation and GND concentration (the latter of which has been shown to be correlated to fatigue crack nucleation in RR1000 [213] and [88,158]) near the twin boundary are argued to lead to high local stored energy density and hence to fatigue crack nucleation at this site.

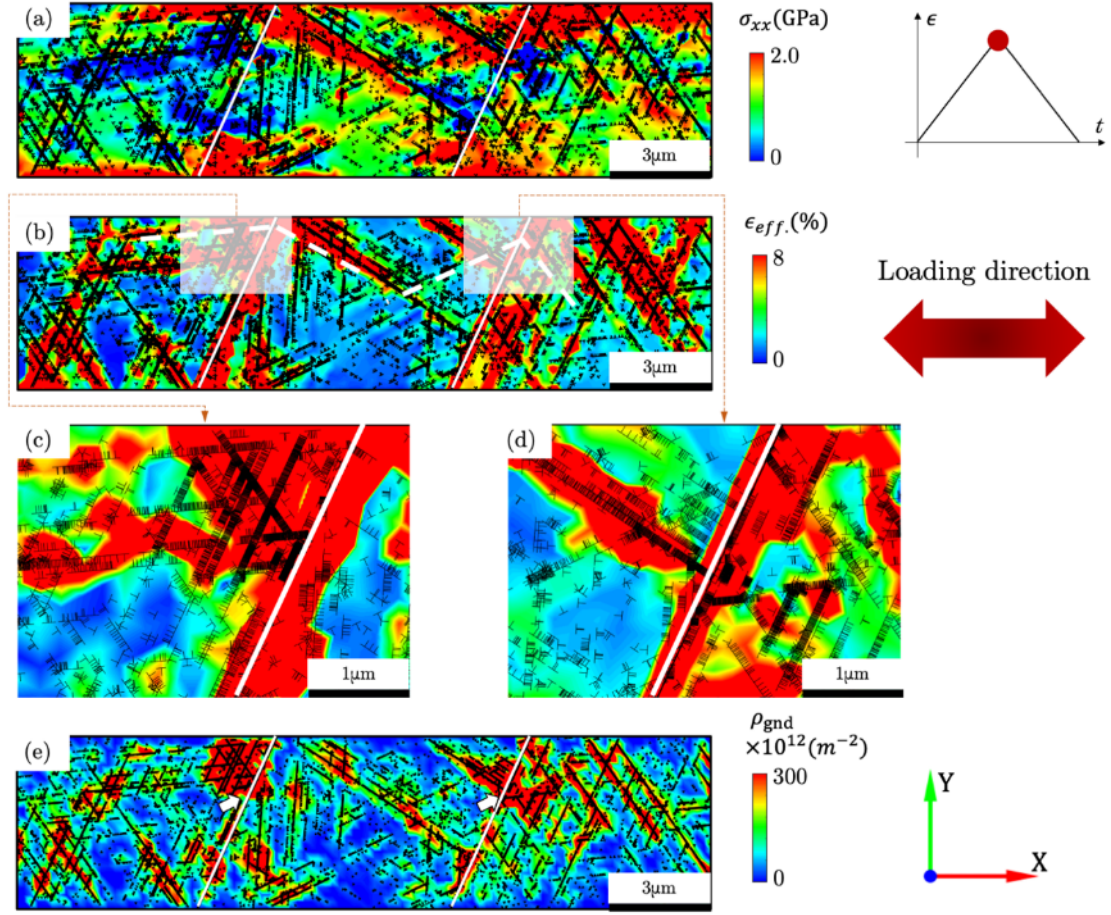


Figure 6-20 - The distribution of the (a) stress, (b-d) effective strain and (e) geometrically necessary dislocation (GND) in the DDP sub-model. The results are obtained at the instant of peak applied loading.

6.8.1 On the effect of elastic anisotropy

Previous research has attributed the susceptibility of fatigue crack nucleation near twin boundary to the elastic anisotropy (e.g. [216] and [141]). An isotropic DDP model was employed using the same constraints and boundary conditions as those used for the elastically anisotropic DDP sub-model described above, but the elastic moduli for parent and twin are kept at 200 GPa. The effective strain distribution of the isotropic DDP model is shown in Figure 6-21 (a). Although the strain pattern shows good consistency with the DIC results (see Figure 6-16) with respect to the inclined slip planes, the isotropic model does not predict slip band localisation near the twin boundary, which has been extensively observed in the DIC results and other independent work. The anisotropic DDP model (Figure 6-21 (b)), in contrast, shows

localisation near twin boundary. In addition, the strain predicted by the anisotropic DDP model shows a more inhomogeneous distribution with hotspots concentrated near the twin boundary as opposed to the interior of grains, which could lead to eventual fatigue crack nucleation. Therefore, this reinforces existing experimental observations that the elastic anisotropy is vital in the localisation of strain near the twin boundary.

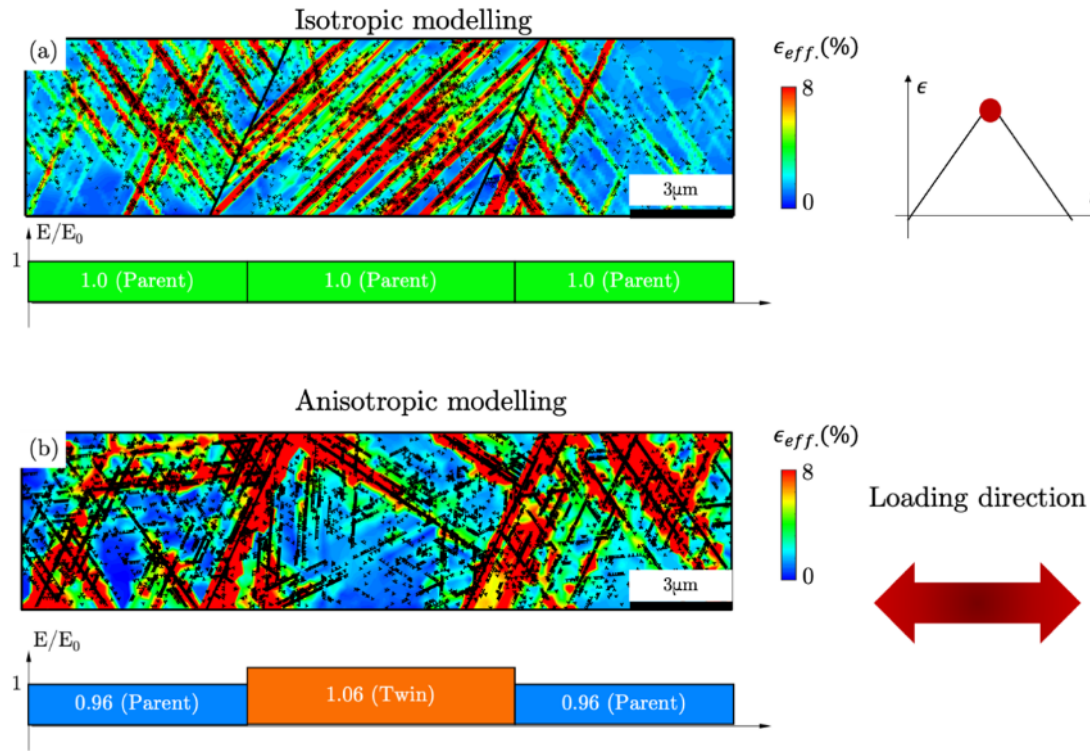


Figure 6-21 - the comparison of effective strain distribution predicted by (a) the isotropic DD modelling and (b) the anisotropic DD modelling.

6.9 Discussion

6.9.1 Competition between inclusion and twin fatigue crack nucleation

Current consensus on the competition between inclusion and twin boundary fatigue crack nucleation agrees that non-metallic inclusions are dominant in fatigue nucleation [92], especially at elevated stresses. In this study, a fatigue crack nucleated at a twin boundary near to the inclusion agglomerate after 6000 cycles of loading. The twin boundary fatigue crack

nucleates in a grain experiencing high levels of strain and parallel slip banding (see Figure 6-15) both symptomatic of twin boundary crack nucleation according to independent studies [141].

The twin boundary fatigue crack nucleates in a grain subject to unique conditions. Favourable orientation with respect to the loading axis promotes high slip, however the grain is also unique compared with the mean sample microstructure. For instance, the twin boundary length is 6x the average grain size in the sample. The adjacency to the agglomerate region is likely to promote the local slip as it does in similar studies (e.g. [87,217]). These factors fulfil the prerequisites for fatigue crack nucleation at the twin boundary.

Inclusion decohesion and particle fracture occur within the first cycle of loading (similar to [87]) and nucleate microstructural fatigue cracks after continued loading. Several studies suggest that particle fracture and decohesion increase the likelihood of fatigue crack nucleation due to the increase in stored energy density accumulation [52,68,144]. Fracture and decohesion are therefore precursors to fatigue crack nucleation and growth.

It is therefore possible to hypothesise that, in the absence of inclusion fracture and decohesion, twin boundary crack nucleation may be promoted. Several conditions must be satisfied for this to occur: (i.) stresses must be low enough to prevent inclusion fracture and decohesion, (ii.) the grain morphology must be favourably oriented with respect to the loading direction, (iii) the twinned grain must be located near the agglomerate to promote stress elevation.

6.10 Summary

A low-cycle fatigue experiment has been performed on an RR1000 beam with an inclusion agglomerate subject to elevated uniform temperature (300° C). Widespread fracture and decohesion of non-metallic inclusions occurred within the first cycle of loading. After

continued cyclic loading, voids from decohesion and fracture grew to form microcracks. Microstructural (crystallographic) fatigue cracks were observed after 6000 cycles.

Despite fatigue crack nucleation within the inclusion agglomerate, a fatigue crack also nucleated adjacent to a twin boundary. The twin boundary was located within a coarse grain near the inclusion with a twin boundary length 6x the average grain diameter. Residual elastic stresses pre-deformation were relatively low in the grain combination suggesting no promotion of early plasticity. Early plasticity during the first cycle is found to be a function of orientation and proximity to the non-metallic inclusion. The twin and parent grains led to high localised slip and intragranular lattice distortion.

A faithfully representative discrete dislocation plasticity model was created to obtain predictions of slip band interactions near the twin boundary. Elevated GND density was predicted to accumulate at a location near the twin boundary. The importance of crystal anisotropy in strain localisation adjacent to twin boundary was contrasted against an isotropic material model.

7 Conclusion and outlook

7.1 Conclusions

In this thesis, the mechanisms that drive fatigue crack nucleation near non-metallic inclusion were explored and investigated. Firstly, the conditions under which decohesion and fracture take place were found in an inclusion agglomerate within RR1000. The use of a cohesive zone methodology showed that the decohesion and inclusion fracture could be controlled by a stress threshold criterion. It was also confirmed that the stresses necessary to drive decohesion and fracture occur early in the cyclic loading. By assuming that the decohesion and fracture strengths were infinite, it was found that the fatigue life was marginally improved compared with models in which decohesion and fracture occur.

The comparative performance of microstructural features in low cycle fatigue was investigated using a synthetic microstructure. Principally, a twin boundary and a non-metallic inclusion were contrasted. It was found that in all cases, the non-metallic inclusion accumulated significantly more stored energy density and thus was most likely to develop fatigue cracks compared with the twin boundary. In addition, the slip localisation and stored energy density in the vicinity of the twin lamellae was characterised. Stored energy density accumulates on the twin boundary due to the highly stresses slip systems immediately parallel and incident to the boundary. The stress-threshold dependency of the decohesion phenomena prompted an investigation into the probability of cyclic decohesion in stress-controlled loading. Several hardening models, both isotropic and kinematic, were introduced to compare the cyclic stress change $d\sigma/dN$ local to the inclusion. Under no hardening model was cyclic decohesion predicted, supporting the argument that decohesion is a deformation event driven by strong monotonic loading specifically for the stress-controlled case. It is however noted that strong

kinematic effects may be exhibited under higher R-ratios [155]. This may imply that under low peak loads, fatigue life is improved by the absence of decohesion of the inclusion.

To improve the spatial resolution of strain maps and detect discontinuous deformation in images, the DIC method was improved upon by integration of a subset splitting methodology. Each subset in a DIC map was treated independently such that discontinuous motion could be detected from partitioning the subset and obtaining zeroth order displacements for each partition. To improve the correlation coefficient, a global correction method was used in which a bivariate polynomial was fit to coarse, rigid body displacements.

Elevated temperature, low cycle fatigue experiments were performed on a three-point bend sample containing a non-metallic inclusion agglomerate. Temperature was incorporated via a set of infrared lamps which were able to maintain a stable temperature with a control system. While the far field stress acting on the agglomerate was lower than that of the previous investigation, widespread decohesion and inclusion fracture were observed within the first cycle of loading. Fatigue cracks began to nucleate near non-metallic inclusions from voids introduced by both decohesion and inclusion fracture. After 6000 cycles, fatigue cracks had grown to the width of the agglomerate field and a fatigue crack was detected near the inclusion agglomerate on a twin boundary. HR-EBSD analysis of the twin region showed significant intragranular rotation in the grain in which the fatigue crack nucleated. A representative discrete dislocation plasticity model showed that elastic anisotropy was required to reproduce strain localisation adjacent to the twin boundary, and that high densities of GND densities and slip concentration near twin boundary could result in elevated stored energy density accumulation on the twin boundary which may then result in fatigue crack nucleation within RR1000.

7.2 Future work

In this thesis, it has been assumed that in the absence of decohesion and inclusion fracture, fatigue cracks could still appear around the inclusion in the form of slip-driven cracks, either in persistent slip bands or at grain boundaries. This prompts the need for an experiment in which the applied stresses are kept low enough to not generate high maximum principal stresses within the inclusions and high normal stresses on the inclusion-matrix interface. After continued cyclic loading and the development of persistent slip bands impinging upon the agglomerate, fatigue cracks should nucleate. As the stresses are lower, the experiment will have to be designed to accommodate for the longer fatigue lives expected. Detailed modelling analysis of the system are required prior to performing the experiment to ensure that these stresses are kept to the minimum.

Further experimental validation is essential to confirm several conclusions within this thesis. The decohesion and fracture strength of inclusions is inferred from a model containing 45 discrete inclusions. This needs to be validated with additional experiments under similar loading conditions. In addition, low load, stress-controlled experiments are required to confirm the nature of cyclic decohesion.

Temperature experiments performed in this work have been kept isothermally at 300°C. Further investigation is required to determine the effect of higher temperatures. This would resolve the temperature dependency of the inclusion decohesion and fracture strengths as well as provide telling information on the plastic deformation of the matrix under higher temperatures for which a transition from octahedral to cuboidal slip is expected. Turbine discs are also routinely subject to complex thermal loading histories which may affect the fatigue lifetimes. Isothermal is, in isolation, a useful first order approximation of the conditions in which the inclusions are subject to when in service. However, with consideration that the

coefficients of thermal expansion are different for inclusion and matrix, and that local plasticity may be expected from a simple monotonic thermal load (e.g. [52,75]); it may be expected that a complex thermal loading history introduce some local plasticity which may affect the stored energy accumulation.

The digital image correlation implementation performs a zeroth-order displacement estimation on both sides a discontinuity such as a slip band. Due to the widespread use of optimisation on higher order displacement functions, it is possible to obtain more displacement gradient terms at the subset level. In the current algorithm, the displacement gradient is calculated based on neighbourhoods of displacements rather than at the subset level.

If optimisation on the second-order displacement function is performed for a subset with a slip band, a full description of the deformation gradient may be possible for both sides. It may therefore be possible to obtain a measure of geometrically necessary dislocations of both sides of a slip band. In the spirit of [218], by use of in-situ capture of the speckle field, the elastic strains may be estimated. Elastic residual strains may of course also be obtained from correlation-based HR-EBSD. With this information in mind, it is possible to estimate the stored energy density for both sides of the slip band. The stored energy accumulation at the slip band could be accurately measured over the loading history of a sample.

References

- [1] R.C. Reed, The Superalloys Fundamentals and Applications, 2006. <https://doi.org/10.1017/CBO9780511541285>.
- [2] M.P. Boyce, Gas Turbine Engineering Handbook, 2006. <https://doi.org/10.1016/B978-0-7506-7846-9.X5000-7>.
- [3] C. Veiga, J.P. Davim, A.J.R. Loureiro, Properties and applications of titanium alloys: A brief review, *Rev. Adv. Mater. Sci.* 32 (2012) 133–148.
- [4] T.M. Pollock, S. Tin, Nickel-Based Superalloys for Advanced Turbine Engines: Chemistry, Microstructure and Properties, *J. Propuls. Power.* 22 (2006) 361–374. <https://doi.org/10.2514/1.18239>.
- [5] C. Ruiz, P.H.B. Boddington, K.C. Chen, An investigation of fatigue and fretting in a dovetail joint, *Exp. Mech.* (1984). <https://doi.org/10.1007/BF02323167>.
- [6] S.P. Zhu, Q. Liu, Q. Lei, Q. Wang, Probabilistic fatigue life prediction and reliability assessment of a high pressure turbine disc considering load variations, *Int. J. Damage Mech.* (2018). <https://doi.org/10.1177/1056789517737132>.
- [7] M.P. Jackson, R.C. Reed, Heat treatment of UDIMET 720Li: The effect of microstructure on properties, *Mater. Sci. Eng. A.* 259 (1999) 85–97. [https://doi.org/10.1016/S0921-5093\(98\)00867-3](https://doi.org/10.1016/S0921-5093(98)00867-3).
- [8] S. Biroasca, G. Liu, R. Ding, J. Jiang, T. Simm, C. Deen, M. Whittaker, The dislocation behaviour and GND development in a nickel based superalloy during creep, *Int. J. Plast.* 118 (2019) 252–268. <https://doi.org/10.1016/j.ijplas.2019.02.015>.
- [9] B.H. Kear, H.G.F. Wilsdorf, Dislocation Configurations in Plastically Deformed Polycrystalline Cu₃Au Alloys, *Trans. Am. Inst. Mining, Metall. Pet. Eng.* (1962).

- [10] P. Kantzos, P. Bonacuse, J. Telesman, T. Gabb, R. Barrie, A. Banik, Effect of powder cleanliness of the fatigue behaviour of powder metallurgy Ni-disk alloy Udimet 720, in: Superalloys, TMS (The Minerals, Metals & Materials Society), 2004.
- [11] P.A. Whitey, Fatigue failure of the De Havilland Comet I, in: Fail. Anal. Case Stud. II, Elsevier, 2001: pp. 185–192. <https://doi.org/10.1016/b978-0-08-043959-4.50018-3>.
- [12] E.J. France, The Alexander L. Kielland Disaster Revisited: A Review by an Experienced Welding Engineer of the Catastrophic North Sea Platform Collapse, J. Fail. Anal. Prev. 19 (2019) 875–881. <https://doi.org/10.1007/s11668-019-00680-4>.
- [13] BEA, Accident to the AIRBUS A380-861, 2017. www.bea.aero (accessed February 28, 2021).
- [14] S. Suresh, Fatigue of Materials, Cambridge University Press, Cambridge, 1998. <https://doi.org/10.1017/CBO9780511806575>.
- [15] W. Schütz, A history of fatigue, Eng. Fract. Mech. 54 (1996) 263–300. [https://doi.org/10.1016/0013-7944\(95\)00178-6](https://doi.org/10.1016/0013-7944(95)00178-6).
- [16] L.F. Coffin, A study of the effects of cyclic thermal stresses on a ductile metal, Trans. Am. Soc. Mech. Eng. (1954).
- [17] S. Manson, Behavior of materials under conditions of thermal stress, 1953. <https://books.google.co.uk/books?hl=en&lr=&id=88pCAQAAIAAJ&oi=fnd&pg=PA16&dq=Behavior+of+materials+under+conditions+of+thermal+stress&ots=3QPn5vf9Zd&sig=BC5rVSQEWeh4rVWXoZc-afubrvA> (accessed February 28, 2021).
- [18] G.A. Webster, A.N. Ezeilo, Residual stress distributions and their influence on fatigue lifetimes, Int. J. Fatigue. 23 (2001) 375–383. [https://doi.org/10.1016/s0142-1123\(01\)00133-5](https://doi.org/10.1016/s0142-1123(01)00133-5).

- [19] R.L. Barrie, T.P. Gabb, J. Telesman, P.T. Kantzos, A. Prescenzi, T. Biles, P.J. Bonacuse, Effectiveness of shot peening in suppressing fatigue cracking at non-metallic inclusions in Udimet®720, *Mater. Sci. Eng. A.* 474 (2008) 71–81. <https://doi.org/10.1016/j.msea.2007.03.100>.
- [20] Z. Zheng, D.S. Balint, F.P.E. Dunne, Dwell fatigue in two Ti alloys: An integrated crystal plasticity and discrete dislocation study, *J. Mech. Phys. Solids.* 96 (2016) 411–427. <https://doi.org/10.1016/j.jmps.2016.08.008>.
- [21] H. Mughrabi, F. Ackermann, K. Herz, Persistent slipbands in fatigued face-centered and body-centered cubic metals, in: *ASTM Spec. Tech. Publ.*, ASTM, 1979: pp. 69–105. <https://doi.org/10.1520/stp35885s>.
- [22] Z.Q. Wang, I.J. Beyerlein, R. LeSar, Slip band formation and mobile dislocation density generation in high rate deformation of single fcc crystals, *Philos. Mag.* (2008). <https://doi.org/10.1080/14786430802129833>.
- [23] W.A. Wood, Formation of fatigue cracks, *Philos. Mag.* (1958). <https://doi.org/10.1080/14786435808237004>.
- [24] F.P.E. Dunne, Fatigue crack nucleation: Mechanistic modelling across the length scales, *Curr. Opin. Solid State Mater. Sci.* 18 (2014). <https://doi.org/10.1016/j.cossms.2014.02.005>.
- [25] Y. Guo, T.B. Britton, A.J. Wilkinson, Slip band-grain boundary interactions in commercial-purity titanium, *Acta Mater.* (2014). <https://doi.org/10.1016/j.actamat.2014.05.015>.
- [26] M.D. Sangid, H.J. Maier, H. Sehitoglu, A physically based fatigue model for prediction of crack initiation from persistent slip bands in polycrystals, *Acta Mater.* 59 (2011) 328–

341. <https://doi.org/10.1016/j.actamat.2010.09.036>.
- [27] A.N. Stroh, The formation of cracks as a result of plastic flow, *Proc. R. Soc. London. Ser. A. Math. Phys. Sci.* 223 (1954) 404–414. <https://doi.org/10.1098/rspa.1954.0124>.
- [28] D.L.L. McDowell, F.P.E.P.E. Dunne, Microstructure-sensitive computational modeling of fatigue crack formation, *Int. J. Fatigue.* 32 (2010) 1521–1542. <https://doi.org/10.1016/j.ijfatigue.2010.01.003>.
- [29] A. Fatemi, D.F. Socie, A critical plane approach to multiaxial fatigue damage including out-of-phase loading, *Fatigue Fract. Eng. Mater. Struct.* (1988). <https://doi.org/10.1111/j.1460-2695.1988.tb01169.x>.
- [30] M.D. Sangid, H.J. Maier, H. Sehitoglu, The role of grain boundaries on fatigue crack initiation - An energy approach, *Int. J. Plast.* (2011). <https://doi.org/10.1016/j.ijplas.2010.09.009>.
- [31] V.V.C. Wan, J. Jiang, D.W. MacLachlan, F.P.E. Dunne, Microstructure-sensitive fatigue crack nucleation in a polycrystalline Ni superalloy, *Int. J. Fatigue.* 90 (2016) 181–190. <https://doi.org/10.1016/j.ijfatigue.2016.04.013>.
- [32] EASA, Certification Memorandum: The integrity of nickel powder metallurgy rotating critical parts for gas turbines, 2017.
- [33] Q. You, H. Yuan, L. Zhao, J. Li, X. You, S. Shi, Y. Tan, X. Ding, Removal inclusions from nickel-based superalloy by induced directional solidification during electron beam smelting, *Vacuum.* 156 (2018) 39–47. <https://doi.org/10.1016/j.vacuum.2018.07.014>.
- [34] M.H. Manjili, M. Halali, Removal of Non-metallic Inclusions from Nickel Base Superalloys by Electromagnetic Levitation Melting in a Slag, *Metall. Mater. Trans. B.* 49 (2018) 61–68. <https://doi.org/10.1007/s11663-017-1137-z>.

- [35] X. Lou, P.L. Andresen, R.B. Rebak, Oxide inclusions in laser additive manufactured stainless steel and their effects on impact toughness and stress corrosion cracking behavior, *J. Nucl. Mater.* 499 (2018) 182–190.
<https://doi.org/10.1016/j.jnucmat.2017.11.036>.
- [36] Y. Sun, R.J. Hebert, M. Aindow, Non-metallic inclusions in 17-4PH stainless steel parts produced by selective laser melting, *Mater. Des.* 140 (2018) 153–162.
<https://doi.org/10.1016/j.matdes.2017.11.063>.
- [37] N. Sanaei, A. Fatemi, Defects in additive manufactured metals and their effect on fatigue performance: A state-of-the-art review, *Prog. Mater. Sci.* (2020) 100724.
<https://doi.org/10.1016/j.pmatsci.2020.100724>.
- [38] D.A. Jablonski, The effect of ceramic inclusions on the low cycle fatigue life of low carbon astroloy subjected to hot isostatic pressing, *Mater. Sci. Eng.* 48 (1981) 189–198.
[https://doi.org/10.1016/0025-5416\(81\)90004-5](https://doi.org/10.1016/0025-5416(81)90004-5).
- [39] D.R. Chang, D.D. Krueger, R. a. Sprague, Superalloy Powder Processing, Properties, and Turbine Disk Applications, *Superalloys 1984 (Fifth Int. Symp. (1984))* 245–273.
https://doi.org/10.7449/1984/Superalloys_1984_245_273.
- [40] B.Q. Lin J, Review and Analysis of Powder Prior Boundary (PPB) Formation in Powder Metallurgy Processes for Nickel-based Super Alloys, *J. Powder Metall. Min.* 04 (2015) 1–6. <https://doi.org/10.4172/2168-9806.1000127>.
- [41] C.E. Shamblen, D.R. Chang, Effect of inclusions on LCF life of HIP plus heat treated powder metal René 95, *Metall. Trans. B.* 16 (1985) 775–784.
<https://doi.org/10.1007/BF02667513>.
- [42] T. Zhang, Understanding Fatigue Crack Nucleation From Inclusions in a Powder Nickel

Alloy Using Micromechanics, Imperial College London, 2015.

- [43] M.J. Caton, A.H. Rosenberger, J.M. Larsen, Divergence of Mechanisms and the Effect on the Fatigue Life Variability of Rene' 88 DT, in: Superalloys, 2004: pp. 305–312.
- [44] D. Hu, T. Wang, Q. Ma, X. Liu, L. Shang, D. Li, J. Pan, R. Wang, Effect of inclusions on low cycle fatigue lifetime in a powder metallurgy nickel-based superalloy FGH96, *Int. J. Fatigue*. 118 (2019) 237–248. <https://doi.org/10.1016/j.ijfatigue.2018.09.019>.
- [45] J. Jiang, F.P.E. Dunne, T. Ben Britton, Toward Predictive Understanding of Fatigue Crack Nucleation in Ni-Based Superalloys, *JOM*. 69 (2017). <https://doi.org/10.1007/s11837-017-2307-9>.
- [46] M.D. Sangid, The physics of fatigue crack initiation, *Int. J. Fatigue*. 57 (2013) 58–72. <https://doi.org/10.1016/j.ijfatigue.2012.10.009>.
- [47] K.S. Chan, Roles of microstructure in fatigue crack initiation, *Int. J. Fatigue*. 32 (2010) 1428–1447. <https://doi.org/10.1016/j.ijfatigue.2009.10.005>.
- [48] J. Grison, L. Remy, Fatigue Failure Probability in a Powder Metallurgy Ni-base Superalloy, *Eng. Fract. Mech.* 57 (1997) 41–55. [https://doi.org/10.1016/S0013-7944\(97\)00006-4](https://doi.org/10.1016/S0013-7944(97)00006-4).
- [49] B. Chen, J. Jiang, F.P.E. Dunne, Is stored energy density the primary meso-scale mechanistic driver for fatigue crack nucleation?, *Int. J. Plast.* 101 (2018) 213–229. <https://doi.org/10.1016/j.ijplas.2017.11.005>.
- [50] A. Neimitz, U. Janus, Analysis of Stress and Strain Fields in and around Inclusions of Various Shapes in a Cylindrical Specimen Loaded in Tension, *Arch. Metall. Mater.* 61 (2016) 569–576. <https://doi.org/10.1515/amm-2016-0097>.
- [51] T. Zhang, J. Jiang, B. Britton, B. Shollock, F. Dunne, Crack nucleation using combined

- crystal plasticity modelling , high-resolution digital image correlation and high-resolution electron backscatter diffraction in a superalloy containing non-metallic inclusions under fatigue Subject Areas :, *Proc. R. Soc. A.* 472 (2016) 20150792. <https://doi.org/10.1098/rspa.2015.0792>.
- [52] R. Bandyopadhyay, M.D. Sangid, Crystal plasticity assessment of inclusion- and matrix-driven competing failure modes in a nickel-base superalloy, *Acta Mater.* 177 (2019) 20–34. <https://doi.org/10.1016/j.actamat.2019.07.024>.
- [53] M.E. Kartal, F.P.E. Dunne, A.J. Wilkinson, Determination of the complete microscale residual stress tensor at a subsurface carbide particle in a single-crystal superalloy from free-surface EBSD, *Acta Mater.* 60 (2012) 5300–5310. <https://doi.org/10.1016/j.actamat.2012.06.027>.
- [54] Y. Shi, D. Yang, X. Yang, G. Miao, D. Shi, S. Li, X. Hu, F. Liu, W. Huang, The effect of inclusion factors on fatigue life and fracture-mechanics-based life method for a P/M superalloy at elevated temperature, *Int. J. Fatigue.* 131 (2020) 105365. <https://doi.org/10.1016/j.ijfatigue.2019.105365>.
- [55] K. Gall, M.F. Horstemeyer, B.W. Degner, D.L. McDowell, J. Fan, On the driving force for fatigue crack formation from inclusions and voids in a cast A356 aluminum alloy, *Int. J. Fract.* 108 (2001) 207–233. <https://doi.org/10.1023/A:1011033304600>.
- [56] J.H. Park, Y. Kang, Inclusions in Stainless Steels – A Review, *Steel Res. Int.* 88 (2017) 1–26. <https://doi.org/10.1002/srin.201700130>.
- [57] H. V. Atkinson, G. Shi, Characterization of inclusions in clean steels: A review including the statistics of extremes methods, *Prog. Mater. Sci.* 48 (2003) 457–520. [https://doi.org/10.1016/S0079-6425\(02\)00014-2](https://doi.org/10.1016/S0079-6425(02)00014-2).

- [58] D.P. Naragani, P.A. Shade, P. Kenesei, H. Sharma, M.D. Sangid, X-ray characterization of the micromechanical response ahead of a propagating small fatigue crack in a Ni-based superalloy, *Acta Mater.* (2019). <https://doi.org/10.1016/j.actamat.2019.08.005>.
- [59] T. Gabb, J. Telesman, Major Effects of Nonmetallic Inclusions on the Fatigue Life of Disk Superalloy Demonstrated, in: G.R. Gallagher, J.P. Halford (Eds.), *Thirty-First Natl. Symp. Fatigue Fract. Mech.*, 2000: pp. 110–127.
- [60] M.N. Shabrov, A. Needleman, An analysis of inclusion morphology effects on void nucleation, *Model. Simul. Mater. Sci. Eng.* 10 (2002) 163–183. <https://doi.org/10.1088/0965-0393/10/2/305>.
- [61] J. Yao, X.H. Qu, X.B. He, L. Zhang, Effect of inclusion size on the high cycle fatigue strength and failure mode of a high v alloyed powder metallurgy tool steel, *Int. J. Miner. Metall. Mater.* 19 (2012) 608–614. <https://doi.org/10.1007/s12613-012-0602-6>.
- [62] N. Salajegheh, D.L. McDowell, Microstructure-sensitive weighted probability approach for modeling surface to bulk transition of high cycle fatigue failures dominated by primary inclusions, *Int. J. Fatigue.* 59 (2014) 188–199. <https://doi.org/10.1016/j.ijfatigue.2013.08.025>.
- [63] A. Pineau, S.D. Antolovich, Probabilistic approaches to fatigue with special emphasis on initiation from inclusions, *Int. J. Fatigue.* 93 (2016) 422–434. <https://doi.org/10.1016/j.ijfatigue.2016.09.002>.
- [64] Y.Q. Chen, S.P. Pan, M.Z. Zhou, D.Q. Yi, D.Z. Xu, Y.F. Xu, Effects of inclusions, grain boundaries and grain orientations on the fatigue crack initiation and propagation behavior of 2524-T3 Al alloy, *Mater. Sci. Eng. A.* 580 (2013) 150–158. <https://doi.org/10.1016/j.msea.2013.05.053>.

- [65] X. Xie, L. Zhang, M. Zhang, J. Dong, K. Bain, Micro-Mechanical Behavior Study of Non-Metallic Inclusions in P / M Disk, *Miner. Met. Mater. Soc.* (2004).
- [66] S.R. Yeratapally, J.D. Hochhalter, T.J. Ruggles, M.D. Sangid, Investigation of fatigue crack incubation and growth in cast MAR-M247 subjected to low cycle fatigue at room temperature, *Int. J. Fract.* (2017) 1–18. <https://doi.org/10.1007/s10704-017-0213-3>.
- [67] J.E. Bozek, J.D. Hochhalter, M.G. Veilleux, M. Liu, G. Heber, S.D. Sintay, A.D. Rollett, D.J. Littlewood, A.M. Maniatty, H. Weiland, R.J. Christ, J. Payne, G. Welsh, D.G. Harlow, P.A. Wawrzynek, A.R. Ingraffea, A geometric approach to modeling microstructurally small fatigue crack formation: I. Probabilistic simulation of constituent particle cracking in AA 7075-T651, *Model. Simul. Mater. Sci. Eng.* 16 (2008) 065007. <https://doi.org/10.1088/0965-0393/16/6/065007>.
- [68] B.J. Schäfer, P. Sonnweber-Ribic, H. Ul-Hassan, A. Hartmaier, Micromechanical modeling of fatigue crack nucleation around non-metallic inclusions in martensitic high-strength steels, *Metals (Basel)*. 9 (2019) 1–28. <https://doi.org/10.3390/met9121258>.
- [69] Y. Murakami, M. Endo, Effects of defects, inclusions and inhomogeneities on fatigue strength, *Int. J. Fatigue*. 16 (1994) 163–182. [https://doi.org/10.1016/0142-1123\(94\)90001-9](https://doi.org/10.1016/0142-1123(94)90001-9).
- [70] E.S. Huron, P.G. Roth, The Influence of Inclusions on Low Cycle Fatigue Life in a P/M Nickel-Base Disk Superalloy, *Superalloys 1996*. (1996) 359–368. https://doi.org/10.7449/1996/Superalloys_1996_359_368.
- [71] J. Fan, D.L. McDowell, M.F. Horstemeyer, K. Gall, Cyclic plasticity at pores and inclusions in cast Al-Si alloys, *Eng. Fract. Mech.* 70 (2003) 1281–1302. [https://doi.org/10.1016/S0013-7944\(02\)00097-8](https://doi.org/10.1016/S0013-7944(02)00097-8).

- [72] M.M. Shenoy, R.S. Kumar, D.L. McDowell, Modeling effects of nonmetallic inclusions on LCF in DS nickel-base superalloys, *Int. J. Fatigue*. 27 (2005) 113–127. <https://doi.org/10.1016/j.ijfatigue.2004.06.008>.
- [73] J.D. Eshelby, The determination of the elastic field of an ellipsoidal inclusion, and related problems, *Proc. R. Soc. London. Ser. A. Math. Phys. Sci.* (1957) 209–229. https://doi.org/10.1007/1-4020-4499-2_18.
- [74] D. Naragani, M.D. Sangid, P.A. Shade, J.C. Schuren, H. Sharma, J.S. Park, P. Kenesei, J. V. Bernier, T.J. Turner, I. Parr, Investigation of fatigue crack initiation from a non-metallic inclusion via high energy x-ray diffraction microscopy, *Acta Mater.* 137 (2017) 71–84. <https://doi.org/10.1016/j.actamat.2017.07.027>.
- [75] T. Zhang, D.M. Collins, F.P.E.E. Dunne, B.A. Shollock, Crystal plasticity and high-resolution electron backscatter diffraction analysis of full-field polycrystal Ni superalloy strains and rotations under thermal loading, *Acta Mater.* 80 (2014) 25–38. <https://doi.org/10.1016/j.actamat.2014.07.036>.
- [76] J. Wang, H.P. Li, R. Stevens, Hafnia and hafnia-toughened ceramics, *J. Mater. Sci.* 27 (1992) 5397–5430. <https://doi.org/10.1007/BF00541601>.
- [77] S.L. Dole, Elastic properties of monoclinic hafnium oxide, (1977) 129.
- [78] J. Zhang, R. Prasannavenkatesan, M.M. Shenoy, D.L. McDowell, Modeling fatigue crack nucleation at primary inclusions in carburized and shot-peened martensitic steel, *Eng. Fract. Mech.* 76 (2009) 315–334. <https://doi.org/10.1016/j.engfracmech.2008.10.011>.
- [79] C. Przybyla, R. Prasannavenkatesan, N. Salajegheh, D.L. McDowell, Microstructure-sensitive modeling of high cycle fatigue, *Int. J. Fatigue*. 32 (2010) 512–525.

<https://doi.org/10.1016/j.ijfatigue.2009.03.021>.

- [80] J.M. Hyzak, I.M. Bernstein, The effect of defects on the fatigue crack initiation process in two p/m superalloys: part i. fatigue origins, *Metall. Trans. A.* 13 (1982) 33–43. <https://doi.org/10.1007/BF02642413>.
- [81] V. Paidar, D.P. Pope, V. Vitek, A theory of the anomalous yield behavior in L12 ordered alloys, *Acta Metall.* (1984). [https://doi.org/10.1016/0001-6160\(84\)90117-2](https://doi.org/10.1016/0001-6160(84)90117-2).
- [82] C. Qiu, X. Wu, High cycle fatigue and fracture behaviour of a hot isostatically pressed nickel-based superalloy, *Philos. Mag.* 94 (2014) 242–264. <https://doi.org/10.1080/14786435.2013.852287>.
- [83] J.-C. Stinville, E. Martin, M. Karadge, S. Ismonov, M. Soare, T. Hanlon, S. Sundaram, M.P. Echlin, P.G. Callahan, W.C. Lenthe, J. Miao, A.E. Wessman, R. Finlay, A. Loghin, J. Marte, T.M. Pollock, Competing Modes for Crack Initiation from Non-metallic Inclusions and Intrinsic Microstructural Features During Fatigue in a Polycrystalline Nickel-Based Superalloy, *Metall. Mater. Trans. A.* 49 (2018) 3865–3873. <https://doi.org/10.1007/s11661-018-4780-3>.
- [84] A. Pineau, S. Forest, Effects of inclusions on the very high cycle fatigue behaviour of steels, *Fatigue Fract. Eng. Mater. Struct.* 40 (2017) 1694–1707. <https://doi.org/10.1111/ffe.12649>.
- [85] J.C. Stinville, E. Martin, M. Karadge, S. Ismonov, M. Soare, T. Hanlon, S. Sundaram, M.P. Echlin, P.G. Callahan, W.C. Lenthe, V.M. Miller, J. Miao, A.E. Wessman, R. Finlay, A. Loghin, J. Marte, T.M. Pollock, Fatigue deformation in a polycrystalline nickel base superalloy at intermediate and high temperature: Competing failure modes, *Acta Mater.* 152 (2018) 16–33. <https://doi.org/10.1016/j.actamat.2018.03.035>.

- [86] D. Texier, A.C. Gómez, S. Pierret, J.M. Franchet, T.M. Pollock, P. Villechaise, J. Cormier, Microstructural Features Controlling the Variability in Low-Cycle Fatigue Properties of Alloy Inconel 718DA at Intermediate Temperature, *Metall. Mater. Trans. A Phys. Metall. Mater. Sci.* 47 (2016). <https://doi.org/10.1007/s11661-015-3291-8>.
- [87] T. Zhang, J. Jiang, B.A. Shollock, T. Ben Britton, F.P.E. Dunne, Slip localization and fatigue crack nucleation near a non-metallic inclusion in polycrystalline nickel-based superalloy, *Mater. Sci. Eng. A.* 641 (2015) 328–339. <https://doi.org/10.1016/j.msea.2015.06.070>.
- [88] J. Jiang, J. Yang, T. Zhang, F.P.E. Dunne, T. Ben Britton, On the mechanistic basis of fatigue crack nucleation in Ni superalloy containing inclusions using high resolution electron backscatter diffraction, *Acta Mater.* 97 (2015) 367–379. <https://doi.org/10.1016/j.actamat.2015.06.035>.
- [89] D. Texier, J.-C.C. Stinville, M.P. Echlin, S. Pierret, P. Villechaise, T.M. Pollock, J. Cormier, Short crack propagation from cracked non-metallic inclusions in a Ni-based polycrystalline superalloy, *Acta Mater.* 165 (2019) 241–258. <https://doi.org/10.1016/j.actamat.2018.11.051>.
- [90] D. Texier, J. Cormier, P. Villechaise, J.C. Stinville, C.J. Torbet, S. Pierret, T.M. Pollock, Crack initiation sensitivity of wrought direct aged alloy 718 in the very high cycle fatigue regime: the role of non-metallic inclusions, *Mater. Sci. Eng. A.* 678 (2016) 122–136. <https://doi.org/10.1016/j.msea.2016.09.098>.
- [91] M. Goto, D.M. Knowles, Initiation and propagation behaviour of microcracks in Ni-base superalloy Udimet 720 LI, *Eng. Fract. Mech.* 60 (1998) 1–18. [https://doi.org/10.1016/S0013-7944\(98\)00003-4](https://doi.org/10.1016/S0013-7944(98)00003-4).
- [92] D. Texier, J.C. Stinville, M.A. Charpagne, Z. Chen, V. Valle, P. Villechaise, T.M.

- Pollock, J. Cormier, Role of Non-metallic Inclusions and Twins on the Variability in Fatigue Life in Alloy 718 Nickel Base Superalloy, in: *Miner. Met. Mater. Ser.*, Springer Science and Business Media Deutschland GmbH, 2020: pp. 629–639. https://doi.org/10.1007/978-3-030-51834-9_61.
- [93] D.L. McDowell, Simulation-based strategies for microstructure-sensitive fatigue modeling, *Mater. Sci. Eng. A.* 468–470 (2007) 4–14. <https://doi.org/10.1016/j.msea.2006.08.129>.
- [94] J. Lankford, Inclusion-matrix debonding and fatigue crack initiation in low alloy steel, *Int. J. Fract.* (1976). <https://doi.org/10.1007/BF00036019>.
- [95] C. Landron, O. Bouaziz, E. Maire, J. Adrien, Characterization and modeling of void nucleation by interface decohesion in dual phase steels, *Scr. Mater.* 63 (2010) 973–976. <https://doi.org/10.1016/j.scriptamat.2010.07.021>.
- [96] A.S. Argon, M.L. Seleznev, C.F. Shih, X.H. Liu, Role of controlled debonding along fiber/matrix interfaces in the strength and toughness of metal matrix composites, *Int. J. Fract.* 93 (1998) 351–371. <https://doi.org/10.1023/A:1007447008739>.
- [97] A. Needleman, A Continuum Model for Void Nucleation by Inclusion Debonding, *J. Appl. Mech.* 54 (1987) 525. <https://doi.org/10.1115/1.3173064>.
- [98] J. Galkiewicz, Cohesive model application to micro-crack nucleation and growth, *Procedia Struct. Integr.* 2 (2016) 1619–1626. <https://doi.org/10.1016/j.prostr.2016.06.205>.
- [99] X. Xu, A. Needleman, Void nucleation by inclusion debonding in a crystal matrix, *Model. Simul. Mater. Sci. Eng.* (1993).
- [100] D. Chen, X. Zhang, X. Meng, R. Ma, R. Li, Z. Wang, B. Su, D. Lang, T. Yang, D. Meng,

- Mechanisms of void formation during uniaxial tensile testing in a low-temperature-aged U-Nb alloy, *Mater. Sci. Eng. A.* 723 (2018) 182–193. <https://doi.org/10.1016/j.msea.2018.03.031>.
- [101] J. Telesman, T.P. Gabb, P.T. Kantzos, P.J. Bonacuse, R.L. Barrie, C.A. Kantzos, Effect of a large population of seeded alumina inclusions on crack initiation and small crack fatigue crack growth in Udimet 720 nickel-base disk superalloy, *Int. J. Fatigue.* 142 (2021) 105953. <https://doi.org/10.1016/j.ijfatigue.2020.105953>.
- [102] J. Jiang, J. Yang, T. Zhang, J. Zou, Y. Wang, F.P.E. Dunne, T.B. Britton, Microstructurally sensitive crack nucleation around inclusions in powder metallurgy nickel-based superalloys, *Acta Mater.* 117 (2016) 333–344. <https://doi.org/10.1016/j.actamat.2016.07.023>.
- [103] V.V.C. Wan, D.W. Maclachlan, F.P.E. Dunne, A stored energy criterion for fatigue crack nucleation in polycrystals, *Int. J. Fatigue.* 68 (2014) 90–102. <https://doi.org/10.1016/j.ijfatigue.2014.06.001>.
- [104] J. Hodowany, G. Ravichandran, a Rosakis, P. Rosakis, Partition of plastic work into heat and stored energy in metals, *Exp. Mech.* 40 (2000) 113–123. <https://doi.org/10.1007/BF02325036>.
- [105] A. Rusinek, J.R. Klepaczko, Experiments on heat generated during plastic deformation and stored energy for TRIP steels, *Mater. Des.* 30 (2009) 35–48. <https://doi.org/10.1016/j.matdes.2008.04.048>.
- [106] K. Tanaka, T. Mura, A theory of fatigue crack initiation at inclusions, *Metall. Trans. A.* 13 (1982) 117–123. <https://doi.org/10.1007/BF02642422>.
- [107] K. Tanaka, T. Mura, A Dislocation Model for Fatigue Crack Initiation, *J. Appl. Mech.*

- 48 (1981) 97. <https://doi.org/10.1115/1.3157599>.
- [108] D.S. Dugdale, Yielding of steel sheets containing slits, *J. Mech. Phys. Solids*. 8 (1960) 100–104. [https://doi.org/10.1016/0022-5096\(60\)90013-2](https://doi.org/10.1016/0022-5096(60)90013-2).
- [109] G.I. Barenblatt, The Mathematical Theory of Equilibrium of Crack in Brittle Fracture, *Adv. Appl. Mech.* 7 (1962) 55–129. <https://doi.org/>Last accessed: 14/04/2016.
- [110] S.A. Ponnusami, S. Turteltaub, S. van der Zwaag, Cohesive-zone modelling of crack nucleation and propagation in particulate composites, *Eng. Fract. Mech.* 149 (2015) 170–190. <https://doi.org/10.1016/j.engfracmech.2015.09.050>.
- [111] N. Chandra, H. Li, C. Shet, H. Ghonem, Some issues in the application of cohesive zone models for metal-ceramic interfaces, *Int. J. Solids Struct.* 39 (2002) 2827–2855. [https://doi.org/10.1016/S0020-7683\(02\)00149-X](https://doi.org/10.1016/S0020-7683(02)00149-X).
- [112] Y. Wei, J.W. Hutchinson, Toughness of Ni/Al₂O₃ interfaces as dependent on micron-scale plasticity and atomistic-scale separation, *Philos. Mag.* 88 (2008) 3841–3859. <https://doi.org/10.1080/14786430802311092>.
- [113] J. Dohr, D.E.J. Armstrong, E. Tarleton, T. Couvant, S. Lozano-Perez, The influence of surface oxides on the mechanical response of oxidized grain boundaries, *Thin Solid Films*. 632 (2017) 17–22. <https://doi.org/10.1016/j.tsf.2017.03.060>.
- [114] A. Elzas, B. Thijssse, Cohesive law describing crack growth at iron/precipitate interfaces, *Comput. Mater. Sci.* (2017). <https://doi.org/10.1016/j.commatsci.2017.01.042>.
- [115] T.L. Anderson, FRACTURE MECHANICS Fundamentals and Applications, *Angew. Chemie Int. Ed.* (2001). [https://doi.org/10.1002/1521-3773\(20010316\)40:6<9823::AID-ANIE9823>3.3.CO;2-C](https://doi.org/10.1002/1521-3773(20010316)40:6<9823::AID-ANIE9823>3.3.CO;2-C).
- [116] M.L. Benzeggagh, M. Kenane, Measurement of mixed-mode delamination fracture

- toughness of unidirectional glass/epoxy composites with mixed-mode bending apparatus, *Compos. Sci. Technol.* 56 (1995) 439–449. [https://doi.org/https://doi.org/10.1016/0266-3538\(96\)00005-X](https://doi.org/https://doi.org/10.1016/0266-3538(96)00005-X).
- [117] K. Park, G.H. Paulino, Cohesive Zone Models: A Critical Review of Traction-Separation Relationships Across Fracture Surfaces, *Appl. Mech. Rev.* 64 (2013) 060802. <https://doi.org/10.1115/1.4023110>.
- [118] J.H. Rose, J. Ferrante, J.R. Smith, Universal binding energy curves for metals and bimetallic interfaces, *Phys. Rev. Lett.* 47 (1981) 675–678. <https://doi.org/10.1103/PhysRevLett.47.675>.
- [119] K. Park, G.H. Paulino, J.R. Roesler, A unified potential-based cohesive model of mixed-mode fracture, *J. Mech. Phys. Solids.* 57 (2009) 891–908. <https://doi.org/10.1016/j.jmps.2008.10.003>.
- [120] D. Peirce, R.J. Asaro, A. Needleman, An analysis of nonuniform and localized deformation in ductile single crystals, *Acta Metall.* (1982). [https://doi.org/10.1016/0001-6160\(82\)90005-0](https://doi.org/10.1016/0001-6160(82)90005-0).
- [121] Abaqus Unified FEA - SIMULIA™ by Dassault Systèmes®, (n.d.). <https://www.3ds.com/products-services/simulia/products/abaqus/> (accessed February 23, 2021).
- [122] F.P.E. Dunne, D. Rugg, A. Walker, Lengthscale-dependent, elastically anisotropic, physically-based hcp crystal plasticity: Application to cold-dwell fatigue in Ti alloys, *Int. J. Plast.* 23 (2007) 1061–1083. <https://doi.org/10.1016/j.ijplas.2006.10.013>.
- [123] E.H. Lee, Elastic-Plastic Deformation at Finite Strains, *J. Appl. Mech.* 36 (1969) 1. <https://doi.org/10.1115/1.3564580>.

- [124] R.J. Asaro, J.R. Rice, Strain localization in ductile single crystals, *J. Mech. Phys. Solids*. (1977). [https://doi.org/10.1016/0022-5096\(77\)90001-1](https://doi.org/10.1016/0022-5096(77)90001-1).
- [125] J.P. Hirth, On dislocation interactions in the fcc lattice, *J. Appl. Phys.* 32 (1961) 700–706. <https://doi.org/10.1063/1.1736074>.
- [126] U. Messerschmidt, M. Bartsch, Generation of dislocations during plastic deformation, in: *Mater. Chem. Phys.*, Elsevier, 2003: pp. 518–523. [https://doi.org/10.1016/S0254-0584\(03\)00064-6](https://doi.org/10.1016/S0254-0584(03)00064-6).
- [127] M.F. Ashby, The deformation of plastically non-homogeneous materials, *Philos. Mag.* 21 (1970) 399–424. <https://doi.org/10.1080/14786437008238426>.
- [128] N.A. Fleck, G.M. Muller, M.F. Ashby, J.W. Hutchinson, Strain gradient plasticity: Theory and experiment, *Acta Metall. Mater.* 42 (1994) 475–487. [https://doi.org/10.1016/0956-7151\(94\)90502-9](https://doi.org/10.1016/0956-7151(94)90502-9).
- [129] A. Arsenlis, D.M. Parks, Crystallographic aspects of geometrically-necessary and statistically-stored dislocation density, *Acta Mater.* 47 (1999) 1597–1611. [https://doi.org/10.1016/S1359-6454\(99\)00020-8](https://doi.org/10.1016/S1359-6454(99)00020-8).
- [130] J.F. Nye, Some geometrical relations in dislocated crystals, *Acta Metall.* 1 (1953) 153–162. [https://doi.org/10.1016/0001-6160\(53\)90054-6](https://doi.org/10.1016/0001-6160(53)90054-6).
- [131] Z. Zheng, N.G. Prastiti, D.S. Balint, F.P.E. Dunne, The dislocation configurational energy density in discrete dislocation plasticity, *J. Mech. Phys. Solids*. 129 (2019) 39–60. <https://doi.org/10.1016/j.jmps.2019.04.015>.
- [132] A.D. Rollett, A.M. Maniatty, J.E. Bozek, A.R. Ingraffea, D.J. Littlewood, M.G. Veilleux, J.D. Hochhalter, A geometric approach to modeling microstructurally small fatigue crack formation: III. Development of a semi-empirical model for nucleation,

- Model. Simul. Mater. Sci. Eng. 19 (2011) 035008. <https://doi.org/10.1088/0965-0393/19/3/035008>.
- [133] L. Wang, R.I. Barabash, Y. Yang, T.R. Bieler, M.A. Crimp, P. Eisenlohr, W. Liu, G.E. Ice, Experimental characterization and crystal plasticity modeling of heterogeneous deformation in polycrystalline α -Ti, Metall. Mater. Trans. A Phys. Metall. Mater. Sci. 42 (2011) 626–635. <https://doi.org/10.1007/s11661-010-0249-8>.
- [134] P.H. Geubelle, J.S. Baylor, Impact-induced delamination of composites: A 2D simulation, Compos. Part B Eng. 29 (1998) 589–602. [https://doi.org/10.1016/S1359-8368\(98\)00013-4](https://doi.org/10.1016/S1359-8368(98)00013-4).
- [135] G. Alfano, M.A. Crisfield, Finite element interface models for the delamination analysis of laminated composites: Mechanical and computational issues, Int. J. Numer. Methods Eng. 50 (2001) 1701–1736. <https://doi.org/10.1002/nme.93>.
- [136] Y.F. Gao, A.F. Bower, A simple technique for avoiding convergence problems in finite element simulations of crack nucleation and growth on cohesive interfaces, Model. Simul. Mater. Sci. Eng. 12 (2004) 453–463. <https://doi.org/10.1088/0965-0393/12/3/007>.
- [137] B. Chen, K. Janssens, F. Dunne, Multiaxial and non-proportional microstructure-sensitive fatigue crack nucleation, 12th Int. Conf. Multiaxial Fatigue Fract. (2019) 010001. <https://doi.org/https://doi.org/10.1051/mateconf/201930001001>.
- [138] A. Heinz, P. Neumann, Crack initiation during high cycle fatigue of an austenitic steel, Acta Metall. Mater. 38 (1990) 1933–1940. [https://doi.org/10.1016/0956-7151\(90\)90305-Z](https://doi.org/10.1016/0956-7151(90)90305-Z).
- [139] J. Miao, T.M. Pollock, J. Wayne Jones, Crystallographic fatigue crack initiation in

- nickel-based superalloy René 88DT at elevated temperature, *Acta Mater.* 57 (2009) 5964–5974. <https://doi.org/10.1016/j.actamat.2009.08.022>.
- [140] J.C. Stinville, N. Vanderesse, F. Bridier, P. Bocher, T.M. Pollock, High resolution mapping of strain localization near twin boundaries in a nickel-based superalloy, *Acta Mater.* 98 (2015) 29–42. <https://doi.org/10.1016/j.actamat.2015.07.016>.
- [141] J.C. Stinville, W.C. Lenthe, J. Miao, T.M. Pollock, A combined grain scale elastic-plastic criterion for identification of fatigue crack initiation sites in a twin containing polycrystalline nickel-base superalloy, *Acta Mater.* 103 (2016). <https://doi.org/10.1016/j.actamat.2015.09.050>.
- [142] J. Miao, T.M. Pollock, J. Wayne Jones, Microstructural extremes and the transition from fatigue crack initiation to small crack growth in a polycrystalline nickel-base superalloy, *Acta Mater.* 60 (2012) 2840–2854. <https://doi.org/10.1016/j.actamat.2012.01.049>.
- [143] S. Gustafson, W. Ludwig, P. Shade, D. Naragani, D. Pagan, P. Cook, C. Yildirim, C. Detlefs, M.D. Sangid, Quantifying microscale drivers for fatigue failure via coupled synchrotron X-ray characterization and simulations, *Nat. Commun.* 11 (2020) 3189. <https://doi.org/10.1038/s41467-020-16894-2>.
- [144] A. Bergsmo, F.P.E. Dunne, Competing mechanisms of particle fracture, decohesion and slip-driven fatigue crack nucleation in a PM nickel superalloy, *Int. J. Fatigue.* 135 (2020) 105573. <https://doi.org/10.1016/j.ijfatigue.2020.105573>.
- [145] C. Hennessey, G.M. Castelluccio, D.L. McDowell, Sensitivity of polycrystal plasticity to slip system kinematic hardening laws for Al 7075-T6, *Mater. Sci. Eng. A.* 687 (2017) 241–248. <https://doi.org/10.1016/j.msea.2017.01.070>.
- [146] C.J. Bayley, W.A.M. Brekelmans, M.G.D. Geers, A comparison of dislocation induced

- back stress formulations in strain gradient crystal plasticity, *Int. J. Solids Struct.* (2006).
<https://doi.org/10.1016/j.ijsolstr.2006.05.011>.
- [147] S.R. Yeratapally, M.G. Glavicic, M. Hardy, M.D. Sangid, Microstructure based fatigue life prediction framework for polycrystalline nickel-base superalloys with emphasis on the role played by twin boundaries in crack initiation, *Acta Mater.* 107 (2016).
<https://doi.org/10.1016/j.actamat.2016.01.038>.
- [148] B. Chen, K. Janssens, F.P.E. Dunne, Role of geometrically necessary dislocation density in multiaxial and non-proportional fatigue crack nucleation, *Int. J. Fatigue.* 135 (2020).
<https://doi.org/10.1016/j.ijfatigue.2020.105517>.
- [149] R. Quey, P.R. Dawson, F. Barbe, Large-scale 3D random polycrystals for the finite element method: Generation, meshing and remeshing, *Comput. Methods Appl. Mech. Eng.* 200 (2011) 1729–1745. <https://doi.org/10.1016/j.cma.2011.01.002>.
- [150] B. Barzdajn, A Galling Failure Model, Imperial College London, 2019.
<https://doi.org/https://doi.org/10.25560/68729>.
- [151] MTEX Toolbox | MTEX, (n.d.). <https://mtex-toolbox.github.io/> (accessed April 8, 2021).
- [152] J.C. Stinville, E.R. Yao, P.G. Callahan, J. Shin, F. Wang, M.P. Echlin, T.M. Pollock, D.S. Gianola, Dislocation dynamics in a nickel-based superalloy via in-situ transmission scanning electron microscopy, *Acta Mater.* 168 (2019) 152–166.
<https://doi.org/10.1016/j.actamat.2018.12.061>.
- [153] C.A. Stein, A. Cerrone, T. Ozturk, S. Lee, P. Kenesei, H. Tucker, R. Pokharel, J. Lind, C. Hefferan, R.M. Suter, A.R. Ingraffea, A.D. Rollett, Fatigue crack initiation, slip localization and twin boundaries in a nickel-based superalloy, *Curr. Opin. Solid State*

- Mater. Sci. 18 (2014) 244–252. <https://doi.org/10.1016/j.cossms.2014.06.001>.
- [154] C.O. Frederick, P.J. Armstrong, A mathematical representation of the multiaxial Bauschinger effect, Mater. High Temp. 24 (1966) 1–26. <https://doi.org/10.3184/096034007X207589>.
- [155] R. Bandyopadhyay, S.E. Gustafson, K. Kapoor, D. Naragani, D.C. Pagan, M.D. Sangid, Comparative assessment of backstress models using high-energy X-ray diffraction microscopy experiments and crystal plasticity finite element simulations, Int. J. Plast. 136 (2021) 102887. <https://doi.org/10.1016/j.ijplas.2020.102887>.
- [156] K. Kapoor, Y.S.J. Yoo, T.A. Book, J.P. Kacher, M.D. Sangid, Incorporating grain-level residual stresses and validating a crystal plasticity model of a two-phase Ti-6Al-4 V alloy produced via additive manufacturing, J. Mech. Phys. Solids. 121 (2018) 447–462. <https://doi.org/10.1016/j.jmps.2018.07.025>.
- [157] J. Dobrzański, Internal damage processes in low alloy chromium-molybdenum steels during high-temperature creep service, in: J. Mater. Process. Technol., Elsevier, 2004: pp. 297–303. <https://doi.org/10.1016/j.jmatprotec.2004.09.047>.
- [158] Y. Guan, B. Chen, J. Zou, T. Ben Britton, J. Jiang, F.P.E. Dunne, Crystal plasticity modelling and HR-DIC measurement of slip activation and strain localization in single and oligo-crystal Ni alloys under fatigue, Int. J. Plast. 88 (2017) 70–88. <https://doi.org/10.1016/j.ijplas.2016.10.001>.
- [159] W. Wan, F.P.E. Dunne, Microstructure-interacting short crack growth in blocky alpha Zircaloy-4, Int. J. Plast. 130 (2020) 102711. <https://doi.org/10.1016/j.ijplas.2020.102711>.
- [160] D. Wilson, W. Wan, F.P.E. Dunne, Microstructurally-sensitive fatigue crack growth in

- HCP, BCC and FCC polycrystals, *J. Mech. Phys. Solids.* 126 (2019).
<https://doi.org/10.1016/j.jmps.2019.02.012>.
- [161] R. Jiang, F. Pierron, S. Octaviani, P.A.S. Reed, Characterisation of strain localisation processes during fatigue crack initiation and early crack propagation by SEM-DIC in an advanced disc alloy, *Mater. Sci. Eng. A.* 699 (2017) 128–144.
<https://doi.org/10.1016/j.msea.2017.05.091>.
- [162] D. Lunt, R. Thomas, M. Roy, J. Duff, M. Atkinson, P. Frankel, M. Preuss, J.Q. da Fonseca, Comparison of sub-grain scale digital image correlation calculated using commercial and open-source software packages, *Mater. Charact.* (2020).
<https://doi.org/10.1016/j.matchar.2020.110271>.
- [163] B. Pan, Recent Progress in Digital Image Correlation, *Exp. Mech.* 51 (2011) 1223–1235.
<https://doi.org/10.1007/s11340-010-9418-3>.
- [164] H. Schreier, J.-J. Orteu, M.A. Sutton, *Image Correlation for Shape, Motion and Deformation Measurements*, 2009. <https://doi.org/10.1007/978-0-387-78747-3>.
- [165] H.A. Bruck, S.R. McNeill, M.A. Sutton, W.H. Peters, Digital image correlation using Newton-Raphson method of partial differential correction, *Exp. Mech.* 29 (1989) 261–267. <https://doi.org/10.1007/BF02321405>.
- [166] V. Valle, S. Hedan, P. Cosenza, A.L. Fauchille, M. Berdjane, Digital Image Correlation Development for the Study of Materials Including Multiple Crossing Cracks, *Exp. Mech.* 55 (2015) 379–391. <https://doi.org/10.1007/s11340-014-9948-1>.
- [167] J. Poissant, F. Barthelat, A novel “subset splitting” procedure for digital image correlation on discontinuous displacement fields, *Exp. Mech.* 50 (2010) 353–364.
<https://doi.org/10.1007/s11340-009-9220-2>.

- [168] F. Bourdin, J.C. Stinville, M.P. Echlin, P.G. Callahan, W.C. Lenthe, C.J. Torbet, D. Texier, F. Bridier, J. Cormier, P. Villechaise, T.M. Pollock, V. Valle, Measurements of plastic localization by heaviside-digital image correlation, *Acta Mater.* 157 (2018) 307–325. <https://doi.org/10.1016/j.actamat.2018.07.013>.
- [169] J.C. Stinville, P.G. Callahan, M.A. Charpagne, M.P. Echlin, V. Valle, T.M. Pollock, Direct measurements of slip irreversibility in a nickel-based superalloy using high resolution digital image correlation, *Acta Mater.* 186 (2020) 172–189. <https://doi.org/10.1016/j.actamat.2019.12.009>.
- [170] J.C. Stinville, T. Francis, A.T. Polonsky, C.J. Torbet, M.A. Charpagne, Z. Chen, G.H. Balbus, F. Bourdin, V. Valle, P.G. Callahan, M.P. Echlin, T.M. Pollock, Time-Resolved Digital Image Correlation in the Scanning Electron Microscope for Analysis of Time-Dependent Mechanisms, *Exp. Mech.* (2020). <https://doi.org/10.1007/s11340-020-00632-2>.
- [171] G.M. Hassan, A. V. Dyskin, C.K. MacNish, E. Pasternak, I. Shufrin, Discontinuous Digital Image Correlation to reconstruct displacement and strain fields with discontinuities: Dislocation approach, *Eng. Fract. Mech.* 189 (2018) 273–292. <https://doi.org/10.1016/j.engfracmech.2017.11.022>.
- [172] J. Réthoré, S. Roux, F. Hild, From pictures to extended finite elements: extended digital image correlation (X-DIC), *Comptes Rendus - Mec.* 335 (2007) 131–137. <https://doi.org/10.1016/j.crme.2007.02.003>.
- [173] Autograph AGS-X Series : SHIMADZU (Shimadzu Corporation), (n.d.). <https://www.shimadzu.com/an/products/materials-testing/uni-ttm/autograph-ags-x-series/index.html> (accessed February 16, 2021).
- [174] A.W. Mello, A. Nicolas, M.D. Sangid, Fatigue strain mapping via digital image

- correlation for Ni-based superalloys: The role of thermal activation on cube slip, *Mater. Sci. Eng. A.* 695 (2017) 332–341. <https://doi.org/10.1016/j.msea.2017.04.002>.
- [175] 2400 Temperature Controller / Programmer - Eurotherm by Schneider Electric, (n.d.). <https://www.eurotherm.com/en/products/temperature-controllers-en/single-loop-temperature-controllers-en/2400-temperature-controller-programmer/> (accessed February 16, 2021).
- [176] B.O. Poole, Deformation mechanisms in iron-base hard facing alloys, Imperial College London, 2020.
- [177] Picotech information sheet, (n.d.). <https://www.picotech.com/library/application-note/improving-the-accuracy-of-temperature-measurements> (accessed February 14, 2021).
- [178] R. Przeliorz, J. Piątkowski, THERMOPHYSICAL PROPERTIES OF NICKEL-BASED CAST SUPERALLOYS, 2015.
- [179] Research Inc. SpotIR manual, (n.d.). http://www.pcscontrols.com/sites/default/files/SpotIR_Model4150_User_Manual.pdf (accessed February 15, 2021).
- [180] J. Jiang, T. Zhang, F.P.E.E. Dunne, T. Ben Britton, Deformation compatibility in a single crystalline Ni superalloy, *Proc. R. Soc. A Math. Phys. Eng. Sci.* 472 (2016) 20150690. <https://doi.org/10.1098/rspa.2015.0690>.
- [181] G. Bradski, The OpenCV Library, Dr Dobbs J. Softw. Tools. (2000).
- [182] Joblib: running Python functions as pipeline jobs — joblib 1.1.0.dev0 documentation, (n.d.). <https://joblib.readthedocs.io/en/latest/> (accessed February 15, 2021).
- [183] C.R. Harris, K.J. Millman, S.J. van der Walt, R. Gommers, P. Virtanen, D. Cournapeau,

- E. Wieser, J. Taylor, S. Berg, N.J. Smith, R. Kern, M. Picus, S. Hoyer, M.H. van Kerkwijk, M. Brett, A. Haldane, J.F. del Río, M. Wiebe, P. Peterson, P. Gérard-Marchant, K. Sheppard, T. Reddy, W. Weckesser, H. Abbasi, C. Gohlke, T.E. Oliphant, Array programming with NumPy, *Nature*. (2020). <https://doi.org/10.1038/s41586-020-2649-2>.
- [184] G. Vend Roux, W.G. Knauss, Submicron deformation field measurements: Part 2. Improved digital image correlation, *Exp. Mech.* 38 (1998) 86–92. <https://doi.org/10.1007/BF02321649>.
- [185] M. Guizar-Sicairos, S.T. Thurman, J.R. Fienup, Efficient subpixel image registration algorithms, *Opt. Lett.* 33 (2008) 156. <https://doi.org/10.1364/ol.33.000156>.
- [186] J.P. Lewis, Fast Template Matching, *Vision Interface 95*, Canadian Image Processing and Pattern Recognition Society, n.d.
- [187] P.E. Anuta, Spatial Registration of Multispectral and Multitemporal Digital Imagery Using Fast Fourier Transform Techniques, *IEEE Trans. Geosci. Electron.* 8 (1970) 353–368. <https://doi.org/10.1109/TGE.1970.271435>.
- [188] B. Pan, K. Qian, H. Xie, A. Asundi, Two-dimensional digital image correlation for in-plane displacement and strain measurement: A review, *Meas. Sci. Technol.* 20 (2009) 062001. <https://doi.org/10.1088/0957-0233/20/6/062001>.
- [189] W. Tong, An Evaluation of Digital Image Correlation Criteria for Strain Mapping Applications, *Strain.* 41 (2005) 167–175. <https://doi.org/10.1111/j.1475-1305.2005.00227.x>.
- [190] M. Schneider, E.P. George, T.J. Manescau, T. Zálezák, J. Hunfeld, A. Dlouhý, G. Eggeler, G. Laplanche, Analysis of strengthening due to grain boundaries and annealing

- twin boundaries in the CrCoNi medium-entropy alloy, *Int. J. Plast.* 124 (2020) 155–169.
<https://doi.org/10.1016/j.ijplas.2019.08.009>.
- [191] Z. Zhang, Z. Yang, S. Lu, A. Harte, R. Morana, M. Preuss, Strain localisation and failure at twin-boundary complexions in nickel-based superalloys, *Nat. Commun.* (2020).
<https://doi.org/10.1038/s41467-020-18641-z>.
- [192] Y. Dong, H. Kakisawa, Y. Kagawa, Development of microscale pattern for digital image correlation up to 1400 °C, *Opt. Lasers Eng.* 68 (2015) 7–15.
<https://doi.org/10.1016/j.optlaseng.2014.12.003>.
- [193] A.D. Kammers, S. Daly, Digital Image Correlation under Scanning Electron Microscopy: Methodology and Validation, *Exp. Mech.* 53 (2013) 1743–1761.
<https://doi.org/10.1007/s11340-013-9782-x>.
- [194] P.J. Guruprasad, A.A. Benzerga, Size effects under homogeneous deformation of single crystals: A discrete dislocation analysis, *J. Mech. Phys. Solids.* 56 (2008) 132–156.
<https://doi.org/10.1016/j.jmps.2007.03.009>.
- [195] B. Kondori, A. Needleman, A. Amine Benzerga, Discrete dislocation simulations of compression of tapered micropillars, *J. Mech. Phys. Solids.* 101 (2017) 223–234.
<https://doi.org/10.1016/j.jmps.2017.01.015>.
- [196] E. Tarleton, D.S. Balint, J. Gong, A.J. Wilkinson, A discrete dislocation plasticity study of the micro-cantilever size effect, *Acta Mater.* 88 (2015) 271–282.
<https://doi.org/10.1016/j.actamat.2015.01.030>.
- [197] Y. Xu, D.S. Balint, D. Dini, A new hardness formula incorporating the effect of source density on indentation response: A discrete dislocation plasticity analysis, *Surf. Coatings Technol.* 374 (2019) 763–773. <https://doi.org/10.1016/j.surfcoat.2019.06.045>.

- [198] V.S. Deshpande, A. Needleman, E. Van Der Giessen, Discrete dislocation plasticity analysis of static friction, *Acta Mater.* 52 (2004) 3135–3149. <https://doi.org/10.1016/j.actamat.2004.03.018>.
- [199] D.S. Balint, V.S. Deshpande, A. Needleman, E. Van Der Giessen, Size effects in uniaxial deformation of single and polycrystals: A discrete dislocation plasticity analysis, *Model. Simul. Mater. Sci. Eng.* 14 (2006) 409–422. <https://doi.org/10.1088/0965-0393/14/3/005>.
- [200] R. Maaß, S. Van Petegem, D. Ma, J. Zimmermann, D. Grolimund, F. Roters, H. Van Swygenhoven, D. Raabe, Smaller is stronger: The effect of strain hardening, *Acta Mater.* 57 (2009) 5996–6005. <https://doi.org/10.1016/j.actamat.2009.08.024>.
- [201] S.S. Shishvan, R.M. McMeeking, T.M. Pollock, V.S. Deshpande, Discrete dislocation plasticity analysis of the high-temperature cyclic response of composites, *Mater. Sci. Eng. A.* 712 (2018) 714–719. <https://doi.org/10.1016/j.msea.2017.12.034>.
- [202] S.S. Shishvan, R.M. McMeeking, T.M. Pollock, V.S. Deshpande, Discrete dislocation plasticity analysis of the effect of interfacial diffusion on the creep response of Ni single-crystal superalloys, *Acta Mater.* 135 (2017) 188–200. <https://doi.org/10.1016/j.actamat.2017.06.026>.
- [203] M.P. O’Day, W.A. Curtin, Bimaterial interface fracture: A discrete dislocation model, *J. Mech. Phys. Solids.* 53 (2005) 359–382. <https://doi.org/10.1016/j.jmps.2004.06.012>.
- [204] T.E.J. Edwards, F. Di Gioacchino, H.P. Springbett, R.A. Oliver, W.J. Clegg, Stable Speckle Patterns for Nano-scale Strain Mapping up to 700 °C, *Exp. Mech.* 57 (2017) 1469–1482. <https://doi.org/10.1007/s11340-017-0317-8>.
- [205] C. Zhao, D. Stewart, J. Jiang, F.P.E. Dunne, A comparative assessment of iron and

- cobalt-based hard-facing alloy deformation using HR-EBSD and HR-DIC, *Acta Mater.* 159 (2018) 173–186. <https://doi.org/10.1016/j.actamat.2018.08.021>.
- [206] A.J. Wilkinson, G. Meaden, D.J. Dingley, High-resolution elastic strain measurement from electron backscatter diffraction patterns: New levels of sensitivity, *Ultramicroscopy*. 106 (2006) 307–313. <https://doi.org/10.1016/j.ultramic.2005.10.001>.
- [207] T.B. Britton, A.J. Wilkinson, Measurement of residual elastic strain and lattice rotations with high resolution electron backscatter diffraction, *Ultramicroscopy*. 111 (2011) 1395–1404. <https://doi.org/10.1016/j.ultramic.2011.05.007>.
- [208] W. Pantleon, Resolving the geometrically necessary dislocation content by conventional electron backscattering diffraction, *Scr. Mater.* 58 (2008) 994–997. <https://doi.org/10.1016/j.scriptamat.2008.01.050>.
- [209] E. Van der Giessen, A. Needleman, Discrete dislocation plasticity: A simple planar model, *Model. Simul. Mater. Sci. Eng.* 3 (1995) 689–735. <https://doi.org/10.1088/0965-0393/3/5/008>.
- [210] J.R. Rice, TENSILE CRACK TIP FIELDS IN ELASTIC-IDEALLY PLASTIC CRYSTALS, 1987.
- [211] Y. Xu, K. Fox, D. Rugg, F.P.E. Dunne, Cyclic plasticity and thermomechanical alleviation in titanium alloys, *Int. J. Plast.* 134 (2020). <https://doi.org/10.1016/j.ijplas.2020.102753>.
- [212] D. Kiener, P.J. Guruprasad, S.M. Keralavarma, G. Dehm, A.A. Benzerga, Work hardening in micropillar compression: In situ experiments and modeling, *Acta Mater.* 59 (2011) 3825–3840. <https://doi.org/10.1016/j.actamat.2011.03.003>.
- [213] N. Prastiti, D. Balint, Y. Xu, F. Dunne, Discrete dislocation, crystal plasticity and

- experimental studies of fatigue crack nucleation in single-crystal nickel, *Int. J. Plast.* 126 (2020). <https://doi.org/10.1016/j.ijplas.2019.10.003>.
- [214] Y. Xu, D.S. Balint, D. Dini, A method of coupling discrete dislocation plasticity to the crystal plasticity finite element method, *Model. Simul. Mater. Sci. Eng.* 24 (2016) 045007. <https://doi.org/10.1088/0965-0393/24/4/045007>.
- [215] M.A. Sutton, N. Li, & D.C. Joy, A.P. Reynolds, X. Li, Scanning Electron Microscopy for Quantitative Small and Large Deformation Measurements Part I: SEM Imaging at Magnifications from 200 to 10,000, (n.d.). <https://doi.org/10.1007/s11340-007-9042-z>.
- [216] M.I. Latypov, J.C. Stinville, J.R. Mayeur, J.M. Hestoffer, T.M. Pollock, I.J. Beyerlein, Insight into microstructure-sensitive elastic strain concentrations from integrated computational modeling and digital image correlation, *Scr. Mater.* 192 (2021) 78–82. <https://doi.org/10.1016/j.scriptamat.2020.10.001>.
- [217] B. Chen, J. Jiang, F.P.E. Dunne, Microstructurally-sensitive fatigue crack nucleation in Ni-based single and oligo crystals, *J. Mech. Phys. Solids.* 106 (2017) 15–33. <https://doi.org/10.1016/j.jmps.2017.05.012>.
- [218] Y. Xu, W. Wan, F.P.E. Dunne, Microstructural fracture mechanics: Stored energy density at fatigue cracks, *J. Mech. Phys. Solids.* 146 (2021) 104209. <https://doi.org/10.1016/j.jmps.2020.104209>.

Appendices

Appendix A

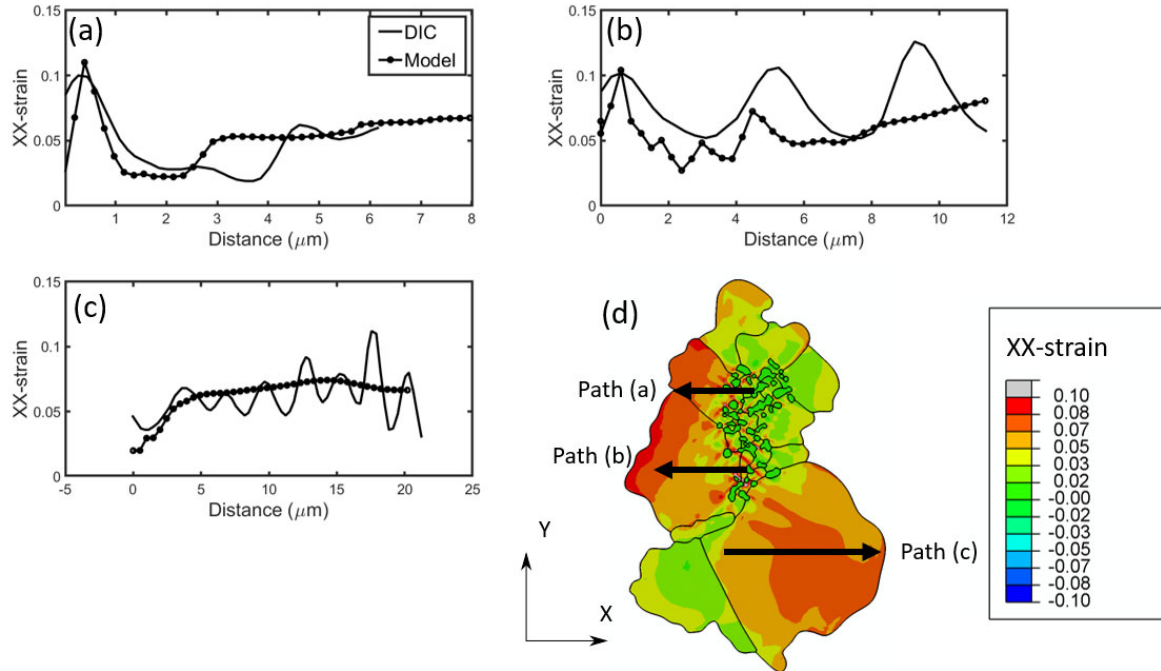


Figure A1, XX-strain across path profiles from DIC measurements [51], and model predictions. Figures a, b and c correspond to paths (a), (b) and (c) respectively

Figure A1 shows variations of XX-strain after the second cycle of loading in the experiment obtained by DIC [51] and predicted by the CPFE model. Three paths are chosen showing relatively good agreement between experiment and model. Naturally, the HR-DIC technique (with sub- μm resolution) picks up highly localised slip activity which the crystal plasticity approach cannot but some of the key features and magnitudes of the strain distributions are captured.